

EXPLORING THE ROLE OF A-TYPE LAMINS IN CELLULAR OXIDATIVE STRESS

Tom Sieprath

A dissertation submitted to Ghent University in partial
fulfilment of the requirements for the degree of
Doctor of Applied Biological Sciences: Cell and Gene Biotechnology,
and to the University of Antwerp in partial
fulfilment of the requirements for the degree of
Doctor of Bioscience Engineering.

2017

Promotors

Prof. Winnok De Vos

Laboratory of Cell Biology and Histology, Department of Veterinary Sciences,
University of Antwerp, Antwerp, Belgium

Prof. Els Van Damme

Biochemistry and Glycobiology, Department of Molecular Biotechnology, Ghent
University

Dean

Prof. Marc Van Meirvenne (Faculty of Bioscience Engineering - Ghent University)

Nick Schryvers (Faculty of Science - University of Antwerp)

Rector

Prof. Rik Van de Walle (Ghent University)

Prof. Herman Van Goethem (University of Antwerp)

Board of examiners

Prof. Stefaan De Smet (Chairman)
Faculty of Bioscience Engineering, Ghent University

Prof. Andreja Rajkovic (Secretary),
Faculty of Bioscience Engineering, Ghent University

Prof. Werner Koopman
Radboud Institute for Molecular Life Sciences, Radboud University Medical Center

Prof. Erik Manders
Institute for Life Sciences, University of Amsterdam

Dr. Filip Matthijssens
Center for Medical Genetics, Ghent University

*Opa, you are the wisest man I know, and the reason I took this road.
Therefore, I would like to dedicate this PhD to you.*

TABLE OF CONTENTS

Table of Contents	i
Acknowledgements	iii
Dankwoord	v
Summary	viii
Samenvatting.....	ix
List of abbreviations.....	xi
Chapter 1: Introduction	1
1 Nuclear lamins.....	2
2 Principles of cellular redox biology	8
3 Oxidative stress as emerging hallmark of laminopathies	15
4 Quantitative Microscopy of Cellular Redox Biology.....	19
5 Scope	25
Chapter 2: Quantitative comparison of experimental perturbations of a-type lamin metabolism	29
Abstract.....	30
1 Introduction.....	30
2 Results	32
3 Discussion	46
4 Materials and methods	48
Chapter 3: High-content quantification of intracellular ros levels and mitochondrial morphofunction.....	53
Abstract.....	54
1 Introduction.....	54
2 Results	55
3 Discussion	61
4 Methods.....	63
Chapter 4: Sustained accumulation of prelamin a and depletion of lamin a/c both cause oxidative stress and mitochondrial dysfunction but induce different cell fates..	71
Abstract.....	72
1 Introduction.....	72
2 Results	73
3 Discussion	78
4 Materials and methods	81
Chapter 5: Persistent perturbation of a-type lamin metabolism induces oxidative stress by inhibition of protein degradation pathways	87
Abstract.....	88
1 Introduction.....	88
2 Results	89

3	Discussion	96
4	Materials and Methods	99
Chapter 6: General discussion		105
1	Sustained siRNA-mediated knockdowns of <i>LMNA</i> and <i>ZMPSTE24</i> recapitulate the hallmarks of their patient-cell counterparts	106
2	High-throughput microscopy offers insight in cellular redox biology with deep coverage	108
3	Lamins as mediators of oxidative stress	110
4	Main results and perspectives	113
Bibliography		115
Curriculum vitae		137

ACKNOWLEDGEMENTS

This research was supported by the University of Antwerp (TTBOF/29267, TTBOF/30112), the Special Research Fund of Ghent University (project BOF/11267/09), the Hercules foundation (AUGE/013), NB-Photonics (Project code 01-MR0110) and the CSBR (Centers for Systems Biology Research) initiative from The Netherlands Organization for Scientific Research (NWO; No: CSBR09/013V). Printing of this manuscript was sponsored by Nikon Belux.

We also acknowledge the invaluable contributions made by the families consenting to donate skin biopsies for fibroblast cultures. Dr. R. Hennekam (University of Amsterdam, The Netherlands) and Prof. Dr. B. Van Engelen (UMC St. Radboud University, the Netherlands) are acknowledged for sharing the HGPS (LMNA+/G608G) and LMNAY259X/Y259X cells.

AAN WIE IK MIJN DOCTORAAT TE DANKEN HEB

In zowat alle soorten geschreven werk is het dankwoord een stukje tekst dat amper gelezen wordt. In een doctoraat daarentegen heeft het de bedenkelijke eer om veruit het meest gelezen stuk van het hele manuscript te zijn. Dit kan liggen aan de vaak droge inhoud van de rest van het werk, maar zeker ook aan het feit dat een doctoraat een resultaat is van vele samenwerkingen, dewelke natuurlijk allemaal willen weten of, en hoe ze bedankt worden. In mijn ogen gebeurde dit meestal met een aaneenschakeling van melige odes aan verschillende collega's en vrienden die eerder verplicht dan vrijwillig leken te zijn. Gaandeweg echter, ben ik erachter gekomen dat het welgemeende uitingen van dankbaarheid en appreciatie zijn, voor mensen zonder wie het voltooien van een doctoraat zo goed als onmogelijk zou geweest zijn. Het is dan ook in dit licht dat mijn dankwoord gezien moet worden, als oprechte dank aan iedereen die bijgedragen heeft aan het welslagen van deze onvergetelijke onderneming.

Winnok, als ik de persoon zou moeten noemen die het meest heeft bijgedragen aan mijn doctoraat ben jij het. Ik was je eerste doctoraatstudent, en omdat we eigenlijk niet zoveel schelen in leeftijd zijn we van in het begin meer vrienden geweest dan baas en werknemer. Desondanks was, en is jouw mening altijd heel belangrijk voor mij. Ik heb dat misschien nooit duidelijk gezegd, maar heel erg bedankt voor de kilometers feedback die je typte bij elk manuscript of bij elke poster of presentatie. Het maakte niet uit of ik het maandag, vrijdag of in het weekend doorstuurde, meestal had ik de dag erna al antwoord. Ik heb er soms zwaar op zitten vloeken, maar ik heb er ook enorm veel aan gehad en het heeft de kwaliteit van mijn onderzoek, en mijn kritische ingesteldheid naar een hoger niveau getild. Ik kan eerlijk zeggen dat ik nooit zover geraakt zou zijn zonder jouw motivatie en hulp. Els, jij fungeerde als mijn promotor in Gent. En ondanks dat je weinig of niets te maken had met het onderzoek dat ik deed, kon ik toch altijd bij jou binnenvallen voor feedback of met administratieve vragen.

Tobias, toen ik begon aan mijn doctoraat, begon jij aan je masterproef en het jaar erna zou je zelf je doctoraat beginnen. Nu, 6 jaar later doen we in dezelfde maand onze publieke verdediging, en ik denk dat ik voor ons beiden spreek als ik zeg dat we een hele leuke tijd beleefd hebben. Door de beperkte omvang van onze groep waren we vaak op ons tweeën aangewezen maar dat werkte perfect. Op professioneel vlak gingen we door dezelfde hoogtes en laagtes en konden we altijd bij elkaar terecht. En ook daarnaast hebben we menig pintje gedeeld en veel plezier gemaakt. Bedankt voor alles maat. Hetzelfde geldt voor Pieter, technisch gezien hoorde je niet bij onze groep, maar in de praktijk zeker wel. Merci voor al de wetenschappelijke (en natuurlijk ook de niet-wetenschappelijke) ping-pong en de hulp, elke keer ik die nodig had.

Kristof, het eerste jaar behoorde jij ook tot het core-team, als laborant heb je me veel protocols aangeleerd en zorgde je voor sfeer in het lab, zoals met de weefselweekfeestjes op vrijdag. Het andere ondersteunende personeel mag ik natuurlijk ook niet vergeten. Sofie en Fien op het secretariaat, de ruggegraat van de vakgroep, niets is teveel voor jullie. Ik kan jullie niet genoeg bedanken voor de hulp

die jullie boden bij álles wat ik vroeg. Ik kan me geen enkele keer herinneren dat jullie me niet onmiddellijk geholpen hebben, ookal was het heel druk met andere dingen, en altijd met de glimlach, alsof het niets was, duizend maal bedankt. Geert, omdat je (bio)veiligheidscoördinator was moest je regelmatig grommelen omdat ik of iemand anders weer eens iets verkeerd had gedaan, sorry daarvoor, maar weet dat ik je echt een schitterende en slimme kerel vind. Ik wil je ook speciaal bedanken voor alle hulp met de microscopie, en voor elke keer dat je me uit de nood hebt geholpen als er weer eens een apparaat stuk ging of moeilijk deed. Aan Julie, de poetsvrouw die elke week vriendelijk mijn bureau kwam poetsen, moest je dit ooit lezen, bedankt voor de vele (v)luchtige babbels, dat was elke keer plezant.

Lander, mede-assistent, jij verdient ook een uitgebreide dankjewel, jij hoort zeker ook in het rijtje van de mensen die onzelfzuchtig hulp bieden élke keer het nodig is. Je zorgt ervoor dat iedereen zich onmiddellijk welkom voelt en je bent altijd te vinden voor een grapje of een grolletje. Je bent 100% goedheid, en dat is fantastisch. Ik mag zeker ook de andere assistenten niet vergeten. Lore, met wie ik samen begon en ook samen eindig, Jonas V, Stefanie, Matthias, Sarah en nu ook Jonas D en Joost. De AAPjes waren altijd een leuke bende, met monkey-day als extraprofessionele exponent hiervan.

Ook bedankt aan alle thesisstudenten die ik heb mogen begeleiden, Ludger, Joke, Sara, Michaël en Jon, het was me een genoegen om elk van jullie te leren kennen en te zien ontwikkelen in zelfstandige en kritische wetenschappers. Jullie zorgden niet alleen voor ambiance, jullie werk heeft ook een mooie bijdrage geleverd aan dit doctoraat. Zeker jij, Joke, je hebt me meermaals last minute uit de nood geholpen.

Uit Nederland wil ik graag Werner bedanken, voor de mogelijkheid om bij u een aantal technieken te komen leren die de basis hebben gevormd voor de ontwikkeling van de microscopische methode die beschreven staat in dit doctoraat, en voor de nuttige feedback bij elk artikel dat eruit voortkwam. Ook bedankt aan Marco om 10 dagen dag en nacht beschikbaar te zijn en mij te helpen tijdens mijn verblijf bij jullie.

Goede samenwerkingen en een aangename sfeer op het werk zijn belangrijk, maar daarbuiten is ook voldoende steun nodig om succesvol te kunnen zijn. Een doctoraat kan soms ook een eenzame onderneming zijn. Dan is het goed dat je hierover met buitenstaanders in hetzelfde schuitje kunt praten. PJ en FM, jullie hebben deze rol met verve opgenomen. Horen dat jullie met dezelfde problemen zaten, of dezelfde dingen doormaakten, plaatste veel dingen in een ander/beter perspectief en was vaak al genoeg om opnieuw vol goede moed verder te kunnen. Daarnaast zijn jullie natuurlijk ook gewoon twee heel goede vrienden, naar wie ik opkijk en met wie ik nog veel glazen wil heffen in de toekomst.

Slechte resulaten, of strakke deadlines kunnen op je gemoed werken en je privéleven beïnvloeden. Ik mag mezelf echter gelukkig prijzen met een ongelooflijk begripvolle en steunende vrouw. Amelie, waar moet ik beginnen? De vaak onregelmatige uren die bij een doctoraat horen zijn nooit een probleem geweest voor jou, je verhuisde dichterbij naar Gent toe voor mij, je beurde mij op als er weer eens een experiment mislukte en was mee enthousiast wanneer de dingen wel goed gingen. Thuiskomen na een lange

dag en onmiddellijk mijn voeten onder tafel kunnen schuiven lijkt maar iets kleins, maar het is een ongelooflijke luxe waar ik altijd enorm dankbaar voor ben geweest. Jij bent mijn soulmate, de persoon die mijn leven op orde houdt en die mij met een paar woorden kan kalmeren en terug op het juiste pad kan brengen. Je noemt mij vaak je rots, maar weet dat jij eigenlijk de echte rots bent.

Een speciale vermelding gaat ook naar mijn schoonouders Martine en Etienne, het schrijven van dit manuscript viel samen met onze verhuis en verbouwingen. Omdat we toen bij jullie konden wonen en we ons van niets iets moesten aantrekken is het gelukt dit alles te combineren. Het zou zeker dubbel zo lang hebben geduurd zonder jullie hulp.

En als laatste natuurlijk mijn ouders, bedankt voor de mogelijkheid om van kleins af aan, en in alle vrijheid mijn dromen na te jagen. Waar ik ook mee afkwam, het was altijd goed en werd altijd gesteund. Zonder deze open mentaliteit zou ik waarschijnlijk nooit aan dit doctoraat begonnen zijn.

Ik ben waarschijnlijk nog mensen vergeten, indien je jezelf niet terug vindt hierboven, neem het me alstublieft niet kwalijk. Veel beter is mij bellen, erop wijzen, en zeggen dat ik je daarom een pintje moet trakteren.

Diepenbeek, september 2016
Tom Sieprath

SUMMARY

Every cell contains the genetic information needed to create an entire organism. This blueprint is stored in the cell nucleus. The nucleus continuously regulates the accessibility of this information based on ever-changing intra- and extracellular stimuli. Therefore, proper functioning of the nucleus is crucial for cellular and organismal survival. The nuclear lamina, a perinuclear network composed of type V intermediate filaments called lamins, is emerging as key regulator in nuclear organization. It physically shapes the nucleus, influences gene expression and modulates cell differentiation. As a direct reflection of this multifunctional role, mutations in *LMNA*, one of three genes encoding lamins, have been linked with more diseases than any other human gene. A recent addition to the expanding list of functions of the nuclear lamina is an apparent involvement in cellular redox homeostasis. Indeed, cells from patients suffering from various laminopathies display increased levels of intracellular reactive oxygen species (ROS) and often show a higher susceptibility towards induced ROS. The underlying pathways however, remain poorly understood. The goal of this PhD dissertation was to obtain a better insight in this novel putative pathogenic feature.

Chapter 1 comprises a general introduction into lamin biology and the state of the art with respect to their involvement in redox biology, next to a guide into fluorescence microscopy of redox-related processes.

In Chapter 2, a quantitative comparison and characterization is presented of various experimental perturbations to interfere with lamin A metabolism in primary fibroblast cells. Based on the results shown in this chapter, perturbations were selected to create the models that were used in the experiments in chapters 4 & 5.

In chapter 3, the development and benchmarking of a novel high-content microscopy method for the simultaneous measurement of intracellular ROS levels and mitochondrial function is outlined, together with a complementary automated analysis pipeline.

The application of the newly developed method from Chapter 3 on the selected models from Chapter 2 culminated in the discovery that distinct lamin variants induce divergent oxidative responses, eventually resulting in different cell fates (Chapter 4), and pointed to the involvement of perturbed protein degradation pathways as a causal factor for oxidative stress (Chapter 5).

SAMENVATTING

Elke cel bevat in zijn DNA de volledige genetische blauwdruk om een functioneel organisme te maken. Op basis van extracellulaire en intracellulaire signalen bepaalt de celkern welke informatie op ieder moment nodig is en beschikbaar wordt gesteld. Het goed functioneren van de celkern is dus uiterst belangrijk voor het overleven van de cel, alsook het organisme waartoe de cel behoort. De nucleaire lamina is een perinucleair netwerk van type V intermediaire filamenten, die lamines genoemd worden, en speelt een belangrijke rol als regulator van de celkern. Lamines geven mechanische ondersteuning aan de kern, ze bepalen mede welke genen er afgeschreven worden via interacties met transcriptie factoren en met het DNA zelf, en kunnen de celcyclus en differentiatie beïnvloeden. Hun multifunctionele rol wordt ook geïllustreerd door het feit dat mutaties in het *LMNA* gen, dat codeert voor een belangrijke subset van lamines, meer ziektes veroorzaken dan mutaties in eender welk ander gen. Recent onderzoek suggereert dat lamines ook betrokken zijn bij de cellulaire redox homeostase. Cellen van patiënten met verschillende laminopathiën vertonen een verhoogde concentratie schadelijke reactieve zuurstofvormen, en vaak ook een verhoogde gevoeligheid hiervoor. De onderliggende mechanismen zijn echter nog niet opgehelderd. Het doel van dit doctoraatsonderzoek was om hier een beter inzicht in te krijgen.

In Hoofdstuk 1 wordt een algemene introductie gegeven over lamines en laminebiologie, en wordt de huidige kennis geschetst met betrekking tot de rol van lamines in de intracellulaire redoxhuishouding. Daarnaast wordt ook beschreven waar men aandacht moet aan besteden bij het meten van redox-gerelateerde processen door middel van fluorescentie microscopie.

Hoofdstuk 2 bevat een kwantitatieve vergelijking en karakterisatie van verschillende methoden om de nucleaire lamina te verstoren en relevante cel modellen te genereren. Op basis hiervan werden de cel modellen geselecteerd die gebruikt werden in de experimenten in hoofdstukken 4 & 5.

Hoofdstuk 3 handelt over de ontwikkeling van een nieuwe high-content microscopie methode voor het meten van intracellulaire reactieve zuurstofvormen samen met een aantal mitochondriale parameters, en over de ontwikkeling van complementaire beeld en data-analyse software.

Deze methode werd toegepast op de geselecteerde modellen uit hoofdstuk 2, wat leidde tot de ontdekking dat specifieke lamine varianten tot een verschillende oxidatieve respons leiden, die uiteindelijk bepaalt welk lot een cel beschoren is (Hoofdstuk 4), en dat verstoorde proteïneafbraak een mogelijke oorzaak is van de geobserveerde oxidatieve stress (Hoofdstuk 5).

LIST OF ABBREVIATIONS

PLA:	prelamin A
PLB:	prelamin B
NLS:	nuclear localization signal
NES:	nuclear export signal
NE:	nuclear envelope
FT:	farnesyl transferase
RCE1:	Ras-converting enzyme 1
ICTM:	isoprenylcysteine carboxyl methyltransferase
ZMPSTE24:	zinc metalloprotease related to the STE24 homolog in yeast
HGPS:	Hutchinson-Gilford progeria syndrome
RD:	restrictive dermopathy
ROS:	reactive oxygen species
RNS:	reactive nitrogen species
$\Delta\psi_m$:	mitochondrial membrane potential
NTkd:	non-targeting knockdown
ZMPSTE24kd:	<i>ZMPSTE24</i> knockdown
LMNAkd:	<i>LMNA</i> knockdown
PDL:	population doubling level
NA:	numerical aperture
CM-H ₂ DCFDA:	5-(and-6)-chloromethyl-2',7'-dichlorodihydrofluorescein diacetate
DCF:	2,7-dichlorofluorescein
TBHP:	tert-butyl hydrogen peroxide
TMRM:	tetramethyl rhodamine methyl ester
DAPI:	4',6-diamino-2-phenylindole
OCR:	oxygen consumption rate
hMSC:	human mesenchymal stem cells
iPSC:	induced pluripotent stem cells
MEF:	mouse embryonic fibroblast
NHDF:	normal human dermal fibroblast
LINC:	trans-envelope linker of nucleus and cytoskeleton
NOX:	NADPH oxidase
GSSG:	glutathione disulfide
SOD:	superoxide dismutase
HT-LKO:	HT1080 <i>LMNA</i> knockout
HT-ZKO:	HT1080 <i>ZMPSTE24</i> knockout
HT-WT:	HT1080 wild-type
SQV:	saquinavir
FTI:	farnesyl transferase inhibitor
AFCMe:	N-acetyl-S-farnesyl-L-cysteine methylester
gRNA:	guide RNA
IL6:	interleukin 6



INTRODUCTION

Parts of this chapter are published in Sieprath et al. 2012¹ and Sieprath et al 2016².

1. Sieprath, T., Darwiche, R. & De Vos, W. H. Lamins as mediators of oxidative stress. *Biochem Biophys Res Commun* **421**, 635–639 (2012).
2. Sieprath, T., Corne, T. D. J., Willems, P. H. G. M., Koopman, W. J. H. & De Vos, W. H. Integrated High-Content Quantification of Intracellular ROS Levels and Mitochondrial Morphofunction. *Adv Anat Embryol Cell Biol* **219**, 149–177 (2016).

1 Nuclear lamins

1.1 Structure of the nuclear lamina

Fibers composed of nuclear lamins are the main components of the nuclear lamina, a dense network, roughly 10~80 nm thick, that is located just below, and is directly connected with, the inner nuclear membrane (**Fig. 1.1**).³⁻⁶ Together with the nuclear membranes, the nuclear lamina is an integral part of the nuclear envelope (NE), a structure that physically separates and protects the nuclear contents from the cytoplasm, and that only allows unrestricted bidirectional transport of macromolecules with a size up to the equivalent of small globular proteins of ~40 kDa, through the nuclear pore complexes.⁴ Larger molecules are conditionally transported through NPC, provided they carry the correct localization signals (Nuclear Localization Signal or NLS, Nuclear Export Signal or NES).

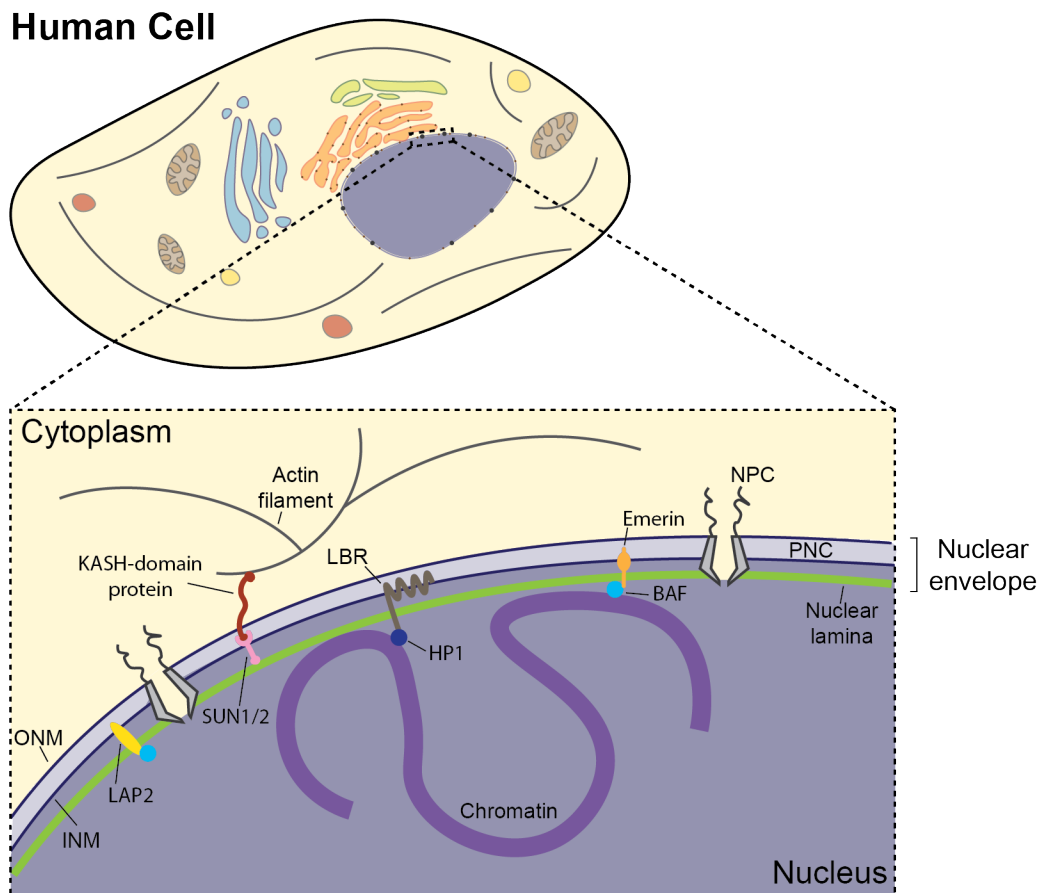


Figure 1.1: localization of the nuclear lamina.

The nuclear lamina (green line) is composed of various lamin proteins and is located just below the inner nuclear membrane. It provides support to the nucleus but also interacts with many different partners, some of which are shown (Lamina associated polypeptides 1 and 2 (LAP1/2), Emerin, Lamina B receptor (LBR) and SUN1/2), LBR contains a binding site for HP1 (heterochromatin protein 1), and emerlin contains a binding site for BAF (barrier to autointegration factor). Both HP1 and BAF link INM proteins to chromatin. Through a linker between nucleoskeleton and cytoskeleton complex (LINC), between SUN1/2 and KASH-domain proteins, the nuclear lamina is connected with the cytoskeleton. Abbreviations: ONM: Outer Nuclear Membrane, INM: Inner Nuclear Membrane, NPC: Nuclear Pore Complex, PNC: Perinuclear Space.

The fibers making up the nuclear lamina are type V intermediate filaments, composed of lamins. Lamins are subdivided into two classes, A-type lamins (lamin A, C, A Δ 10 and C2) and B-type lamins (lamin B1, B2 and B3), based on their biochemical properties, expression profile and their behaviour during mitosis.^{7,8} A-type lamins have a neutral isoelectric point, while B-type lamins are more acidic and during mitosis when the nuclear lamina transiently disassembles, A-type lamins are completely solubilized and dispersed, whereas B-type lamins remain associated with nuclear membranes structures.^{9,10} All A-type lamins are alternative splice-products of the *LMNA* gene, which is located on chromosome 1 and consist of 12 exons.⁹ Lamin A and C are the major A-type lamins, they are expressed in somatic cells and are identical up to codon 566, after which lamin C lacks the terminal part of exon 10 as well as exons 11 and 12³. Lamin A Δ 10 is a less abundant variant missing exon 10 only¹¹, whereas lamin C2 is a variant of lamin C that is uniquely expressed in germ cells and uses an alternative N-terminal exon, located in the first intron of the *LMNA* gene.⁹ Major B-type lamins B1 and B2 are products of *LMNB1* on chromosome 5 and *LMNB2* on chromosome 19, respectively, and are somatically expressed.^{3,12} The minor variant B3 is an alternative splice product of lamin B2 that has, similar to lamin C2, a modified N-terminus and is also only expressed in germ cells.^{9,12} Despite these differences, all lamins share a similar structure with a positively charged globular N-terminal head, a central rod containing four α -helical domains capable of forming coiled-coils (1A, 1B, 2A and 2B) separated by 3 linker regions (L1, L12 and L2), and a positively charged C-terminal globular domain containing an NLS and an immunoglobulin (Ig) fold (**Fig. 1.2A**).^{3,13,14}

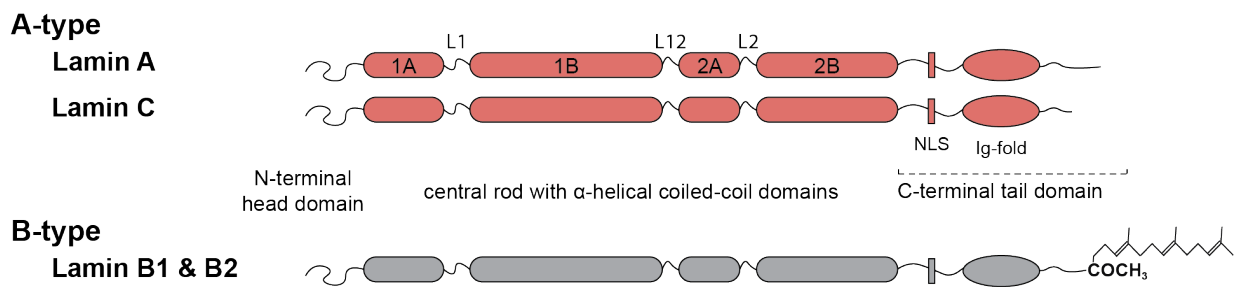


Figure 1.2: Schematic representation of the major A-type (lamin A & C) and B-type (B1 & B2) lamin proteins.

They all contain a positively charged N-terminal head domain, a central rod with 4 α -helical coiled coil domains and a positively charged C-terminal tail domain containing a nuclear localization signal (NLS) domain and an immunoglobulin (Ig) fold. The farnesyl- and methyl groups at the C-terminus of B-type lamins, are missing in A-type lamins.

Lamin C is immediately produced in its mature form. However, Lamin A and each of the B-type lamins are produced as immature prelamins. They all feature a C-terminal CaaX-motif (where 'C' is a Cysteine, 'a' is an aliphatic amino acid, and 'X' is variable but usually Methionine) that defines a site of post-translational farnesylation and carboxymethylation (**Fig. 1.3**).^{15,16} Soon after their synthesis, and presumably

after nuclear import, the cysteine is farnesylated by a soluble farnesyl transferase (FT).^{17,18} Next, the -aaX amino acids are removed by a CaaX prenyl protease (an endopeptidase). For prelamin A (PLA), this reaction is carried out by either Ras-converting enzyme 1 (RCE1) or Zinc metalloprotease related to the STE24 homolog in yeast (ZMPSTE24).¹⁹ For prelamin B (PLB), the cleavage is uniquely carried out by RCE1.²⁰ The now terminally farnesylated cysteine is then methylated by isoprenylcysteine carboxyl methyltransferase (ICTM).¹⁷ RCE1, ZMPSTE24 and ICTM all are integral membrane proteins located in the INM with their active sites facing the nucleoplasm, or in the ER membrane, with their active sites facing the cytoplasm.¹⁷ Attachment of the farnesyl and methyl groups enhances hydrophobic interactions with the inner nuclear membrane, presumably facilitating targeting of the lamins to the nuclear envelope. However, farnesylation is no absolute requirement for lamina localization because lamin C, that lacks a CaaX motif, also localizes to the nuclear envelope²¹. Once localized to the INM, lamin A, but not lamin B1 or B2, undergoes a final upstream endoprotease cleavage, also mediated by ZMPSTE24, removing the C-terminal 15 amino acids, including the farnesyl and methyl group.^{3,16,22}

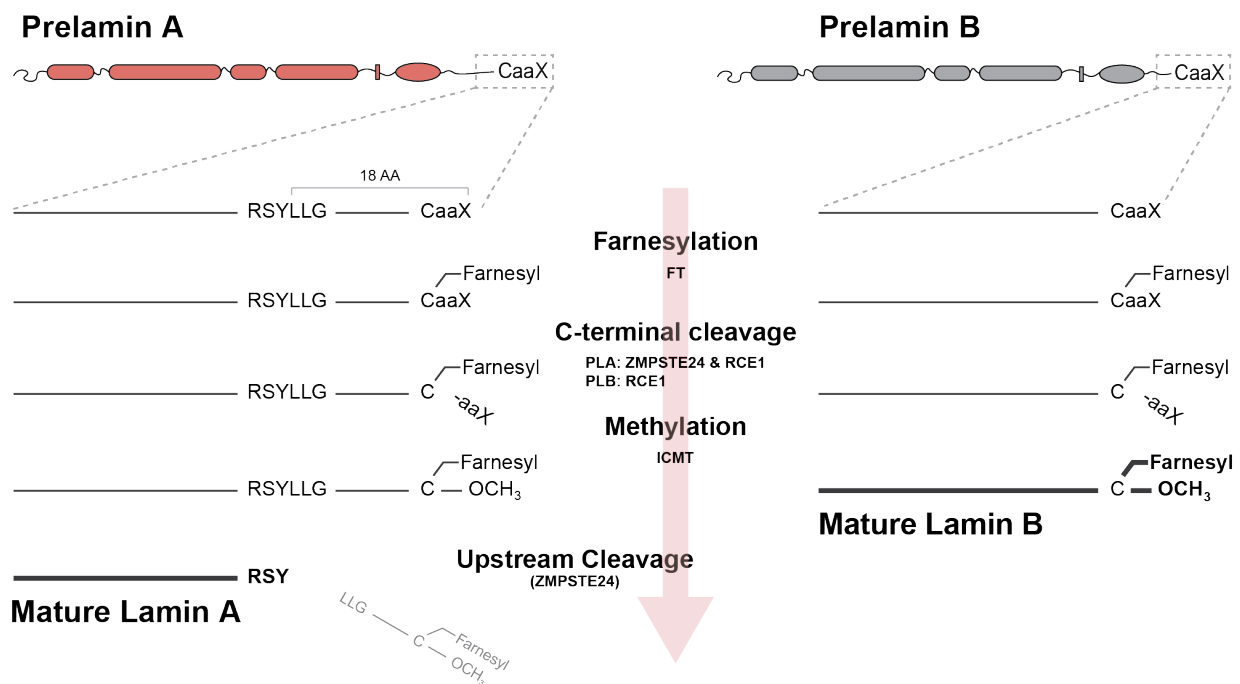


Figure 1.3: The carboxyterminal processing of A and B-type lamins.

The post-translational C-terminal processing of newly synthesized A-type lamins consists of 4 and that of B-type lamins of 3 distinct steps. First the cysteine of the C-terminal CaaX motif is farnesylated by farnesyl transferase (FT). Subsequently, the terminal 3 amino acids (aaX) are removed. In PLA this is done by Ras-converting enzyme 1 (RCE1) or Zinc metalloprotease related to the STE24 homolog in yeast (ZMPSTE24), in prelamin B (PLB) this is exclusively done by RCE1. In the third (and final for PLB) step, the now terminal cysteine residue is methylated by isoprenylcysteine carboxyl methyltransferase (ICTM). PLA then undergoes a final upstream cleavage of the terminal 15 amino acids including the farnesyl and methyl groups that is mediated by ZMPSTE24

In vivo, individual lamin polypeptides assemble into parallel homodimers, which in turn associate longitudinally to form polar head-to-tail polymer structures. These

head-to-tail polymers interact laterally to form protofilaments, which form mature lamin filaments of highly variable length, ranging from a few dozen to a few thousand nm. (Fig. 1.4).^{6,23} A- and B-type lamin filaments are distributed evenly, but in discrete patches, throughout the nuclear lamina.²⁴ A-type lamins, due to the lacking farnesyl, can also be found inside the nucleoplasm, this fraction is distinct from peripheral lamin A, in that it is not or less polymerized and is more soluble.²⁵

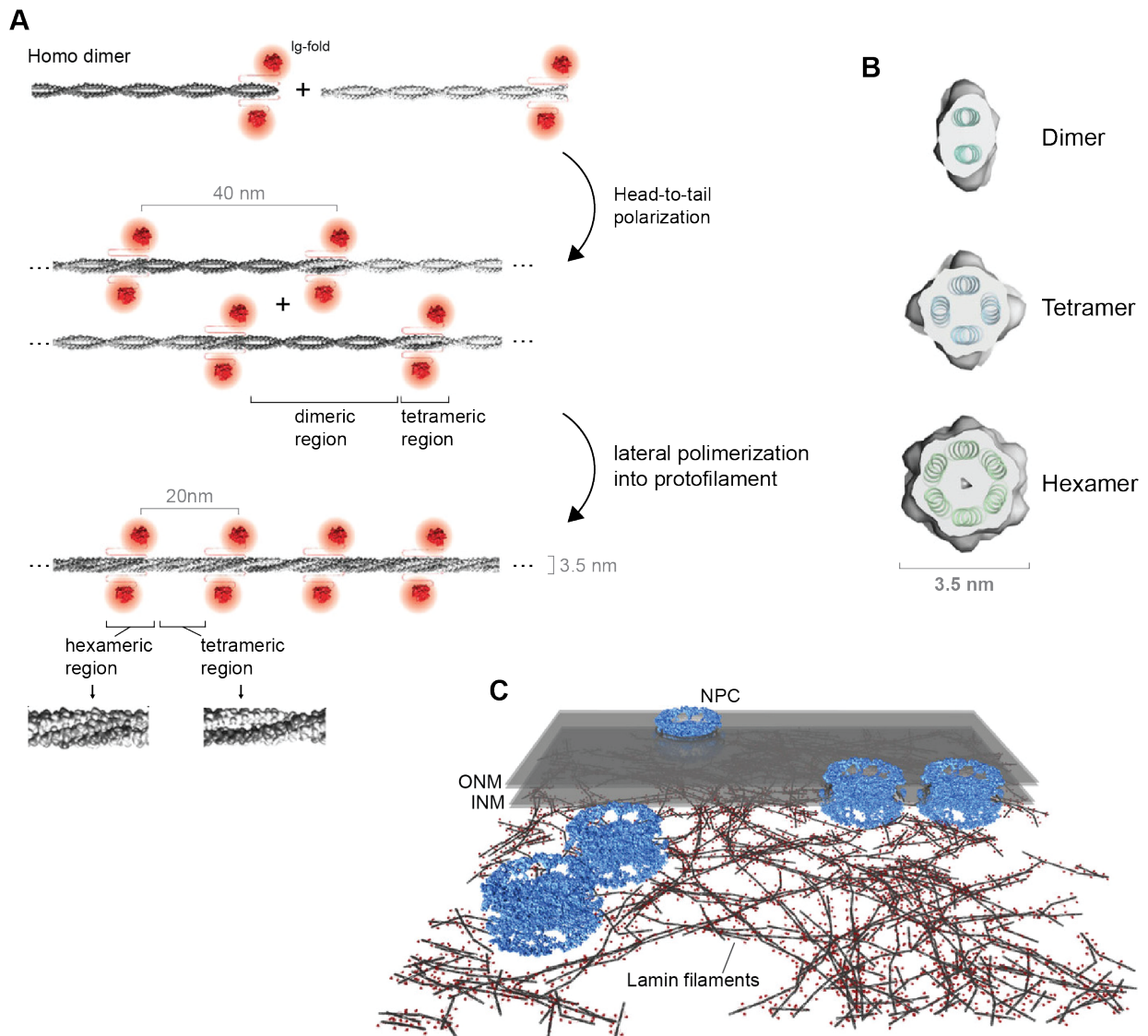


Figure 1.4: Polymerization of lamins into higher order structures.

(A) Individual Lamin polypeptides assemble first into parallel dimers. These dimers then associate longitudinally to produce polar head-to-tail polymer structures. Two head-to-tail polymers interact laterally to form protofilaments. (B) Representation of a cross-section through lamin dimers, tetramers and hexamers. (C) Model of the *in vivo* distribution of lamins in the nuclear envelope based cryo-tomogram. NPCs are shown in blue. The INM and ONM in transparent grey were added for visual orientation. Figure adapted from Turgay *et al.* 2017⁶

1.2 Functions of the nuclear lamina

The nuclear lamina has a multitude of functions, the most prominent one being its role in providing mechanical support for the nucleus.²⁶ Indeed, cells lacking A-type lamins exhibit increased numbers of misshapen nuclei, have severely reduced nuclear stiffness and are more prone to mechanical stress.^{26,27} Trans-envelope Linker of Nucleus and Cytoskeleton (LINC) complexes, composed of SUN-domain proteins and KASH-domain proteins (nesprins), connect the lamina to the cytoskeleton, creating one mechanosensitive continuum within the cell that allows nuclear positioning and nuclear response to mechanical cues in an integrated manner (**Fig. 1.1**).^{23,28,29} Lamins also modulate gene expression by coordinating chromatin organization.^{30,31} Interaction with chromatin occurs through binding to certain heterochromatic genomic regions, known as lamina-associated domains (LADs). For instance via LBR or emerin (**Fig. 1.1**), which have binding sites for HP1 (heterochromatin protein 1), and BAF (barrier to autointegration factor), respectively^{12,32}, two proteins that interact with specific histone modifications present in heterochromatin. Lamins can also (conditionally) sequester transcriptional regulators at the nuclear periphery, thereby activating or repressing their targets.³³ For example, sequestration of c-Fos by lamin A prevents dimer formation between c-Fos and c-Jun, which in turn suppresses Activation protein 1 (AP1) transcription factor activity.³⁴ AP-1 is involved in multiple essential cellular processes, including cell proliferation and differentiation. Besides direct interaction with transcription factors, lamins can also interact with transcription factors via lamin-associated proteins such as emerin and MAN1. Emerin regulates β -catenin activity by restricting its accumulation in the nucleus, and MAN1 can interact with SMADs and thereby antagonizes bone morphogenetic protein (BMP)- and transforming growth factor beta (TGF β)-signalling.³⁵⁻³⁷ Through these and similar interactions, the nuclear lamina is involved in many cellular processes including cell cycle control and DNA repair mechanisms.³⁸⁻⁴⁰

1.3 Laminopathies

Given the involvement in many cellular processes, it is not surprising that mutations in genes encoding components of the nuclear lamina lead to a plethora of different disorders (laminopathies). There are around 15 diseases directly linked with mutations in the *LMNA* gene, more than with any other human gene.⁴¹ Furthermore, lamin A-related laminopathies can also be caused by mutations in genes encoding prelamina-processing proteins, e.g. *ZMPSTE24*.³ Disease manifestations are very diverse. Some diseases are tissue specific. For instance, Emery-Dreifuss muscular dystrophy (AD-EDMD2/3)⁴², Limb-girdle muscular dystrophy (LGMD1B)⁴³ and dilated cardiomyopathy (CDM1A)⁴⁴ all affect striated muscle tissue, while Dunnigan-type familial partial lipodystrophy (FPLD2)⁴⁵ is characterized by loss of adipose tissue and Charcot-Marie-Tooth syndrome (CMT-2B1)⁴⁶ displays loss of peripheral nerve myelination. Other diseases have a systemic occurrence, like the Hutchinson-Gilford Progeria Syndrome (HGPS)^{47,48} or restrictive dermopathy (RD).^{49,50}

These last two diseases are caused by mutations interfering with the maturation process of lamin A. HGPS is most commonly caused by a single silent point mutation in exon 11 (C1824T). This mutation does not affect the coding sequence (G608G) but instead promotes the use of an alternative splice location leading to the deletion of 50 amino acids from PLA, including the final cleavage site for ZMPSTE24, resulting in the synthesis of a permanently farnesylated PLA variant called progerin (**Fig. 1.5**).^{51,52} RD in turn is caused by mutations resulting in the loss of ZMPSTE24, which also leads to the formation of farnesylated PLA.⁵⁰ Despite these diverse pathological phenotypes, laminopathies do share several features on the cellular level including misshapen nuclei, disorganization of heterochromatin, defects in the DNA damage response pathway and increased oxidative stress (cfr. below).^{1,7} These have prompted the proposal of several non-exclusive general hypotheses trying to explain disease development. The structural hypothesis suggests that *LMNA* mutations render the nucleus more fragile, causing cell death and progressive disease in tissues subjected to mechanical load, such as muscle.^{53,54} However, this does not explain the redistribution of adipose tissue in FPLD, or the systemic symptoms in HGPS. The gene regulation hypothesis postulates that perturbed interaction with tissue-specific transcription factors underlies the development of different disease phenotypes.^{3,54,55} A third hypothesis states that lamin perturbations lead to an impairment of adult stem cell function, either through increased cell death of fragile lamin A-deficient cells in tissues subjected to mechanical stress, or as a result of high cell turnover.^{56,57} Laminopathies can also be subdivided based on their causing mutations. Mutations resulting in loss of functional lamin A (loss-of-function mutations) and mutations leading to the synthesis of a toxic (pre)lamin A variant (toxic gain-of-function mutations). Loss-of-function mutations oftentimes correlate with muscular dystrophies³ and the structural hypothesis, while gain-of-function mutations regularly correlated with lipodystrophies or systemic progeroid syndromes.⁵⁸⁻⁶⁰

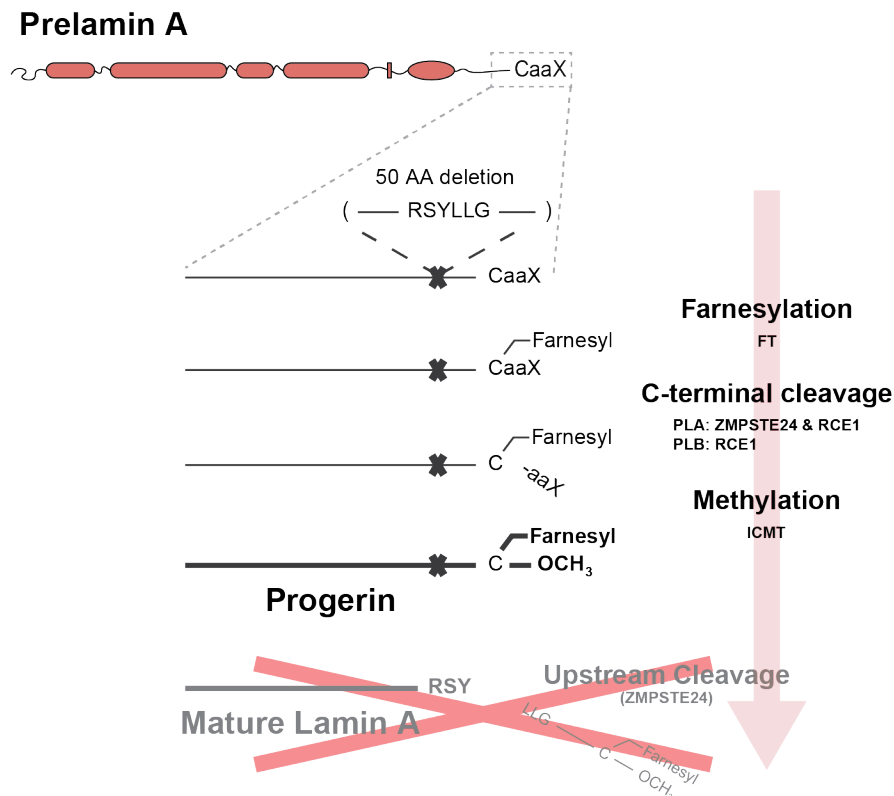


Figure 1.5: Synthesis of progerin.

The Hutchinson-Gilford Progeria Syndrome (HGPS) is caused by a silent point mutation resulting in the deletion of 50 C-terminal amino acids in PLA, including the final cleavage site for ZMPSTE24. As a consequence, a permanently farnesylated PLA variant called 'progerin' is synthesized.

2 Principles of cellular redox biology

Reactive oxygen species (ROS) are small, short-lived derivatives of molecular oxygen (O_2) of radical and non-radical nature.⁶¹ Radical ROS variants include: superoxide ($O_2^{\cdot-}$), hydroperoxyl (HO_2^{\cdot}), hydroxyl ($\cdot OH$), peroxy (RO_2^{\cdot}), alkoxy (RO^{\cdot}), carbonate ($CO_3^{\cdot-}$), carbon dioxide ($CO_2^{\cdot-}$), and singlet oxygen ($O_2^1\Sigma g^+$). Non-radical variants include: hydrogen peroxide (H_2O_2), hypobromous acid ($HOBr$), hypochlorous acid ($HOCl$), ozone (O_3), singlet oxygen ($O_2^1\Delta g$), organic peroxides ($ROOH$), peroxyxynitrite ($ONOO^-$), peroxyxynitrate (O_2NOO^-), nitrosoperoxyxynitrate ($ONOOOCO_2^-$) and peroxyxynitrate ($HOOCO_2^-$).⁶¹ Of these ROS, $ONOO^-$ and O_2NOO^- are also reactive nitrogen species (RNS). RNS further include nitric oxide (NO^{\cdot}), nitrogen dioxide (NO_2^{\cdot}), nitrate radical (NO_3^{\cdot}) and many other nitrogen derivatives.

ROS were originally described as molecular constituents of the defence system of phagocytic cells, but it has become clear that besides their damaging properties, they also function as signalling molecules and mediate a variety of other cellular responses including cell proliferation, differentiation, gene expression and migration.^{62,63} However, excessive ROS levels induce a state of oxidative stress, which is accompanied by irreversible oxidative damage to DNA, lipids and proteins.

Plasmamembrane Cyclooxygenases Lipoxygenases NAD(P)H oxidases Prostaglandin synthases	Lysosomes b-type cytochrome Flavins Myeloperoxidases Ubiquinone	Nucleus Nox4	ER/microsomes Cyt-b ₅ Cyt-P450 Nox4
Cytoplasm Catecholamines Riboflavin Xanthine oxidase	Transition metals Cu ⁺ /Cu ²⁺ Fe ²⁺ /Fe ³⁺	Exogenous Air pollutants Drugs γ-radiation Oxidants Smoke UV radiation	Peroxisomes Oxidases Peroxidases Flavoproteins
			Mitochondria

Figure 1.6: Sources of cellular reactive oxygen species (ROS).

Overview of various sources of ROS. Mitochondrial sources are outlined in more detail in Figure 1.8.

2.1 Intracellular ROS metabolism

ROS can be generated at various sites in the cell (**Fig. 1.6**). This can be either deliberately, e.g. by NADPH oxidases (NOX), or as a byproduct, e.g. during normal cellular respiration in mitochondria.⁶⁴⁻⁶⁶ The NOX family of NADPH oxidases (NOX1, NOX2, NOX3, NOX4, NOX5, DUOX1 and DUOX2) are proteins that transport electrons (e⁻) from NADPH across biological membranes (plasma or endomembranes).^{67,68} The activation mechanisms and tissue distribution of the isoforms differ but they all use O₂ as e⁻-acceptor, producing O₂^{•-}. Through ROS generation, they play a role in many cellular processes including host defence, regulation of gene expression and cell differentiation.⁶⁸ Despite their sometimes-significant contribution to the global ROS pools, NOX are not the predominant source of intracellular ROS. Mitochondria, in particular under pathological conditions, have this honor. Mitochondrial ROS are generated as a byproduct of the oxidative phosphorylation (OXPHOS, cfr. below).

Irrespective of its source, ROS production generally starts with the reduction of O₂ to O₂^{•-}, which is the precursor of most other ROS (**Fig. 1.7A**). Three major pathways can be discerned. First, O₂^{•-} can be converted, either spontaneously or, more likely, catalyzed by a superoxide dismutase (SOD), into H₂O₂ at a rate close to the diffusion limit ($k=2 \cdot 10^9 \text{ M}^{-1}\text{s}^{-1}$ at pH 7.4).⁶⁹⁻⁷² This damaging molecule is defused by several systems. It can be converted into water (H₂O) by multiple enzymes including peroxiredoxins, catalase (CAT) and glutathione peroxidases (GPX).⁷³ Proper function of these systems further requires the action of glutathione reductase (GR), thioredoxin (TRX), thioredoxin reductase (TRXR), glutaredoxin (GRX), peroxiredoxin (PRX), sulfiredoxin (SRX), the glutathione (GSH)-synthesizing enzymes glutathione synthase (GS), glutamate cysteine ligase (GCL) and ceruloplasmin.⁷³ In addition to enzymatic systems active in the cytoplasm and mitochondria, cells and tissues also contain antioxidants of non-enzymatic nature including phytochemicals, vitamins (A,C,E), ceruloplasmin and taurine, but especially glutathione (GSH) and thioredoxin (TRX).⁷³ Interestingly, these last two

systems are also active inside the nucleus, where they maintain a balance independently from the cytoplasm.⁷⁴ The cofactor NADPH (the reduced form of nicotinamide adenine dinucleotide phosphate) is central to cellular ROS removal through the GSH and TRX/PRX systems (**Fig. 1.7A**). In mitochondria, NADPH is mainly produced via: (i) NADP⁺-dependent isocitrate dehydrogenase and malic enzyme, and (ii) nicotinamide nucleotide transhydrogenase (Nnt). The latter enzyme utilizes the proton motive force (PMF) to generate NADPH from NADH and NADP⁺.⁷⁵ Besides the conversion into H₂O₂, O₂^{•-} can also react with nitric oxide (NO[•]), produced in a two-step reaction from L-arginine (L-arg), catalyzed by nitric oxide synthases (NOS). This gives rise to the production of reactive nitrogen species (RNS) peroxyntirite (ONOO⁻) and peroxyntirous acid (ONOOH). Various other reactions downstream of ONOO⁻ lead to formation of [•]OH, CO₃^{•-} and NO₂[•] (**Fig. 1.7A**).^{76,77} In the presence of ferric iron (Fe³⁺) the O₂^{•-} anion is converted into O₂ and ferrous iron (Fe²⁺), which can further react with H₂O₂ to reform Fe³⁺, hydroxide (OH⁻) and the highly reactive [•]OH (**Fig. 1.7A**).⁷⁸ [•]OH is one of the strongest oxidants in nature and is extremely damaging to biomolecules like DNA, proteins and lipids.^{79,80} It can initiate formation of lipid (L[•]) and lipid peroxy (LOO[•]) radicals (lipid peroxidation), which is counterbalanced by the action of various antioxidant systems including vitamin E/α-tocopherol (α-TOH), vitamin C/ascorbate (AscH⁻), NADPH/NADP⁺, GSH, GPX/GST and GR (**Fig. 1.7A**). Ultimately, sustained stimulation of lipid peroxidation will lead to formation of pentane and the reactive aldehydes malondialdehyde (MDA) and 4-hydroxynonenal (4-HNE). When generated at low levels, 4-HNE can interact with signaling targets, including JNK, P38 MAPK, cell cycle regulators, PKCβ, and PKCδ, leading to numerous cellular responses, ranging from increased expression of the antioxidant enzyme TRXR1 to irreversible cytotoxic injuries and cell death.^{81,82} Mitochondrial aldehyde dehydrogenase 2 (ALDH2) can protect against oxidative stress by detoxification of these cytotoxic aldehydes.⁸³

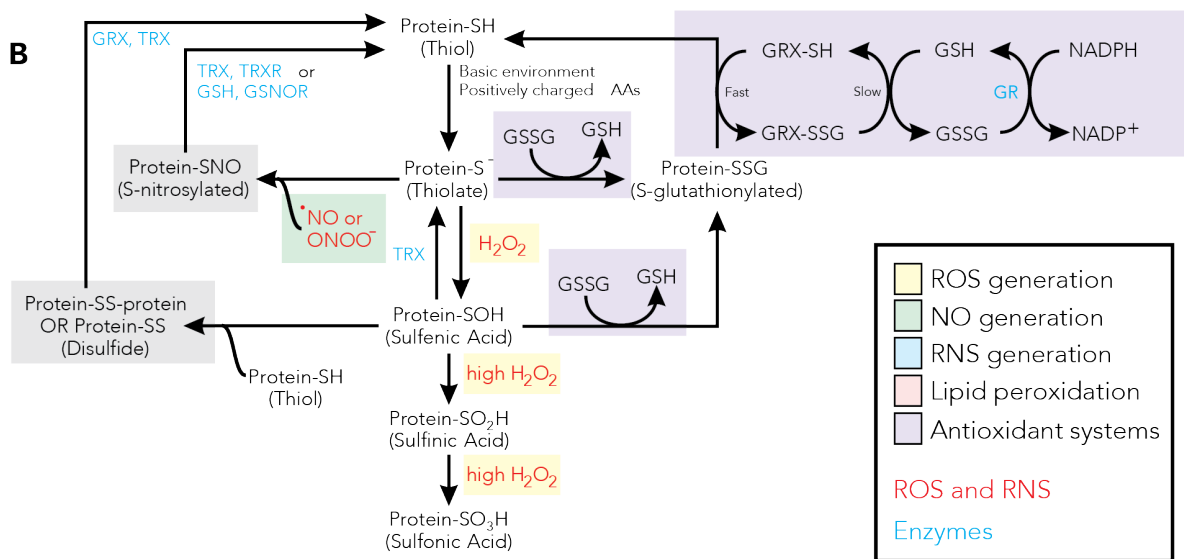
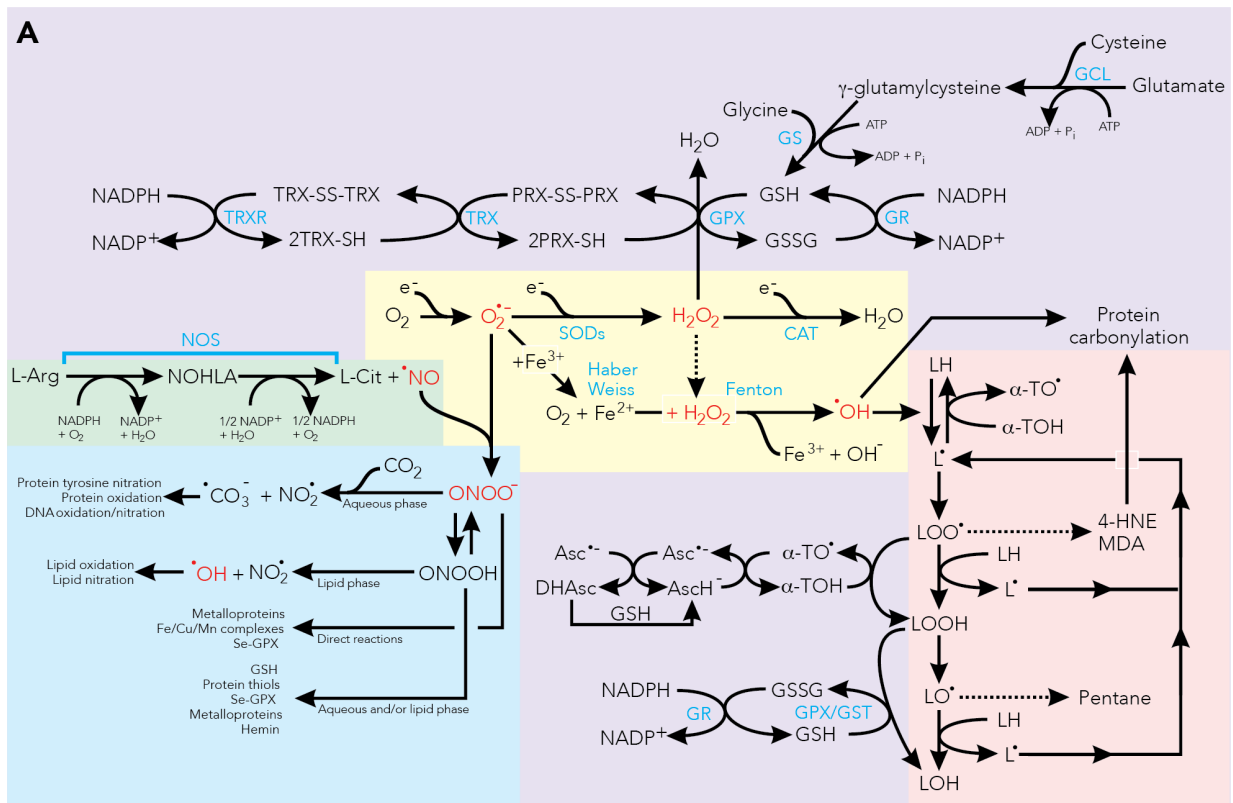


Figure 1.7: Redox homeostasis in mammalian cells.

(A) Formation of ROS and NO/RNS, their removal by antioxidant systems and role in lipid peroxidation. (B) Reactions of protein thiol (protein-SH) groups leading to reversible S-nitrosylation (protein-SNO), intra or inter-protein disulfide bond formation (SS) or S-glutathinylation (protein-SSG). **Abbreviations:** 4-HNE, 4-hydroxynonenal; α -TOH, α -tocopherol; α -TO \cdot , α -tocopherol radical; Asc \cdot^- , ascorbyl radical; AscH $^-$, ascorbate; CAT, catalase; GCL, glutamate cysteine ligase; GPX, glutathione peroxidase; GR, glutathione reductase; GS, glutathione synthase; GSH, glutathione; GSNOR, S-nitrosoglutathione reductase; GSSG, oxidized glutathione; MDA, malondialdehyde; NADPH, reduced nicotinamide adenine dinucleotide phosphate; NOS, nitric oxide synthase; NOHLA, Nw-hydroxy-L-arginine; PRX, peroxiredoxin; RNS, reactive nitrogen species; ROS, reactive oxygen species; SOD, superoxide dismutase; TRX, thioredoxin; TRXR, thioredoxin reductase. The data for this figure was compiled from: Auchère and Rusnak 2002⁷²; Szabó et al. 2007⁷⁷; Sachdev and Davies 2008⁸⁴; Benhar et al. 2009⁸⁵; Rasmussen et al. 2010⁸⁶; Finkel 2011⁸⁷; Traber and Stevens 2011⁸⁸; Pastore and Piemonte 2012⁸⁹; Marí et al. 2013⁹⁰; Nathan and Cunningham-Bussell 2013⁹¹; Saaranen and Ruddock 2013⁹²,

ROS can react covalently with certain atomic elements in biological macromolecules (**Fig. 1.7B**).⁹¹ At low ROS levels, these modifications are usually reversible, whereas at high ROS levels, they are not. Reversibility is also confined to specific atoms: reversible modifications occur on selenium (Se; in seleno-Cys) and sulfur (S; in certain Cys and Met), whereas iron-sulfur (Fe-S) clusters and carbon (C) atoms (Arg, Lys, Pro, Thr and nucleosides) are irreversibly modified. Reactions of primary ROS with proteins include reversible oxidative formation of methionine sulfoxide (by $\cdot\text{OH}$) and irreversible formation of 2-oxo-histidine (by $\text{H}_2\text{O}_2/\text{Fe}^{2+}$), chlorotyrosine (by HOCl) and protein carbonyls (by $\cdot\text{OH}$).⁹⁸ When protein thiol (SH) groups (pKa ~ 8.5) are within a basic environment (such as the mitochondrial matrix) or have their pKa lowered by proximity to positively charged amino acids they deprotonate and are present in their thiolate (S^-) form (**Fig. 1.7B**).⁹⁶ Protein thiolate groups reversibly react with ROS (H_2O_2 , HOCl) to form protein sulfinic acid (SOH). In the presence of high H_2O_2 levels, the SOH form is subsequently and irreversibly converted into sulfinic acid (SO_2H) and sulfonic acid (SO_3H) forms. The thiolate form can also react with: (i) glutathione disulfide (GSSG) to form S-glutathionylated (SSG) proteins and (ii) RNS to form S-nitrosated/S-nitrosylated (SNO) proteins.^{85,99} Starting from the SOH form, the reaction of protein thiols with GSH also leads to formation of S-glutathionylated proteins. By reacting with other SH groups, the SOH form can induce inter- or intra-molecular disulfide bond formation (**Fig. 1.7B**). The SH groups in the SSG, SNO and disulfide proteins can be reformed via various reactions involving GRX, TRX, TRXR and NADPH (**Fig. 1.7B**), allowing redox-dependent cell signaling events.^{85,97,100,101}

To minimize the deleterious effects of ROS, the cell maintains a subtle balance between the production and removal of the different ROS molecules to keep their intracellular concentration at a physiological level. Any perturbation to this fragile steady-state that increases intracellular ROS provokes a state of oxidative stress, a phenomenon associated with the natural aging process, as well as various multispectrum diseases including cancer and laminopathies.^{1,60,102-105} When this happens, cells usually respond by altering gene expression. Apart from their direct damaging effects to coding sequences¹⁰⁶, ROS can alter gene expression through epigenetic and genetic mechanisms. Whereas the epigenetic mechanisms mainly concern alterations in DNA-methylation patterns⁷⁹, the genetic mechanisms rely on the activation of various redox-sensitive transcription factors, such as Rb, p53, FoxO, NF- $\kappa\beta$, and NRF2.^{107,108} These regulatory proteins become activated by an oxidative signal in the cytoplasm after which they translocate into the nucleus. There, specific cysteine residues within the DNA-binding domain of each transcription factor are reduced by thioredoxin 1 and redox factor-1. This reduction is necessary for transcription-factor binding to the DNA and subsequent anti-

oxidative gene activation. Thus, oxidants in the cytoplasm activate redox signaling, whereas oxidative stress in the nuclear compartment blocks this process.¹⁰⁹

2.2 Range of action of ROS

A surplus of ROS is highly unwanted as it allows them to interact with various cellular constituents. However, to react with biomolecules, ROS need to be able to reach them. Once generated, the range-of-action of individual ROS differs substantially. For instance, in the presence of GSH (2 mM), values of 50 μm and 1.5 mm were computed for ONOO^- and H_2O_2 , respectively.¹¹⁰ The same study reported that the range-of-action for H_2O_2 dropped to $< 7 \mu\text{m}$, in the presence of 20 μM PRX2 (the main H_2O_2 -removing enzyme) and was even lower for $\cdot\text{OH}$ (0.35 μm). In aqueous solution the average 3D diffusion distance or “Kuramoto length” (Δx) was calculated to be $< 0.16 \mu\text{m}$ for $\text{O}_2^{\cdot-}$ and between 0.23-0.46 μm for H_2O_2 .¹¹¹

Importantly, several ROS, including $\text{O}_2^{\cdot-}$, are charged molecules, which prevents their passive transmembrane permeation. When generated in the mitochondrial matrix, $\text{O}_2^{\cdot-}$ is highly unlikely to leave this compartment unless facilitated. Currently there are no reports of superoxide permeation of the inner membrane. However, it has been proposed that the voltage-dependent anion channel (VDAC) in the mitochondrial outer membrane could mediate $\text{O}_2^{\cdot-}$ release from mitochondria.¹¹² Taken together, due to their physicochemical properties and the action of (non)enzymatic conversion cascades, various ROS types display different ranges of action within cells and subcellular compartments including mitochondria. This strongly suggests that both ROS-induced damage and signaling are affected by restricted diffusion and compartmentalization.¹¹⁰ In this respect, it appears that mitochondria-generated $\text{O}_2^{\cdot-}$ acts locally, whereas H_2O_2 and $\text{NO}\cdot$, owing to their membrane permeability and relative stability, can function as both a cytosolic and extracellular messenger ($t_{1/2}$ for H_2O_2 is 10^{-2} ms and for $\text{NO}\cdot$ between 1-30 s, compared to 10^{-3} ms and 10^{-6} ms for $\text{O}_2^{\cdot-}$ and $\cdot\text{OH}$).^{76,113-115} The diffusion properties of H_2O_2 likely depend on its site of generation and (local) conversion. Cytoplasmic microdomains of elevated H_2O_2 levels were demonstrated in cells stimulated with growth factors, suggesting that this type of ROS does not freely diffuse through the cytoplasm.^{116,117}

2.3 Mitochondria are prime sources and targets of ROS

In total, mitochondria account for 90% to 95% of the cellular oxygen consumption and up to 3% of that pool can be converted into $\text{O}_2^{\cdot-}$, depending on the mitochondrial functional state or ‘mitochondrial health’.⁸⁰ A widely used indicator of mitochondrial health is the magnitude of the membrane potential ($\Delta\psi_m$) across the mitochondrial inner membrane. This potential is central to virtually all functions of the mitochondrion, as it reflects the proton motive force that drives OXPHOS and mitochondrial Ca^{2+} uptake.⁶⁵ $\Delta\psi_m$ is sustained by the action of the four complexes (complex I–IV) of the electron transport chain (ETC), located on the inner mitochondrial membrane, and the adjoined export of protons into the intermembrane space (**Fig. 1.8**). Proton backflow through the $\text{F}_0\text{F}_1\text{-ATPase}$

(complex V) is then used to drive the production of ATP production in the mitochondrial matrix. ROS can be produced at many locations inside the mitochondrion (**Fig. 1.8**), but it generally results from electron leakage at complex I of the electron transport chain (ETC) when $\Delta\psi_m$ is highly negative. However, both de- and hyperpolarization have been associated with increased ROS production.^{66,118-121} Various mitochondrial proteins are susceptible to reversible and irreversible redox modifications, allowing local regulation of their function and/or affecting pathological processes. For instance, reversible S-nitrosylation of Complex I at Cys39 of the ND3 subunit decreased ROS production, oxidative damage and tissue necrosis and thereby protected against injury during cardiac ischemia-reperfusion *in vivo*.¹²²

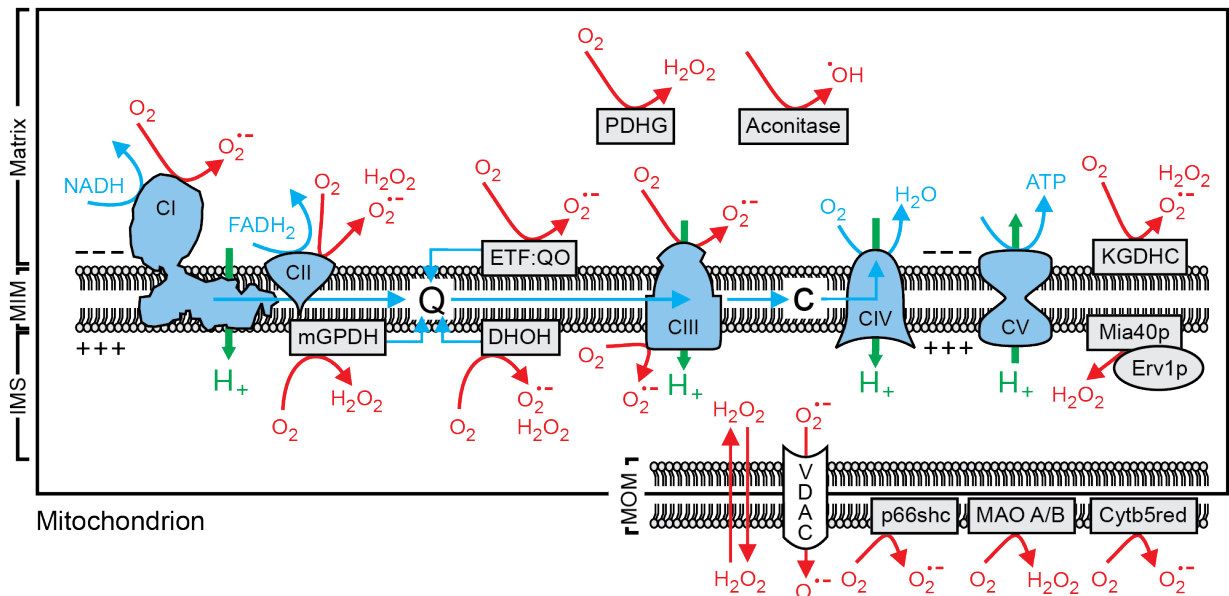


Figure 1.8: Mitochondrial sources of $O_2^{\bullet-}$ and H_2O_2 .

The scheme depicts the five complexes of the mitochondrial oxidative phosphorylation system involved in ATP production (CI-CV; blue). CI is the major source of superoxide ($O_2^{\bullet-}$) production, but ROS can also be generated at many other mitochondrial proteins (grey boxes). Once formed, the anionic $O_2^{\bullet-}$ cannot move across membranes, whereas H_2O_2 can more freely diffuse. Abbreviations: Cytb5red, cytochrome b5 reductase; DHOH, dihydroorotate dehydrogenase; Erv1p/Mia40p, redox system that forms disulfide bridges on proteins to be imported by mitochondria; ETF:QO, electron transfer flavoprotein-ubiquinone oxidoreductase; KGDHC, α -ketoglutarate dehydrogenase complex; MAO, monoamine oxidase; mGPDH, mitochondrial glycerol-3-phosphate dehydrogenase; p66shc, 66-kDa src collagen homologue (shc) adaptor protein; PDHG, pyruvate dehydrogenase complex; VDAC, voltage-dependent anion channel. The data for this figure was compiled from: Giustarini et al. 2009¹²³; Koopman et al. 2010¹¹¹; Marchi et al. 2012⁸⁰; Brown and Borutaite 2012¹²⁴; Nathan and Cunningham-Bussell 2013⁹¹; Woolley et al. 2013¹²⁵; Mailloux et al. 2013⁹⁶.

Although a full understanding is still lacking, net mitochondrial morphology, a result of continuous fusion and fission events, appears to be linked to mitochondrial function, ROS generation and redox state as well.¹²⁶ An accumulating body of evidence points to direct involvement of ROS (and RNS) in the short-term regulation of mitochondrial morphology and function via non-transcriptional pathways, i.e., through reversible and non-reversible redox modifications (S-nitrosylation, disulfide

bond formation) on/in proteins involved in the fission-fusion machinery of mitochondria.¹²⁶ Fragmentation appears correlated with increased ROS production and apoptosis^{127,128}, while a more filamentous phenotype has been linked to nutrient starvation and protection against mitophagy (Fig. 1.9).¹²⁹

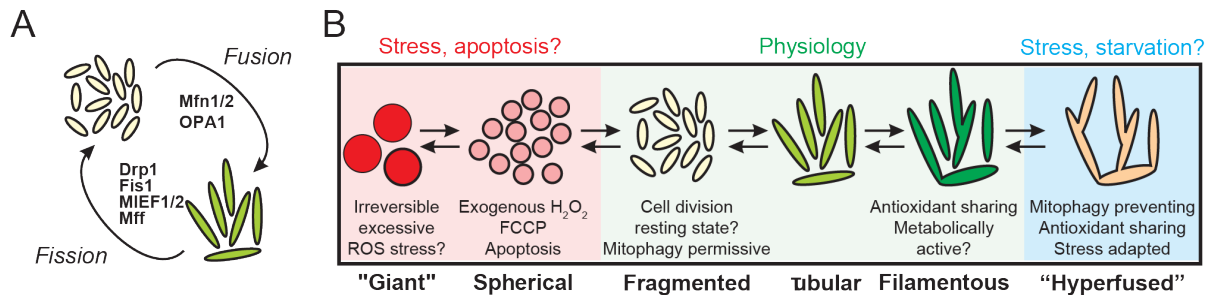


Figure 1.9: Mitochondrial morphology is correlated with its functional status.

(A) The balance between mitochondrial fusion and fission determines its morphology. Eight core proteins regulate these processes: Mfn1, Mfn2, OPA1 (fusion) and Drp1, Fis1, MIEF1/MiD51, MIEF2/MiD49 and Mff (fission) (B) The resulting net morphology depends on cell type and/or metabolic state. In physiological (healthy) conditions (green), mitochondria are motile and continuously fuse and divide. This state is associated with morphologies ranging between fragmented and filamentous. Stress conditions are associated with giant/spherical (red) or hyperfused morphologies (blue) that appear to be linked to apoptosis induction and stress adaptation, respectively. This figure was adapted and reproduced with permission from Willems *et al.* 2015.¹²⁶

3 Oxidative stress as emerging hallmark of laminopathies

3.1 Laminopathies are correlated with oxidative stress at the cellular level

Recent data point to a relationship between lamin mutations and altered ROS homeostasis. Both A-type and B-type lamins seem to have a dual function in this respect, both as sensors and as elicitors of oxidative stress. Elevated levels of ROS and an increased sensitivity to oxidative stress have been reported in cells from patients suffering from many different laminopathies involving A-type lamins, such as FPLD and other lipodystrophies^{60,130}, Amyotrophic quadricipital syndrome with cardiac involvement¹³¹, AD-EDMD¹³², HGPS¹³³ and RD¹³³. Reduction of the levels of mature lamin A and the presence or accumulation of aberrant (pre)lamin variants alter intracellular ROS levels as well as the concentration of antioxidant enzymes. In particular, accumulation of the farnesylated form of PLA seems to induce excessive ROS and protein oxidation.^{50,59,60,133,134} Yet, also non-farnesylated PLA variants might be harmful, as they have been implicated in cardiomyopathy and several lipodystrophies.¹³⁵⁻¹³⁷ In addition, reduced levels of CAT and GPX have been observed in HGPS fibroblasts¹³⁸, while elevated levels of SOD, CAT and GST have been detected in lamin deficient patient fibroblasts (LMNA^{Y259X/Y259X})^{132,139}.

Next to the involvement of A-type lamins, there is also evidence for a role of B-type lamins in redox biology. Exposure to oxidative stress induces lamin B1 accumulation in a p38-MAPK dependent manner.¹⁴⁰ Plausibly, lamin B1 attempts to

decrease the ROS levels by regulating stress-responsive gene expression. But under conditions of chronic oxidative stress lamin B1 eventually decreases and fails to prevent senescence. Indeed, downregulation of lamin B1 has been shown to alter the expression of several anti-oxidants either through regulation of Oct1 or p53.¹⁴¹⁻¹⁴³ Downstream effects of accumulation of ROS, specifically in the context of laminopathies, include protein oxidation, telomere shortening and persistent DNA damage.³⁸ It is well established that there is an exponential correlation between intracellular ROS levels and telomere shortening rates.¹⁴⁴ Increased telomere shortening has also been observed in several human fibroblast cell lines overexpressing different mutant LMNA variants. Interestingly, overexpression of wild-type LMNA also causes accelerated telomere shortening.¹⁴⁵ Telomere shortening in turn is known to induce premature cell cycle arrest by activation of p53 (tumor suppressor), thereby promoting senescence. p53 then represses PGC-1a and PGC-1b, both master regulators of mitochondrial physiology and metabolism.¹⁴⁶ This way, a direct reinforcing loop is initiated of increased ROS, telomere shortening and impaired mitochondrial function.

It has also been shown that, under oxidative stress conditions, telomerase, the major enzyme for telomere length homeostasis, can translocate from the nucleus to the cytosol and the mitochondria to exert a regulatory role in apoptosis.^{147,148} Furthermore, telomerase appears to repress ROS-dependent cellular responses to tumor necrosis factor- α (TNF α) without affecting NF- κ B activation.¹⁴⁹

In the context of laminopathies, ROS have also been linked with persistent DNA damage. DNA double-strand breaks, induced by ROS are repaired efficiently in normal human fibroblasts, but appear to be un-repairable in HGPS fibroblasts. These breaks are a major cause of the poor growth of the HGPS fibroblasts since adding N-acetyl cysteine, a ROS scavenger, to the culture medium reduces DSBs and markedly decreases population doubling times.¹⁰⁶

3.2 Lamin-dependent mechanisms of oxidative stress response

Despite indications for a link between a dysfunctional lamina and disturbed redox biology, the underlying pathways remain mostly elusive. A dysfunctional lamina can arise from mutations in the lamin-coding genes and in the genes responsible for the processing of PLA. We refer to this hereditary form of dysfunction as *innate lamina dysfunction*. However, Lamina perturbation can also originate from drug treatments such as anti-retroviral protease inhibitors (HIV-PIs) that, as a side effect, also block ZMPSTE24, which induced PLA accumulation (**Fig. 1.3**)¹⁵⁰, or it can originate from irreversible (oxidative) damage to normal mature lamins¹³². It has been suggested that lamin A, due to its high abundance and the presence of oxidizable cysteine residues, can act as a ROS-buffer inside the nucleus, protecting other, less abundant and more critical proteins from transient, mild oxidative damage.¹³² This has also been reported for other abundant structural proteins inside the cytosol like actin.¹⁵¹ But upon chronic or highly acute oxidative stress, irreversible oxidative damage to some conserved cysteine residues (C522, C588, and C591) leads to a loss of function.¹³² Together, we refer to this type of dysfunction with the term

acquired lamina dysfunction. A dysfunctional lamina, innate or acquired, may influence ROS in several ways (**Fig. 1.10**). It is known that the lamina serves as a docking station inside the nucleus, but presumably also in the cytoplasm, e.g. through components of the LINC complex, a mechanical connection between the nucleo- and cytoskeleton involved in signaling pathways and gene regulation.^{23,28,29} Inside the nucleus this docking function results in gene regulation, either by direct interactions with chromatin or transcriptional complexes or indirect via interaction with transcription factors. As for direct interactions, lamins play a key role in intranuclear positioning and compaction of chromosomal domains.¹⁵² Aberrant chromatin organization has been observed in various conditions of abnormal lamin expression: lamin deficiency as well as overexpression of progerin leads to the depletion of heterochromatin and abnormal nuclear morphology.^{58,153} This may induce activation of repressed genes and alter DNA binding of transcription factors and regulatory proteins. Indeed, in HeLa cells expressing different disease inducing *LMNA* mutations, DNA damage repair is perturbed due to incorrect localization of ataxia telangiectasia-mutated and Rad3- related (ATR) kinase due to disturbed lamin-chromatin interactions.¹⁵⁴ Indirect influence of the lamina on gene expression can mostly be brought back to the reversible associations of lamins with a multitude of redox-responsive transcription factors including Rb, SREBP1, Ankrd2, NRF2 and Oct1.^{33,35,141,155,156} In lamin B1 deficient mouse embryonic stem cells (MEFs), the transcription factor Oct-1, is no longer properly sequestered at the nuclear lamina. This leads to an increase of free Oct-1 inside the nucleus and higher expression of genes that are involved in oxidative stress response such as GPX3, IL-6 and SOD1.¹⁴¹ Conversely, in *LMNA* knockout MEFs as well as in lamin A/C deficient patient cells (*LMNA*^{Y259X/Y259X}), repetitive ruptures of the nuclear membrane lead to a temporary and local translocation of nuclear Oct-1 from nucleus to cytoplasm.¹³⁹ This lowers the concentration of free Oct-1 inside the nucleus and, has opposite downstream effects on Oct1-dependent gene expression compared to the lamin B deficient cells.¹³⁹ Nevertheless, both *LMNA*^{-/-} and *LMNB1*^{Δ/Δ} MEFs eventually show elevated ROS levels and higher susceptibility to oxidative stress compared to wild type cells, pointing to a delicate balance between pro- and antioxidants in regulation of the oxidative stress response. Another example is Ankrd2, a stress responsive protein mainly expressed in muscle cells. Upon oxidative stress, it translocates into the nucleus where it interacts with lamin A and regulates the activity of genes involved in cellular response to stress including. However, an EDMD2-lamin A mutant was found to bind and mislocalize Ankrd2 in the nucleus even under basal conditions, disturbing proper function and increasing sensitivity towards oxidative stress.¹⁵⁵ A similar mechanism was reported for NRF2, a transcription factor that activates multiple antioxidant and cytoprotective genes through binding to antioxidant-responsive elements (ARE) motifs in their promoters. In HGPS, NRF2 is mislocalized to the nuclear lamina, leading to oxidative stress.¹⁵⁶ From the cytoplasmic side, changes can occur in spatial concentration of ROS defusing or ROS generating enzymes.¹⁵⁷ Fabrini et al.¹⁵⁸ postulated the presence of a nuclear shield, a 300 nm thick perinuclear hyper-crowding of protective enzymes,

among which ROS defusing enzymes like CAT, GPX and GST are highly represented, up to seven times higher than in the cytosol. It concerns mainly cationic enzymes that assemble through electrostatic interactions. The role of this shield could be the protection of the nuclear DNA against oxidative stress. To induce assembly, the anionic nesprin 1 and nesprin 2 were postulated as charge-counterparts and scaffolding proteins. These giant proteins directly link the actin cytoskeleton to the nuclear lamina via the LINC complex.²⁹ Lamin A/C is essential for proper nesprin 2 localization at the nuclear membrane¹⁵⁹, thus absence of normal and/or presence of mutant lamin A can disturb proper formation of this nuclear shield, leading to a local decline of antioxidants around the nucleus which could in turn elicit a higher susceptibility to oxidative stress.

Next to a perturbed docking function, a dysfunctional lamina can also cause repetitive and transient disruptions of the nuclear envelope.^{139,160} This leads to an intermixing of cytoplasmic and nuclear components, ranging from small diffusible molecules such as transcription factors to large macromolecular complexes such as PML bodies and mitochondria. Indeed, in patient cells of several different laminopathies, functional mitochondria were observed inside the nucleoplasm.^{139,161} Obviously, the close proximity of these ROS-sources to genomic DNA greatly increases the risk of oxidative damage and senescence. This is indirectly demonstrated by the fact that mitochondrial DNA (mtDNA) shows increasing amounts of damage with increasing age, likely attributed to the proximity of the mtDNA to the source of ROS.¹⁶² Mitochondria are not the only ROS sources that could become displaced, another potential source is NADPH oxidase 4 (NOX4), which contributes to superoxide ($O_2^{\bullet-}$) and H_2O_2 generation, and has been shown to colocalize with lamin A/C, especially after hepatitis C virus infection.^{163,164}

Recent data also points to a relationship between lamins and mitochondrial dysfunction. Cells, which accumulate farnesylated PLA, (either due to LMNA mutations or HIV-PI therapy), show a lowered expression of the mtDNA encoded subunit II of the cytochrome oxidase complex IV (COX 2). This disrupts the electron transport chain, lowering the mitochondrial potential, perturbing ATP production and generating ROS.⁶⁰ It is not yet known, whether the downregulation is caused by direct interactions with prelamin isoforms or due to reduction in functional lamin A. Similarly, after silencing of lamin B1, the expression of the mitochondrial SOD2 gene decreases¹⁴² and the expression of p53, which plays a central role in mitochondrial oxidative phosphorylation, increases.¹⁶⁵ In addition, a whole organism study on *Zmpste24*^{-/-} mice, which accumulate farnesylated PLA, revealed an enhancement of mitochondrial function, especially the tricarboxylic acid (TCA) cycle and electron transport chain, to such a level that it causes oxidative damage, further supporting the relationship between defective PLA processing, mitochondrial dysfunction and oxidative stress.¹⁶⁶

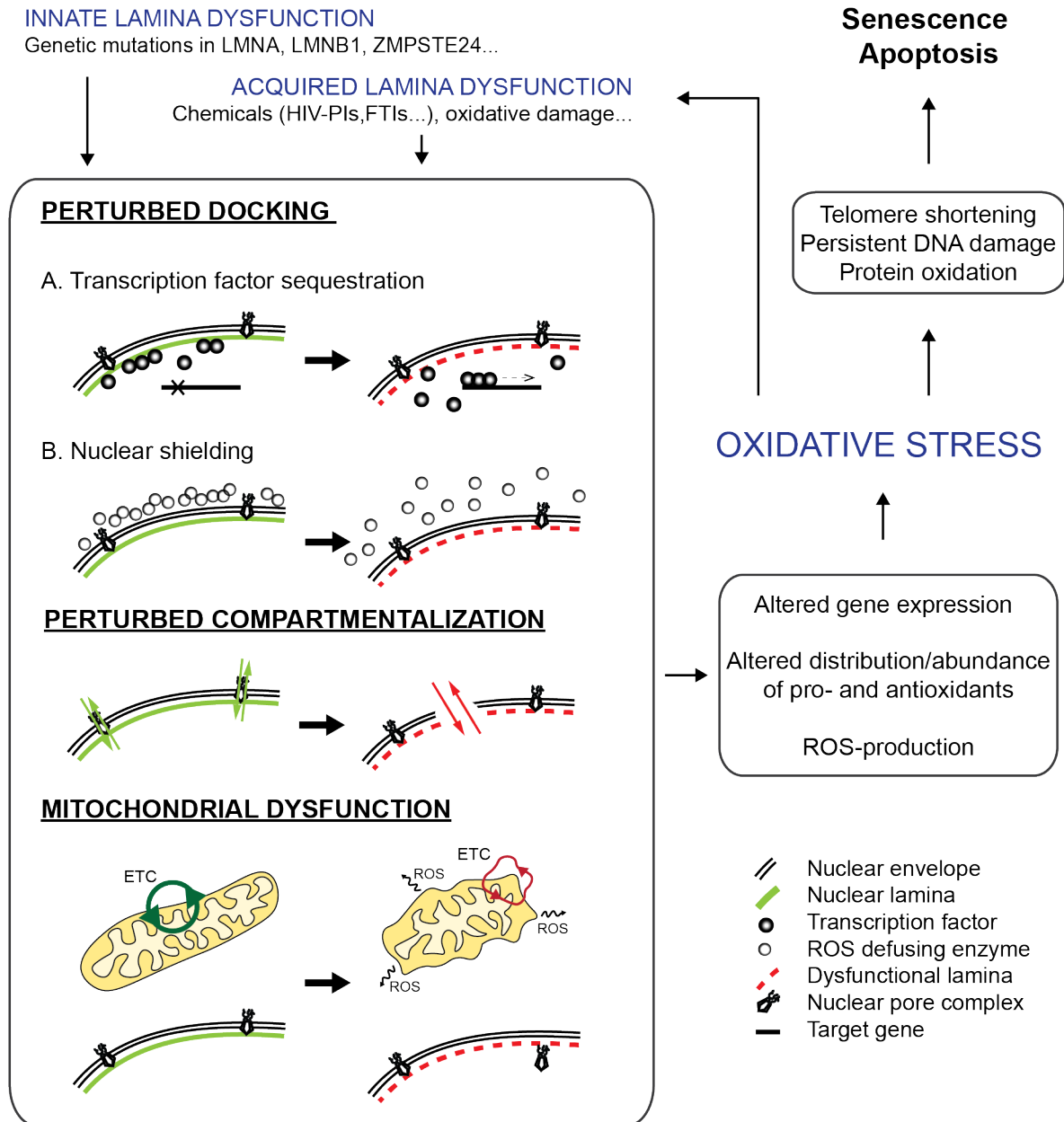


Figure 1.10: Framework for reciprocal interactions between lamins and oxidative stress.

Genetic (innate) or non-genetic (acquired) mechanisms cause lamina dysfunction, which leads to an altered affinity (docking) for redox-responsive transcription factors and/or ROS defusing enzymes, reduced compartmentalization potential (ruptures) or mitochondrial dysfunction. This causes changes in stress-responsive gene expression and/or spatial redistribution of pro-oxidants (mitochondria, NOX) and anti-oxidants (CAT, SOD, ...), inducing a state of oxidative stress. Chronic oxidative stress induces telomere shortening, protein oxidation and persistent DNA damage, eventually heralding cellular senescence or apoptosis.

4 Quantitative Microscopy of Cellular Redox Biology

To investigate the relationship between lamin perturbations, mitochondrial function and oxidative stress, these parameters are ideally measured together, in single living cells. Fluorescence-based assays are well suited for this purpose, as they

allow multiple simultaneous readouts. Microplate readers are regularly used to measure fluorescence intensities, but the readout is highly prone to confounding factors, such as variable cell density and autofluorescence, and it also lacks single cell resolution and morphological information. Although flow cytometry measures all cells individually, which greatly increases sensitivity and accuracy, this technique still does not provide spatial information and also lacks temporal information (no time-dependent kinetics), and it imposes an operational stress factor (cell detachment) when working with adherent cell cultures. These disadvantages are avoided upon using fluorescence microscopy. Microscopy allows gauging redox and mitochondrial parameters in individual adherent cells through time at subcellular resolution and with high sensitivity, both pre- and post-stimulus, i.e., *in fluxo*. However, to enable robust and accurate measurements of intracellular ROS and individual mitochondria, all aspects of the imaging pipeline, from sample preparation to image analysis, have to be highly standardized.

4.1 Cell culture conditions

Culture conditions should be optimized for each cell type individually and should be meticulously controlled prior to the measurements in order to obtain robust and reproducible results. For instance, the composition of the culture medium as well as the imaging buffer can greatly affect mitochondrial morphology and function. Nutrient starvation generally leads to a more filamentous mitochondrial phenotype^{129,167}, while high glucose concentrations have been linked to increased ROS production and mitochondrial fission.^{168,169} Cells should be seeded at least 24h before actual measurements, at fixed splitting ratios so as to obtain a sub-confluent culture of 70%-80% (substrate occupation) at the time point of measurement. This guarantees optimal performance of downstream image analyses (in particular cell segmentation). Furthermore, imaging buffer/medium should be devoid of potential autofluorescent components, such as phenol-red, riboflavin or tryptophan, in order to reduce non-specific background intensity.¹⁷⁰ Also, to minimize the influence of plate-induced variation, sample distribution should be homogenized across the plate and the outer wells should not be used for measurements since they are prone to edge effects (they can however be used to take background images for a downstream flatfield correction).

4.2 Sensors

A second point of attention involves the selection of the appropriate reporter molecules (**Table 1.1**). As most ROS molecules tend to have a short lifetime (nanoseconds to seconds), the ideal reporter for fluorescent detection of intracellular redox changes has a high sensitivity combined with fast and reversible binding kinetics, a high dynamic range, shows little or no photobleaching or (photo)toxicity and can be loaded into the cells quickly and easily.¹⁷¹ Currently available ROS probes can be subdivided into two categories: synthetic small molecule dyes and

genetically encoded fluorescent proteins. These probes don't necessarily possess all the ideal properties mentioned above, but many are still widely used. The most commonly used small molecule ROS probes are dihydroethidium (DHE), mitochondrial targeted DHE (MitoSOX) and the chemically reduced and acetylated forms of 2',7'-dichlorofluorescein (DCF).¹⁷² CM-H₂DCFDA (5-(and-6)-chloromethyl-2',7'-dichlorodihydrofluorescein diacetate, acetyl ester) is a widely used chloromethyl derivative of H₂DCFDA that is used to measure general intracellular oxidant levels. It diffuses passively into the cell where its acetate groups are cleaved by intracellular esterases, decreasing its capacity to traverse the cell membrane, and thereby trapping it inside the cell. Its thiol-reactive chloromethyl group allows for covalent binding to intracellular components, increasing retention of the dye even further. Following oxidation, highly fluorescent DCF is formed. With an excitation maximum of 502 nm and an emission peak of 523 nm, DCF fluorescence can be readily monitored using standard filter combinations for GFP or FITC.¹⁷³⁻¹⁷⁵ Other general small molecule ROS probes include Thioltracker[®] and the CellROX[®] family of indicators (Life Technologies[®]). Dyes that are more specific to certain types of ROS exist as well. DHE is generally used as a probe for O₂^{•-}.¹⁷⁶ The reaction between DHE and O₂^{•-} generates highly red fluorescent 2-hydroxyethidium (2-OH-E⁺; ex. 518 nm, em. 605 nm). Reaction with other oxidants, however, can produce ethidium (E⁺), which strongly binds DNA, is also red fluorescent (ex. 525 nm, em. 616 nm) and is often present at a much higher concentration.¹⁷⁷ Discrimination between these two is still possible, however, due to an extra excitation band between 350 and 400 nm for 2-OH-E⁺.¹⁷⁸ However, as the ratio E⁺/2-OH-E⁺ is often 10 or more, contribution of E⁺ might still be significant.¹⁷⁷ MitoSOX is a DHE derivative coupled to a positively charged triphenylphosphonium group (TPP⁺), enabling efficient targeting to the mitochondria for selective detection of mitochondrial O₂^{•-}.¹⁷⁹ The recently described HKSOX1 family of probes is also specific for •O₂.¹⁸⁰ and a family of boronate-based sensors (peroxy family e.g. PF1, PF3, PG1, PO1, PY1, MitoPY1...) targeting to the cytosol or the mitochondria can be used for the detection of H₂O₂.¹⁸¹⁻¹⁸⁴ H₂O₂-mediated removal of a boronate group greatly increases fluorescence of these sensors. They also display a range of fluorescent wavelengths, making them useful for multicolor experiments. For a more extensive overview of small molecule fluorescent probes for ROS the reader is referred to Gomes et al.¹⁷³ Next to small molecule fluorescent probes, ROS can also be monitored using genetically encoded fluorescent protein based probes. While labelling is more complex, usually involving liposome- or virus-based transfection procedures, the selectivity of these dyes is generally higher. Moreover, genetic reporters can easily be targeted to a variety of intracellular destinations and they are maintained for prolonged periods of time allowing long-term and transgenerational follow-up. They either are ROS-sensitive fluorophores or standard fluorophores fused to ROS-sensing domains borrowed from other proteins like SoxR and OxyR, i.e., transcription factors found in *E. coli* that become activated upon oxidation by O₂^{•-} or H₂O₂, respectively.^{185,186} In SoxR the regulatory domain contains a 2Fe-2S cluster, while that of OxyR has several redox active cysteine residues. Both of them

undergo a significant conformational change upon activation. In order to translate this into a quantifiable change in fluorescence, these domains are linked to circularly permuted (cp) versions of fluorescent proteins.^{187,188} The HyPer family of fluorescent probes was created by inserting a cpYFP in the regulatory domain of OxyR¹⁸⁹⁻¹⁹¹. HyPer acts as a ratiometric H₂O₂ probe with 2 excitation maxima (420 and 500 nm) corresponding to the protonated and anionic forms of the protein, respectively, and one emission maximum (516 nm). Upon oxidation, a disulfide bond is formed between Cys 199 and Cys 208, resulting in a decrease of the 420 nm excitation peak and a proportional increase of the 500 nm excitation peak. This ratiometric determination greatly reduces the influence of expression level differences between individual cells. Unfortunately, HyPer is also sensitive to pH changes. Acidification of the cellular environment leads to protonation, thus mimicking reduction of the probe; alkalization on the other hand mimics oxidation.¹⁸⁹ SypHer, a H₂O₂-insensitive HyPer variant (C199S) is a pH sensor and can be used as a control.¹⁹² Another family of fluorescent protein based redox-sensitive probes are the roGFPs, which were created by introducing oxidizable cysteine residues on the outside of the β -barrel structure of GFP near the location of the chromophore. They can be used to ratiometrically measure the thiol redox state (GSH/GSSG-ratio). roGFPs, just like HyPer, have 2 excitation peaks, which correspond to their oxidized and reduced states, but in contrast to HyPer they are considered insensitive to pH.¹⁹³ One of the drawbacks of roGFP reporters is their slow kinetics. A fusion between roGFP and glutaredoxin 1 (Grx1-roGFP) resulted in a probe with faster kinetics.¹⁹⁴ However, it still takes minutes or longer to equilibrate with cellular redox potential changes, which is still too slow to detect fast transient events.¹⁹⁵ Another variant is Orp1-roGFP, a fusion between roGFP and the yeast peroxidase Orp1, which functions as an intracellular, ratiometric, pH-stable H₂O₂ probe.¹⁹⁶ Its response to H₂O₂ is similar to that observed with HyPer, although oxidation is slower.¹⁹⁶ Next to direct ROS probes, one could also use probes that assess ROS indirectly by measuring the downstream damage such as lipid peroxidation. C11-BODIPY^{581/591}, for example, is a ratiometric sensor for lipid peroxidation¹⁹⁷, while MitoPeroX (a mitochondria targeted derivative of C11- BODIPY^{581/591}) is a ratiometric probe for the specific assessment of mitochondrial phospholipid peroxidation.¹⁹⁸ Several fluorescent dyes have also been developed for measuring mitochondrial morphology and $\Delta\psi_m$. They all are cell-permeant and become readily sequestered by active mitochondria in a $\Delta\psi_m$ -dependent manner.¹⁹⁹ Of these, the red-orange fluorescent tetramethylrhodamine methyl ester (TMRM) is one of the most efficient because it equilibrates fastest across membranes, is least toxic and demonstrates the lowest aspecific binding.²⁰⁰ With its excitation and emission maxima being 550nm and 576nm, respectively, it is also compatible with many probes that are fluorescent in the GFP region, like the HyPers and roGFPs, or CM-H₂DCFDA. MitoTracker[®] dyes (MTRs) should only be used for morphological analysis. Although they are also sequestered to the mitochondria based on $\Delta\psi_m$, they are retained there as a result of covalent interaction with mitochondrial biomolecules, making it impossible to measure dynamic changes of $\Delta\psi_m$.²⁰¹

Table 1.1: Characteristics and usage of common ROS, redox and mitochondrial probes

Type	Name	Indicator for	Ex/Em (nm)	Remarks	References
Chemical	DHE	$O_2^{\cdot-}$	518/605	Excitation between 350-400 nm to differentiate 2-	Zielonka <i>et al.</i> ¹⁷⁷ , Robinson <i>et al.</i> ¹⁷⁸
	MitoSOX - Red	Mitochondrial $O_2^{\cdot-}$	518/605	OH-E ⁺ from E ⁺	Robinson <i>et al.</i> ¹⁷⁹ , Forkink <i>et al.</i> ²⁰²
	CM-H ₂ DCFDA	General ROS	502/523		Koopman <i>et al.</i> ¹⁷⁴ , Sieprath <i>et al.</i> ²⁰³
	C11-BODIPY	Lipid peroxidation	490/520; 580/590	oxidized product:	Drummen <i>et al.</i> ¹⁹⁷
	MitoPerOx	Mitochondrial lipid peroxidation	490/520; 580/590	490/520; reduced product: 580/590; also 490/520 and 590 can be used	Prime <i>et al.</i> ¹⁹⁸
	TMRM	Mitochondrial morphology and $\Delta\psi_m$	550/576		Nicholls <i>et al.</i> ²⁰⁰ , Koopman <i>et al.</i> ²⁰⁴
	MTRs	Mitochondrial morphology	-	Multiple MTRs with different ex/em	Chazotte <i>et al.</i> ²⁰⁵
	PF3	H ₂ O ₂	492/515	These probes are all sensitive for H ₂ O ₂ but they exhibit different fluorescence ex/em, making them compatible with other probes	Dickinson <i>et al.</i> ¹⁸¹
	PG1	H ₂ O ₂	460/510		Miller <i>et al.</i> ¹⁸⁴
	PO1	H ₂ O ₂	540/565		Dickinson <i>et al.</i> ¹⁸¹
PY1	H ₂ O ₂	519/548	Dickinson <i>et al.</i> ¹⁸¹		
MitoPY1	Mitochondrial H ₂ O ₂	510/528	Dickinson <i>et al.</i> ²⁰⁶		
Protein	HyPer 1	H ₂ O ₂	420 and 500/516	Hyper 2: better dynamic range, slower kinetics; Hyper 3: better dynamic range	Belousov <i>et al.</i> ¹⁸⁹
	HyPer 2	H ₂ O ₂	420 and 500/516		Markvisheva <i>et al.</i> ¹⁹⁰
	HyPer 3	H ₂ O ₂	420 and		Bilan <i>et al.</i> ¹⁹¹

			500/516	and better kinetics	
roGFP1	GSH redox potential	400 and 475/509	400 and 475/509	roGFP2: superior to roGFP1; Grx1-roGFP2: faster kinetics (equilibration time: minutes)	Hanson <i>et al.</i> ²⁰⁷
roGFP2	GSH redox potential	400 and 490/509	400 and 490/509		Dooley <i>et al.</i> ²⁰⁸
Grx1-roGFP2	GSH redox potential	400 and 490/509	400 and 490/509		Gutscher <i>et al.</i> ¹⁹⁴
Orp1-roGFP2	H ₂ O ₂	400 and 490/509	400 and 490/509		Gutscher <i>et al.</i> ¹⁹⁶

4.3 Microscopy

When performing live cell imaging, optimal cellular health conditions are crucial to ensure that the physiological and biological processes under investigation are not altered in any way. For mammalian cells, the temperature must ideally be kept stable at 37°C, pH should be at a physiological level (~pH=7.2-7.4) and changes in osmolarity have to be avoided by minimizing evaporation.¹⁷⁰ However, to reduce vacuolization of internalized dyes and exocytosis, measurements are often performed at lower temperatures.²⁰⁹ Temperature control can be achieved by means of a large incubator enclosing the whole microscope, or a stagetop incubator in combination with objective heaters. To minimize thermally induced focus drift along the z-axis, samples should be allowed to equilibrate on the microscope before imaging. When using bicarbonate-based culture medium, a CO₂ incubation chamber or HEPES-based buffer has to be used to keep pH at a physiological level.²¹⁰ To avoid evaporation of the medium and the resulting changes in osmolarity, relative humidity needs to be kept at nearly 100%. Typically, CO₂ gas is bubbled through a water container to humidify the incubator.¹⁷⁰

As fluorescence excitation can trigger ROS photo-induction (photodamage), it is quintessential to minimize light exposure, especially when aiming at quantification of intracellular ROS and redox-related processes.²¹¹⁻²¹³ The most straightforward way to mitigate photodamage is to reduce the illumination load. This can be achieved by limiting the total imaging duration, but this goes at the expense of the signal-to-noise ratio. Hence, the efficiency of light collection should be optimized as well. This can be done using hard-coated filters, high numerical aperture (NA) lenses and detectors with high quantum efficiency, such as EM-CCD cameras.¹⁷⁰ When scaling a microscopy assay up to a multi-well format, variations in focus levels within and between wells impose another level of complexity. Images need to be perfectly focused to measure morphological and intensity metrics accurately.²⁰⁴ Stage movements and time-resolved revisiting of regions of interest therefore call for accurate autofocusing methods. Hardware-based autofocusing methods, which rely on laser or LED deflection on the substrate, allow for continuous, real-time

correction of the distance drifts between objective and substrate caused by plate imperfections and thermal fluctuations, while software-based methods correct for biological focus variations such as cell and organelle (e.g. mitochondria) positioning by calculating a sharpness or contrast metric in a series of axial recordings.^{170,214} Software-based autofocus methods are not recommended for redox biology imaging, because they require multiple exposures, but sometimes they are crucial to fine-tune hardware-driven axial positioning. To minimize phototoxicity, software-based autofocusing should be done using low intensity transmitted light. Another consideration when scaling up to a multi-well format is the time needed for the acquisition of all wells. The measured signal should be stable from the measurement of the first well to the last, but the total acquisition time increases linearly with the number of wells and the number of individual images recorded in each well. The available time window is dependent on several variables, including the dynamics of the process under investigation and the used staining method (for instance, transient staining with a small molecule dye versus stable expression of a genetic marker).

5 Scope

Lamins are crucial components of the nuclear envelope, and their dysfunction triggers a variety of tissue-specific and systemic disorders. However, a lack of fundamental knowledge about the disease-causing mechanism hampers development of good therapeutic strategies. Despite the diversity observed in laminopathy phenotypes, oxidative stress emerges as a general hallmark at the cellular level, but the causal mechanisms are not well understood. The goal of this dissertation was to contribute to a better understanding of the interplay between A-type lamins and intracellular redox homeostasis, especially under pathological conditions. Proper investigation of the effects of distinct lamin perturbations on redox biology at the cellular level demands specific and reliable cell models, which are currently lacking. Furthermore, interrogation of cellular redox biology requires interpretation of multiple different parameters, preferably measured in the same, living, cells. Implementation of such an assay, and subsequent analysis of this multi-parametric readout requires development of novel strategies and software. These problems define the major research goals of this PhD:

1. *Create robust and reliable models displaying distinct lamin perturbations.*

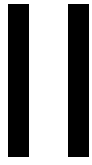
We wanted to investigate the effect of specific lamin A perturbations, namely PLA accumulation and lamin A/C depletion. Therefore, chemical as well as genetic approaches to induce these perturbations were compared phenotypically and genotypically.

2. *Develop a method to quantify redox status at a cellular level.*

To (semi-)quantitatively measure intracellular ROS levels and mitochondrial status, in the same living cells, a high-content microscopy based method was developed and benchmarked.

3. *Use the created models and method to expose causal factors leading to oxidative stress in laminopathies.*

Selected models were used with the developed method to elucidate new mechanisms connecting lamin A perturbations with oxidative stress.



QUANTITATIVE COMPARISON OF EXPERIMENTAL PERTURBATIONS OF A-TYPE LAMIN METABOLISM

Parts of this chapter are published in Sieprath et al. 2015²⁰³ and Robijns et al. 2015¹⁶⁰.

1. Sieprath, T. *et al.* Sustained accumulation of prelamin A and depletion of lamin A/C both cause oxidative stress and mitochondrial dysfunction but induce different cell fates. *Nucleus* **6**, 236–246 (2015).
2. Robijns, J. *et al.* In silico synchronization reveals regulators of nuclear ruptures in lamin A/C deficient model cells. *Sci Rep* **6**, 30325 (2016).

Abstract

Mutations in the *LMNA* gene directly or indirectly cause around 15 diseases. A knockout is often associated with striated muscle laminopathies, while mutations that lead to the formation and accumulation of aberrant forms of lamin A or prolamina A (PLA) are diseases like lipodystrophies and accelerated aging syndromes. However, as yet, there is no view on the differential cellular effects of reduced or complete lamin A/C abundance versus the accumulation of specific PLA variants. This is partly due to the lack of optimized cellular models for *LMNA* deregulation. Therefore, we have compared and characterized various genetic and pharmacological strategies for perturbing A-type lamin production and maturation in primary normal human dermal fibroblasts and HT1080 fibrosarcoma cells. Whereas pharmacological treatments caused PLA accumulation with variable efficiency and side-effects, a sustained siRNA-mediated knockdown of *ZMPSTE24* induced a reproducible PLA accumulation in NHDF cells. Likewise, a sustained knockdown of *LMNA* depleted A-type lamins to background levels. Nuclear morphology after sustained knockdown strongly resembled that of the corresponding patient cells. Crispr/Cas9-mediated knockout of *LMNA* and *ZMPSTE24* in HT1080 cells yielded stable model cells that recapitulate the major hallmarks of patient cells. The sustained knockdown approach can be applied to study progressive or transient effects of lamin perturbations in primary cell cultures, whereas the stable knockout cell lines offer a means to study downstream effects of permanent interventions compared to isogenic controls.

1 Introduction

A-type lamins (lamin A (LA) and lamin C (LC)) are major constituents of the nuclear lamina. This structure physically supports the nucleus and is involved in nuclear organization, gene regulation and intracellular redox homeostasis.^{1,3} The *LMNA* gene encodes both lamin A and lamin C. Lamin C is directly produced in its mature form, but lamin A is produced as a precursor protein, PLA. During maturation, PLA undergoes a sequence of posttranslational modifications, of which the most important are shown **Figure 2.1** (a more detailed scheme can be found in **Fig 1.3**). In brief, The *LMNA* gene is transcribed and translated into PLA, which becomes farnesylated at its C-terminus by a farnesyltransferase. After a C-terminal cleavage and carboxymethylation, the C-terminus, including the farnesyl group, is cleaved off by the metalloprotease *ZMPSTE24*, yielding mature LA.¹⁵⁰

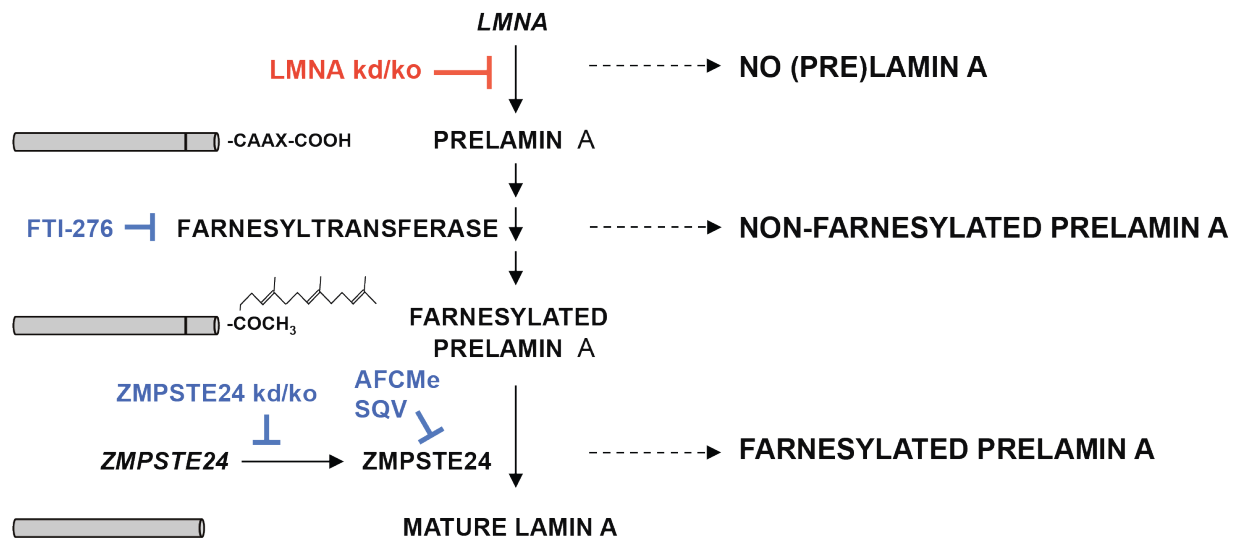


Figure 2.1: Schematic overview of the key steps in the maturation process of PLA to mature lamin A.

A more detailed scheme is shown in figure 3 of chapter 1. In brief: The C-terminus of PLA is farnesylated and carboxymethylated, before it is cleaved off by ZMPSTE24. siRNA-mediated knockdown (kd) or CRISPR/Cas9-mediated knockout (ko) result in lamin A/C depletion and are shown in red. Interferences (chemical, siRNA & CRISPR/Cas9-mediated) that result in PLA accumulation are shown in blue. Pharmacologicals: FTI-276: farnesyl transferase inhibitor 276; SQV: Saquinavir; AFCMe: N-acetyl-S-farnesyl-L-cysteine methyl ester.

There are around 15 diseases linked to mutations in the *LMNA* gene.⁴¹ Many mutations that lead to a knockout of the gene (haplo-insufficiency) are associated with striated muscle laminopathies.³ Other mutations interfere with the maturation process and lead to the formation and accumulation of aberrant forms of lamin A or PLA. For example, in Hutchinson-Gilford Progeria Syndrome (HGPS), a point mutation in exon 11 (C1824T) results in an alternatively spliced PLA variant lacking the ZMPSTE24 cleavage site. This causes the final protein product to remain permanently farnesylated.⁵⁸ Another example is Restrictive Dermopathy (RD).^{49,50} It is caused by mutations resulting in the loss of ZMPSTE24, which also leads to the accumulation of farnesylated PLA. It is especially this accumulation of farnesylated PLA variants that is assumed to be toxic.^{50,59,134} Yet, also non-farnesylated PLA variants might be harmful, as they have been implicated in cardiomyopathy and several lipodystrophies.¹³⁵⁻¹³⁷

As yet, there is no solid view on the differential cellular effects of reduced lamin A/C abundance (haplo-insufficiency) and the accumulation of PLA (farnesylated vs. non-farnesylated) variants. This is partly due to the lack of optimized cellular models for *LMNA* deregulation. Therefore, we have compared and optimized different chemical and genetic strategies for perturbing A-type lamin production and maturation in primary normal human dermal fibroblasts (NHDF) and immortal HT1080 fibrosarcoma cells.

To induce gradual lamin A/C depletion or PLA accumulation in NHDF cells we used a sustained siRNA-mediated knockdown approach targeting the *LMNA* gene or *ZMPSTE24* gene, respectively (**Fig. 2.1**). We also used the chemical compounds farnesyl transferase inhibitor 276 (FTI), Saquinavir (SQV), and N-acetyl-S-farnesyl-

L-cysteine methylester (AFCMe) to interfere with the maturation of PLA in NHDF cells (**Fig. 2.1**). Both SQV and AFCMe treatment resulted in the accumulation of farnesylated PLA. In addition to the transient models described above, we also applied CRISPR/Cas9 genome editing technology in HT1080 cells to create stable knockouts of *LMNA* and *ZMPSTE24*, respectively.

2 Results

2.1 Repetitive siRNA-mediated knockdown enables sustained depletion of A-type lamins

To enable direct comparison with already available laminopathy patient cells, we chose primary normal human dermal fibroblasts (NHDF) as model cell type.^{60,139,215,216}

To silence *LMNA* in NHDF cells, we used an siRNA-mediated approach. 48h after transfection of an *LMNA*-targeting siRNA pool, we noticed a significant (>90%) reduction in mRNA levels (**Fig. 2.2A**). However, quantitative immunofluorescence revealed that Lamin A/C levels were only modestly reduced after this time frame (**Fig. 2.2B**). This is likely due to the slow turnover of lamins, as they are known to be notoriously stable.²¹⁷ Therefore, we implemented additional transfection rounds and monitored both mRNA and protein levels after every round. While the mRNA levels remained similarly low (**Fig. 2.2A**), protein levels significantly dropped with every transfection round. Quantitative immunofluorescence revealed a ~1.3-fold decrease of nuclear lamin A signal intensity after 48 h and a 4-fold decrease after 264 h, thereby essentially equalling background signal levels (**Fig. 2.2B**). These results were semi-quantitatively confirmed by Western blot at 168 h (**Fig. 2.2C**). At this point, lamin A/C bands could no longer be detected, suggesting a strong depletion, as compared to control cells, which had been exposed to non-targeting siRNAs. Cells that had undergone repetitive *LMNA* knockdown, also demonstrated altered nuclear morphology (**Fig. 2.2D**), namely a slightly more elongated, larger phenotype with a higher degree of irregularity (**Fig. 2.2E & F & G**).

siRNA sequence-specific off-target effects or non-specific toxic side-effects such as the activation of the innate immune response or perturbation of miRNA function can greatly influence the experimental results.²¹⁸⁻²²⁰ Since these side-effects are dose-dependent^{220,221}, we analyzed the influence of siRNA concentration on knockdown efficiency. We compared a final siRNA concentration of 50 nM (recommended by the supplier) with a concentration of 10 nM. No significant difference in RNA-level or protein level was observed between both concentrations (**Fig. 2.2H & I**), indicating that a concentration of 10 nM works equally well.

A hallmark of siRNA-mediated knockdown of a gene is its transient nature. Indeed, when cells subjected to two consecutive rounds of transfection were kept in culture without further transfections, they gradually restored their lamin A levels to their original concentration (**Fig. 2.2B** – pink boxplots).

Thus, these data suggest that a robust, yet reversible, reduction of mature A-type lamins can be achieved at the protein level, by means of a sustained depletion procedure consisting of at least two sequential knockdowns.

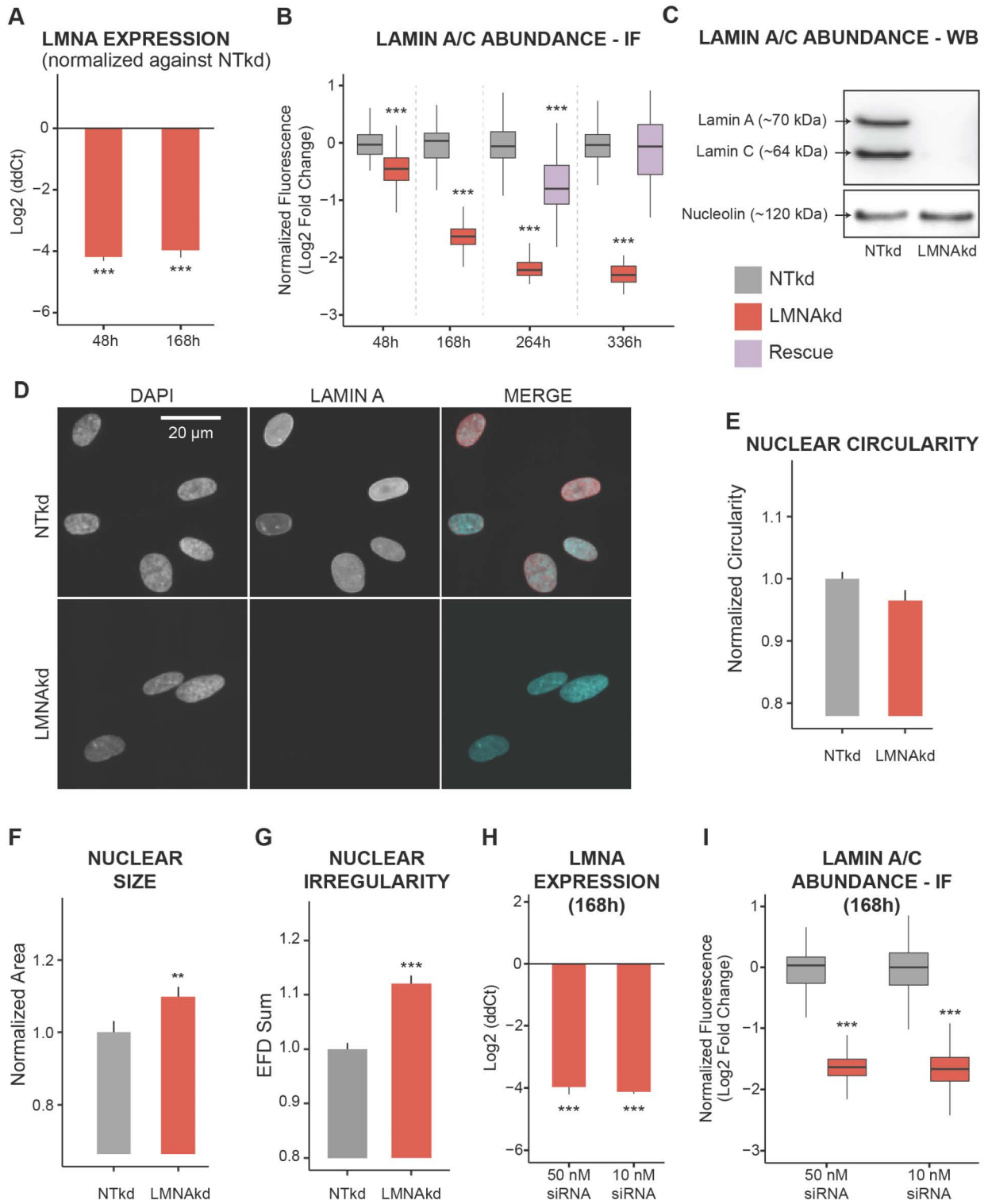


Figure 2.2: Lamin A/C depletion through sustained siRNA-mediated knockdown of LMNA (LMNAkd).

(A) Gene expression levels of *LMNA* measured by real-time qPCR relative to non-targeting control (NTkd). (B) Normalized Lamin A protein levels in LMNAkd cells versus NTkd control, as measured by immunofluorescence staining and quantitative image analysis. The pink boxplots at 264 and 336 h represent the results of a rescue (pulse-chase) experiment: LMNAkd cells at 168 h were no longer transfected with *LMNA*-targeting siRNA and regained their original lamin A level at 336 h. (C) Western blot with an antibody that recognizes lamin A and lamin C, showing absence of lamin A/C in LMNAkd cells at the 168 h time point. Nucleolin was used as a loading control. (D) Representative images of LMNAkd and NTkd control cells at the 264 h time point, after immunofluorescence staining for lamin A (red) and nuclear counterstaining with DAPI (cyan). (H) Gene expression levels of *LMNA* after transfection with 10 or 50 nM siRNA, measured by real-time qPCR relative to non-targeting control (NT). (E & F & G) Normalized nuclear circularity, size and irregularity, as measured by morphological analysis of DAPI-stained nuclei. (I) Lamin A protein levels in LMNAkd cells versus NT control at the 168 h point after transfection with 10 or 50 nM siRNA, measured by immunofluorescence staining and quantitative image analysis. (* = p-value < 0, 05; ** = p-value < 0, 01; *** = p-value < 0, 001).

2.2 CRISPR/Cas9-mediated knockout results in complete loss of A-type lamins

Sustained knockdown offers a means to study progressive or transient effects of lamin A depletion in mortal cells, but precludes long-term follow-up in a stable system. Therefore, we explored the potential of CRISPR/CAS9 genome editing technology to create stable *LMNA* knockout cells. To bypass the poor transfection efficiency and aging character of NHDF cells, we used HT1080 fibrosarcoma cells. After selection, individual clones were grown up to single-cell colonies, further referred to as HT-LKO, and characterized by qPCR, quantitative IF and WB for absence of *LMNA* mRNA and mature lamin A/C proteins. *LMNA* expression (mRNA level) was reduced by more than 64-fold in all selected HT-LKO colonies as compared to mock-transfected wild type (HT-WT) clones (**Fig. 2.3A**). But more importantly, at the protein level, a complete absence of A-type lamins was observed. Immunofluorescence signals for lamin A equalized background signal levels, and detection of A-type lamins with western blot was no longer possible (**Fig. 2.3B & C**).

Furthermore, HT-LKO cells displayed the typical defects in nuclear morphology that are also found in lamin A/C-deficient patient cells (i.e. nuclear irregularity, local depletion of B-type lamins and increased nuclear plasticity²²² - **Fig. 2.3D - I**).

Thus, using CRISPR-Cas9 genome editing, we have established immortalized *LMNA* knockout cell lines that recapitulate the hallmarks of lamin A/C deficiency.

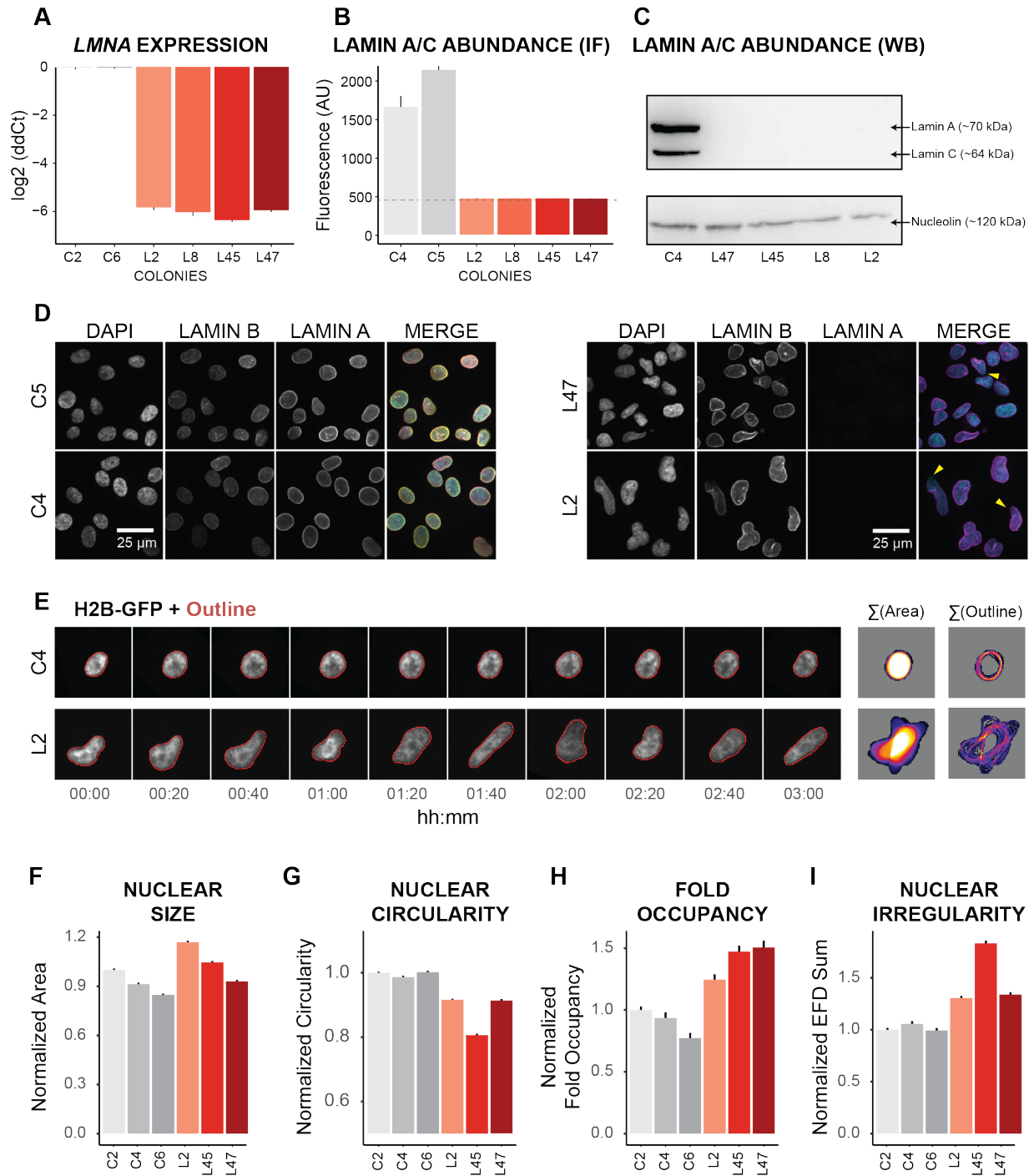


Figure 2.3: HT-LKO cells recapitulate the hallmarks of lamin A/C deficiency.

(A) Quantitative PCR shows an approximate 64-fold reduction (expressed as log₂ fold change of ddCt value) of LMNA transcripts in different LKO colonies as compared to HT-WT clones. (B) Quantitative immuno fluorescence shows a dramatic reduction of A-type lamin levels in HT-LKO colonies, approximating background levels (dotted line). (C) Western blot for lamin A/C reveals the absence of both proteins in HT-LKO cells. (D) Immunostaining and nuclear counterstaining of HT-LKO cells reveals their aberrant nuclear morphology, virtual absence of lamin A (green) and local depletion of lamin B (red; yellow arrows) as opposed to HT-WT cells. (E) Time-lapse recording after H2B-GFP transfection illustrates increased nuclear plasticity of HT-LKO vs. HT-WT cells, as evidenced by their larger projected area (Σ Area) and contour changes (Σ Outline) across time. (F & G & H & I) Normalized nuclear size, circularity, fold occupancy and irregularity, as measured by morphological analysis of DAPI-stained nuclei.

2.3 Sustained accumulation of PLA can be achieved through repetitive siRNA-mediated knockdown of *ZMPSTE24*.

Some laminopathies (e.g. HGPS) are not only associated with a reduction in mature lamin A/C, but also with the accumulation of PLA intermediates. Hence, we next sought to mimic such pathological defect. To trigger PLA accumulation, we used the same repetitive siRNA transfection scheme as presented before, but this time targeting the *ZMPSTE24* gene. Quite alike the knockdown of *LMNA*, *ZMPSTE24* mRNA levels were already at a minimum after one transfection round (48h) (**Fig 2.4A**), whereas PLA protein levels progressively increased with every transfection round, from a 2-fold increase after 48h to a 4-fold increase after three subsequent knockdowns (at 264h) as compared to the NT control (**Fig. 2.4B**). At this point, cells displayed highly dysmorphic nuclei of increased size (**Fig. 2.4D**), with pronounced blebbing and prominent intranuclear LA/PLA staining patterns, reminiscent of an extended nucleoplasmic reticulum²²³(**Fig. 2.4E & F & G**). This phenotype was comparable to nuclei from both HGPS and RD patient fibroblasts (**Fig 2.5 & 2.6**). Thus, our results indicate that a strong and progressive accumulation of farnesylated PLA protein can be achieved by means of the earlier optimized repetitive knockdown procedure.

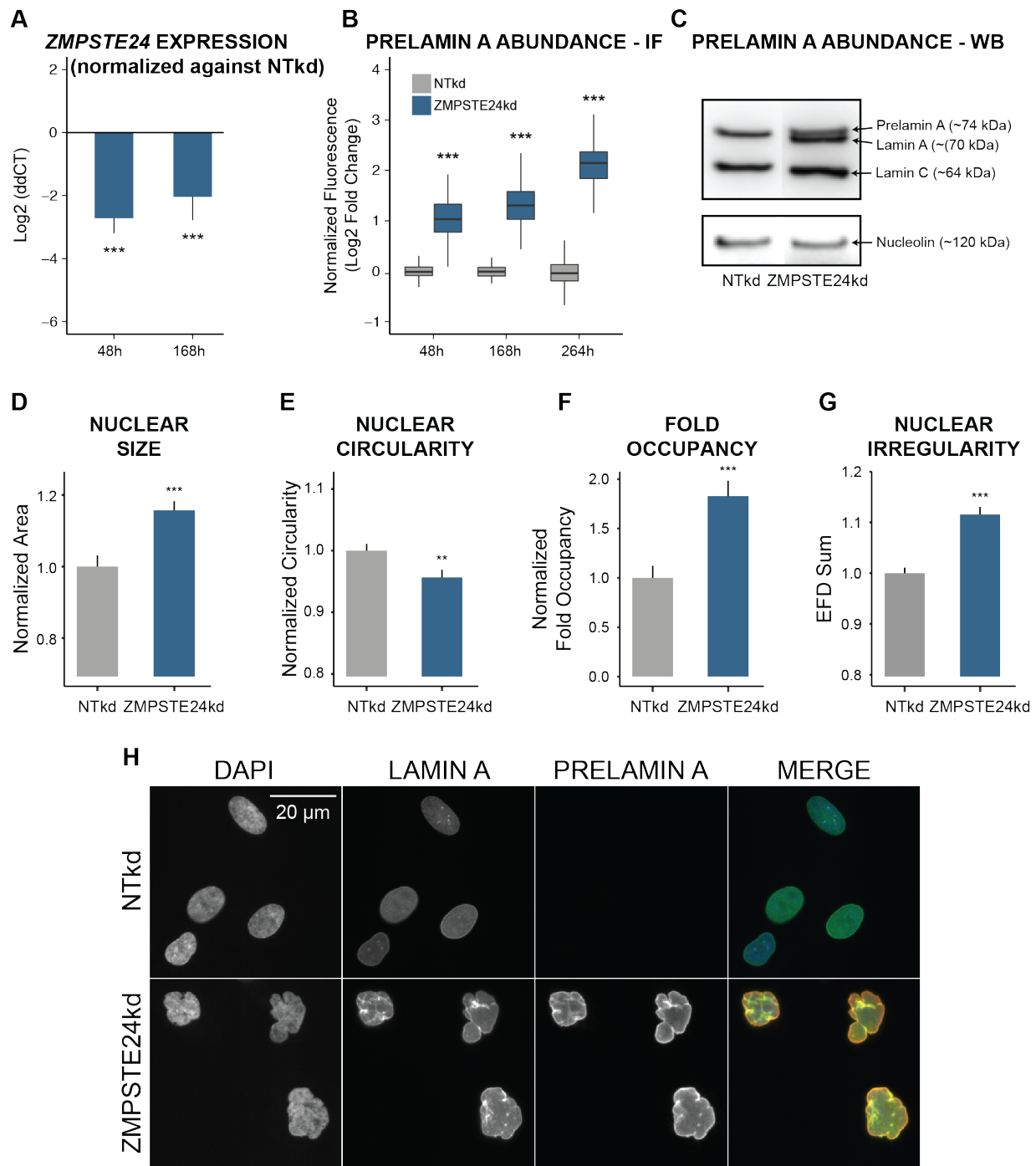


Figure 2.4: PLA accumulation through sustained siRNA-mediated knockdown of ZMPSTE24 (ZMPSTE24kd)

(A) Gene expression levels of *ZMPSTE24* measured by real-time qPCR relative to non-targeting control (NTkd). (B) Normalized PLA protein levels in ZMPSTE24kd cells versus NTkd control, as measured by immunofluorescence staining and quantitative image analysis. (C) Western blot with an antibody that recognizes PLA, showing accumulation of PLA in ZMPSTE24kd cells at the 168 h time point. Nucleolin was used as a loading control. (D & E & G) Normalized nuclear size, circularity and irregularity, as measured by morphological analysis of DAPI-stained nuclei. (F) Normalized fold occupancy, a measure for the relative occupancy of intranuclear lamin structures. (H) Representative images of ZMPSTE24kd and NT control cells at the 264 h time point, after immunofluorescence staining for lamin A (green), PLA (red) and nuclear counterstaining with DAPI (blue). (* = p-value < 0, 05; ** = p-value < 0, 01; *** = p-value < 0, 001).

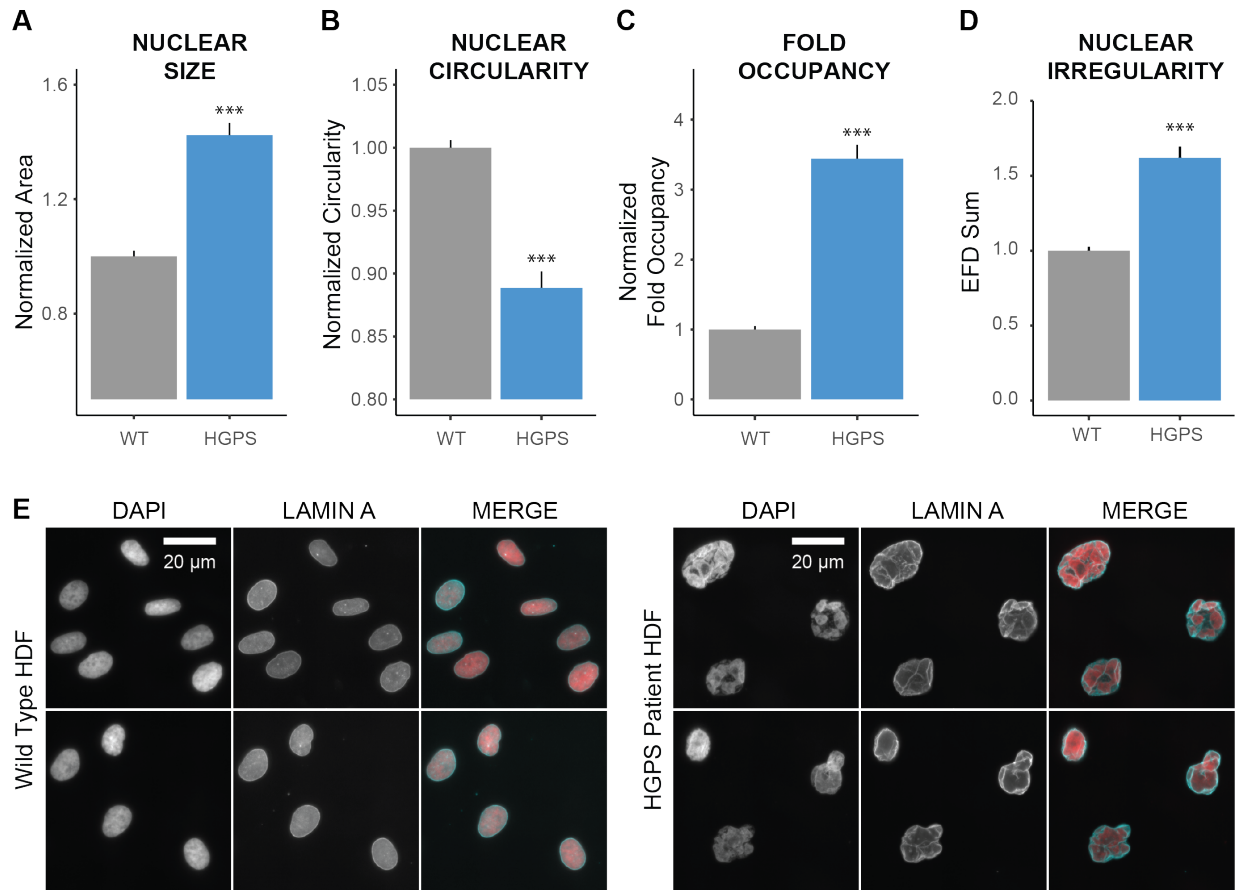


Figure 2.5: Morphology of HGPS patient fibroblast nuclei.

(A & B & D) Normalized nuclear size, circularity and irregularity, as measured by morphological analysis of DAPI-stained nuclei. (C) Normalized fold occupancy, a measure for the relative occupancy of intranuclear lamin structures. (E) Representative images of passage matched HGPS patient fibroblasts and wild type NHDF control cells after immunofluorescence staining for lamin A (cyan) and nuclear counterstaining with DAPI (red). (* = p-value < 0, 05; ** = p-value < 0, 01; *** = p-value < 0, 001).

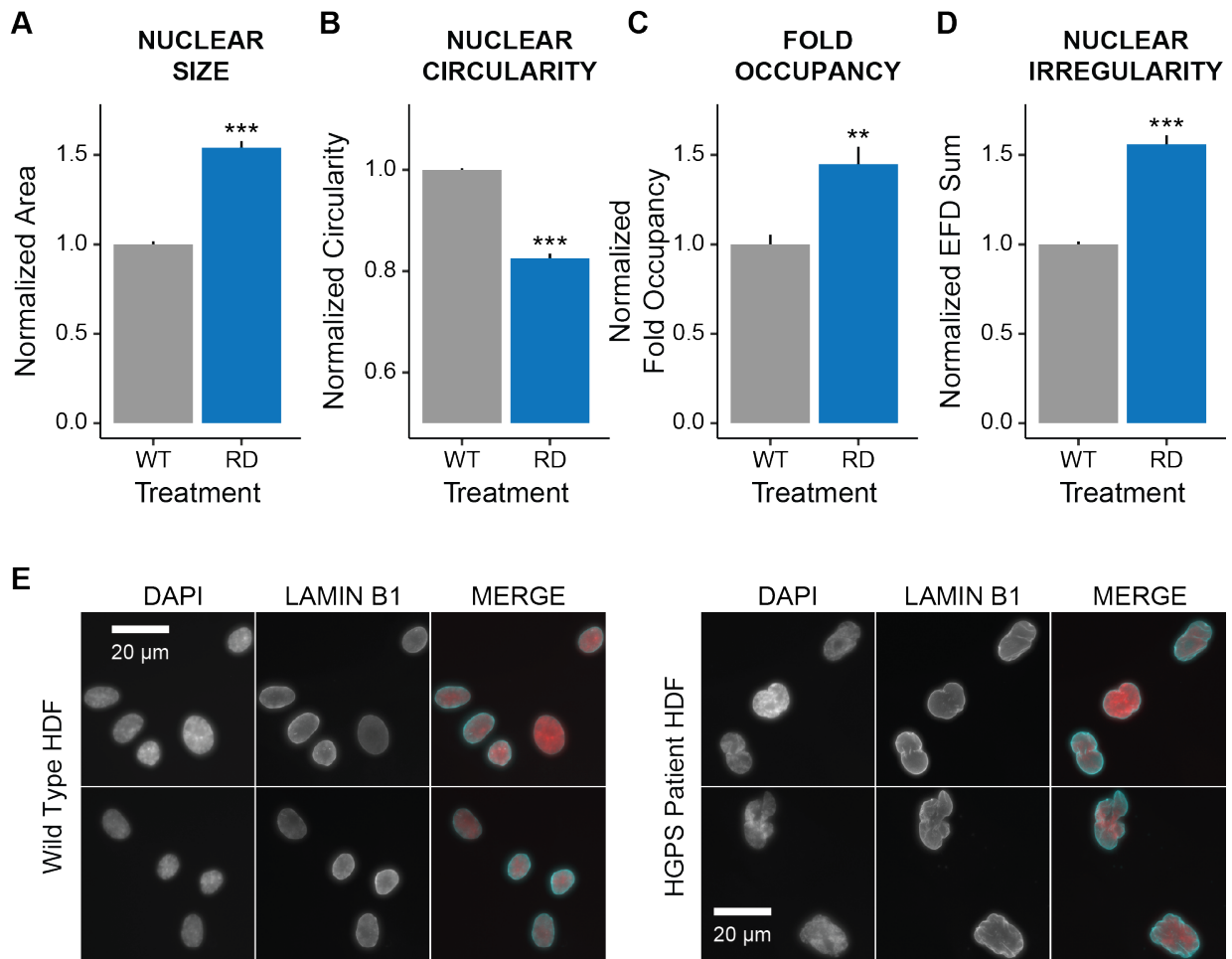


Figure 2.6: Morphology of RD patient fibroblast nuclei.

(A & B & D) Normalized nuclear size, circularity and irregularity, as measured by morphological analysis of DAPI-stained nuclei. (C) Normalized fold occupancy, a measure for the relative occupancy of intranuclear lamin structures. (E) Representative images of passage matched RD patient fibroblasts and wild type NHDF control cells after immunofluorescence staining for lamin B1 (cyan) and nuclear counterstaining with DAPI (red). (* = p-value < 0, 05; ** = p-value < 0, 01; *** = p-value < 0, 001).

2.4 CRISPR/Cas9 mediated knockout of *ZMPSTE24* in HT1080 cells permanently increases PLA accumulation.

Following the same strategy as described for the establishment of HT-LKO cells, CRISPR/Cas9 was used to create a stable *ZMPSTE24* knockout cell lines in HT1080 cells (further referred to as HT-ZKO).

While different HT-ZKO colonies showed variable levels of *ZMPSTE24* mRNA (Fig. 2.7A), all colonies demonstrated a significant accumulation of PLA (Fig. 2.7B). This, at the expense of mature lamin A, as illustrated by the upward shift of the lamin A positive band compared to the HT-WT controls in a WB for A-type lamins (Fig 2.7C). Immunofluorescence staining also revealed aberrant nuclear morphology (blebs), albeit less pronounced as in de NHDF models and with variable penetrance between different colonies (Fig. 2.7D - H).

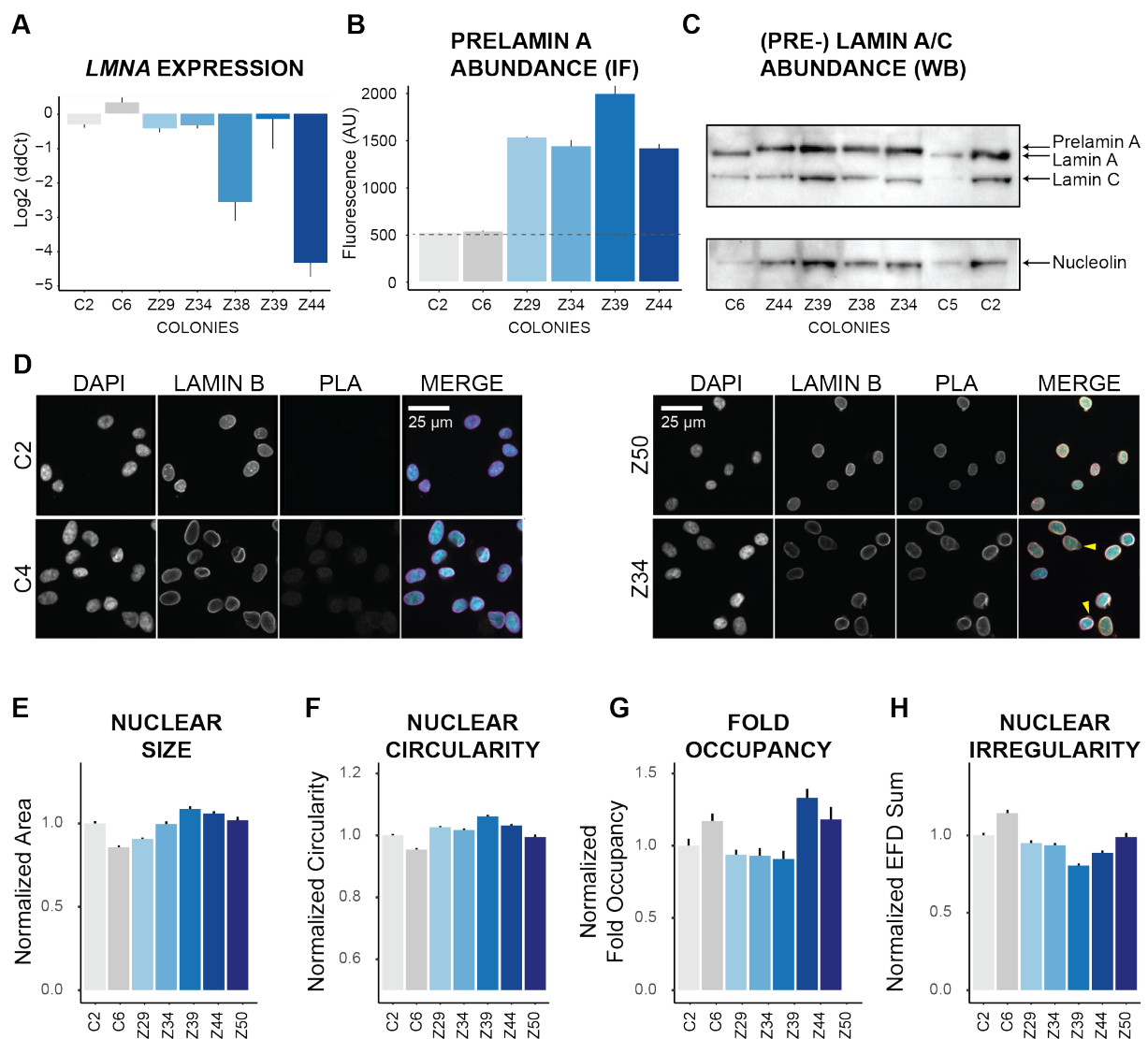


Figure 2.7: Characterization of HT-ZKO colonies.

HT-WT colonies (C2, C4, C5, C6) are labeled in grey tones, and HT-ZKO colonies (Z29, Z34, Z38, Z39, Z44) in blue tones. **(A)** Quantitative PCR shows variable effects on ZMPSTE24 expression in individual HT-ZKO colonies; **(B)** Quantitative immunofluorescence (IF) shows significant accumulation of PLA above background levels (dotted white line) in HT-ZKO cells; **(C)** Western blot (WB) for lamin A/C reveals specific accumulation of PLA, and absence of mature lamin A in HT-ZKO cells, as shown by the upward shift of the lamin A band as compared to the HT WT controls; PLA ~75 kDa, Lamin ~74kDa, lamin C ~64 kDa, nucleolin ~120 kDa **(D)** Immunostaining and nuclear counterstaining of HT-ZKO cells reveals nuclear aberrations (yellow arrowheads) and accumulation of PLA. **(E & F & H)** Normalized nuclear size, circularity and irregularity, as measured by morphological analysis of DAPI-stained nuclei. **(G)** Normalized fold occupancy, a measure for the relative occupancy of intranuclear lamin structures. Normalization was done to the C2-colony.

2.5 Pharmacological induction of PLA variants in NHDF cells.

In an effort to circumvent the expensive process of repetitive transfections, we also explored the use of chemical compounds that are known to interfere with one of the lamin A maturation steps. Specifically, Saquinavir (SQV) and N-acetyl-S-farnesyl-L-cysteine methylester (AFCMe) were used to block the final maturation step, causing

accumulation of farnesylated PLA, whereas farnesyl transferase inhibitor 276 (FTI), was used to trigger accumulation of non-farnesylated PLA. First, dose-response curves were established so as to determine concentrations that are non-cytotoxic on the short-term, i.e., after 48h (**Fig. 2.8**).

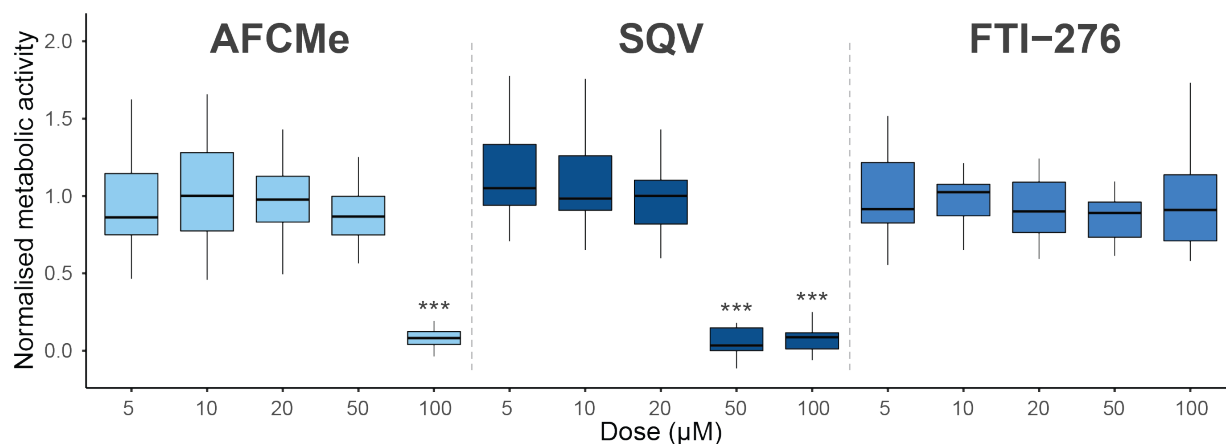


Figure 2.8: Short-term cytotoxicity of AFCMe, SQV and FTI-276.

Normalized metabolic activity in NHDF cells was quantified after 48 h of treatment with various concentrations of the specified chemicals by means of a Presto-Blue colorimetric assay. Lower activity is correlated with higher cytotoxicity of the drug. (* = p-value < 0,05; ** = p-value < 0,01; *** = p-value < 0,001)

Subsequently, the non-toxic concentrations were screened for their capacity to induce PLA accumulation. NHDF cells were again treated for 48 hours followed by an immunofluorescence staining for PLA. Results were then compared to the results obtained with ZMPSTE24kd. After 48h ZMPSTE24kd resulted in a 2-fold increase of intracellular PLA (**Fig. 2.4B**). AFCMe only resulted in significant PLA accumulation at 50 µM (**Fig. 2.9**). SQV (**Fig. 2.10**) and FTI (**Fig. 2.11**) both induced a gradual increase of PLA with increasing concentration. The highest increase (more than 3-fold) was observed with 20 µM SQV. Based on these results, we selected AFCMe (50 µM; 1.57-fold increase), SQV (10 µM & 20 µM; 2.20 and 3.39-fold increase) and FTI (50 µM & 100 µM; 1.56 and 1.84-fold increase) for further analysis.

Next, we quantified nuclear morphology. FTI induced a significant increase in donut-like nuclei, especially at 100 µM (**Fig. 2.12A & B**), which is not observed in ZMPSTE24kd. Therefore we discarded 100 µM FTI from further analyses. For all other treatments, we measured nuclear size (projected area), circularity, fold occupancy and irregularity, after 48h and 144h of treatment. At 48h, AFCMe mainly resulted in the formation of intracellular lamin A structures (**Fig. 2.13C**). SQV induced a smaller and rounder nuclear phenotype (**Fig. 2.13 A & B**), while FTI-treatment produced larger nuclei with increased intranuclear structures and a more irregular contour, accompanied by the aforementioned donuts (**Fig. 2.13 A & C & D**). At 144h, All treatments further increased intracellular lamin A structures (**Fig. 2.13G**). AFCMe also caused a substantial gain in nuclear size (**Fig. 2.13E**), while SQV on the other hand (especially 20 µM) again induced smaller and rounder nuclei (**Fig. 2.13 E & F**). Representative images for all treatments are shown in **Figure 2.13 I & J**.

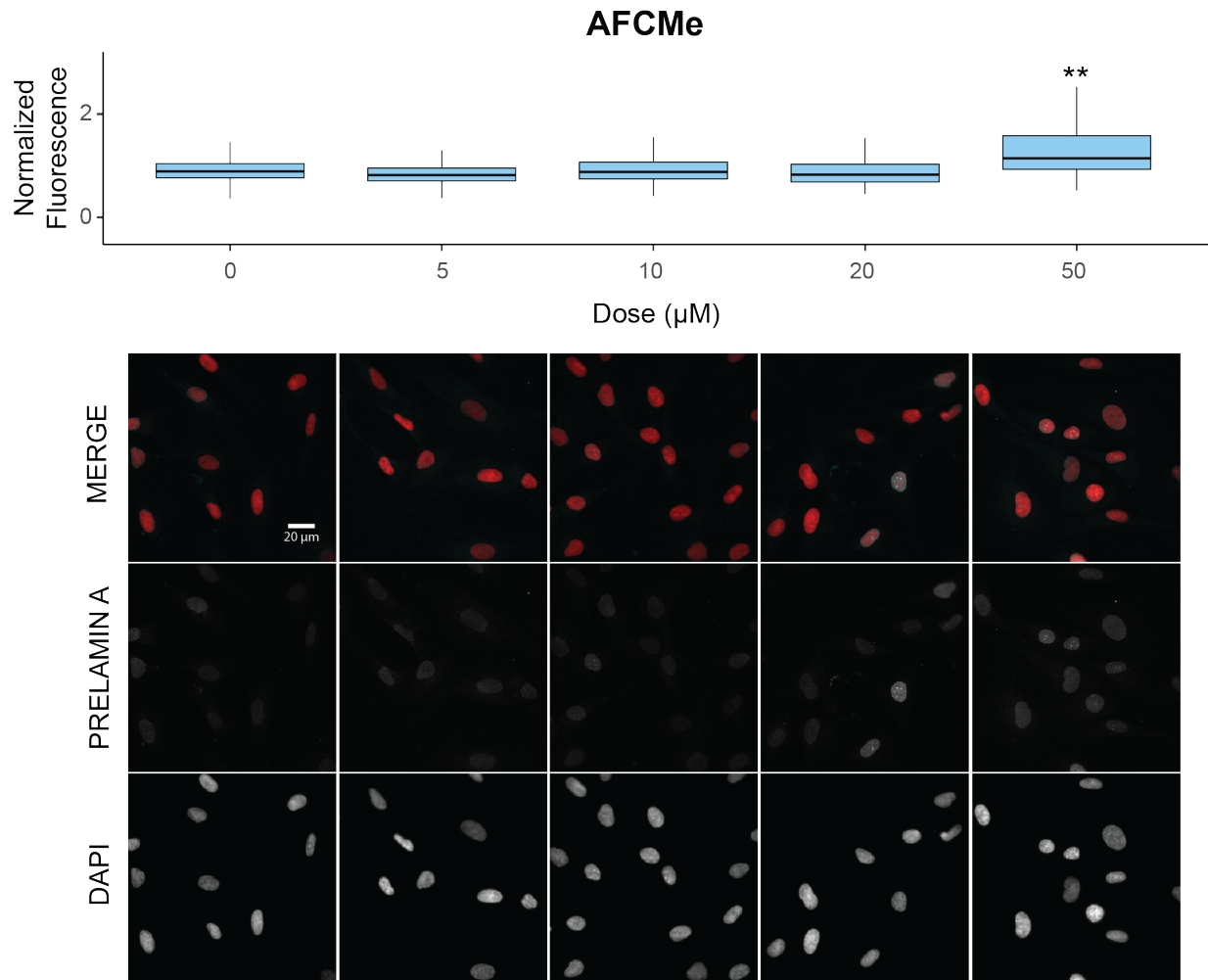


Figure 2.9: PLA accumulation upon AFCMe treatment.

(A) PLA accumulation after treatment of NHDF cells for 48h with increasing concentrations of AFCMe (5, 10, 20 and 50 μM) or vehicle (methanol), as measured by immunofluorescence staining and quantitative image analysis. (B) Representative images of AFCMe treated and control cells after immunofluorescence staining for PLA (cyan) and nuclear counterstaining with DAPI (red). (* = p-value < 0, 05; ** = p-value < 0, 01; *** = p-value < 0, 001).

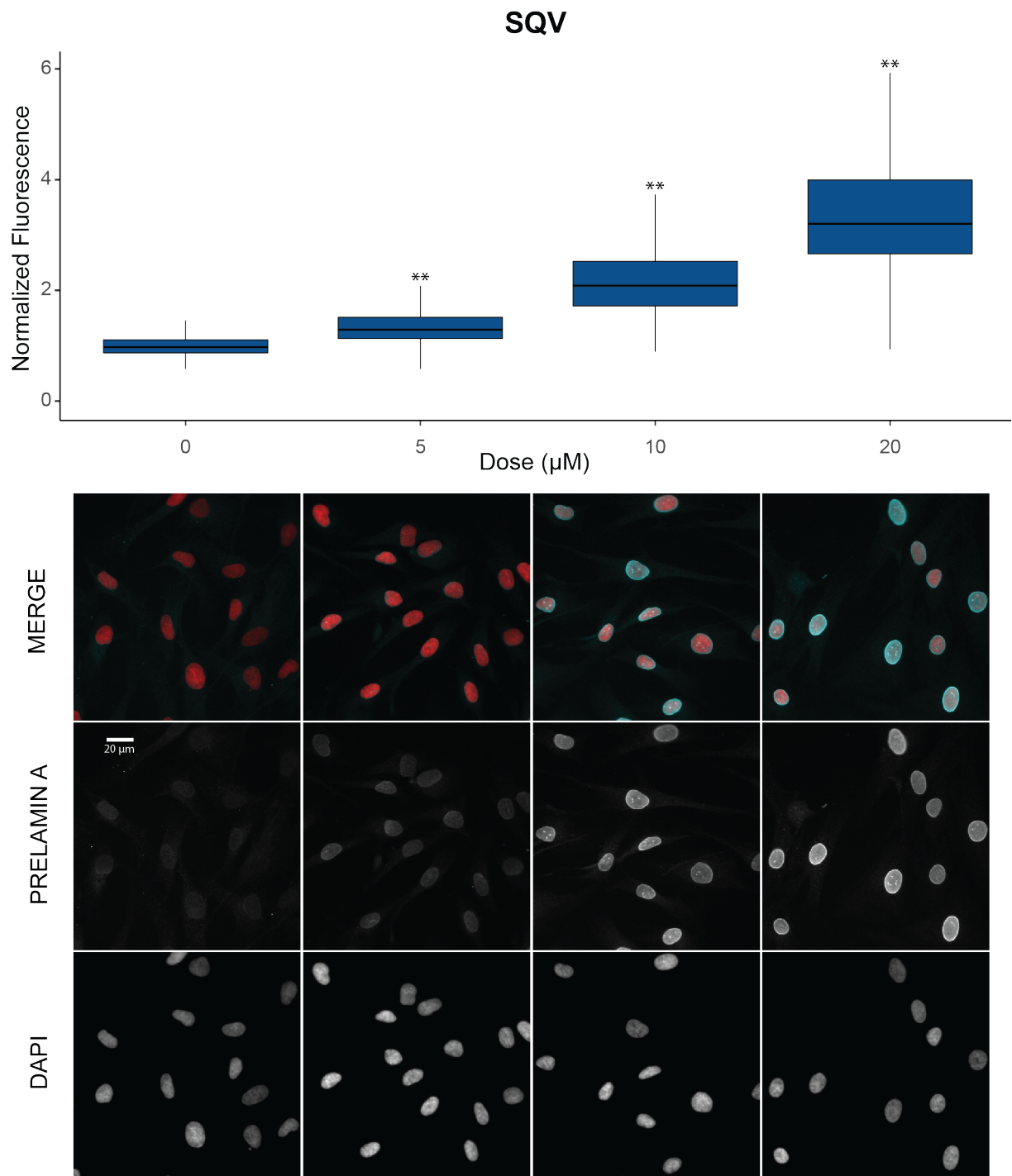


Figure 2.10: PLA accumulation upon SQV treatment.

(A) PLA accumulation after treatment of NHDF cells for 48h with various concentrations of SQV (5, 10 and 20 μM) or vehicle (DMSO), as measured by immunofluorescence staining and quantitative image analysis. (B) Representative images of SQV treated and control cells after immunofluorescence staining for PLA (cyan) and counterstaining with DAPI (red). (* = p-value < 0, 05; ** = p-value < 0, 01; *** = p-value < 0, 001).

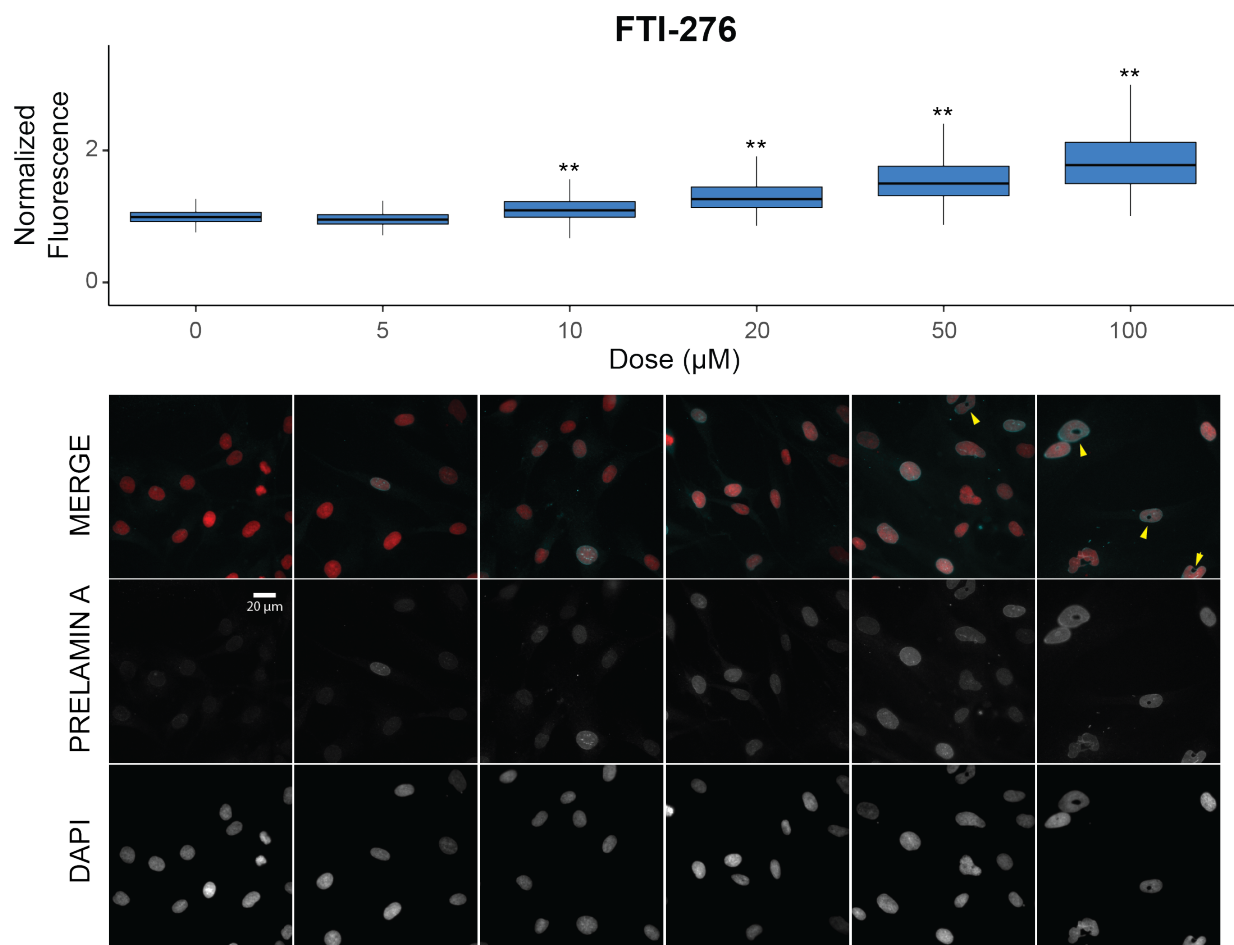


Figure 2.11: PLA accumulation upon treatment with FTI-276

(A) PLA accumulation after treatment of NHDF cells for 48h with various concentrations of FTI-276 (5, 10, 20, 50 and 100 µM) or vehicle (DMSO), as measured by immunofluorescence staining and quantitative image analysis. (B) Representative images of FTI treated and control cells after immunofluorescence staining for PLA (cyan) and counterstaining with DAPI (red). Yellow arrows indicate donut-shaped nuclei. (* = p-value < 0, 05; ** = p-value < 0, 01; *** = p-value < 0, 001).

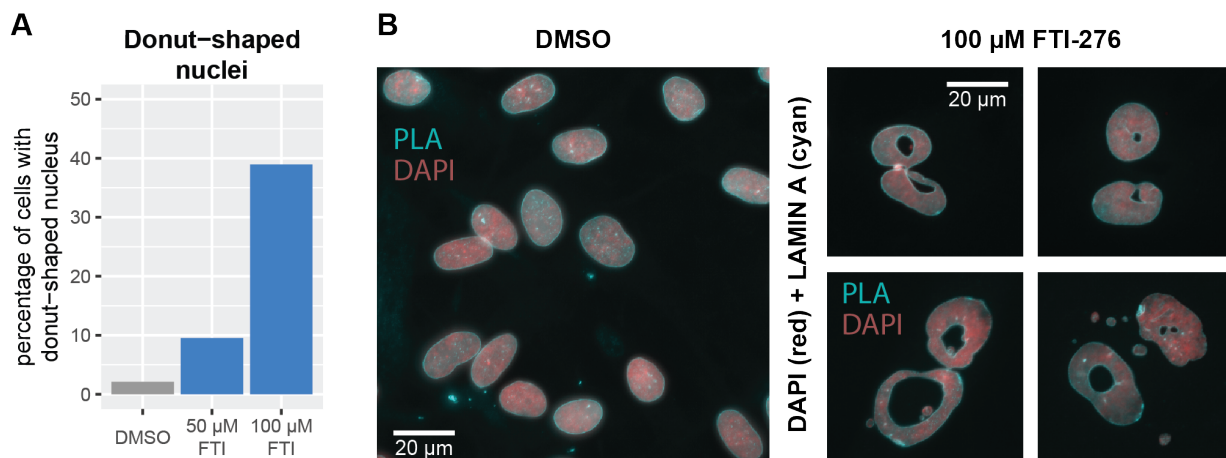


Figure 2.12: FTI-276 induces the formation of donut-shaped nuclei

(A) Percentage of screened cells with donut-shaped nuclei. (B) Representative images of donut-shaped nuclei upon FTI-treatment.

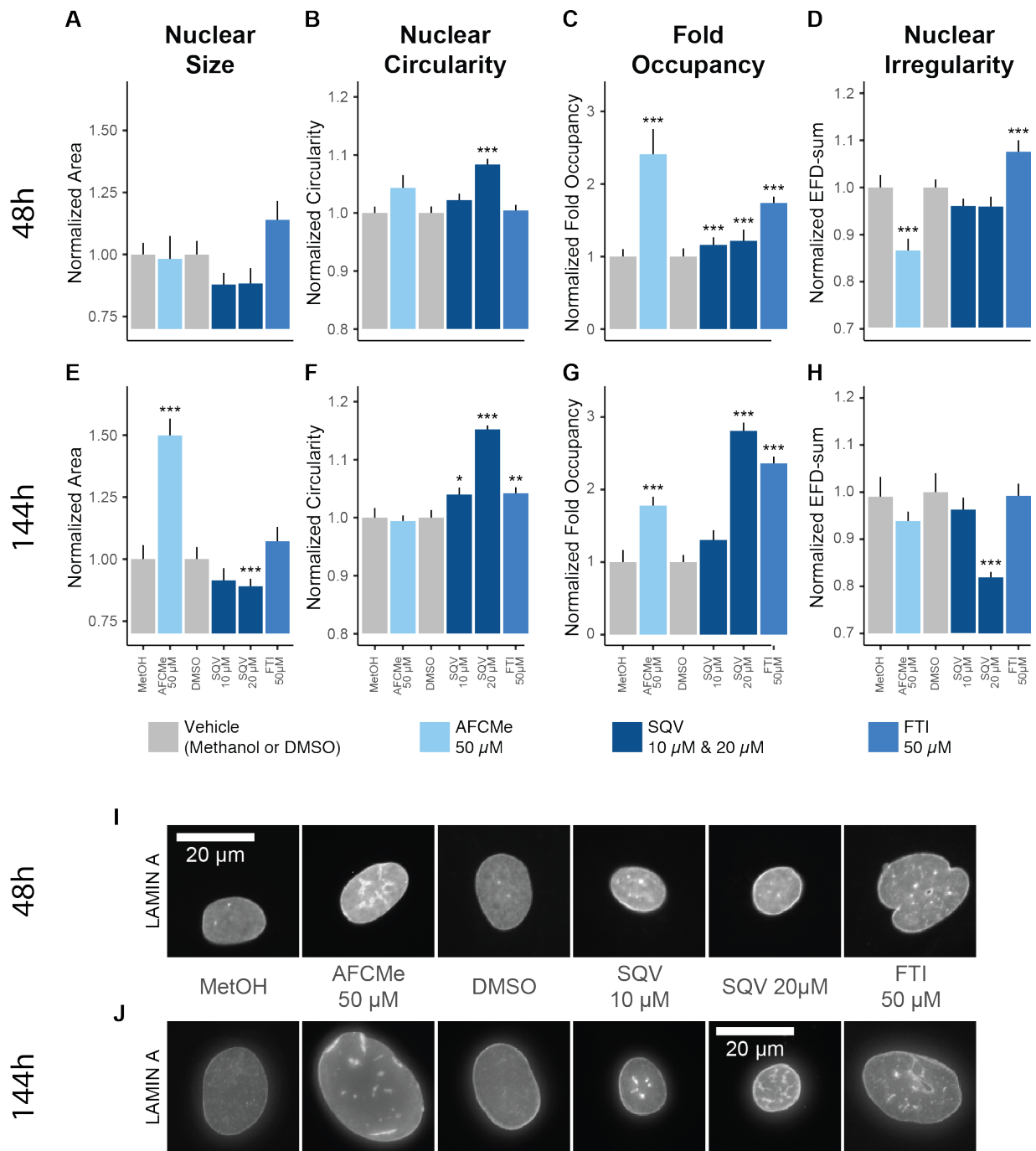


Figure 2.13: Nuclear morphology upon 48h and 144h treatment with selected compounds.

(A & B & D & E & F & H) Normalized nuclear size, circularity and irregularity, as measured by morphological analysis of DAPI-stained nuclei. (C & G) Normalized fold occupancy, a measure for the relative occupancy of intranuclear lamin structures. (I & J) Representative images of NHDF control cells and cells treated with the selected compounds after immunofluorescence staining for lamin A (* = p-value < 0, 05; ** = p-value < 0, 01; *** = p-value < 0, 001. All levels of significance are with to the respective controls, for AFCMe this is Methanol, for SQV and FTI this is DMSO). (* = p-value < 0, 05; ** = p-value < 0, 01; *** = p-value < 0, 001. All levels of significance are with to the respective controls, for AFCMe this is Methanol, for SQV and FTI this is DMSO)

3 Discussion

In this chapter, we have characterized and optimized a set of perturbations to interfere with A-type lamin production in a targeted manner. First, we have optimized two approaches to deplete lamin A/C, namely through sustained knockdown (RNAi) or knockout (CRISPR/Cas9) of the *LMNA* gene. Mature lamin A has a slow protein turnover because of its firm integration in the nuclear lamina.²¹⁷ This was confirmed in our initial attempts to reduce lamin A/C levels by means of a single knockdown, where we found a solid reduction of *LMNA* mRNA but a very modest impact on the protein levels. Hence, we introduced a new approach to trigger sustained knockdown by submitting NHDF cells to subsequent rounds of siRNA transfection. After 3 transfection rounds, 11 days after the initial transfection, virtually no lamin A/C could be detected, and this was also accompanied by changes in nuclear morphology. Nuclei were slightly bigger and more dysmorphic as compared to their mock-transfected counterparts. This higher degree of nuclear irregularity might indicate that the nuclei experience a higher degree of plasticity, as previously documented in nuclei of other *LMNA*-deficient cell models.^{139,224,225} Lowering the transfected siRNA concentration five-fold had no apparent effect on the knockdown efficiency. However, by reducing the siRNA concentration, potential sequence-specific off-target effects or sequence-non-specific toxic side-effects such as the activation of inflammatory cytokines and type I interferon, or perturbation of miRNA function can be minimized, increasing the reliability of downstream experiments.^{218-220,226}

Next to the sustained knockdown, a CRISPR/Cas9-mediated genome editing strategy was applied to permanently knock out the *LMNA* gene in HT1080 cells. Colonies with significantly decreased lamin A/C concentrations were selected and further characterized. *LMNA* expression in these HT-LKO cells was virtually absent and they displayed a nuclear morphology bearing all the hallmarks of *LMNA* deficient cells.^{139,222} The major advantage of this model over the sustained knockdown is their ease of use. Once created these stable cell lines do not need extra treatment and can be used directly in downstream experiments. A disadvantage is that HT1080 cells are tumor-derived, rendering them physiologically less relevant than primary cells, especially for research into aging-related diseases or processes. Also, immortal (cancer) cell lines have inherent higher inter-colony variability than primary cells²²⁷, which increases experimental noise. Finally, long-term culturing might select for cells that have developed counter-mechanisms for better coping with this molecular handicap. This may decrease the physiological relevance towards the original pathologies.

Since many laminopathies are associated with the accumulation of PLA variants, we also explored methods to specifically block the lamin A maturation pathway. Because the farnesylated variant is presumed to be the most toxic PLA variant, most of these strategies targeted the ZMPSTE24 enzyme.

As with *LMNA*, a sustained knockdown was obtained through repetitive transfections with siRNA targeting the *ZMPSTE24* transcript. Again, RNA

expression dropped quickly to a minimum, while PLA accumulation increased steadily (up to 4-fold) over time and was accompanied with changes in nuclear morphology. The dramatic increase of nuclear folds and blebs was in accordance with observations in *Zmpste24*-deficient mouse embryonic fibroblasts (MEF)²²⁸ and HGPS and RD patient fibroblasts, both in own experiments, as in literature.¹⁰⁶ Also similar to *LMNA*, a CRISPR/Cas9-mediated *ZMPSTE24*-knockout HT1080 cell line (HT-ZKO) was created. HT-ZKO colonies were selected based on their PLA accumulation. In contrast to HT-LKO colonies, where lamin A depletion was always accompanied by a decreased expression of *LMNA*, some HT-ZKO clones still showed *ZMPSTE24* expression despite a marked PLA accumulation. The expressed *ZMPSTE24* mRNA in these specific clones is likely a truncated mRNA prone to nonsense-mediated decay²²⁹, or gives rise to a non-functional ZMPSTE24 enzyme. Nuclear aberrations in these cells were visibly less pronounced than in the NHDF-ZMPSTE24kd model cells, but they still displayed an increase of blebs and folds. NHDF-ZMPSTE24kd cells were all analysed 2 to 11 days after initiation of the knockdown, HT-ZKO cells on the other hand went through selection and clonal expansion before analysis, which takes significantly longer than 11 days. Therefore, these cells might already have adapted to the accumulation of PLA, possibly explaining the less aberrant nuclei.

As the pathway of lamin A maturation is well-known, we exploited this knowledge to explore the impact of selected pharmacological treatments (AFCMe, SQV and FTI-276), again in NHDF cells. After determining doses that did not result in acute cytotoxicity (i.e. after 48h), PLA levels were monitored and the resulting cells were characterized. SQV had the strongest PLA accumulation, reaching a 2 to 3-fold increase with 10 and 20 μ M respectively. Accumulation in AFCMe and FTI treated cells was more moderate at 1.5-fold with 50 μ M, compared to vehicle treated control cells. However, with increasing concentrations, also certain side effects became apparent. Treatment with FTI-276 was accompanied by the formation of donut-shaped nuclei. This phenotype is likely caused by a centrosome separation defect due to disturbed lamin B1 processing.²³⁰ Lamin B1, like lamin A, is produced as a prelamins B1 (PLB1), which undergoes the same processing steps as PLA, except for the defarnesylation step mediated by ZMPSTE24. Lamin B1 thus stays permanently farnesylated. But upon FTI treatment, unfarnesylated Lamin B1 is produced, interfering with its role in centrosome separation.^{231,232} Treatment with SQV, in turn, induced nuclear shrinkage and increased nuclear circularity, in contrast to the larger and more dysmorphic nuclei observed in NHDF-ZMPSTE24kd and HGPS patient cells. Finally, AFCMe induced only a minor (1.5 fold) increase of PLA when compared to ZMPSTE24kd and also mostly lacks the nuclear irregularity that is expected upon PLA accumulation.

In summary, using sustained siRNA-mediated knockdown and CRISPR/Cas9 genome editing we have established robust cellular models to study *LMNA* and *ZMPSTE24* dependent pathways. Pharmacological interventions proved less effective, with non-toxic concentrations yielding subtle effects on nuclear morphology, while higher doses resulted in side-effects. The sustained knockdown

approach can be applied in primary cell cultures to transiently interfere with lamin A/C metabolism, while, CRISPR/Cas9-mediated genome editing allows for more permanent interventions. While we have currently only presented proof-of-principle using knockout strategies, there lies strong potential in complementary knock-in approaches to introduce exact pathology-causing point mutations and create even more exact models.

4 Materials and methods

4.1 Cell culture

Normal human dermal fibroblasts (NHDF, LMNA^{+/+}, Promo-Cell, C-12300), fibroblasts from a patient suffering from HGPS (LMNA^{G608G/C})²³³, fibroblasts from a patient suffering from RD (ZMPSTE24^{C1085-1086insT/C1085-1086insT})¹³⁴, and human fibrosarcoma cells (HT-1080, kindly shared by Prof. K. Wolf, Radboud University of Nijmegen, The Netherlands) were cultured in DMEM high glucose with L-glutamine medium (Lonza, BE12-604F) supplemented with 10% fetal bovine serum (Gibco, 10500-064) and 1% penicillin/streptomycin (Lonza, DE17-602E/12), at 37°C and 5% CO₂, according to standard procedures. All experiments were performed with cells in between passage 9 and 18. In case of direct comparison, passage-matched cells were used.

4.2 Chemical treatments

Saquinavir (SQV; Sigma-Aldrich - S8451) and N-acetyl-S-farnesyl-L-cysteine methylester (AFCMe; Enzo Life Sciences -ALX-290-010-M010) were used to specifically accumulate farnesylated PLA. SQV was originally developed as a HIV-protease inhibitor but also targets ZMPSTE24.²³⁴ AFCMe is a non-peptidomimetic compound that impairs binding of ZMPSTE24 to prelamin A through noncompetitive inhibition.²³⁵ Accumulation of non-farnesylated PLA was induced with farnesyl transferase inhibitor 276 (FTI; Sigma-Aldrich - F9553). Stock solutions of SQV and FTI-276 were dissolved in DMSO, AFCMe in methanol.

Chemical treatments started one day after seeding the cells, when the culture density was around 50%, and compound-containing medium was replenished every day.

See **Fig. 2.1** for a schematic overview of the different treatments and their targets.

4.3 Sustained siRNA-mediated knockdown

Expression of *LMNA* and *ZMPSTE24* was silenced with siGENOME Lamin A/C Control siRNA (GE Healthcare Dharmacon, D-001050-01-20) and siGENOME Human ZMPSTE24 siRNA (GE Healthcare Dharmacon, M-006104-02-0020), respectively. Stealth RNAi siRNA Negative Control, Med GC (Thermo Scientific, 12935-300) was used as a negative non-targeting control (NT). siRNA transfections were performed using Lipofectamine[®] RNAi-MAX Transfection Reagent (Thermo Scientific, 13778075), according to manufacturer's instructions and following the scheme outlined in **Fig. 2.13**. We used 9.6 μL of Lipofectamine[®] RNAi-MAX

Transfection Reagent and 50 nM or 10 nM of total siRNA per T25 tissue culture flask.

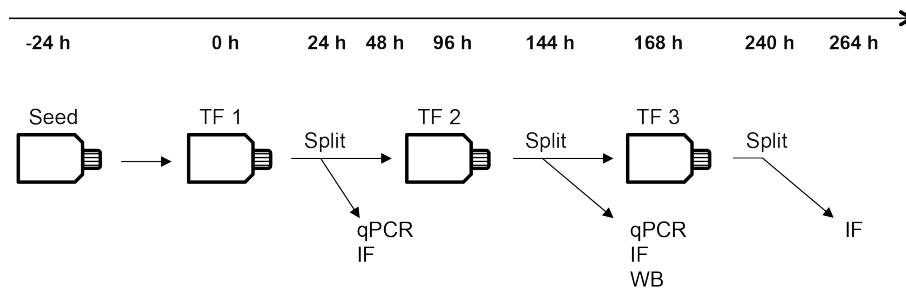


Figure 2.14: Experimental design.

Scheme of the sustained siRNA-mediated knockdowns by repetitive transfections (TFs) and subsequent experiments.

4.4 Genome editing

To obtain stable knockout HT1080 cell lines for *LMNA* (HT-LKO), *ZMPSTE24* (HT-ZKO) and controls (HT-WT), we used the CRISPR-Cas9 genome editing system. The plasmids containing guide RNAs (gRNA) and Cas9 were constructed starting from pSpCas9(BB)-2A-GFP (PX458) or pSpCas9(BB)-2A-Puro (PX459) (from Feng Zhang’s lab, Addgene # 48138 and 48139). They were made based on the protocol of Ran *et al.*²³⁶, and were delivered to cells by plasmid transfection using lipofectamine 2000 (Thermo Scientific, 11668027). The gRNA sequence targeting the first exon of the *LMNA* gene was 5’ – CCTTCGCATCACCGAGTCTGAAG - 3’ , the one targeting the first exon of the *ZMPSTE24* gene was 5’ - GGCCGAGAAGCGTATCTTCGGGG - 3’. They were designed with the CRISPR oligo design tool (Feng Zhang lab). 48 h after transfection, cells were selected either by culturing them in the presence of puromycin (1 µg/ml) or by FACS. Control cells underwent the same treatment mentioned above but with a construct containing no gRNA. Individually selected cells were grown to colonies and screened by quantitative immunofluorescence for absence of lamin A/C. Targeting efficiency was validated by high-resolution melt (HRM) analysis around the cut position of the Cas9 protein using the following primers: for *LMNA*: forward: 5’ - GCATCACCGAGTCTGAAGAG -3’ , reverse: 5’ -ACTGAGTCAAGGGTCTTGCG - 3’ , and for *ZMPSTE24*: forward: 5’ -CTGGACGCTTTGTGGGAGAT -3’ , reverse: 5’ -CGCTGTGCTAGGAAGGTCTC -3’ . Four of the most abundant potential offtarget sites (determined with the CRISPR oligo design tool mentioned above) were amplified and analyzed with Sanger sequencing. None of these sequences showed a change compared to the control, indicating the specificity of the system.

4.5 qPCR

RNA was extracted from cells using the RNAeasy mini kit (Qiagen, 74104), with on-column DNase digestion. Concentrations of purified RNA were measured with the NanoDrop 2000 (Thermoscientific). Per sample, 1 mg of RNA was converted to cDNA using SuperScript® III Reverse Transcriptase (RT) (Life Technologies, 18080–044). All qPCR reactions were performed on a RotorGene 3000 (Qiagen/Corbett), using the SensiMix™ SYBR® No-ROX Kit (Bioline, QT650) according to the manufacturer's instructions. Abundance of *LMNA* transcripts (forward: TGGACGAGTACCAGGAGCTT; reverse: ACTCCAGTTTGCCTTTTTG), and *ZMPSTE24* transcripts (forward: CGAGAAGCGTATCTTCGGG; reverse: TGTGCTAGGAAGGTCTCCCA), was measured relative to *ACTB* (forward: CCTTGCACATGCCGGAG; reverse: GCACAGAGCCTCGCCTT) and *GAPDH* (forward: TGCACCACCAACTGCTTAGC; reverse: GGCATGGACTGTGGTCATGAG) reference transcripts. Ct-values were calculated using the 'comparative quantification' (CQ) method supplied as part of the Rotor Gene 3.0 software (Corbett Research). Analysis was done using the $\Delta\Delta C_t$ -method.²³⁷

4.6 Western Blot

Cells were grown in T75 culture flasks and lysed using the whole-cell extraction protocol of the Nuclear Extract Kit (Active Motif, 40010). Protein concentration was measured with the Pierce 660 nm assay (Thermo Scientific, 22662). Cell lysates were subjected to SDS-PAGE (8% bis-tris with MOPS running buffer) and transferred to BioTrace PVDF membranes (Pall Corporation, 66542). Primary antibodies were directed against lamin A/C (Santa Cruz Biotechnology Inc., sc-56139) and nucleolin (control) (Novus Biologicals, NB600–241). HRP conjugated goat anti-mouse (Sigma-Aldrich, A4416) and HRP conjugated goat anti-rabbit (Sigma-Aldrich, A6154) were used as secondary antibodies. Proteins were detected by chemiluminescence with Immobilon Western chemiluminescent HRP substrate (Millipore, WBKLS0100) using a western blot imager (Biorad, ChemiDoc™ XRS+). Bands were analysed using Fiji (<http://fiji.sc>), a packaged version of ImageJ freeware.

4.7 Immunofluorescence staining

NHDF cells were grown on glass coverslips and fixed in 4% paraformaldehyde for 15 minutes at room temperature and washed (3x, 5 minutes) with PBS. Subsequently, cells were permeabilized with 0.5% Triton X-100 (5 minutes), after which they were blocked with 50% fetal bovine serum (FBS) for 30 minutes and incubated with primary antibody diluted in 50% FBS for 60 minutes. After minimally 3 PBS wash steps, slides were incubated with secondary antibody diluted in 50% FBS for 30 minutes, washed again, and mounted with VECTASHIELD™ Mounting Medium (VWR, 101098–042) containing 1 mg/ml 4',6-diamino-2-phenylindole (DAPI). Primary antibodies were directed against lamin A (Abcam, ab26300) and PLA (Santa Cruz Biotechnology Inc., SC-6214). As secondary antibodies DyLight

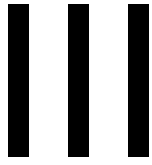
488 conjugated donkey anti-rabbit (Jackson ImmunoResearch Laboratories Inc., JAC-705606147), and DyLight 649 conjugated donkey anti-goat (Jackson ImmunoResearch Laboratories Inc., JAC-705496147) were used. Immunofluorescent stained cells were visualized using a Nikon Ti Eclipse inverted widefield fluorescence microscope (Nikon Instruments) with Nikkor 20x Plan Apo air (NA = 0.75), 40x Plan Apo oil (NA = 1.3) and 60x Plan Apo VC (NA = 1.4) objectives.

4.8 Image analysis

All image processing was performed in FIJI (<http://fiji.sc>), a packaged version of ImageJ freeware (W.S. Rasband, USA. National Institutes of Health, Bethesda, Maryland, USA, <http://rsb.info.nih.gov/ij/>, 1997–2014). Quantification of nuclear signal intensities of immunostained cell cultures was done using a custom-designed image processing pipeline, which is essentially based on a high-content analysis workflow described before.²⁷ (De Vos et al., Cytometry 2010). For the analysis of nuclear morphology, we used another in house developed plugin termed Blebbed Nuclei Detector (BLEND).²³⁸ The following parameters were quantified: nuclear area, the projected area of the segmentation based on a DAPI nuclear counterstain; nuclear circularity, the circularity of the same DAPI segmentation; fold occupancy, a measure for the relative area of the nucleus that is covered with intranuclear lamin structures such as folds and intranuclear tubules; nuclear irregularity, measured by the sum of 50 Elliptic Fourier Descriptors (EFD) of the nuclear contour, the more the contour deviates from an ellipse, the higher the value. All scripts are available upon request.

4.9 Statistical analyses

Data analysis and visualization was performed in R statistical freeware (<http://www.r-project.org>). Standard statistical methods were employed, including the Shapiro-Wilk Normality Test to assess normality of the data, Levene's test to assess homoscedasticity, student's t-test, ANOVA and the Kruskal-Wallis rank sum test to assess differences between the group means and Tukey (after ANOVA) and Dunnett type (After Kruskal-Wallis) post-hoc tests to assess significance for each group. When criteria for normality or homoscedasticity were not met, non-parametric multivariate tests from the nparcomp package were used.²³⁹ If only 2 treatments are compared two sample tests for the nonparametric Behrens-Fisher problem are performed. For more than 2 treatments, a non-parametric contrast-based multiple comparison test is used. Significance levels were indicated as follows: $p < 0.05$ (*), $p < 0.01$ (**), and $p < 0.001$ (***). For graphics and annotation, the R program was expanded with the ggplot2 package.²⁴⁰



HIGH-CONTENT QUANTIFICATION OF INTRACELLULAR ROS LEVELS AND MITOCHONDRIAL MORPHOFUNCTION

Redrafted from Sieprath et al. 2016² and Sieprath et al. 2017²⁴¹

1. Sieprath, T., Corne, T. D. J., Willems, P. H. G. M., Koopman, W. J. H. & De Vos, W. H. Integrated High-Content Quantification of Intracellular ROS Levels and Mitochondrial Morphofunction. *Adv Anat Embryol Cell Biol* **219**, 149–177 (2016).
2. Sieprath, T., Corne, T., Robijns, J., Koopman, W. J. H. & De Vos, W. H. Cellular Redox Profiling Using High-content Microscopy. *J Vis Exp* e55449–e55449 (2017). doi:10.3791/55449

Abstract

Oxidative stress arises from an imbalance between the production of reactive oxygen species (ROS) and their removal by cellular antioxidant systems. Especially under pathological conditions, mitochondria constitute a relevant source of cellular ROS. These organelles harbor the electron transport chain, bringing electrons in close vicinity to molecular oxygen. Although a full understanding is still lacking, intracellular ROS generation and mitochondrial function are also linked to changes in mitochondrial morphology. To study the intricate relationships between the different factors that govern cellular redox balance in living cells, we have developed a high-content microscopy-based strategy for simultaneous quantification of intracellular ROS levels and mitochondrial morphofunction. Using this method, we show that a multi-parametric redox readout enables the unambiguous classification of chemically perturbed cells, as well as laminopathy patient cells.

1 Introduction

The concentration of intracellular ROS is meticulously regulated through a dynamic interplay between ROS producing and ROS defusing systems. Imbalance between the two provokes a state of oxidative stress. Among the major sources of pathogenic ROS are dysfunctional mitochondria.² Given their role in cellular respiration, they are responsible for the bulk of intracellular superoxide ($O_2^{\cdot-}$) molecules.⁸⁰ This mostly results from electron leakage to O_2 at complex 1 of the electron transport chain under conditions of strong negative inner mitochondrial membrane potential ($\Delta\psi_m$), *i.e.*, mitochondrial hyperpolarization. On the other hand, mitochondrial depolarization has also been correlated with increased ROS production pointing to multiple modes of action.^{66,118-121,242} Furthermore, through redox modifications in proteins of the fission-fusion machinery, ROS co-regulate mitochondrial morphology.¹²⁶ For example, fragmentation is correlated with increased ROS production and apoptosis^{127,128}, while filamentous mitochondria have been linked to nutrient starvation and protection against mitophagy.¹²⁹ Given the intricate relationship between cellular ROS and mitochondrial morphofunction, both should ideally be quantified simultaneously in living cells. To do exactly this, a high-content imaging assay was developed based on automated widefield microscopy and image analysis of adherent cell cultures stained with the fluorescent probes CM-H₂DCFDA (ROS) and TMRM (mitochondrial $\Delta\psi_m$ and morphology). High-content imaging refers to the extraction of spatiotemporally rich (*i.e.*, large number of descriptive features) information about cellular phenotypes using multiple complementary markers and automated image analyses. When combined with automated microscopy many samples can be screened in parallel (*i.e.* high-throughput), thereby increasing the statistical power of the assay. Indeed, a main asset of the protocol is that it allows for simultaneous quantification of multiple parameters in the same cell, and this for a large number of cells and conditions.

After rigorous validation, we applied our workflow to reveal differences in redox status in Normal Human Dermal Fibroblasts (NHDF) upon treatment with the HIV protease inhibitor Saquinavir (SQV) as compared to a mock-treated control, and between different laminopathy patient cells.

2 Results

2.1 High-content microscopy yields a robust and predictable readout of intracellular ROS levels and mitochondrial morphofunction.

Taking into account the considerations for microscopic assessment of redox biology outlined in the introduction, we have established a method for the simultaneous quantification of ROS levels and mitochondrial features in living cells using automated wide-field fluorescence microscopy and automated image analyses and the easily applicable fluorescent indicators 5-(and-6)-chloromethyl-2',7'-dichlorodihydrofluorescein diacetate (CM-H₂DCFDA; Life Technologies, C6827) and tetramethyl rhodamine methyl ester (TMRM, Invitrogen, T-668), for measuring general intracellular ROS levels, and mitochondrial morphology and $\Delta\psi_m$, respectively (Fig 3.1). The method is described in more detail in the methods-section.

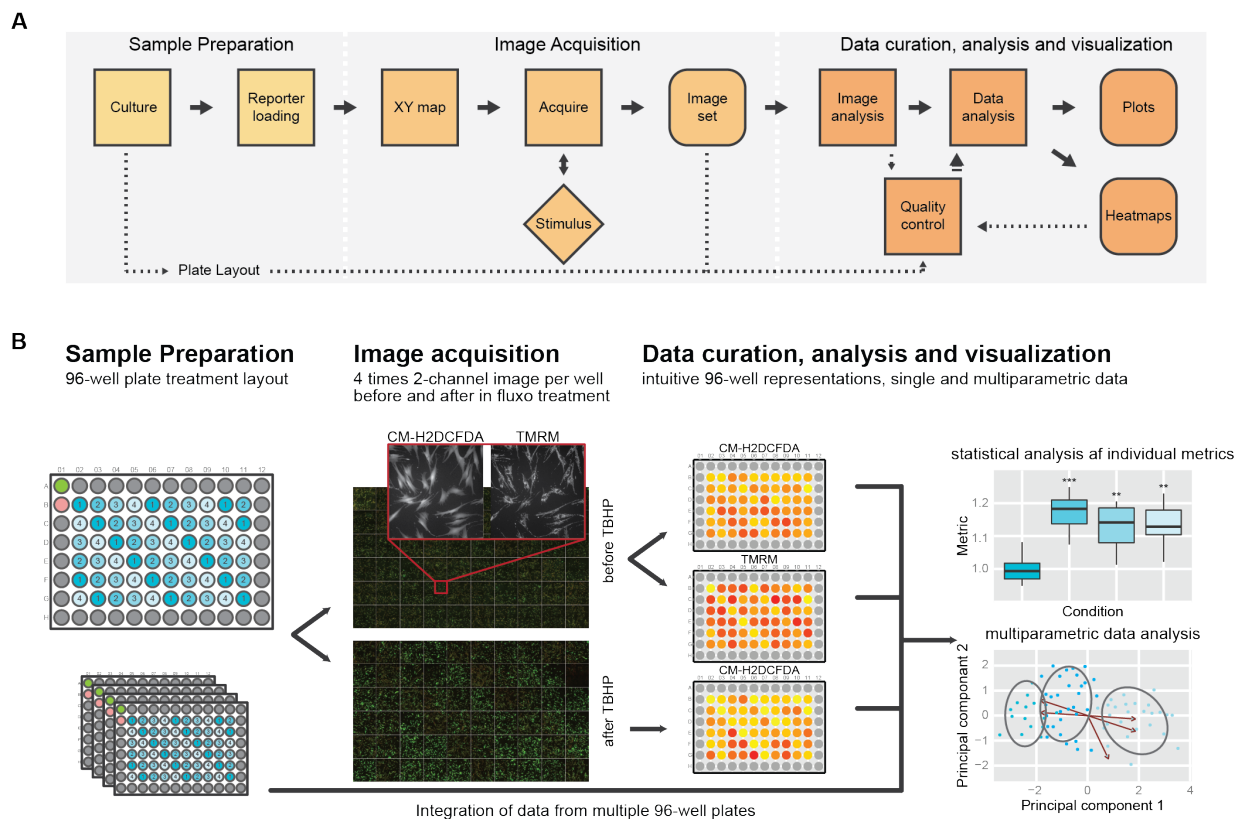


Figure 3.1: General overview of the high-content imaging assay for simultaneous measurement of intracellular basal and induced ROS levels and mitochondrial morphofunction.

(A) Schematic representation of the major operational blocks. (B) Illustrated example: cells are seeded in multiple identical 96-well plates. A standard well plate layout is shown in more detail in **Figure 3.6**. After staining, 4 images are acquired per channel around the center of each well, both *pre* and *post* TBHP treatment, which is illustrated by the large montages with inset. After image analysis, intensity results are visualized using an intuitive heat-map projected onto the well-plate layout. This permits rapid detection of plate effects or aberrant wells. After curation of the complete experimental data sets, final data analysis is performed resulting in single- as well as multi-parameter output.

First, we have validated this workflow with a series of control experiments (**Fig. 3.2**). To verify the correlation between intracellular ROS levels and 2',7'-dichlorodihydrofluorescein (DCF) fluorescence, and to determine its dynamic range, human fibroblasts were treated for 15 minutes with increasing concentrations of TBHP before being measured. Within a dose range of 10-160 μ M TBHP, a linear correlation between ROS level and fluorescent signal was observed (**Fig 3.2A**). The same experimental setup was used for TMRM. Fibroblasts were treated for 30 minutes with increasing concentrations of oligomycin, which induces $\Delta\psi_m$ hyperpolarization²⁴³, before being measured. This approach equally resulted in a linear increase of the measured signal within the 1-10 μ g/ μ l dose range (**Fig 3.2B**). Conversely, when fibroblasts were treated with valinomycin *in fluxo*, a gradual, quantifiable decrease of TMRM fluorescence was measured, corresponding to an expected $\Delta\psi_m$ depolarization²⁴⁴ (**Fig 3.2C**). We also compared the microscopy-based method with spectrophotometry and flow cytometry (**Fig. 3.2D**). Flow cytometry showed a higher dynamic range (as measured after treatment with 20 μ M TBHP), but also a much larger variability in measurements. Spectrophotometry showed a comparable dynamic range and variability.

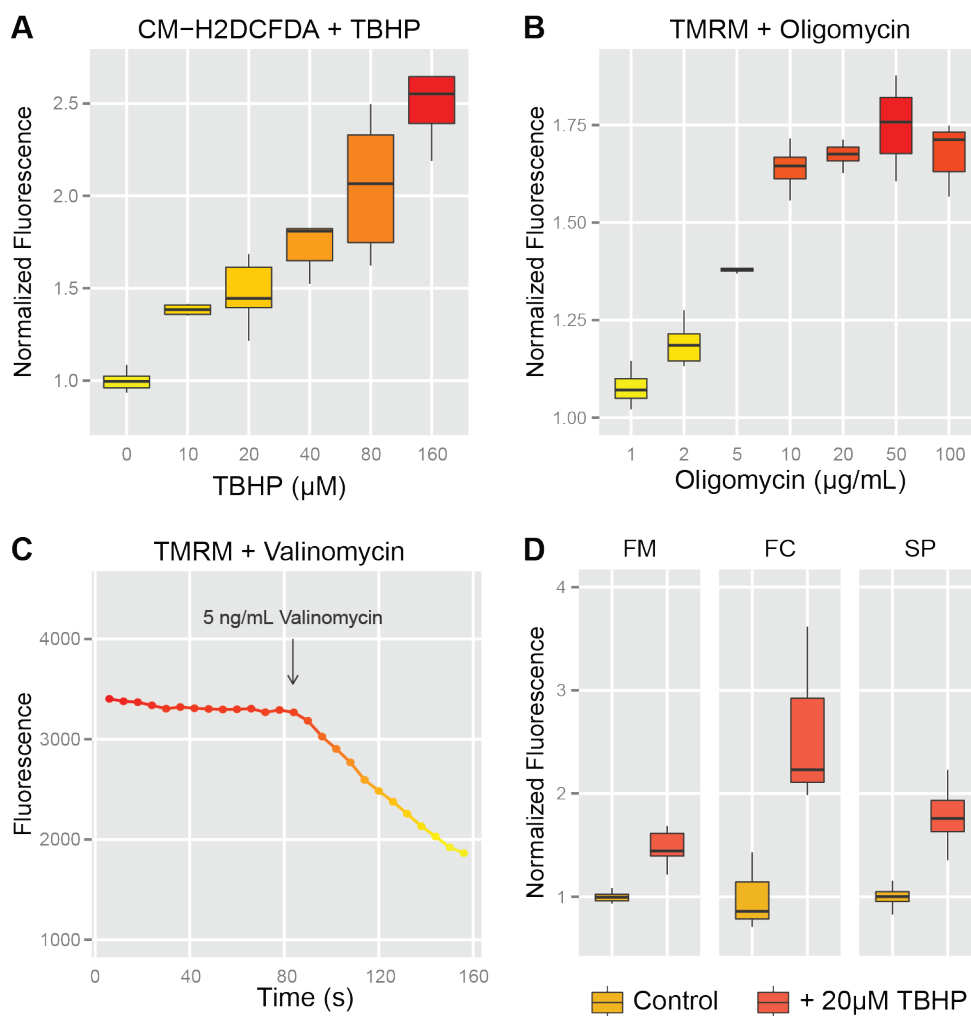


Figure 3.2: Validation of the CM-H₂DCFDA/TMRM-based high content microscopy method.

All experiments were conducted in primary human fibroblasts. **(A)** Normalized levels of intracellular ROS measured as intracellular CM-H₂DCFDA signal after treatment with increasing concentrations of TBHP for 15 min. **(B)** Normalized $\Delta\psi_m$ as measured by mitochondrial TMRM signal after treatment with increasing concentrations of oligomycin for 30 min. **(C)** Live cell imaging of $\Delta\psi_m$ in cells stained with TMRM and treated with 5 ng/mL valinomycin after 85 s. **(D)** Comparison of microscopic, flow cytometric, and spectrophotometric (*plate reader*) measurement of basal intracellular ROS levels using CM-H₂DCFDA in control cells versus cells treated with 20 M TBHP

Finally, we validated the generic character of the methodology by replacing the dye combinations CM-H₂DCFDA/TMRM for Calcein/MitoSOX. Here, Calcein (1 μM) was used to segment cells and to exclude dead cells from the analysis, MitoSOX (5 μM) served to measure mitochondrial O₂^{•-} levels. After staining, primary human fibroblasts were imaged over a time frame of 600 s (at 1/6 fps). Addition of 500 μM TBHP resulted in a clear increase of the MitoSOX signal, when measured per cellular pixel, and even more pronounced when expressed per mitochondrial pixel (**Fig. 3.3**).

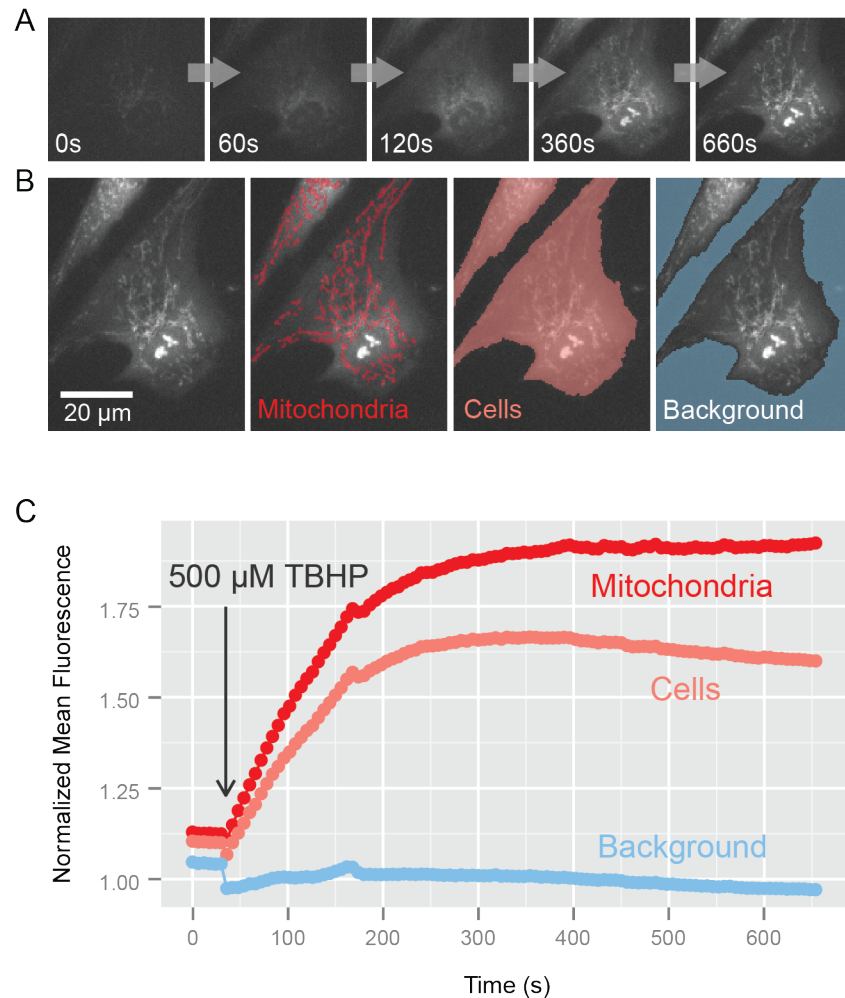


Figure 3.3: Compatibility of the HC assay with MitoSOX measurements.

(A) Response of cells stained with 5 μM MitoSOX towards acute addition of 500 μM TBHP. (B) Masks used to measure fluorescence intensity in different parts of the image. (C) Normalized mean fluorescence in function of time as measured through the different masks shown in (B) (The bump observed after approx. 160 s is due to a floating fluorescent particle (probably a detached cell) passing, out of focus, through the field of view inducing a weak increase in signal in the affected images.)

2.2 Saquinavir triggers changes in ROS levels and mitochondrial morphofunction

After optimization and validation, we have performed a number of experiments to illustrate the performance of the high-content microscopy methodology. As a case study, we have used the established workflow to assess oxidative stress and mitochondrial morphofunction in cells upon treatment with HIV protease inhibitors (HIV PI), which are known to affect redox homeostasis. To this end, primary human fibroblast cells were treated for 72h with 20 μM of the HIV PI Saquinavir. Subsequently, intracellular basal ROS levels, induced ROS levels, mitochondrial morphology and $\Delta\psi_m$ were measured. Basal ROS levels were significantly higher compared to control cells treated with DMSO (Fig. 3.4A). Also the induced ROS

levels were increased, pointing to lowered antioxidant defenses (**Fig. 3.4B**). With respect to the mitochondria, SQV treatment induced a highly fragmented phenotype when compared to control cells, illustrated by a higher circularity and lower average size of the individual mitochondria (**Fig. 3.4D**). $\Delta\psi_m$, measured as average TMRM signal per mitochondrial pixel, was not significantly altered (not shown). Using the dye combination Calcein/MitoSOX, we also quantified mitochondrial $O_2^{\cdot-}$ levels. When applied to fibroblasts, treated for 72h with 10 μ M of SQV, we measured a significant increase in mitochondrial $O_2^{\cdot-}$ levels compared to control cells treated with DMSO (**Fig. 3.4C**).

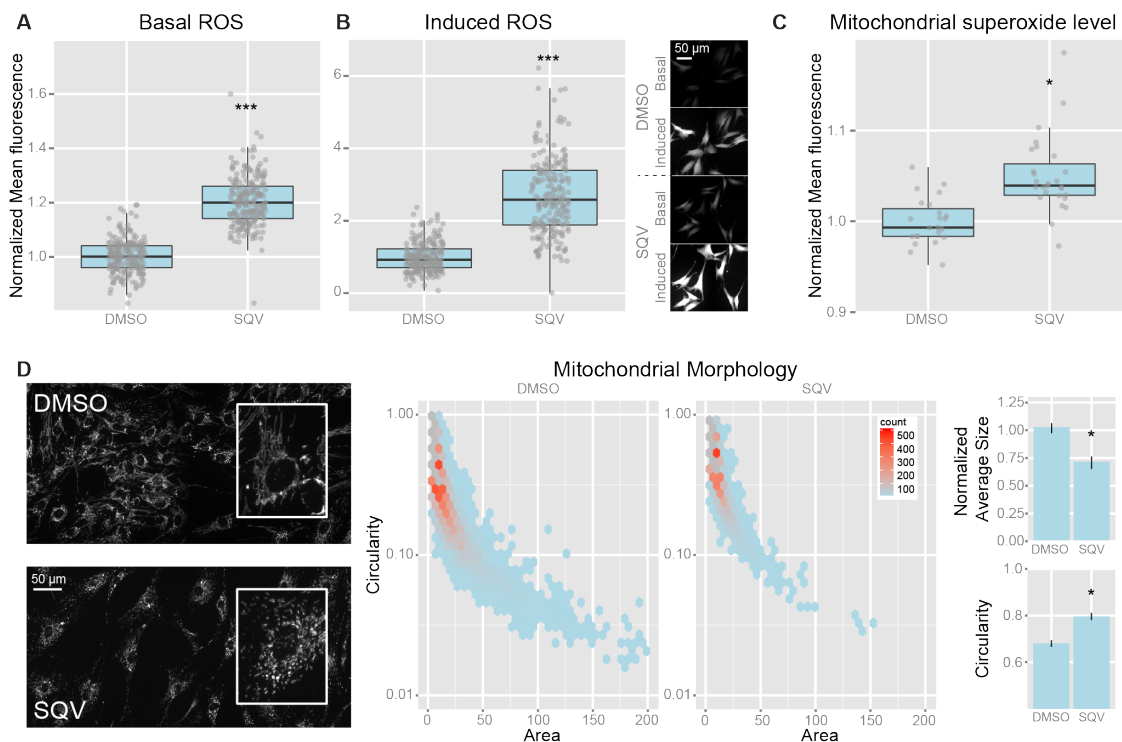


Figure 3.4: Saquinavir alters intracellular redox homeostasis.

(A) Normalized basal levels of intracellular ROS as measured by CM-H₂DCFDA and (B) response towards induced ROS, measured as relative gain in intensity after 20 μ M TBHP addition at different time points after treatment with 20 μ M of SQV. (C) Normalized $O_2^{\cdot-}$ level as measured by average MitoSOX signal per mitochondrial pixel after treatment with 10 μ M SQV. (D) SQV treatment (20 μ M) causes mitochondrial fragmentation as illustrated by (e) a scatterplot of mitochondrial circularity and mitochondrial area (* = p value < 0.05; ** = p value < 0.01; *** = p value < 0.001; the range of the Y-axes has been adjusted to optimally display the differences)

2.3 Multiparametric redox readout enables unambiguous classification of chemically perturbed cells as well as laminopathy patient cells.

Multiparametric analysis of ROS and mitochondria yielded a feature set describing intracellular redox biology. When performing a principal component analysis (PCA) using a subset of only 5 parameters, namely basal and induced ROS levels,

average mitochondrial size, average mitochondrial circularity and $\Delta\psi_m$, we could unambiguously separate the two conditions (control and SQV-treated) independently in three biological replicates with just the first two principal components (which explain 81.4% of the total variance in the data) (**Fig. 3.5A**). This demonstrates the robustness of our workflow and suggests that the combined readout may serve as a sensitive predictor of cellular health condition.

We then ran a similar analysis on cells from two laminopathy patients and a healthy donor. Specifically, we compared fibroblasts from a healthy person, with those from a patient suffering from Hutchinson-Gilford Progeria ($G608G/+$)²³³ and those from a patient with a lethal laminopathy phenotype due to a nonsense $Y259X$ homozygous mutation in the LMNA gene ($Y259X/Y259X$).²⁴⁵ Again, using the same 5 variables and 2 PCs, all three cell types could be readily separated (**Fig. 3.5B**).

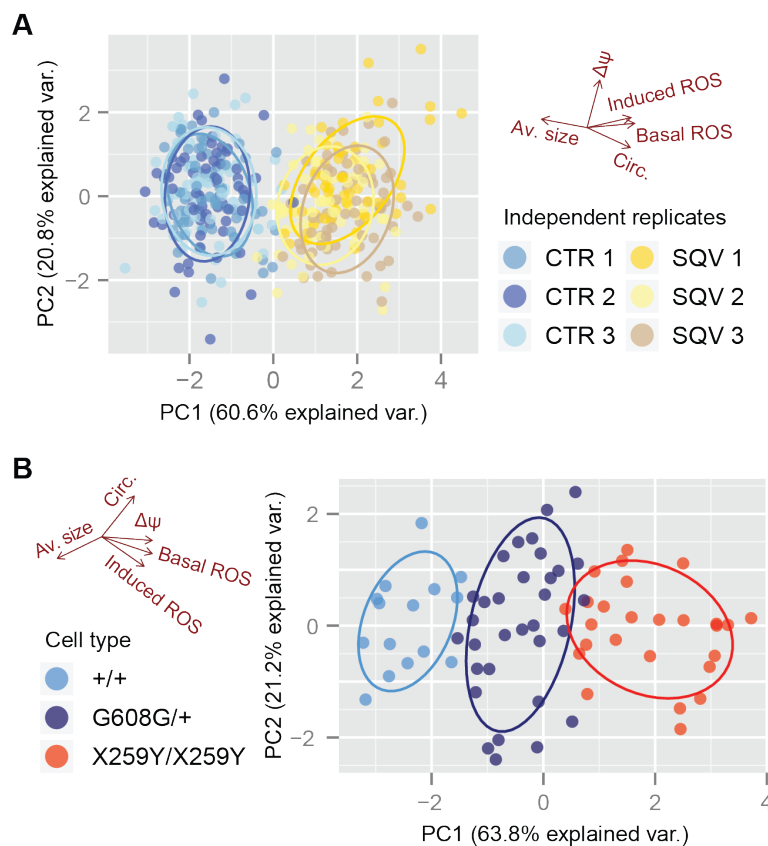


Figure 3.5: Principal component analysis distinguishes chemically perturbed cells and patient cells from healthy controls.

(A) 2D scatterplot of the first 2 principal components (PCs) from a PCA analysis on 5 variables (basal and induced ROS levels, average mitochondrial size, circularity, and $\Delta\psi_m$) from the SQV dataset described in fig. 7. Independent replicates are plotted with a different color. The *brown arrows* represent the directions of the original 5 variables with respect to the principal components. **(B)** 2D scatterplot of the first 2 principal components (PCs) from a PCA analysis on the same 5 variables measured in 2 different laminopathy patient cell lines (*i.e.* LMNA^{G608G/+} and LMNA^{Y259X/Y259X}) and healthy primary human fibroblasts.

3 Discussion

In this work, we have described and benchmarked a workflow for simultaneous quantification of intracellular ROS levels and mitochondrial morphofunction on a cellular level using high-content microscopy. We also compared the microscopy-based method with spectrophotometry and flow cytometry (FC). FC showed a higher dynamic range, and it is definitely faster, a 384-well plate can be screened in as little as 12 minutes with high sensitivity for multiple markers.²⁴⁶ But it also showed a much larger variability in measurements. In addition, FC does not allow for spatiotemporal analysis (*i.e.* subcellular localization, morphological data and/or time dependent kinetics), nor does it allow revisiting the same cells during or after a treatment (*i.e.*, *in fluxo*). Furthermore, cells need to be in suspension, which makes flow cytometry less suited to studying the physiology of adherent cells

Spectrophotometry showed a comparable dynamic range and variability as microscopy. It also is significantly cheaper (a basic setup is available for as low as €4000), and has a shallower learning curve. However, this method, just like flow cytometry, cannot discern morphological details nor is it capable of detecting confounding factors such as abnormal cell density or autofluorescent contaminants in individual wells. Traditional disadvantages of high-content microscopy as compared to the other methods are the need for large image data storage, intensive processing power and complex image analyses. However, the presented assay standardizes the image acquisition process and streamlines the analysis so as to minimize this processing time, increase ease of use and therefore make the assay more accessible.

Once established, the performance of the method was demonstrated with a case study on HIV PI-treated NHDF cells. HIV protease inhibitors (HIV PI) have been shown to induce increased basal ROS levels^{247,248}, and lowered antioxidant defences (represented by lowered expression of SOD2²⁴⁹). Independently, other reports have linked HIV PI to changed mitochondrial morphofunction.²⁴⁹⁻²⁵³ We were able to reproduce and confirm these observations, using the described assay. The important difference is that with this assay, these parameters are measured simultaneously, in the same living cells, together with the extraction of additional morphological data. The major advantage of this approach is its unambiguous determination of both factors together in space and time, which facilitates pinpointing causal relationships.

A PCA on only 5 variables of the acquired dataset allowed the generation of sensitive redox profiles, capable of clearly separating treated from control cells. However, more advanced data mining techniques and (supervised) clustering algorithms can also be used on the extracted data to enable predictive redox profiling. This may be a valuable feature for diagnostic or prognostic classification tools in digital pathology, as well as in screening for therapeutic targets, *e.g.* once robust classification models are created, small molecule libraries can be screened to find therapeutic candidates to counteract oxidative stress, analogous to a recent screen for promising leads in therapy development for human mitochondrial

disorders.²⁵⁴ Nonetheless, the current setup was used on fibroblasts from two laminopathy patients, which could also be easily discriminated from wild type NHDF cells, and from each other, based on the PCA analysis.

The assay was conceived for NHDF cells, which, due to their extremely flat morphology and relatively large size, are well suited for analysis by widefield (non-confocal) fluorescence microscopy.^{174,255} Nevertheless, the method should be applicable to a wide variety of adherent cell types. This requires optimization of the staining protocol. Reporter dye concentrations have to be optimized for each cell type separately, but should always be kept to a minimum as overloading may affect cellular health status and cause non-linear effects due to quenching.²⁵⁶

The assay was optimized for 96-well plates, but it is obviously amenable to further upscaling, e.g. to 384-well plates. The major limiting factor is the plate acquisition time, *i.e.*, the time it takes to acquire images of all the wells. The fluorescent signals have to remain stable during this timeframe so as to be able to confidently compare measurements between individual wells. But, because the staining is transient and the process under investigation is dynamic, this poses a challenge. Therefore, the fluorescent signals were measured in a set of replicated optimization experiments and this showed that both CM-H₂DCFDA and TMRM signals remain stable from 7 to at least 50 minutes after staining (coefficient of variation < 2%). This gives a window of approximately 40 minutes. A 96-well plate typically takes around 10 minutes. Thus, an extrapolation to 384-well plates would keep the acquisition duration within the stable time slot. With an average of 50 cells per image (based on the use of a 20x objective and NHDF cells), this would result in data for approximately 30 000 cells per hour of screening, greatly adding to the statistical power of the assay. Another factor influencing fluorescent signal stability is the temperature. To avoid vacuolization of CM-H₂DCFDA (*i.e.* dye accumulation in intracellular vesicles), which would give rise to heterogeneous staining and non-linear effects, the incubation takes place at room temperature instead of 37 °C. Apart from stability, it is important to note that the exposure of living cells to fluorescence excitation light itself induces ROS production. This implies that the exposure conditions (exposure time and excitation light intensity) should be kept at an absolute minimum. It also means that all wells should only be exposed when the actual images are acquired, which rules out the use of software-enabled autofocus methods and warrants the use of a hardware-based autofocus system.

An advantage of the described method is its generic character. Virtually any combination of spectrally compatible fluorescent reporters can be used. This was demonstrated by using the Calcein/MitoSOX combination to specifically measure mitochondrial ROS. Furthermore, the applications are not limited to the integrated ROS/mitochondrial measurement. The assay can also be extended with a *post hoc* immunostaining (after the second imaging round). Since the exact imaging locations are saved, redox analyses can be directly correlated with location proteomics in the same cells, greatly increasing the molecular readout of the experiment.

In conclusion, and specific to the use of CM-H₂DCFDA and TMRM, the described redox profiling method is robust, sensitive and reliable. Due to its multiparametric

and quantitative nature, it is superior to other fluorescence-based methods. This way, it can help to elucidate the relationship between mitochondrial function and intracellular ROS signaling, which is crucial for better understanding a wide variety of pathologies in which redox homeostasis is perturbed, such as laminopathies.¹ Furthermore, owing to its generic character, the assay allows applications well beyond its original scope.

4 Methods

4.1 Cell Culture

Normal human dermal fibroblasts (NHDF, *LMNA*^{+/+}, Promocell, C-12300), fibroblasts from a patient suffering from HGPS (*LMNA*^{G608G/+})²³³, and fibroblasts from a patient with a lethal laminopathy phenotype due to a nonsense Y259X homozygous mutation in the *LMNA* gene (*LMNA*^{Y259X/Y259X})²⁴⁵ were cultured in DMEM high glucose with L-glutamine medium (Lonza, BE12–604F) supplemented with 10% fetal bovine serum (Gibco, 10500–064) and 1% penicillin/streptomycin (Lonza, DE17-602E/12), at 37°C and 5% CO₂, according to standard procedures. All experiments were performed with cells in between passage 9 and 19. In case of direct comparison, passage-matched cells were used.

4.2 Chemical treatments

Saquinavir (SQV; Sigma-Aldrich - S8451) was originally developed as a HIV-protease inhibitor but also targets the *ZMPSTE24* gene²³⁴, thus inducing synthesis of prelamin A as a side-effect. Treatments were with 10 μM or 20 μM, and started one day after cell seeding, when the culture density was around 50%. Compound-containing medium was replenished every day until measurement at 72h after treatment initiation.

Oligomycin A (Sigma-Aldrich - 75351), Valinomycin (Sigma-Aldrich - V3639) and TBHP (Sigma-Aldrich - 458139) were used for benchmarking and as controls. Oligomycin A triggers mitochondrial hyperpolarization while valinomycin results in depolarization.^{243,244} TBHP was used to increase ROS levels.

4.3 High-content microscopy workflow

An overview of the workflow is given in **Figure 3.1**. A tutorial movie and detailed protocol showing the exact steps of the assay were published separately and can be consulted at www.jove.com/video/55449/cellular-redox-profiling-using-high-content-microscopy.

To make the assay amenable to medium- to high-throughput screens, we have optimized a workflow for 96-well plates. To minimize artefacts, cells are seeded at least 24 hours in advance and they are allowed to grow and equilibrate in conditioned medium. When using different conditions (e.g. controls and perturbations), seeding locations are homogeneously distributed so as to minimize plate effects. The outer wells are filled with medium, but are not imaged, as they are highly prone to edge effects. The only exception is well B01, in which cells are

seeded to use for focus adjustment prior to the automated image acquisition. An illustration of a typical experimental layout is depicted in **Figure 3.6**. To avoid scattering and crosstalk (of excitation and emission) between adjacent wells, we make use of black polystyrene plates with a thin continuous glass bottom (Brooks Matrical Labware).

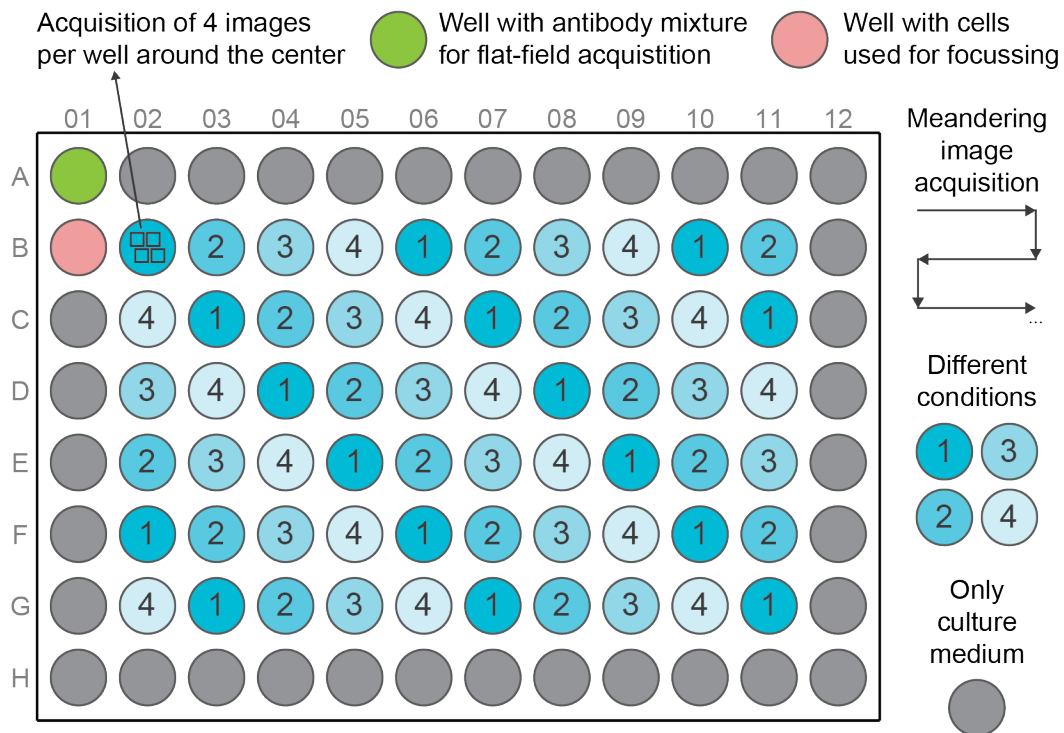


Figure 3.6: A typical experimental 96-well layout

A) 4 different conditions are distributed homogeneously across the inner 60 wells of the plate. Well B01 also contains cells, but is only used to adjust the initial PFS offset just before imaging. The other outer wells are filled only with culture medium to minimize gradients (temperature, humidity...) during cell culture. Image acquisition is performed in a meandering manner, *i.e.*, first from left to right, from well B02 to B11, then back, from right to left, from well C11 to C02 and so on. After image acquisition a flat field image is acquired in well A01, which is used for correcting spatial illumination heterogeneity during image analysis.

4.3.1 Sample preparation and image acquisition

24 h before measurement, cells are transferred to the 96-well plates at a concentration that results in a confluence degree of approx. 70% at the time of measurement, for NHDF, this is 8000-10000 cells per well. As illustrated in **Fig. 3.6**, cells are only seeded in the inner 60-wells of the plate to avoid edge effects, except for well B01, where cells are seeded to be used for focussing before image acquisition. Right before measurement cells are washed in HBSS + 25 μ M Hepes (HH) (pH 7.2), incubated for 25 minutes in the dark at room temperature in HH-buffer containing 2 μ M CM-H₂DCFDA and 20nM TMRM, washed again in HH-buffer and then imaged (also in HH-buffer) on an automated Nikon Ti Eclipse inverted

widefield fluorescence microscope with a 20x air Plan Apo objective (NA 0.75) using a 480/40 nm excitation, 520/35 nm emission filter combination for the CM-H₂DCFDA signal and a 540/25 nm excitation, 605/55 nm emission filter combination for the TMRM signal. Well B01 is used for determination of the optimal focus plane and initialization of an infrared-led based autofocus (Perfect Focus System, Nikon). As this procedure induces an increase in DCF signal intensity²¹², this well (B01) is excluded from further analysis. Next, an acquisition protocol is initialized, using hardware based autofocus that captures a set of 4 fields per channel in the center of each well. With our setup, the plate acquisition time of this protocol is approximately 10 minutes. This has proven to be sufficiently short so as to not cause any significant differences between the first and last wells due to the transient nature of the staining or the dynamics of the processes under investigation.

After the acquisition protocol is completed, a stimulus/perturbation can be given, using an on- or off-stage automated micropipette or multichannel pipette. We make use of the oxidant *tert*-butyl peroxide (TBHP: Sigma-Aldrich, 458139-100mL), as an internal positive control for the CM-H₂DCFDA staining, and as a means to measure induced ROS levels. At a fixed time span after TBHP addition (minimum 3 minutes to allow equilibration), the acquisition protocol is repeated. A maximum of 10 different treatments is used per plate. This way, each plate contains 6 technical replicates with 4 images per replicate. In addition, a minimum of 3 identical plates is measured, increasing the number of images per treatment to a minimum of 72. This guarantees sufficient statistical power to detect even small differences. Finally, a mixture antibodies tagged with fluorescent probes corresponding to CM-H₂DCFDA and TMRM (e.g. Alexa-488 and CY3) are loaded in well A01 and are used to acquire flat field images, required during image processing.

4.3.2 Image processing

After acquisition, raw image data sets are directly backed up to a server, with remote access. A virtual desktop application or command shell interface can be used to organize and analyze image data sets. All image processing is performed in FIJI (<http://fiji.sc>), a packaged version of ImageJ freeware (W.S. Rasband et al., National Institutes of Health, Bethesda, Maryland, USA, <http://rsb.info.nih.gov/ij/>, 1997–2015), which runs directly on the server. We have conceived a dedicated script for automated analysis of intracellular and mitochondrial signals and morphological characteristics (RedoxMetrics.ijm), which is available upon request. The image analysis pipeline can be divided into 4 major blocks, which can be adapted to the specific image quality and cell type, namely 1) preprocessing, 2) object enhancement, 3) segmentation, and 4) analysis (**Fig 3.7**).

1) Preprocessing is generic to all channels and involves a flatfield correction (FF) to correct for spatiotemporal illumination heterogeneity, which arises from imperfections of the acquisition system. The flat field image is acquired in a separate well with no cells (usually well A01), but with dyes.

2) After preprocessing, the objects of interest will be selectively enhanced. Depending on the object, cells (CMDCFDA stains the entire cell) or mitochondria,

different enhancement procedures are followed. For cell segmentation, a combination of local background subtraction (rolling ball, RB), noise reduction (in the form of a Gaussian blur operation, GB), and local contrast enhancement (CE)²⁵⁷ is used. The kernel sizes for these operators are tunable parameters, which are automatically set to optimized values based on the image calibration (pixel size), retrieved from the metadata. In case of mitochondria, a normalized Laplace of Gaussian operator (LG) is applied, for which the optimal scale is automatically selected based on the most salient features in scale space.²⁷ 3) Automatic segmentation demands implementation of a robust thresholding method. A variety of auto-threshold methods have been conceived^{258,259}, and we have found Huang's algorithm²⁶⁰, which minimizes image fuzziness (the difference between the original image and its binary version), to work particularly well for both object types. However, an inherent caveat of auto-threshold methods is that they adjust the cut-off values based on the intensity distribution within the image. This introduces an unwanted bias when aiming at comparative quantifications, which is why we calculate threshold values using intensity information from the entire image data set. Alternatively, the threshold value can be set manually. Before proceeding to image analysis, a binary size filter (SF) is applied so as to exclude objects that fall out of the realistic size range. 4) Once generated, regions of Interest (ROIs) are used for extracting intensity, texture and morphological (size and shape) parameters on the flatfield corrected images. Both ROI sets are used to analyze signals in both channels, enabling spatial discrimination of intensity fluctuations.

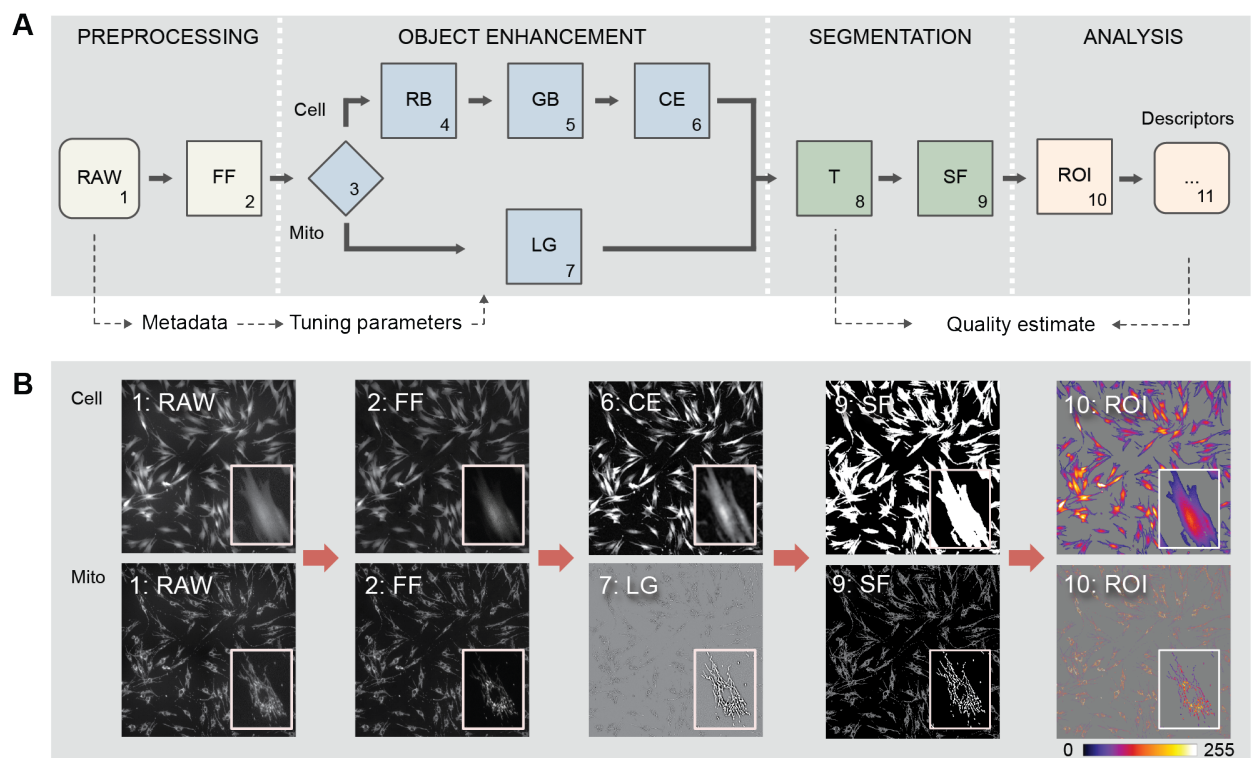


Figure 3.7: Overview of the image analysis workflow.

(A) Schematic representation of the entire image analysis process. Abbreviations: *FF* flatfield correction, *RB* rolling ball background subtraction, *GB* Gaussian blur, *CE* local contrast enhancement, *LG* Laplace of Gaussian, *T* thresholding, *SF* size filter, *ROI* region of interest. (B) Illustrated example. The *top row* represents the analysis of DCF images, the *bottom row* the analysis of TMRM images.

4.3.3 Data analysis and visualization

Data analysis and visualization is done with R statistical freeware (<http://www.r-project.org>) and RStudio (<http://www.rstudio.com>). To quickly obtain and visualize the results, an intuitive Shiny application²⁶¹ (available upon request) has been conceived that integrates and visualizes the data in heatmaps and boxplots, and also performs statistical analyses. In general, the workflow comprises of two consecutive steps. First, data is processed and inspected per 96-well plate. To this end color-coded multi-well plate plots as well as boxplots with outliers labeled with well name and image number are used. The latter allows facile inspection and identification of aberrant data points (extremely high or low values compared to the average values measured for that specific treatment – see **Figure 3.8** for an example). Secondly, curated data from all plates of a given experiment are combined and analyzed using non-parametric multivariate tests²⁶² and a PCA. Significance levels were indicated as follows: $p < 0.05$ (*), $p < 0.01$ (**), and $p < 0.001$ (***). For graphics and annotation, the R program was expanded with the ggplot2 package²⁴⁰ and ggbiplot, a visualization function for PCA, implemented by Vincent Q. Vu and available on github (<https://github.com/vqv/ggbiplot>).

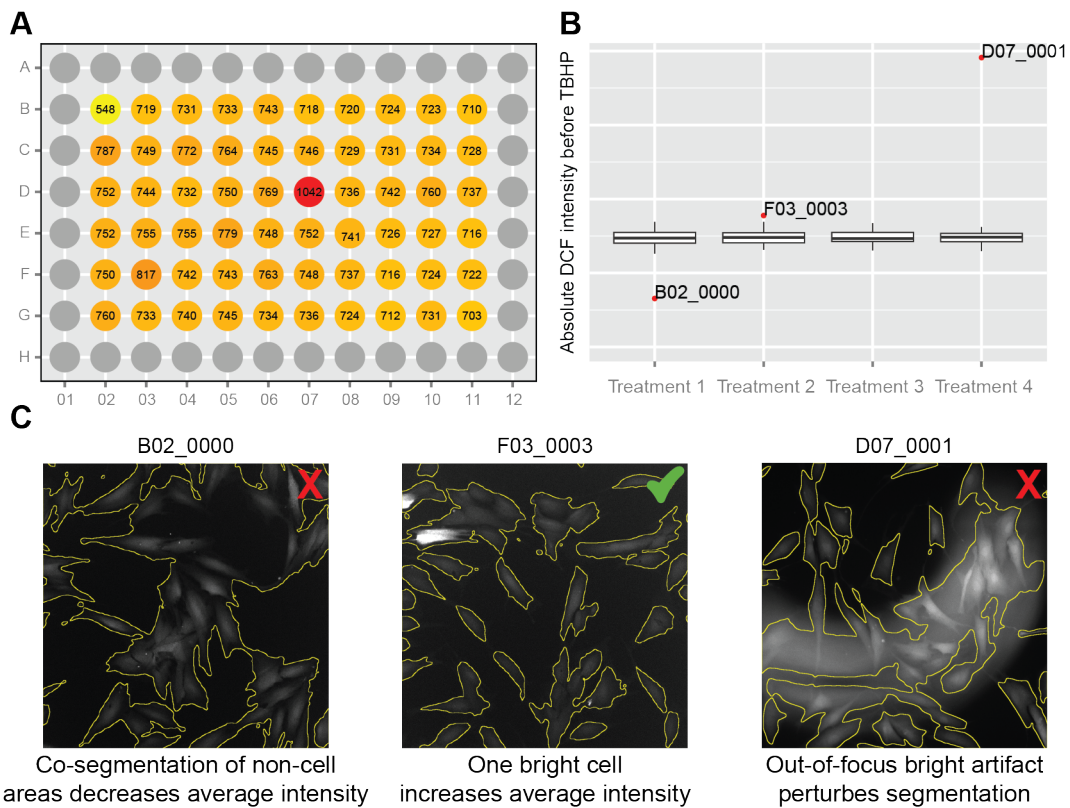


Figure 3.8: Illustrated example of intermediate data visualizations.

(A) Multiwell plate visualization where wells B02 and D07 appear suspicious. **(B)** Boxplot representing the same data, with the outliers labeled with well name and image name. Together with F03_0003, images from B02 and D07 reappear as outliers. **(C)** Visual inspection of these images shows that B02_0000 and D07_0001 should be removed from further analysis because there are segmentation errors (illustrated by the red 'X'). F03_0003 should be kept because there is no apparent segmentation or technical error. (if no technical reason is found for the aberration, the data should not be removed).

IV

SUSTAINED ACCUMULATION OF PRELAMIN A AND DEPLETION OF LAMIN A/C BOTH CAUSE OXIDATIVE STRESS AND MITOCHONDRIAL DYSFUNCTION BUT INDUCE DIFFERENT CELL FATES

Redrafted from Sieprath et al. 2015

Sieprath, T. *et al.* Sustained accumulation of prelamin A and depletion of lamin A/C both cause oxidative stress and mitochondrial dysfunction but induce different cell fates. *Nucleus* **6**, 236–246 (2015).

Abstract

The cell nucleus is structurally and functionally organized by lamins, intermediate filament proteins that form the nuclear lamina. Point mutations in genes that encode a specific subset of lamins, the A-type lamins, cause a spectrum of diseases termed laminopathies. Recent evidence points to a role for A-type lamins in intracellular redox homeostasis. To determine whether lamin A/C depletion and prelamin A accumulation differentially induce oxidative stress, we have performed a quantitative microscopy-based analysis of reactive oxygen species (ROS) levels and mitochondrial membrane potential ($\Delta\psi_m$) in human fibroblasts subjected to sustained siRNA-mediated knockdown of LMNA and ZMPSTE24, respectively. We measured a highly significant increase in basal ROS levels and an even more prominent rise of induced ROS levels in lamin A/C depleted cells, eventually resulting in $\Delta\psi_m$ hyperpolarization and apoptosis. Depletion of ZMPSTE24 on the other hand, triggered a senescence pathway that was associated with moderately increased ROS levels and a transient $\Delta\psi_m$ depolarization. Both knockdowns were accompanied by an upregulation of several ROS detoxifying enzymes. Taken together, our data suggest that both persistent prelamin A accumulation and lamin A/C depletion elevate ROS levels, but to a different extent and with different effects on cell fate. This may contribute to the variety of disease phenotypes witnessed in laminopathies.

1 Introduction

The nuclear lamina provides structural support to the nucleus and plays a central role in nuclear organization and gene regulation.³ Point mutations in the *LMNA* gene, which encodes its major constituent proteins, lamin A and C, cause a broad range of diseases termed laminopathies.³ During maturation, lamin A is extensively processed, with consecutive steps of farnesylation, proteolytic cleavage of the C-terminal three amino acids, carboxymethylation and removal of the C-terminal 15 amino acids, including the farnesyl group.¹⁵⁰ The final step is exclusively catalyzed by the zinc-metalloproteinase ZMPSTE24. Accumulation of different prelamin A (PLA) intermediates is correlated with disease but especially the farnesylated variants are presumed to be cytotoxic.⁵⁹ The Hutchinson-Gilford progeria syndrome (HGPS) for example is caused by an accumulation of the mutant farnesylated PLA intermediate progerin.⁵⁸ Likewise, in restrictive dermopathy (RD), loss of functional ZMPSTE24 results in the accumulation of farnesylated PLA.^{50,134} The underlying disease causing mechanisms are still largely unknown but it is becoming increasingly more clear that next to its structural function and role in nuclear dynamics²²², the nuclear lamina also modulates intracellular redox homeostasis.¹ Various studies have revealed that reactive oxygen species (ROS) levels are increased in laminopathy patient cells and during PLA accumulation.^{60,157,263,264} For example, fibroblasts from various lipodystrophy patients as well as cells treated with HIV protease inhibitors demonstrate increased ROS levels⁶⁰, and

display a distinct redox-profile based on ROS and mitochondrial parameters (**Fig. 3.4B**). Indeed, proteomic and metabolic profiling suggest that the increase of ROS may be attributed to dysfunctional mitochondria.^{166,265} To corroborate these findings we applied a microscopy-based strategy for combined measurement of ROS and mitochondrial membrane potential ($\Delta\psi_m$) in cellular models of PLA accumulation or lamin A deficiency. Using this approach, we found that both accumulation of PLA and reduction of mature lamin A increased intracellular ROS levels, albeit not at the same rate nor to the same extent, and also caused changes in mitochondrial potential ($\Delta\psi_m$). These effects were accompanied by reduced mitochondrial respiration and altered gene expression of ROS detoxifying enzymes.

2 Results

2.1 Sustained knockdown of *ZMPSTE24* and *LMNA* reduce cell proliferation via different mechanisms

Accumulation of PLA or reduction of mature LAMIN A was achieved in human fibroblasts by respectively silencing the expression of *ZMPSTE24* or *LMNA* with specific siRNAs. A pool of non-targeting (NT) siRNAs was used as control. To maintain the knockdowns for prolonged periods of time, repetitive rounds of siRNA transfection were performed, separated by 72 h to 96 h (**cfr. Chapter 2 for more details**).

Both knockdowns had an adverse impact on cell proliferation, resulting in significantly increased population doubling times (decreased population doubling level, PDL) with respect to the NT control (**Fig. 4.1A**). The effect of LMNAkd was markedly stronger than that of ZMPSTE24kd. Quantification of β -galactosidase positive cells and p21-positive cells – two markers for senescence²⁶⁶ – revealed that only ZMPSTE24kd triggered cellular senescence (**Fig. 4.1B & C & E**). LMNAkd predominantly triggered cell death, as evidenced by a marked increase in the number of fragmented and condensed nuclei (**Fig. 4.1D & E**).

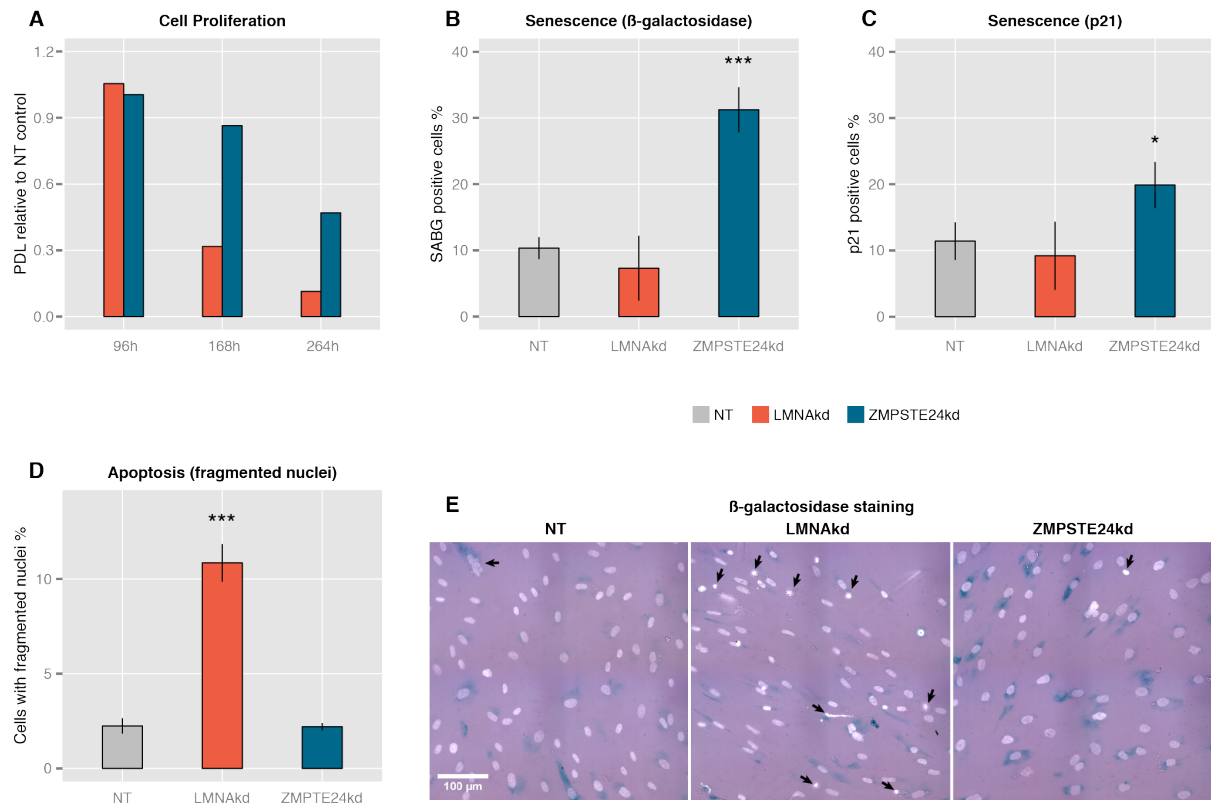


Figure 4.1: Sustained siRNA-mediated knockdown of LMNA and ZMPSTE24 affects cell proliferation.

(A) The relative population doubling speed compared to the NT-control expressed as population doubling level (PDL) at different time points. (B) Quantification of the number of β -galactosidase positive cells at 168 h, relative to the total number of cells. (C) Quantification of the number of p21 positive cells at 168 h, relative to the total number of cells. (D) Quantification of apoptosis, expressed by the number of condensed nuclei relative to the total number of cells. (E) Representative images of β -galactosidase stained NT control, LMNAkd and ZMPSTE24kd cells (senescent cells in blue), merged with DAPI channel (grey/white). Arrows indicate nuclear aberrations. (* = p-value < 0,05; ** = p-value < 0,01; *** = p-value < 0,001).

2.2 LMNAkd significantly raises basal and induced ROS levels; ZMPSTE24kd only causes a modest increase of the basal ROS level

We established and validated a high-content workflow to simultaneously measure intracellular ROS levels and $\Delta\psi_m$, using the fluorescent reporter molecules CM-H₂DCFDA and TMRM, respectively (see M&M and chapter 3 for details). Using this method, we quantified ROS levels in human fibroblasts subjected to sustained knockdown of *ZMPSTE24* or *LMNA* under basal conditions and after acute application of 20 μ M of the oxidant tert-butyl hydrogen peroxide (TBHP). The latter served as proxy for induced ROS and was expressed as the relative increase with respect to the basal ROS levels.

LMNAkd caused a time-dependent increase in both basal and induced ROS levels. Whereas the increase in basal ROS levels only became significant after 168 h, the induced ROS levels were already significantly higher at 96 h. ZMPSTE24kd on the other hand, only resulted in a modest, but significant increase in basal ROS levels

after 264 h. Within the experimental time frame, this treatment did not cause a significant increase of induced ROS (Fig. 4.2A & B).

Next to the knockdowns, passage-matched fibroblasts from specific laminopathy patients ($LMNA^{Y259X/Y259X}$, $LMNA^{C608G/+}$, $LMNA^{+/+}$) were subjected to the same analysis. $LMNA^{Y259X/Y259X}$ cells are incapable of producing mature lamin A/C²⁴⁵ and $LMNA^{C608G/+}$ cells accumulate a truncated, farnesylated prelamins A variant termed progerin.²³³ In line with the results from the sustained knockdown, $LMNA^{Y259X/Y259X}$ demonstrated an increase in both basal and induced ROS, while $LMNA^{C608G/+}$ cells only showed an increase in basal ROS (Fig. 4.2C & D).

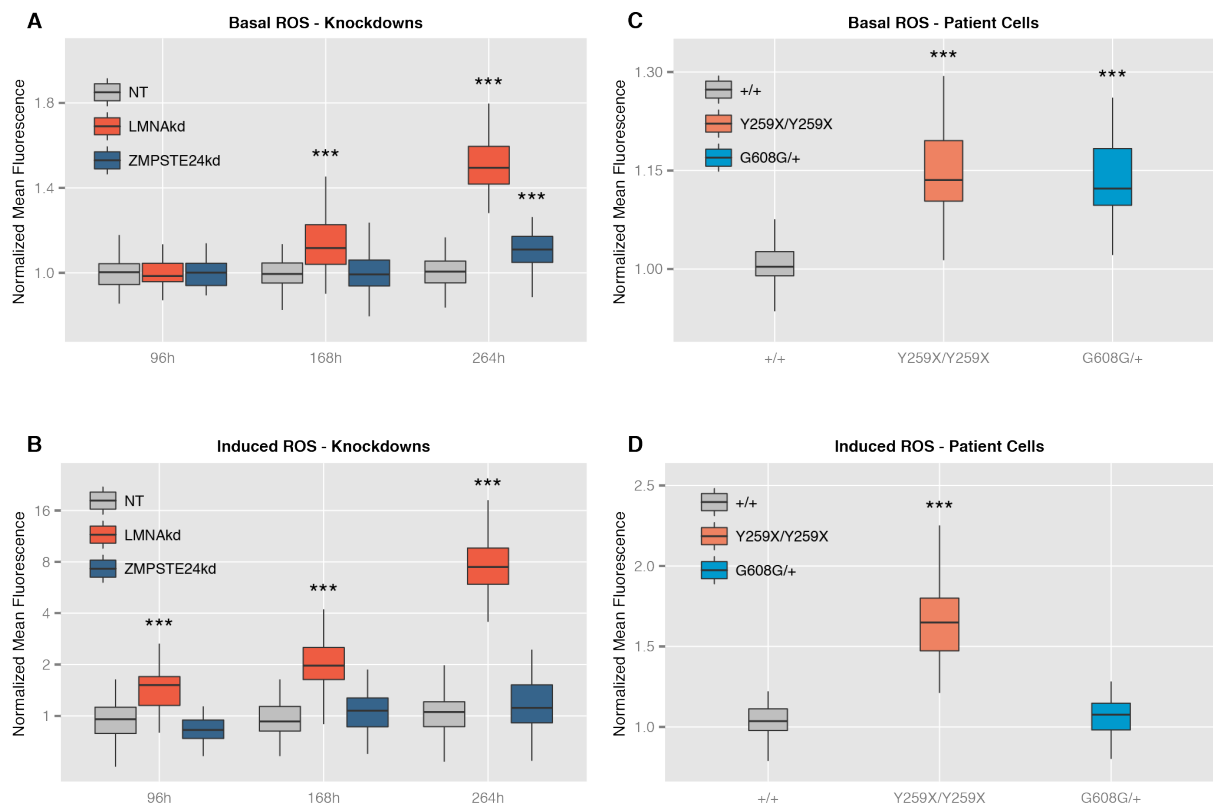


Figure 4.2: Both LMNAkd and ZMPSTE24kd cells have increased basal ROS levels. LMNAkd cells are more susceptible toward induced ROS.

(A & B) Normalized basal levels of intracellular ROS measured by CM-H₂DCFDA high content microscopy analysis and response toward induced ROS, measured as relative gain in intensity after 20 mM TBHP addition at different time points in LMNAkd and ZMPSTE24kd cells. (C & D) Normalized basal levels of intracellular ROS and response toward induced ROS in $LMNA^{Y259X/Y259X}$ and $LMNA^{G608G/+}$ cells. (* = p-value < 0,05; ** = p-value < 0,01; *** = p-value < 0,001; the range of the Y-axes has been adjusted to optimally display the differences).

2.3 ZMPSTE24kd and LMNAkd affect $\Delta\psi_m$ in a time-dependent manner

As dysfunctional mitochondria can generate increased amounts of ROS, we estimated $\Delta\psi_m$ by quantifying the mitochondrial accumulation of the reporter dye TMRM using the high content microscopy method mentioned before. Dynamic and

time-dependent changes were observed for the different treatments. LMNAkd induced $\Delta\psi_m$ depolarization at 96 h and 168 h and $\Delta\psi_m$ hyperpolarization at 264 h. On the other hand, ZMPSTE24kd resulted in a transient $\Delta\psi_m$ depolarization at 168 h (Fig. 4.3A). In the case of patient cells, LMNA^{Y259X/Y259X} fibroblasts displayed slight $\Delta\psi_m$ hyperpolarization that was not significantly different from LMNA^{+/+} control cells. In contrast, LMNA^{G608G/+} fibroblasts displayed significant $\Delta\psi_m$ depolarization (Fig. 4.3B).

2.4 ZMPSTE24kd and LMNAkd decrease basal oxygen consumption rates

Since the TMRM measurements suggested a (transient) defect in mitochondrial function, we next investigated mitochondrial oxygen consumption (Fig. 4.3C-F). At the 168 h time point, we found strong deviations between the respiration curves (Fig. 4.3C & D). Especially, the basal oxygen consumption rate (OCR) was significantly lower in both ZMPSTE24kd and LMNAkd cells (Fig. 4.3E). This was also the case for LMNA^{Y259X/Y259X} and LMNA^{G608G/+} patient fibroblasts (Fig. 4.3F).

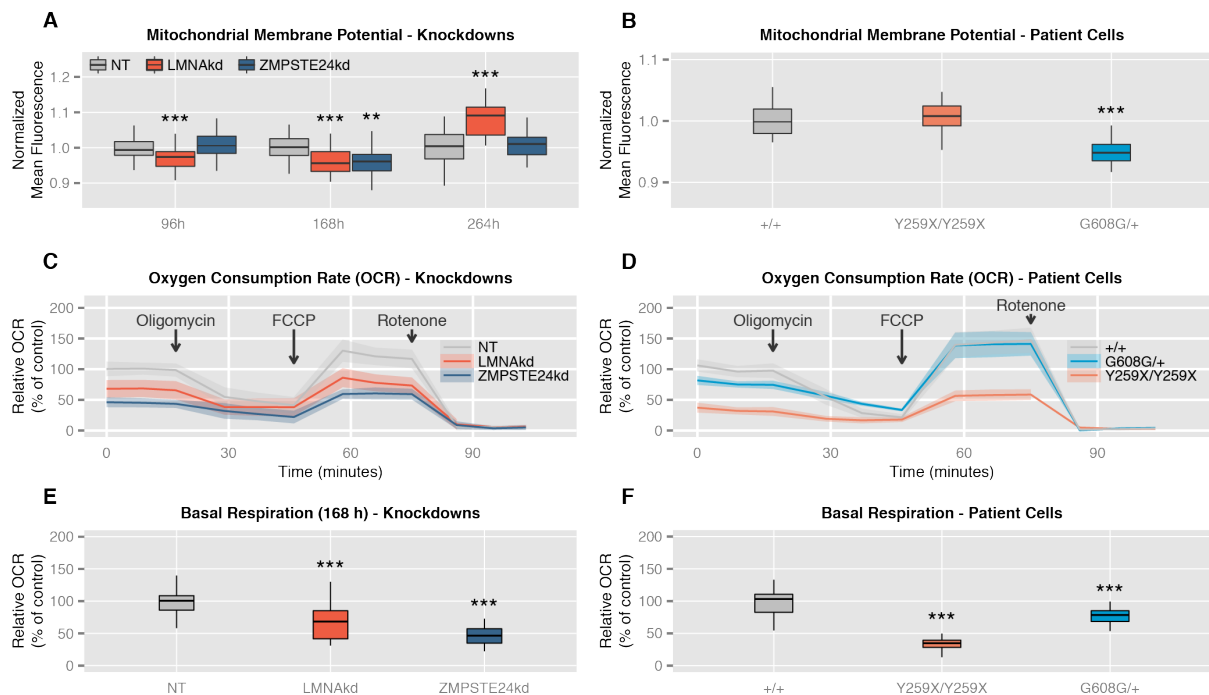


Figure 4.3: Sustained siRNA-mediated knockdown of LMNA and ZMPSTE24 induces time-dependent alterations in mitochondrial membrane potential ($\Delta\psi_m$) and decreased basal mitochondrial respiration.

(A) Normalized $\Delta\psi_m$ as measured by TMRM at different time points in LMNAkd and ZMPSTE24kd cells. (B) Normalized $\Delta\psi_m$ in LMNA^{Y259X/Y259X} and LMNA^{G608G/+} cells. (C & D) Normalized respiration profiles of LMNAkd, ZMPSTE24kd, LMNA^{Y259X/Y259X} and LMNA^{G608G/+} cells. The shaded region represents the standard error on the measurements. See the materials and methods section for more information about the different chemical components that were added. (E & F) Normalized basal respiration of LMNAkd, ZMPSTE24kd, LMNA^{Y259X/Y259X} and LMNA^{G608G/+} cells. (* = p-value < 0,05; ** = p-value < 0,01; *** = p-value < 0,001; the range of the y-axes has been adjusted to optimally display the differences).

2.5 Sustained LMNAkd increases mitochondrial superoxide

To verify whether a change in $\Delta\psi_m$ was accompanied by a change in mitochondrial superoxide ($O_2^{\bullet-}$) production, we measured the latter using the mitochondria-targeted $O_2^{\bullet-}$ sensor MitoSOX. After 168h hours, no significant change in $O_2^{\bullet-}$ levels was observed, despite a transient decrease in $\Delta\psi_m$ in both knockdowns. After 264h LMNAkd cells displayed a significant increase in $\Delta\psi_m$ as well as in $O_2^{\bullet-}$ (Fig. 4.3A & Fig. 4.4)

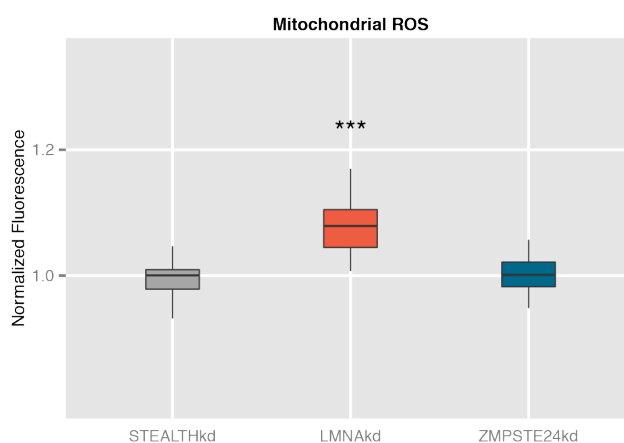


Figure 4.4: 264h of sustained siRNA-mediated knockdown of LMNA results in significantly increased mitochondrial ROS levels.

Normalized basal levels of mitochondrial ROS after 264h of knockdown, as measured by quantification of MitoSOX signal intensities using fluorescence microscopy. (* = p-value < 0,05; ** = p-value < 0,01; *** = p-value < 0,001)

2.6 LMNAkd and ZMPSTE24kd differentially affect antioxidant gene expression

Oxidative stress arises from an imbalance between ROS production and removal. To find out whether the accumulation of ROS correlated with a change in expression of ROS detoxifying enzymes, we performed a qPCR analysis. In general, LMNAkd more profoundly affected the expression of these enzymes than ZMPSTE24kd. In both conditions, most of the investigated genes became upregulated with the strongest effect being observed on the *GSTT2* transcript levels. Strikingly, ZMPSTE24kd and LMNAkd oppositely affected the expression of the mitochondrial manganese-(Mn)-superoxide dismutase (*SOD2*). This ROS-detoxifying enzyme converts superoxide ($O_2^{\bullet-}$) into hydrogen peroxide (H_2O_2). Expression of *SOD2* is regulated by the key cytokine *IL6*.²⁶⁷ Subsequent quantification of *IL6* transcript levels revealed a strong upregulation in ZMPSTE24kd and downregulation in LMNAkd cell cultures (Fig. 4.5A). The same opposite expression pattern was also observed in LMNA^{Y259X/Y259X} and LMNA^{C608G/+} patient fibroblasts (Fig. 4.5B).

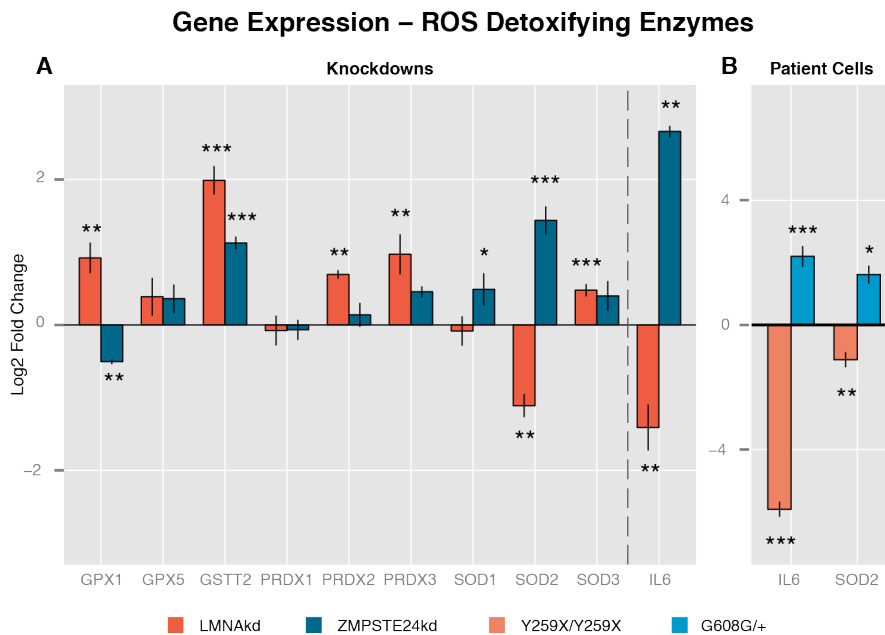


Figure 4.5: LMNAkd and ZMPSTE24kd cells show altered gene expression of ROS defusing enzymes. (A) Gene expression levels of GPX1, GPX5, GSTT2, PRDX1, PRDX2, PRDX3, SOD1, SOD2, SOD3 and IL6 were measured in LMNAkd and ZMPSTE24kd cells by real-time qPCR relative to NT control at 168 h. (B) Gene expression levels of IL6 and SOD2 were measured in LMNA^{Y259X/Y259X} and LMNA^{G608G/+} fibroblasts by real-time qPCR relative to untreated passage matched control fibroblasts. The values in this plot represent the average of 3 technical replicates, but only one biological replicate because we only have one cell line for each mutation. Therefore we cannot provide biologically relevant errorbars. (* = p-value < 0,05; ** = p-value < 0,01; *** = p-value < 0,001).

3 Discussion

With this work we set out to enhance our understanding of how PLA accumulation and lamin A deficiency affect cellular redox homeostasis. Since mature lamin A is firmly integrated within the nuclear lamina, it is characterized by low turnover rates.²¹⁷ This makes studying lamin A biology by acute siRNA-mediated knockdown strategies unreliable. We therefore induced sustained knockdown in human fibroblasts by repetitive siRNA transfection. As a rough validation, we extended our experiments with measurements of cells from LMNA^{Y259X/Y259X} and LMNA^{G608G/+} patients, although it should be noted that the patient's genetic background might play a role in the outcome of the experiments. In addition, knockdown of ZMPSTE24 causes accumulation of a farnesylated full-length PLA, whereas HGPS cells (LMNA^{G608G/+}) produce a different farnesylated PLA variant lacking 50 amino acids. To measure ROS levels and mitochondrial function in a robust and reliable manner, we used the high-content microscopy workflow that we established and benchmarked in chapter 3. We measured both intracellular ROS levels and mitochondrial membrane potential ($\Delta\psi_m$). Using this approach, we observed that both accumulation of farnesylated PLA and reduction of mature lamin A increased intracellular ROS levels, albeit at different rates. Compared to ZMPSTE24kd,

LMNAkd induced a progressive increase in basal ROS that was much more pronounced and started much earlier in the experimental time frame. And whereas ZMPSTE24kd cells showed no significant alteration in their response to the exogenous oxidant TBHP, LMNAkd cells proved to be hypersensitive. These observations correlate well with those obtained by Pekovic et al.¹³² and support the hypothesis that the nuclear lamina acts as an intracellular ROS-sink via redox-reactive cysteine residues within the lamin tail.¹³² When A-type lamins (and their cysteine residues) are depleted, the ability of the lamina to act as a ROS buffering system is abrogated, rendering the cell more sensitive against (potentially dangerous) increases of the intracellular ROS levels. PLA accumulation however does not decrease the concentration of these cysteine residues, plausibly leaving the ROS-sink intact. It has been shown that fibroblasts from centenarians accumulate moderate levels of PLA due to downregulation of *ZMPSTE24*, and that this primes the cells for a prompt response to DNA damage and oxidative stress, arguing for a physiological role of PLA.²⁶⁸ Above a certain threshold, however, PLA becomes toxic and ROS levels increase, as witnessed in ZMPSTE24kd cells at 264 h.

To determine whether elevated ROS levels correlated with mitochondrial dysfunction, we also quantified $\Delta\psi_m$. Our results revealed that LMNAkd induces $\Delta\psi_m$ depolarization at early time points, followed by $\Delta\psi_m$ hyperpolarization at 264 h. In contrast, ZMPSTE24kd induced a transient $\Delta\psi_m$ depolarization. In accordance with the increase in $\Delta\psi_m$, we also observed a significant increase in mitochondrial $O_2^{\bullet-}$ levels in LMNAkd cells after 264h, as reported by the MitoSOX sensor dye. Indeed, it has been demonstrated before that mitochondria produce more ROS at high membrane potential.^{65,118} In line with a defect in mitochondrial function, and consistent with observations in *Zmpste24*^{-/-} mouse adult fibroblasts²⁶⁵, the basal mitochondrial respiration rate in both LMNAkd and ZMPSTE24kd cells as well as in *LMNA*^{Y259X/Y259X} and *LMNA*^{G608G/+} patient cells was lowered.

Since mitochondria are the initial sites of oxidative damage and the instigators of oxidative stress in the cytosol upon proteasome overload²⁶⁹, a possible connection with the knockdowns may lie in their potential to cause proteasome dysfunction. Indeed, overexpression of LA mutants and depletion of LA have been linked to the accumulation of nuclear envelope proteins (SUN2, Emerin and Nesprin-1) in the endoplasmic reticulum and upregulation of various ubiquitin ligases, which might induce proteasome overload.²⁷⁰⁻²⁷²

Parallel to the increase in intracellular ROS, both knockdowns showed increased expression of ROS detoxifying enzymes. Although the number of upregulated genes was higher in LMNAkd with respect to ZMPSTE24kd cells, their failure to suppress ROS increase could be explained by the absence of the aforementioned ROS sink. In both conditions the general trend was preserved except a differential expression of *GPX1* and *SOD2*. *SOD2* is a mitochondrial superoxide converting enzyme, the expression of which is regulated by IL6, a senescence associated cytokine.²⁷³⁻²⁷⁵ We found that both *IL6* and *SOD2* were upregulated in ZMPSTE24kd and downregulated in LMNAkd cells. The same opposite expression was observed in

LMNA^{G608G/+} and *LMNA*^{Y259X/Y259X} fibroblasts, respectively, even with a much stronger (~78 fold) downregulation of *IL6* in *LMNA*^{Y259X/Y259X} cells. The upregulation of *SOD2* in ZMPSTE24kd cells might explain why these cells display no significant increase in mitochondrial superoxide. When following this reasoning, downregulation of *SOD2* should then trigger a rise in mitochondrial ROS levels, which we indeed observed in LMNAkd cells after 264h.

Previously, we have shown that repetitive ruptures of the nuclear envelope in lamin A/C deficient cells temporarily relocate various transcription factors, several of which controlling the oxidative stress response.¹³⁹ In addition, we found that lamin A/C deficiency caused cytoplasmic translocation of nuclear PML bodies²⁷⁶, known sensors of oxidative stress and regulators of redox homeostasis.^{277,278} It is conceivable that these phenomena contribute to the oxidative stress phenotype witnessed in LMNAkd cells as well.

Irrespective of the ROS source, we witnessed a decreased cell proliferation in both ZMPSTE24kd and LMNAkd cells. However, the actual cell fate between both knockdowns differed. Whereas ZMPSTE24kd cells resorted to a senescence pathway (shown by β -galactosidase and p21 staining as well as upregulation of *IL6*), LMNAkd cells rather experienced increased apoptosis (evidenced by an increased number of cells with fragmented nuclei and $\Delta\psi_m$ hyperpolarization, which is known to precede apoptosis^{279,280}). These results align well with earlier findings. Indeed, premature senescence was observed in *Zmpste24*^{-/-} MEFs, *Lmna*^{G609G/G609G} MEFs, ZMPSTE24 depleted hMSCs and HGPS fibroblasts^{273,281-283}, and apoptosis was increased in *Lmna*^{-/-} MEFs, especially when subjected to mechanical stress^{26,272}, in myocytes from *Lmna*^{E82K/+} transgenic mice²⁸⁴ and in *Lmna*^{+/-} atrioventricular nodal mouse myocytes.²⁸⁵ This bifurcation in cell fate might be triggered by the extent of mature lamin A reduction, which translates into a ROS dosage effect. It has been shown that modestly increased levels of intracellular ROS induce and maintain cellular senescence, as observed in ZMPSTE24kd cells, while higher doses provoke apoptosis, as we now witnessed in LMNAkd cells.²⁸⁶⁻²⁸⁹

In conclusion, we demonstrated that sustained knockdown of *LMNA* or *ZMPSTE24* resulted in increased basal ROS levels, which were accompanied by changes in mitochondrial function and altered gene expression of ROS detoxifying enzymes. Reduction of LAMIN A caused a dramatic increase in basal and, especially, induced ROS levels ultimately leading to $\Delta\psi_m$ hyperpolarization and apoptosis. Depletion of *ZMPSTE24* on the other hand, triggered a senescence pathway, associated with moderately increased ROS levels and transient $\Delta\psi_m$ depolarization. Thus, lamin A and PLA differentially regulate cell fate, in part via a redox-dependent pathway. Uncovering the molecular details of this pathway will help understanding laminopathy diversity and disease progression.

4 Materials and methods

4.1 Cell culture

Normal human dermal fibroblasts (NHDF, $LMNA^{+/+}$, Promocell, C-12300), fibroblasts from a patient with a lethal laminopathy phenotype due to a nonsense Y259X homozygous mutation in the $LMNA$ gene ($LMNA^{Y259X/Y259X}$)²⁴⁵ and fibroblasts from a patient suffering from HGPS ($LMNA^{G608G/+}$)²³³ were cultured in T25 or T75 culture flasks in DMEM High Glucose with L-Glutamine medium (Lonza, BE12-604F) supplemented with 10% fetal bovine serum (Gibco, 10500-064) and 1% penicillin/streptomycin/L-glutamine (Gibco, 10378-016), at 37°C and 5% CO₂, according to standard procedures. All experiments were performed with cells in between passage 9 and 20. In case of direct comparison, passage-matched cells were used. At set time points, viable cells were counted using Trypan blue and a Bürker chamber. Proliferative capacity was expressed in terms of population doubling level (PDL), the base 2 logarithm of the number of cells at the current time point divided by the number of cells that was seeded.

4.2 siRNA-mediated knockdown

Expression of $ZMPSTE24$ and $LMNA$ was silenced with siGENOME Lamin A/C siRNA (Thermo Scientific, D-001050-01-20) and siGENOME Human $ZMPSTE24$ siRNA (Thermo Scientific, M-006104-02-0020), respectively. Stealth RNAi siRNA Negative Control, Med GC (Life Technologies, 12935-300) was used as a negative non-targeting control (NT). siRNA transfections were performed using Lipofectamine® RNAi-MAX Transfection Reagent (life technologies, 13778-075), according to manufacturer's instructions following the scheme outlined in **Figure 4.6**. A more detailed description can be found in **Chapter 2**.

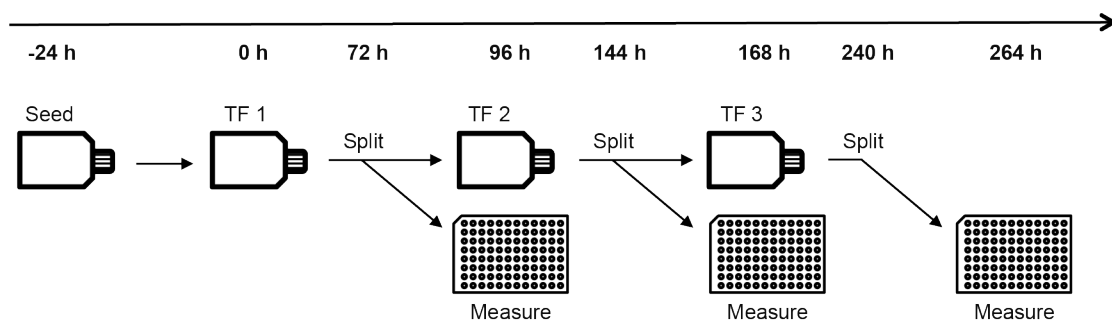


Figure 4.6: Experimental design.

Scheme of the sustained siRNA-mediated knockdown by repetitive transfections (TFs), and timing of the subsequent experiments.

4.3 Quantitative PCR

RNA was extracted from cells using the RNAeasy mini kit (Qiagen, 74104), with on-column DNase digestion. Concentrations of purified RNA were measured with the NanoDrop 2000 (Thermoscientific). Per sample, 1µg of RNA was converted to

cDNA using SuperScript® III Reverse Transcriptase (RT) (Life Technologies, 18080-044). All qPCR reactions were performed on a RotorGene 3000 (Qiagen/Corbett) using the SensiMix™ SYBR® No-ROX Kit (Bioline, QT650) according to the manufacturers instructions. Relative abundance of *LMNA* transcripts (forward: TGGACGAGTACCAGGAGCTT; reverse: ACTCCAGTTTGCCTTTTTG), *ZMPSTE24* transcripts (forward: CGAGAAGCGTATCTTCGGG; reverse: TGTGCTAGGAAGGTCTCCA), *SOD1* transcripts (forward: GACCTGCACTGGTACAGCCT; reverse: GCATCATCAATTTTCGAGCAG), *SOD2* transcripts (forward: GGAGAAGTACCAGGAGGCGT; reverse: TAGGGCTGAGGTTTGTCCAG), *SOD3* transcripts (forward: TCTCTTGGAGGAGCTGGAAA; reverse: CGAGTCAGAGTTGGGCTCC), *IL6* transcripts (forward: AGTGAGGAACAAGCCAGAGC; reverse: GTCAGGGGTGGTTATTGCAT), *GSTT2* transcripts (forward: ACGCTCAAGGATGGTGATTT; reverse: AGGTACTCATGAACACGGGC), *GPX1* transcripts (forward: CCGAGAAGGCATACACCGAC; reverse: GCCGGCCAGTTAAAAGGAGG), *GPX5* transcripts (forward: ACAAGTCCCAAGCAGGAGAA; reverse: TGACGAAGAGGATGTGCTTG), *PRDX1* transcripts (forward: GCTGTTATGCCAGATGGTCAG; reverse: GGGCACACAAAGGTGAAGTC), *PRDX2* transcripts (forward: GTCCTTCGCCAGATCACTGT; reverse: TGGGCTTAATCGTGTCCTG) and *PRDX3* transcripts (forward: CCACATGAACATCGCACTCT; reverse: TTGACGCTCAAATGCTTGAT) were measured relative to *ACTB* (forward: CCTTGACATGCCGGAG ; reverse: GCACAGAGCCTCGCCTT) and *GAPDH* (forward: TGCACCACCAACTGCTTAGC; reverse: GGCATGGACTGTGGTCATGAG) reference transcripts. Ct-values were calculated using the ‘comparative quantification’ (CQ) method supplied as part of the Rotor Gene 3.0 software (Corbett Research). Analysis was done using the $\Delta\Delta C_t$ -method.²³⁷

4.4 Immunofluorescence staining

NHDF cells were grown on glass coverslips and fixed in 4% paraformaldehyde for 15 minutes at room temperature and washed (3x, 5 minutes) with PBS. Subsequently, cells were permeabilized with 0.5% Triton X-100 (5 minutes), after which they incubated with primary antibody diluted in 50% fetal bovine serum (FBS) for 60 minutes. After minimally 3 PBS wash steps, slides were incubated with secondary antibody diluted in 50% FBS for 30 minutes, washed again, and mounted with VECTASHIELD™ Mounting Medium (VWR, 101098-042) containing 1 µg/ml 4',6-diamino-2-phenylindole (DAPI). Primary antibodies were directed against lamin A (Abcam, ab26300) and prelamin A (Santa Cruz Biotechnology Inc., SC-6214). As secondary antibodies DyLight 488 conjugated donkey anti-rabbit (Jackson ImmunoResearch Laboratories Inc., JAC-705606147), and DyLight 649 conjugated donkey anti-goat (Jackson ImmunoResearch Laboratories Inc., JAC-705496147) were used. Immunofluorescent stained cells were visualized using a Nikon Ti

Eclipse inverted widefield fluorescence microscope (Nikon Instruments) with 40x Plan Apo oil (NA = 1.3) and 60x Plan Apo VC (NA = 1.4) objectives.

4.5 β -galactosidase staining

NHDF cells were grown on glass coverslips and fixed in 4% paraformaldehyde for 15 minutes at room temperature and washed (2x, 5 minutes) with PBS. Fixed cells were incubated overnight at 37°C in 1 mg/ml X-Gal, 40 mM citric acid/phosphate buffer (pH 6), 5 mM ferricyanide, 5 mM ferrocyanide, 2 mM MgCl₂ and 150 mM NaCl. After incubation, the cells were washed (3x, 5 minutes) with PBS and permeabilized with 0.5% Triton X-100 (5 minutes). The cells were washed (3x, 5 minutes) with PBS and mounted with VECTASHIELD™ Mounting Medium (VWR, Belgium, 101098-042) containing 1 μ g/ml 4',6-diamino-2-phenylindole (DAPI). Cells were visualized using a Nikon Ti Eclipse inverted widefield fluorescence microscope (Nikon Instruments) with a 40x Plan Apo oil (NA = 1.3) objective.

4.6 Western blot

Cells were grown in T75 culture flasks and lysed using the whole-cell extraction protocol of the Nuclear Extract Kit (Active Motif, 40010). Protein concentration was measured with the Pierce 660 nm assay (Thermo Scientific, 22662). Cell lysates were subjected to SDS-PAGE (8% bis-tris with MOPS running buffer) and transferred to BioTrace PVDF membranes (Pall Corporation, 66542). Primary antibodies were directed against lamin A/C (Santa Cruz Biotechnology Inc., sc-56139) and nucleolin (control) (Novus Biologicals, NB600-241). HRP conjugated goat anti-mouse (Sigma-Aldrich, A4416) and HRP conjugated goat anti-rabbit (Sigma-Aldrich, A6154) were used as secondary antibodies. Proteins were detected by chemiluminescence with Immobilon Western chemiluminescent HRP substrate (Millipore, WBKLS0100).

4.7 High content live cell imaging of intracellular ROS and $\Delta\psi_m$

Intracellular ROS and $\Delta\psi_m$ were measured after dual staining with the fluorescent cell-permeable probes 5-(and-6)-chloromethyl-2',7'-dichlorodihydrofluorescein diacetate (CM-H₂DCFDA) (Life Technologies, C6827) and tetramethyl rhodamine methyl ester (TMRM, Invitrogen, T-668). Measurements were done 96 h, 168 h and 264 h after initiation of the knockdown (**Fig. 4.6**). 24 h before measurement, cells were transferred to 96-well plates (Greiner - μ CLEAR-Plate, Black, 655090) at 2500 cells per well. Right before measurement they were washed in HBSS + 25 μ M HEPES (HH) (pH 7.2), incubated for 25 minutes in the dark at room temperature in HH-buffer containing 2 μ M CM-H₂DCFDA and 20nM TMRM, washed again in HH-buffer and then imaged (also in HH-buffer) on a Nikon Ti Eclipse inverted widefield fluorescence microscope with a 20x air Plan Apo objective (NA 0.75) using a 480/40 nm excitation, 520/35 nm emission filter combination for the CM-H₂DCFDA signal and a 540/25 nm excitation, 605/55 nm emission filter combination for the TMRM signal. Since fluorescence excitation induces the formation of ROS²¹², the CM-

H₂DCFDA signal increases during microscopic observation. To avoid this effect from biasing the results, we used diffuse transmitted illumination to initialize an infrared-led based autofocus (Perfect Focus System, Nikon), after which images were acquired automatically across the plate (4 images per well and per channel), the CM-H2DCFDA channel first. After the complete plate was imaged, 20 μ M *tert*-butyl peroxide (Sigma-Aldrich, 458139-100mL) was added to all wells and after a 3-minute interval the acquisition was repeated. The method was benchmarked with different doses of TBPH and validated with flow cytometry (**cf. Chapter 3**). TMRM reporter potential was validated with valinomycin (Sigma) and oligomycin (Sigma), known inducers of $\Delta\psi_m$ depolarization, resp. hyperpolarization.^{243,244} (**cf. Chapter 3**)

An analogous experimental setup was used for measuring mitochondrial superoxide levels with MitoSOX Red Reagent (Life technologies – M36008). This dye was combined with the pan-cellular, viability dye Calcein Green (Life Technologies – C34852) to simplify cell segmentation in downstream image analysis and exclude dead cells from the analysis.²⁹⁰ In brief, cells were grown in 96-well plates, washed in HH-buffer, incubated in HH-buffer with 5 μ M MitoSOX Red Reagent and 0.930 μ M Calcein for 10 minutes at 37°C in the dark, washed again and imaged 1x with the same 4 images/well acquisition protocol.

All experiments were performed with at least 8 replicates per treatment per plate (depending on the experiment), on at least 3 different plates.

4.8 Image analysis

All image processing was performed in FIJI (<http://fiji.sc>), a packaged version of ImageJ freeware (W.S. Rasband, U.S.A. National Institutes of Health, Bethesda, Maryland, USA, <http://rsb.info.nih.gov/ij/>, 1997–2014). Quantification of nuclear signal intensities of immunostained cell cultures was done using INSCYDE.ijm, a script for high content analysis.²⁷ Automated analysis of intracellular ROS and mitochondrial characteristics was done using RedoxMetrics.ijm, (**cf. Chapter 3**). In brief, the image analysis pipeline consists of a flatfield correction to correct for illumination heterogeneity, noise reduction by Gaussian filtering and cell or mitochondrial segmentation and subsequent feature analysis of regions of interest. For CM-H2DCFDA or Calcein counterstained images, cells were segmented by autothresholding according to Huang's algorithm and average intensities were measured within the segmented regions. For measurement of mitochondrial signals, mitochondria were first selectively enhanced by local contrast enhancement and multi-scale Laplacian filtering²⁷ after which binarization was performed using Huang's algorithm. The resulting mask was used for analyzing shape metrics of objects larger than a predefined size (> 3 pixels) on the original image. All scripts are available upon request.

4.9 Respirometry

The Seahorse Extracellular Flux XF24 analyzer (Seahorse Bioscience) was used to provide a comprehensive assessment of the relative state of aerobic metabolism in

live cells in assessing mitochondrial function. Seeding density and concentration of Mitostress kit (Seahorse Bioscience, 101848-400) components were optimized according to the manufacturers guidelines. Fibroblasts were seeded at a concentration of 20000 cells per well the day prior to the experiment. OCR was measured before addition of any compound (basal OCR), after addition of oligomycin (0.5 μ M final concentration), carbonyl cyanide p-trifluoromethoxyphenylhydrazone (FCCP, 0.5 μ M) and rotenone/antimycin (0.5 and 0.05 μ M). The OCR linked to coupled respiration was obtained by subtracting OCR after the addition of oligomycin from basal OCR. OCR after addition of the mitochondrial uncoupler FCCP reflected the maximal respiratory rate (spare respiratory capacity). Non-mitochondrial respiration was defined as the rate after rotenone/antimycin A application and was subtracted from the basal OCR to determine the mitochondrial OCR.

4.10 Statistical analyses

Data analysis and visualization was performed in R statistical freeware (<http://www.r-project.org>). Standard statistical methods were employed, including the Shapiro-Wilk Normality Test to assess normality of the data, Levene's test to assess homoscedasticity, student's t-test, ANOVA and the Kruskal-Wallis rank sum test to assess differences between the group means and Tukey (after ANOVA) and Dunnett type (After Kruskal-Wallis) post-hoc tests to assess significance for each group. We also used non-parametric contrast-based multiple comparison tests.²⁹¹ Significance levels were indicated as follows: $p < 0.05$ (*), $p < 0.01$ (**), and $p < 0.001$ (***). For graphics and annotation, the R program was expanded with the ggplot2 package.²⁴⁰

V

PERSISTENT PERTURBATION OF A-TYPE LAMIN METABOLISM INDUCES OXIDATIVE STRESS BY INHIBITION OF PROTEIN DEGRADATION PATHWAYS

Manuscript in preparation

Abstract

A-type lamins are defining constituents of the nuclear lamina, a filamentous network that supports the nuclear membrane and organizes many nuclear as well as cellular processes. An increasing amount of evidence also suggests a role in intracellular redox homeostasis, either indirectly through interactions with redox-responsive proteins and transcription factors, or directly, by serving as a nuclear scavenger of reactive oxygen species (ROS). Mutations in the *LMNA* gene leading to depletion of A-type lamins, or accumulation of prelamin A variants are accompanied by mitochondrial dysfunction and oxidative stress. Previously, we have shown differential effects of lamin A/C depletion and PLA accumulation on cellular redox balance. Yet, the underlying mechanisms are still largely unknown. To contribute to a better understanding, we have now quantified these differences at the level of the individual cell. We found that complete depletion of A-type lamins leads to a sharp increase of basal, but especially of induced ROS, while accumulation of PLA was correlated with a linear increase of ROS levels, pointing to different underlying pathways. Whereas both perturbations decreased proteasomal function, lamin A/C depletion also significantly decreased autophagy. Failure to compensate lower proteasomal degradation by autophagy, might explain the more dramatic phenotype observed upon lamin A/C depletion compared to PLA accumulation. Promotion of protein degradation by sulforaphane improved the oxidative stress phenotype in both conditions. This observation suggests a potential novel therapeutic entry point for laminopathies, especially as an addition to the current treatments.

1 Introduction

Laminopathies are orphan diseases predominantly caused by point mutations in the *LMNA* gene. *LMNA* encodes lamin A and C proteins, both important constituents of the nuclear lamina, filamentous network that supports the nuclear membrane. Lamin A is produced as a precursor protein, prelamin A (PLA), which becomes post-translationally processed starting with a farnesylation near the C-terminus, followed by a proteolytic cleavage of the C-terminal three amino acids, then a carboxymethylation and finally the removal of the C-terminal 15 amino acids, including the farnesyl group¹⁵⁰ (cfr. **Chapter 1, Figure 3**). This last step is exclusively catalyzed by the zinc-metalloproteinase ZMPSTE24. Point mutations in specific recognition sites for posttranslational steps interfere with the maturation process, causing prelamin A intermediates to accumulate. Among these isoforms, the farnesylated variants are assumed to be particularly cytotoxic. For instance, in the Hutchinson-Gilford Progeria Syndrome (HGPS), a single point mutation (C1824T) in the *LMNA* gene activates a cryptic splice site that causes the ZMPSTE24 cleavage site to disappear, leading to the accumulation of a truncated, permanently farnesylated prelamin A, termed progerin.³ Similarly, in restrictive dermopathy (RD), the loss of functional ZMPSTE24 leads to the accumulation of farnesylated PLA (fPLA).^{50,134}

The nuclear lamina is well known for its mechanical properties, as support for the nuclear envelope or as a component in the LINC-complex, connecting the nucleoskeleton with the cytoskeleton.^{3,28} However, an accumulating body of evidence suggests that the nuclear lamina is also involved in intracellular redox homeostasis.^{1,203} Lamins may indirectly contribute to the redox balance through interactions with redox-responsive proteins and transcription factors.^{141,155,156} They may also directly affect redox status, e.g. by serving as ROS scavengers (by virtue of their oxidizable cysteine residues).¹³² Direct or indirect, human fibroblasts in which *LMNA* is silenced, or *LMNA*-deficient patient cells, display increased levels of ROS and hypersensitivity towards induced ROS.^{132,203} Yet, depletion of A-type lamins is not a sole contributor to oxidative stress. Indeed, the accumulation of farnesylated PLA has also been shown to raise cellular ROS levels, albeit to a lower extent than lamin A/C deficiency.^{60,203} As the accumulation of immature prelamin A is not expected to alter their ROS scavenging function, alternative lamin-dependent pathways may operate to promote oxidative stress. One such candidate is impaired protein degradation. Decreased proteasomal function or proteasomal overload leads to the buildup of unprocessed proteins and the formation of protein aggregates, the accumulation of which can interfere with many cellular processes such as mitochondrial electron transport and can subsequently cause increased ROS production.²⁶⁹ Indeed, both mitochondrial dysfunction and decreased proteasome function have already been observed in cells with disturbed A-type lamin metabolism and HGPS patient cells.^{133,166,203,215,265} In addition, overexpression of lamin A variants and depletion of lamin A have been linked to the mislocalization and subsequent proteasomal degradation of nuclear envelope proteins (SUN2, Emerin and Nesprin-1), and to the upregulation of various ubiquitin ligases, possibly resulting in proteasome overload.^{270-272,292} Besides, upregulation of both proteasomal protein degradation and autophagy have been reported to ameliorate nuclear blebbing and early senescence associated with the HGPS phenotype.^{215,293} With this work, we evaluated the effect of lamin A/C depletion and PLA accumulation, respectively, on the intracellular redox balance at the level of the individual cell. We found that only complete depletion of A-type lamins induced a strong rise of basal, but especially induced ROS, while accumulation of PLA was correlated with a gradual linear increase indicating that different underlying mechanisms are at play. We also found a potential connection with defective protein degradation pathways.

2 Results

2.1 Below a critical threshold level, lamin A/C depletion triggers oxidative stress

Previously, we have established a high-content microscopy-based pipeline that enables interrogating redox balance in primary fibroblasts (NHDF) (**Chapter 3**).^{2,241} Using this pipeline, we found that sustained siRNA-mediated depletion of lamin A

significantly increases both basal and induced ROS levels at the population level (**Chapter 4**).²⁰³ We now extended this assay, by performing post-hoc immunofluorescent (IF) staining for lamin A. This allowed for correlating lamin A levels with ROS levels at the level of the individual cell. Representative images of the different parameters in the same cells are displayed in **Figure 5.1**.

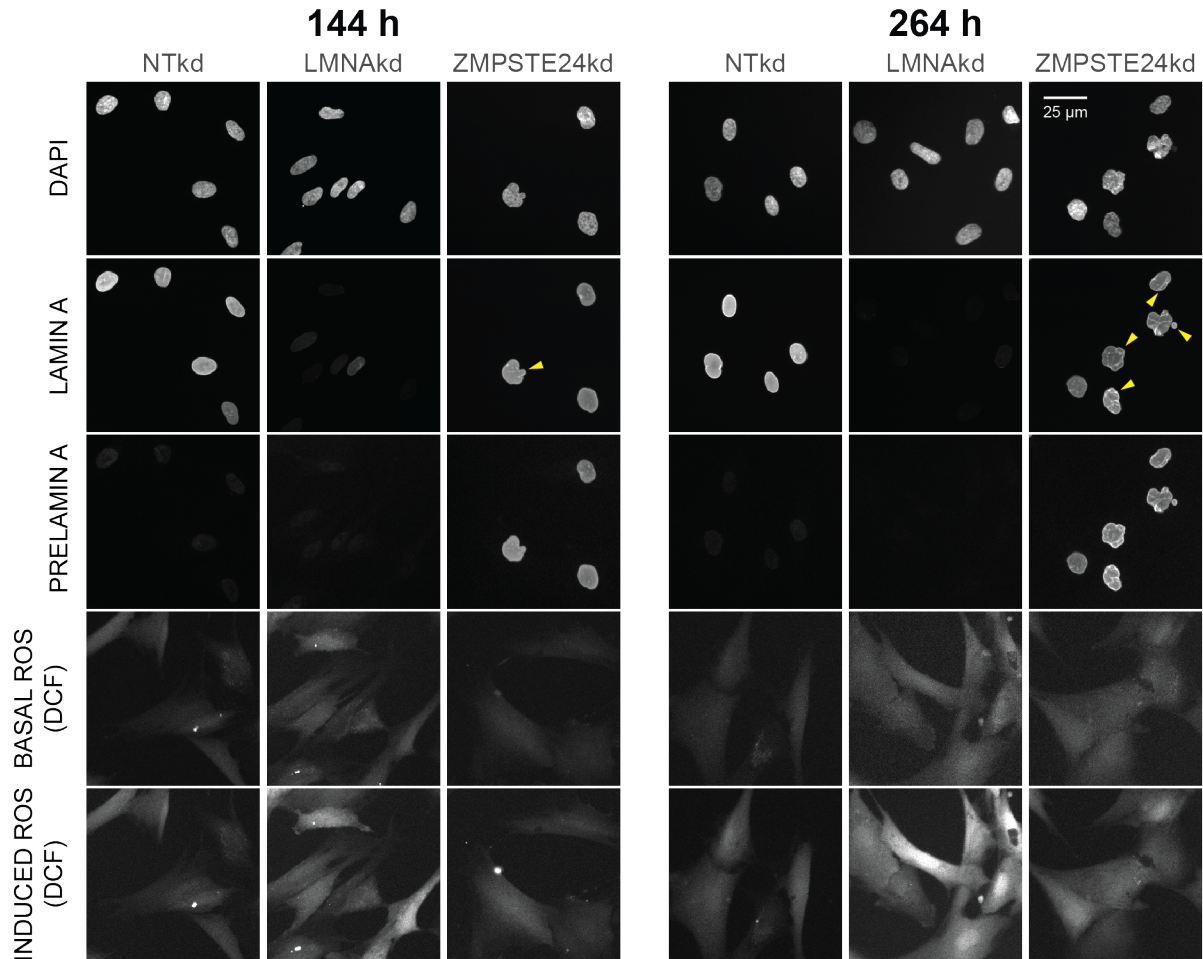


Figure 5.1: High-content live-cell ROS imaging extended with post-hoc immunofluorescent stainings. Representative images showing the different parameters (lamin A, prelamin A, basal ROS, induced ROS), and a nuclear counterstain (DAPI), in the same cells, yellow arrows indicate typical nuclear aberrations upon PLA accumulation.

When correlating lamin A abundance with ROS levels at the single cell level, we found a non-linear, concentration-dependent effect. More specifically, at 144h after one knockdown, most cells demonstrated a significant (> two-fold) reduction in lamin A levels (**Fig. 5.2A & D**), but no change in basal ROS levels (**Fig. 5.2B & D**), whereas at 264h, after three subsequent knockdowns, lamin A levels were further (> 4-fold) reduced and only then, many cells with significantly increased basal ROS levels were found (**Fig. 5.2A & B & D**). This effect became even more pronounced for induced ROS levels, i.e., ROS levels after addition of the oxidant TBHP (**Fig. 5.2C & E**). Thus, depletion of A-type lamins induces an increase of basal and induced ROS levels at the level of the individual cell, but only when this depletion

exceeds a critical threshold. In other words, only virtual absence of A-type lamins triggers oxidative stress. Even then, this correlation is not complete, since not all cells that demonstrate over 4-fold loss of A-type lamins show significantly higher levels of ROS.

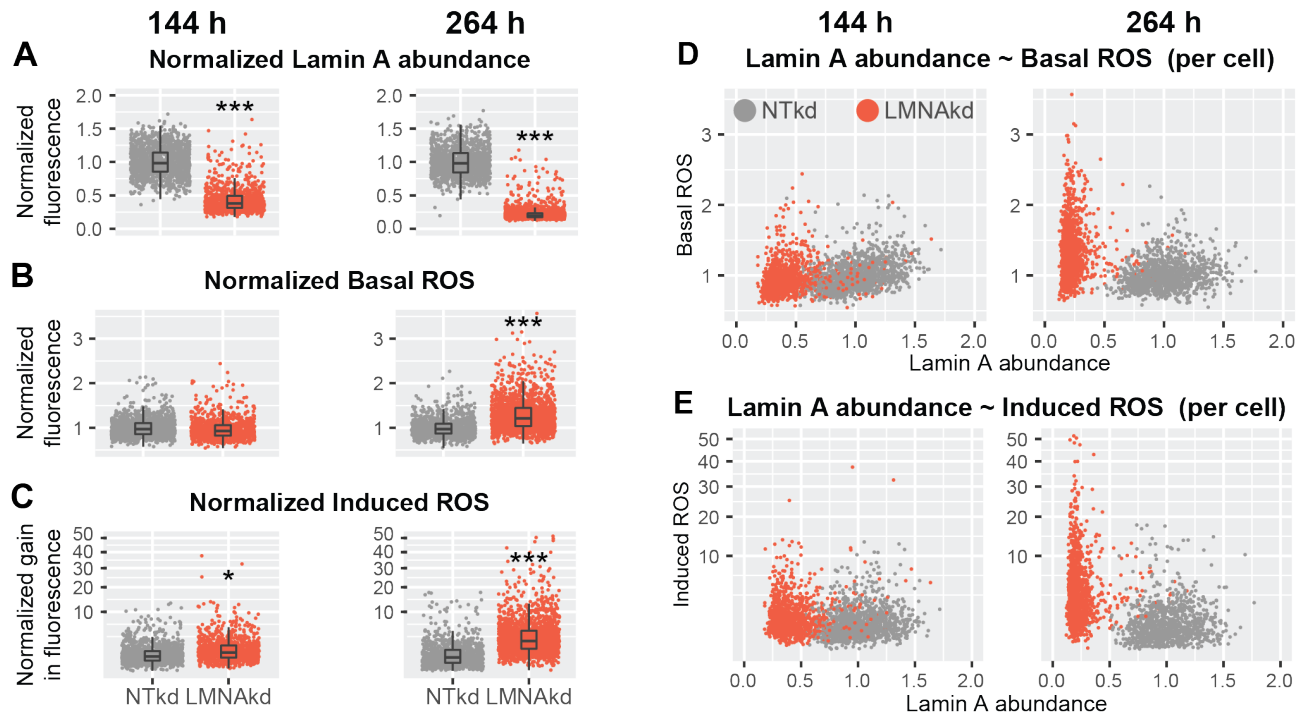


Figure 5.2: Correlation between lamin A/C depletion and oxidative stress at the cellular level.

(A) Normalized lamin A protein levels in LMNAkd cells compared to NTkd control cells, as measured by immunofluorescence staining and quantitative image analysis. (B & C) Normalized basal levels of intracellular ROS measured by CM-H₂DCFDA high content microscopy analysis and response towards induced ROS, measured as relative gain in intensity after 20 mM TBHP addition in LMNAkd cells compared to NTkd control cells. (D & E) Lamin A abundance versus basal and induced ROS levels at the single cell level, as measured by quantitative immunofluorescence imaging. (F) Representative images showing the different parameters (lamin A, prelamin A, basal ROS, induced ROS), and a nuclear counterstain (DAPI), in the same cells, yellow arrows indicate typical nuclear aberrations upon PLA accumulation. (* = p-value < 0,05; ** = p-value < 0,01; *** = p-value < 0,001)

2.2 Prelamin A raises ROS levels in a concentration-dependent manner

Using a similar correlative approach as described above, we also investigated the effect of experimentally-induced, sustained prelamin A accumulation, namely by repetitive siRNA-mediated knockdown of *ZMPSTE24*. Here, we used a prelamin A antibody for post-hoc IF. Representative images of the different parameters in the same cells are displayed in **Figure 5.1**. At 144 h (after 1 knockdown), an average 3.5-fold increase in PLA levels was measured (as nuclear fluorescence signal intensity in the PLA channel after IF), which further increased up to a 3.8 fold at 264 h (96h after the third transfection round) (**Fig. 5.3A**). At the population level, PLA accumulation caused a significant decrease of basal intracellular ROS levels at

144h but a significant increase of basal and induced ROS levels at 264h (**Fig. 5.3B & D**). At the individual cell level, a broad range was observed of cells displaying a 1 to 8-fold change in PLA levels. Along with this, there was a linear trend between intracellular PLA concentration and basal ROS levels, both at 144h and 264h (Pearson's correlation coefficients of 0.46 and 0.45 at 144h and 264h, respectively – **Fig. 5.3D**). No correlation was measured between PLA concentration and induced ROS, despite the significant increase of induced ROS at the population level (**Fig. 5.3C & E**).

Thus, in contrast with lamin A/C depletion, where a decrease of A-type lamins below a critical threshold results in an acute rise of basal and especially induced ROS levels, PLA accumulation follows a linear concentration-dependent trend with basal intracellular ROS levels while the increase in induced ROS levels seems to be rather time-dependent than PLA-concentration dependent. Taken together, this suggests that depletion of A-type lamins and accumulation of PLA trigger oxidative stress via alternative pathways.

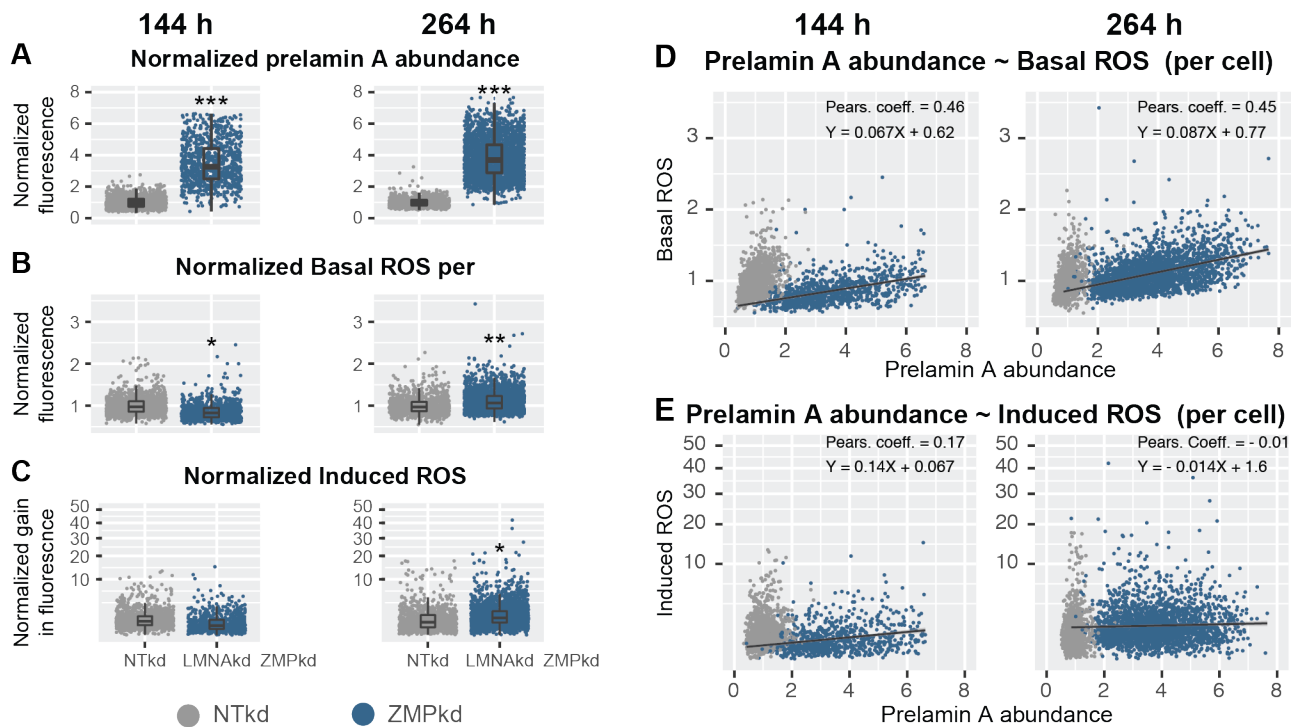


Figure 5.3: Correlation between PLA accumulation and oxidative stress at the cellular level.

(A) Normalized prelamina A protein levels in ZMPSTE24kd cells compared to NTkd control cells, as measured by immunofluorescence staining and quantitative image analysis. (B & C) Normalized basal levels of intracellular ROS measured by CM-H₂DCFDA high content microscopy analysis and response towards induced ROS, as measured as relative gain in intensity after 20 mM TBHP addition in ZMPSTE24kd cells compared to NTkd control cells. (D & E) Prelamina A abundance versus basal and induced ROS levels at the single cell level, as measured by quantitative immunofluorescence imaging. (* = p-value < 0,05; ** = p-value < 0,01; *** = p-value < 0,001)

2.3 Lamin A/C depletion and prelamin A accumulation differentially inhibit protein degradation pathways

Aberrantly folded or immature proteins are usually degraded by the proteasomal machinery. However, when the amount of aberrant proteins becomes too high, the proteasome may become saturated, thereby inhibiting their normal function.²⁹⁴ We reasoned that this might be the case for PLA accumulation and that this could be a trigger for concentration-dependent ROS production. Therefore, we measured proteasome 20S activity in both LMNAkd and ZMPSTE24kd cells at 264h. We found that ZMPSTE24kd indeed significantly reduced proteasomal activity (by 4%). However, we also discovered that LMNAkd reduced proteasomal activity even more (7%) (**Fig. 5.4A**). In fact, the reduction in lamin A/C-depleted cells was comparable to that observed after treatment of wild type NHDF (NHDF-WT) cells with the proteasomal inhibitor MG-132 (**Fig. 5.4A**). It has been proposed that the proteasomal pathway is complemented by autophagy, as an alternative protein degradation pathway. Both pathways lead to degradation of misfolded and mislocalized proteins, and display compensatory effects when one is dysfunctional (communicating vessels).^{295,296} Hence, we analyzed autophagy induction in the knockdown models using a fluorescent reporter that selectively labels autophagic puncta, using the autophagy enhancer rapamycin as a positive control. Indeed, treatment of wild type NHDF (NHDF-WT) with MG132, resulted in a significant 38% increase in the number of autophagic vesicles (**Fig. 5.4B**). Interestingly however, LMNAkd showed a significant decrease (22%) at 264h, while ZMPSTE24kd had no apparent effect (**Fig. 5.4B**).

Thus, lamin A/C depletion and PLA accumulation are both correlated with decreased proteasomal activity, which is not compensated for by autophagy. In LMNAkd cells, autophagy is even reduced.

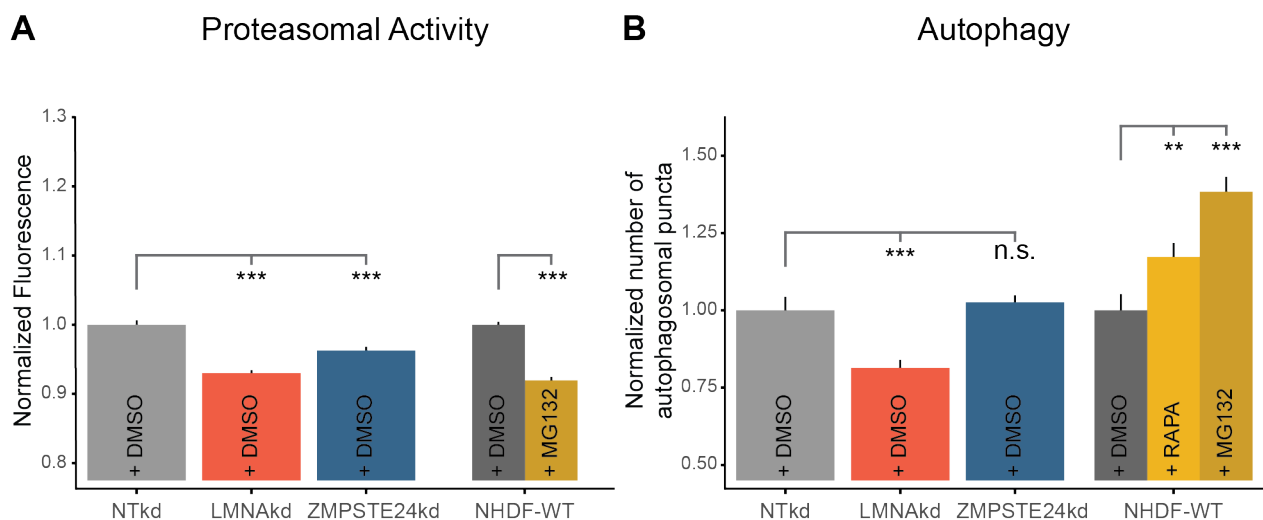


Figure 5.4: Protein degradation activity (proteasomal degradation & autophagy)

(A) Normalized 20S proteasomal activity in LMNAkd, ZMPSTE24kd and NTkd cells, as measured by fluorescence microscopy. (B) Normalized number of autophagic puncta in LMNAkd, ZMPSTE24kd and NTkd cells, as measured by fluorescence microscopy. (* = p-value < 0,05; ** = p-value < 0,01; *** = p-value < 0,001; error bars represent standard error)

2.4 Sulforaphane promotes protein degradation and lowers basal ROS levels

Assuming that the decreased protein degradation (partially) underlies the oxidative stress phenotype witnessed in our lamin perturbation models, we next sought to promote proteasomal activity and autophagy using sulforaphane (SFN). SFN is a plant derived isothiocyanate (1-isothiocyanato-4-methylsulfinylbutane) known to enhance protein degradation.^{297,298} As expected, SFN was found to increase the activity of both proteasomal degradation pathways by 17-29% (proteasome) and approximately 40% (autophagic activity) in all models compared to their vehicle (DMSO)-treated counterparts (**Fig. 5.5A & B**).

We next assessed whether this positive effect was also reflected in a milder oxidative stress phenotype. In all cellular models, basal ROS levels decreased significantly as compared to vehicle-treated (DMSO) counterparts. A reduction of 14% was observed in LMNAkd cells and of 17% in ZMPSTE24kd cells. The latter essentially fell back to the same level as the vehicle-treated NTkd control cells. SFN treatment of NTkd cells and NHDF-WT cells also significantly reduced basal intracellular ROS levels (**Fig. 5.5C**).

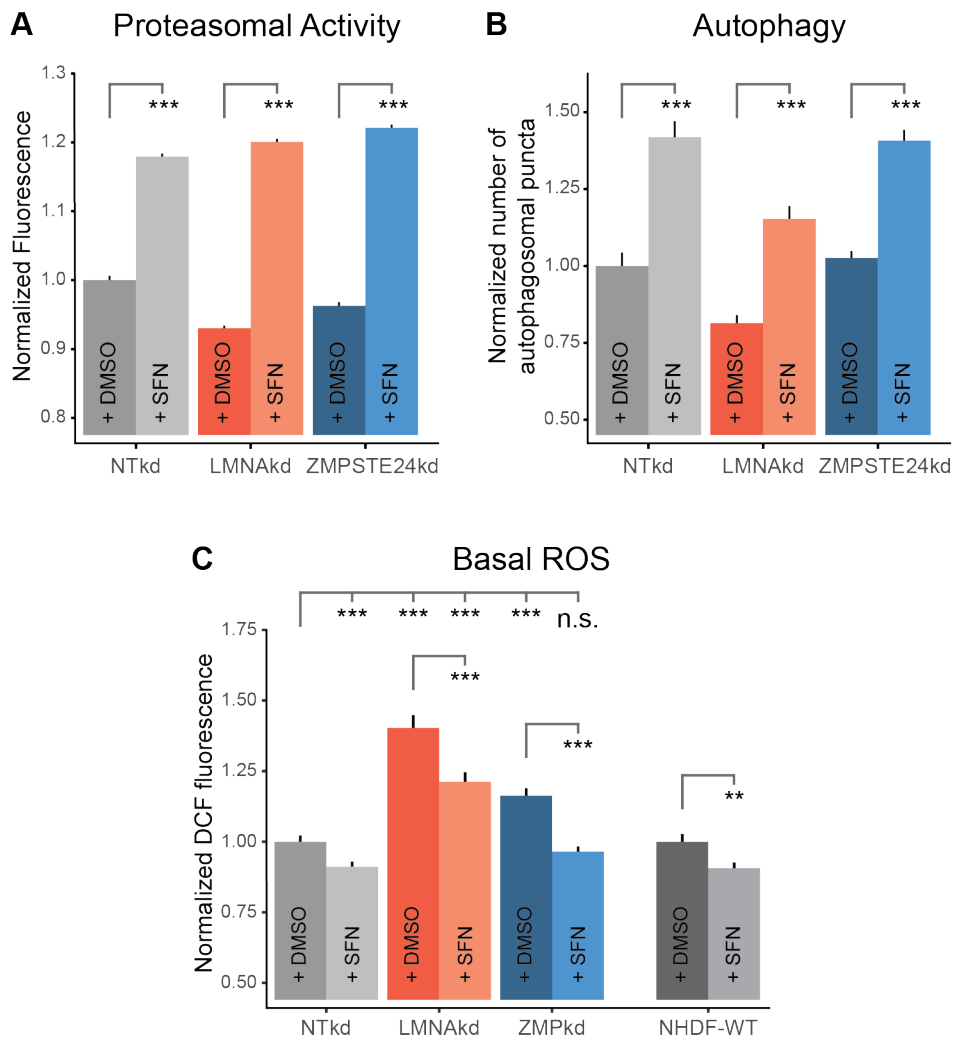


Figure 5.5: Protein degradation activity and basal intracellular ROS levels upon treatment with sulforaphane

(A) Normalized 20S proteasomal activity in LMNAkd, ZMPSTE24kd and NTkd cells upon treatment with 5 μ M SFN or vehicle (DMSO) for 24h, as measured by fluorescence microscopy. (B) Normalized number of autophagic puncta in LMNAkd, ZMPSTE24kd and NTkd cells upon treatment with 5 μ M SFN or vehicle (DMSO) for 24h, as measured by fluorescence microscopy. (C) Normalized basal ROS levels in LMNAkd, ZMPSTE24kd and NTkd cells upon treatment with 5 μ M SFN or vehicle (DMSO) for 24h, as measured by fluorescence microscopy. (* = p-value < 0,05; ** = p-value < 0,01; *** = p-value < 0,001; error bars represent standard error)

2.5 Sulforaphane does not restore mitochondrial membrane potential

The oxidative stress that follows proteasome inhibition has previously been attributed to mitochondrial dysfunction.²⁶⁹ To quantify this dysfunction in LMNAkd and ZMPSTE24kd cells we quantified the mitochondrial membrane potential ($\Delta\psi_m$, measured as average mitochondrial intensity of the TMRM channel), and the average size (projected mitochondrial area) of individual mitochondria using high-content microscopy.

At 264 h, both LMNAkd and ZMPSTE24kd cells exhibited increased $\Delta\psi_m$ and a more fragmented mitochondrial phenotype compared to NTkd cells (Fig. 5.6).

Next, we evaluated whether SFN could also mitigate these effects. SFN treatment led to a recovery of mitochondrial size in LMNAkd cell compared to NTkd. In ZMPSTE24kd cells, the increase was smaller, but still significant when compared to vehicle treated control cells (**Fig. 5.6B**). However, SFN treatment did not lower $\Delta\psi_m$ back to control (NTkd) levels in LMNAkd or ZMPSTE24kd cells. In LMNAkd cells, it even induced an increase in $\Delta\psi_m$ (**Fig. 5.6A**). Taken together, SFN could only partially alleviate mitochondrial dysfunction upon lamin A depletion or PLA accumulation.

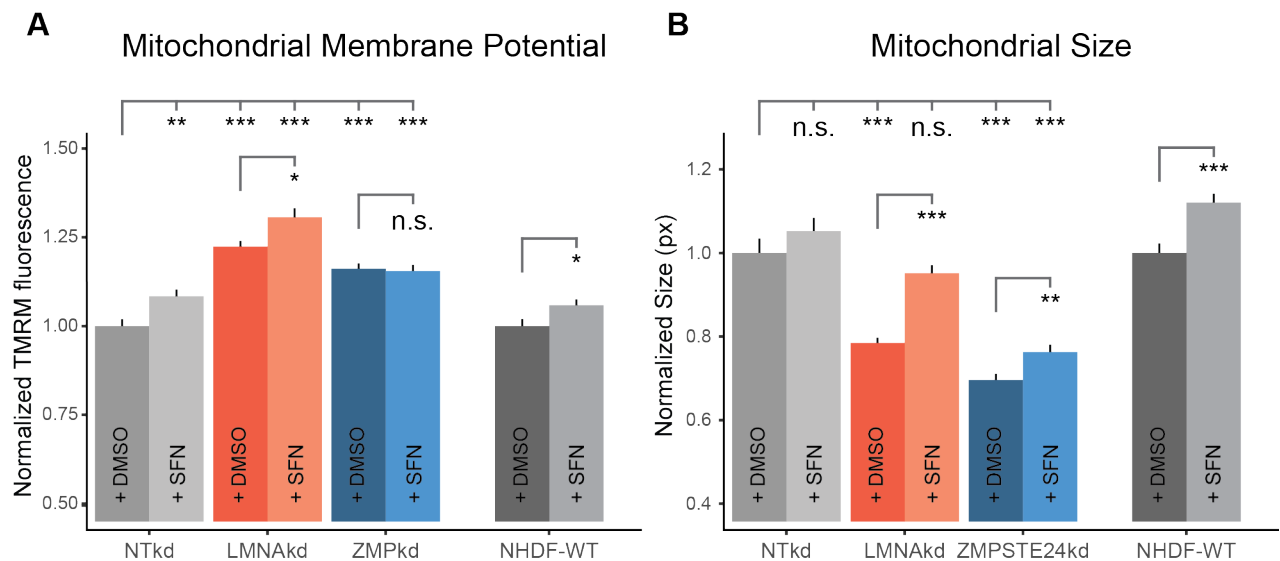


Figure 5.6: Mitochondrial function.

(A) Normalized $\Delta\psi_m$ in LMNAkd, ZMPSTE24kd and NTkd cells upon treatment with 5 μ M SFN or vehicle (DMSO) for 24h, as measured by fluorescence microscopy using the intensity of the TMRM signal. (B) Normalized mitochondrial size in LMNAkd, ZMPSTE24kd and NTkd cells upon treatment with 5 μ M SFN or vehicle (DMSO) for 24h, as measured by fluorescence microscopy using the projected area of the TMRM signal. (* = p-value < 0,05; ** = p-value < 0,01; *** = p-value < 0,001; error bars represent standard error).

3 Discussion

Many laminopathies are characterized by increased oxidative stress at a cellular level.^{1,60,130,131,133,203,264} The underlying causal mechanisms however still remain largely undetermined. Previous results showed that both lamin A depletion and PLA accumulation are correlated with increased intracellular ROS levels, but that they induce different cell fates.²⁰³ Reduction of lamin A was correlated with increased apoptosis, while PLA accumulation triggered a senescence pathway.

With this work, we set out to further elucidate the differential effects of lamin A/C depletion versus the accumulation of farnesylated prelamin A on the intracellular redox status of the cell. In line with previous results²⁰³, we found an upregulation of intracellular ROS levels after long-term (sustained) perturbation of lamin A/C metabolism (Lamin A/C depletion or PLA accumulation). However, we now also investigated this connection at higher resolution, *i.e.*, at the individual cell level. In doing so, we discovered a marked difference in the way lamin A/C and prelamin A

levels correlate with intracellular ROS levels. Whereas the intracellular ROS concentration scales linearly with PLA levels, the inverse correlation is far less obvious for lamin A/C. In fact, it appears that ROS levels remain rather constant within a fairly large window of lamin A/C abundance (at least factor 2), and only significantly increase, when lamin A/C levels fall below a critical threshold (>4-fold decrease). This threshold effect was even more pronounced for induced ROS, suggesting that only cells that virtually lack A-type lamins become hypersensitive to ROS. This might be due to the lowered ROS buffering capacity of A-type lamins. Through the oxidation of their cysteine residues they can act as a sink for ROS, protecting other more valuable components of the nucleus¹³², much like actin in the cytoplasm.¹⁵¹ The depletion of lamin A reduces this buffer capacity and subsequently renders the cell and nucleus more sensitive to induced ROS. A slight decrease, similar to haploinsufficiency, still leaves enough buffer capacity to cope with normal cellular redox homeostasis, but when the capacity declines below a certain threshold, the cell can no longer maintain a stable basal ROS level and becomes very sensitive to induced ROS, which in turn leads to an abrupt and acute escalation of oxidative stress. However, not all cells with a < 4-fold decrease in A-type lamins display higher ROS levels. A possible explanation is that the decrease of lamin A/C does not directly cause increased ROS production, but rather renders the cell more vulnerable when it does happen. Time might be a key-factor in this case, the longer the cell goes without A-type lamins, the higher the probability of experiencing acute oxidative stress.

In contrast to the threshold effect observed in lamin A/C depleted cells, modest PLA accumulation (up to 4-fold) on the other hand resulted in a gradual increase of basal ROS with increasing PLA concentration. This observation implies that a different mechanism is at work here. It is also worth noting that 144h after the first knockdown, basal ROS levels were lower and showed a non-significant, but visible decrease in sensitivity to induced ROS. Later, at 264h and after 3 successive knockdowns, this effect was no longer visible. This might reflect a time-dependent effect, as PLA accumulation could initially increase the ROS buffering capacity, before other, slower effects, still result in oxidative stress. A viable candidate here is protein degradation. Accumulation of PLA itself, or PLA-induced mislocalization of other NE protein (e.g. emerin), could induce a proteasomal overload. The resulting build-up of protein aggregates can in turn perturb normal mitochondrial function and causes oxidative stress.^{269,299}

Decreased protein degradation has already been measured in HGPS patient fibroblasts.^{133,215} We measured proteasome function at 264h after the initial knockdown, and indeed observed a decrease of proteasomal activity upon PLA accumulation. Interestingly, also lamin A depletion decreased proteasomal activity. Autophagy, an alternative protein degradation pathway, has been observed to compensate when the proteasome is dysfunctional.^{295,296} We therefore also quantified autophagic activity, by measuring the number of autophagosomal puncta per cell. We found that autophagy was not compensating for the decreased proteasomal activity, in contrast, its activity was even reduced in LMNAkd cells,

while no effect was measured in ZMPSTE24kd cells. These data confirm that intracellular protein degradation pathways are perturbed upon perturbation of A-type lamin metabolism, with most pronounced effects observed upon lamin A/C depletion. The observation that autophagy was differentially affected between lamin A/C depletion and PLA accumulation might add to the difference in oxidative stress level. Besides the abrogated ROS buffer, LMNAkd cells also experience a higher degree of inhibition of protein degradation, which in turn results in more acute mitochondrial dysfunction and ROS generation. It must be stated however, that reduced autophagy has been observed in HGPS patient cells²¹⁵, which accumulate progerin, a PLA variant. This does not correspond with our observations, but this might again be a time-dependent effect, long-term PLA accumulation might still result in reduced autophagy.

To see whether reduced protein degradation was correlated with mitochondrial dysfunction, we measured mitochondrial membrane potential ($\Delta\psi_m$) and average mitochondrial size to assess mitochondrial status. At 264h, both lamin A depletion and PLA accumulation resulted in increased $\Delta\psi_m$ and a more fragmented mitochondrial phenotype compared to NTkd cells, both of which are correlated with mitochondrial dysfunction and increased ROS production.^{2,121,126,127} This suggests that the measured oxidative stress upon lamin A/C depletion and PLA accumulation might indeed originate from increased mitochondrial ROS production that is caused by decreased protein degradation.

In an effort to normalize protein degradation and subsequently restore ROS balance, a treatment with sulforaphane was performed. Sulforaphane is an antioxidant derived from cruciferous vegetables that is known to enhance both proteasome activity and autophagy.^{297,298} It has already proven its potential to ameliorate HGPS phenotypes on a cellular level²¹⁵, and has been or is currently involved in more than 30 clinical trials for treatment of diverse diseases including sickle cell disease, prostate cancer, obstructive pulmonary disease and type-2 diabetes.³⁰⁰⁻³⁰³

After 24h of treatment, all models showed a significant increase in proteasomal and autophagic activity compared to their vehicle (DMSO) treated counterparts, which was accompanied by a decrease in basal ROS levels. In ZMPkd cells this decrease brought the basal ROS levels back to the same level as NTkd cells. In LMNAkd cells, the decrease was significant, but did not result in complete normalization of basal ROS. These results are in accordance with previous observations where enhancement of protein degradation with rapamycin, another inducer of protein degradation, more specific of autophagy, resulted in improvement of the HGPS phenotype.^{293,304-306} Mitochondria also partly recovered after SFN treatment, their size increased again, which indicates lower fragmentation, but $\Delta\psi_m$ remained high and increased even further in LMNAkd cells. This might be due to the short duration of the treatment (24 h), or it can be a dosage effect, but it can also mean that there are still other (non-exclusive) processes involved. For instance, lamins also interact with a multitude of redox-responsive transcription factors including Ankrd2, Oct1 and NRF2.^{141,155,156} Disturbed interaction or mislocalization of these can also lead to

oxidative stress, bypassing protein degradation. Indeed NRF2, a transcription factor that activates multiple antioxidant and cytoprotective genes through binding to antioxidant-responsive elements (ARE) motifs in their promoters¹⁰⁸, was found to be mislocalized to the nuclear lamina in HGPS patient cells.¹⁵⁶

Taken together, our results point to distinct differences in the effects of lamin A/C depletion and PLA accumulation on the cellular redox status, but also strengthen the hypothesis that perturbed protein degradation is a common factor correlated with increased oxidative stress and mitochondrial dysfunction, and that SFN possesses valuable pharmacological properties to (partially) alleviate these symptoms.

4 Materials and Methods

4.1 Cell culture

Normal human dermal fibroblasts (NHDF, *LMNA*^{+/+}, Promocell, C-12300) were cultured in T25 or T75 culture flasks in DMEM High Glucose with L-Glutamine medium (Lonza, BE12-604F) supplemented with 10% fetal bovine serum (Gibco, 10500-064) and 1% penicillin/streptomycin (Lonza, DE17-602E/12), at 37°C and 5% CO₂, according to standard procedures. All experiments were performed with passage matched cells in between passage 9 and 16.

4.2 siRNA-mediated knockdown

Expression of *ZMPSTE24* and *LMNA* was silenced with siGENOME Lamin A/C siRNA (Thermo Scientific, D-001050-01-20) and siGENOME Human ZMPSTE24 siRNA (Thermo Scientific, M-006104-02-0020), respectively. Stealth RNAi siRNA Negative Control, Med GC (Life Technologies, 12935-300) was used as a negative non-targeting control (NT). siRNA transfections were performed according to the manufacturer's instructions using Lipofectamine® RNAi-MAX Transfection Reagent (9,6 µL for 1 T25 culture flask) (life technologies, 13778-075), and 10 nM of total siRNA, following the scheme outlined in **Figure 5.7**.

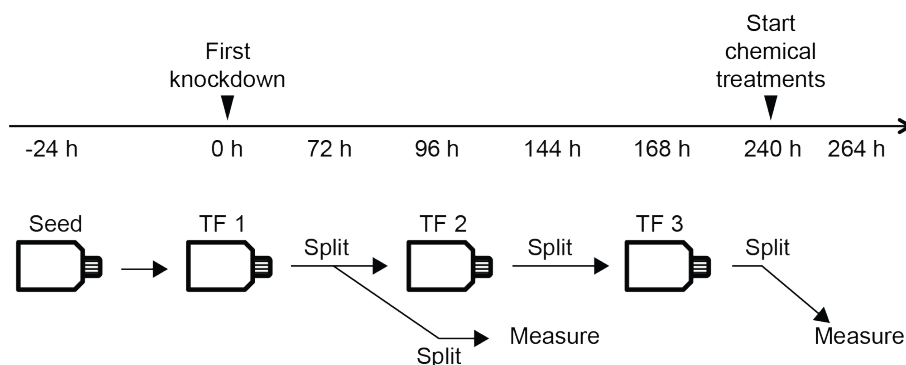


Figure 5.7: Experimental design.

Scheme of the sustained siRNA-mediated knockdown by repetitive transfections (TFs), and timing of the subsequent experiments.

4.3 Chemical treatments

Proteasome inhibitor MG132 (Santa Cruz – SC-201270) was used as a positive control in the proteasomal activity assay at a concentration of 2 μ M for 24h. Autophagy enhancer rapamycin (part of the CYTO-ID[®] autophagy detection kit (Enzo - ENZ-51031-0050)) was used as a positive control in the autophagy activity assay at a concentration of 2 μ M for 24h. DL-Sulforaphane (Sigma-Aldrich - 4478-93-7) was used at 5 μ M for 24h. When chemical treatments were combined with knockdowns, the treatments were always initiated 24h before measurement (**Fig 5.7**).

4.4 High content live cell imaging of intracellular ROS complemented with immunofluorescence staining.

Intracellular ROS was measured using the fluorescent cell-permeable probe 5-(and-6)-chloromethyl-2',7'-dichlorodihydrofluorescein diacetate (CM-H₂DCFDA) (Life Technologies, C6827). Measurements were done 144 h and 264 h after initiation of the knockdown (**Fig. 5.7**), and according to a previously described workflow (**cf. Chapter 3**). Briefly, 24 h before measurement, cells were seeded in black glass bottom 96-well plates (Brooks, Matrical Labware - MGB096-1-2-L-G-L) at 10000 cells per well. Right before measurement they were washed in HBSS + Hepes (HH) (pH 7.2), incubated for 25 minutes in the dark at room temperature in HH-buffer containing 2 μ M CM-H₂DCFDA, washed again in HH-buffer and then automatically imaged (also in HH-buffer) on a Nikon Ti Eclipse inverted widefield fluorescence microscope with a Nikkor 20x air Plan Apo objective (NA 0.75) using a 480/40 nm excitation, 520/35 nm emission filter combination for the CM-H₂DCFDA signal. 9 images were acquired on predefined and saved locations in each well. After the complete plate was imaged, 20 μ M *tert*-butyl peroxide (TBHP; Sigma-Aldrich, 458139-100mL) was added to all wells and after a 3-minute interval the acquisition was repeated to measure induced ROS. Subsequently the cells were fixed in the 96-well plates using 4% paraformaldehyde for 15 minutes at room temperature and washed (3x, 5 minutes) with PBS, followed by permeabilization with 0.5% Triton X-100 (5 minutes) and blocking with 50% fetal bovine serum (FBS). Cells were then incubated with primary antibody diluted in 50% FBS for 60 minutes. After minimally 3 PBS wash steps, cells were incubated with secondary antibody diluted in 50% FBS for 30 minutes, washed again, and then incubated with 1 μ g/mL 4',6- diamino-2-phenylindole (DAPI) diluted in PBS. Primary antibodies were directed against lamin A (Abcam, ab26300) and prelamin A (Santa Cruz Biotechnology Inc., SC-6214). As secondary antibodies, we used Cy3-conjugated donkey anti-rabbit (Jackson ImmunoResearch Laboratories Inc., 711-166-152), and Cy5-conjugated donkey anti-goat (Jackson ImmunoResearch Laboratories Inc., 705-175-147). Immunofluorescent stained cells were visualized using the same microscopic setup as the ROS measurement, using the saved locations to reacquire the same cells. All experiments were performed with at least 10 replicates per treatment per plate (depending on the experiment), on at least 3 different plates.

4.5 Proteasomal activity measurement

To measure proteasomal activity, we used the fluorimetric Proteasome 20S Activity Assay Kit (Abcam - ab112154). This assay measures the chymotrypsin-like protease activity associated with the proteasome complex in cultured cells. It uses LLVY-R110 as a fluorogenic indicator for proteasome activities. Cleavage of LLVY-R110 by the proteasome generates strongly green fluorescent R110 that is monitored fluorometrically at 520-530 nm with excitation at 480-500 nm. We extended the assay by also adding Hoechst 33342 (10 mg/mL; Thermo Fisher Scientific – H3570) to allow for normalization for cell density. Cells were seeded in black glass bottom 96-well plates (Brooks, Matrical Labware - MGB096-1-2-L-G-L) at a density of 8000 - 10000 cells per well and left to attach overnight. After 24 h, medium was discarded and 100 μ L of fresh medium or medium containing a chemical treatment was added to each well. At 41 h, 100 μ L proteasome assay solution, supplemented with 1/2000 Hoechst stock solution, was added to all wells followed by an incubation of 3 h at 37°C and 5% CO₂. Then fluorescence was measured using a Tecan Infinite 200 with excitation/emission set at 490/525 nm for GFP and 340/480 nm for Hoechst.

4.6 Autophagy measurement

The autophagic vacuoles in treated and mock-treated fibroblasts were quantified using the CYTO-ID[®] autophagy detection kit (Enzo - ENZ-51031-0050), according to the manufacturers instructions. Cells were prepared similar as for the proteasome activity assay. Cells were seeded in black glass bottom 96-well plates (Brooks, Matrical Labware - MGB096-1-2-L-G-L) at a density of 8000 - 10000 cells per well and left to attach overnight. After 24 h, medium was replenished and chemical treatments were initiated. At 43 h, cells were washed with 1x assay buffer and loaded for 30 minutes with dual color detection solution containing CYTO-ID green detection reagent and Hoechst 33342. Cells were then washed again, twice, with 1x assay buffer and fixed with 4% paraformaldehyde for 20 minutes followed by a final washing step and image acquisition on a Nikon Ti Eclipse inverted widefield fluorescence microscope with a Nikkor 40x air Plan Apo objective (NA 0.95)

4.7 Image analysis

All image processing was performed in FIJI (<http://fiji.sc>), a packaged version of ImageJ freeware (W.S. Rasband, U.S.A. National Institutes of Health, Bethesda, Maryland, USA, <http://rsb.info.nih.gov/ij/>, 1997–2014). For the quantification of lamin A, PLA and ROS levels in the same cells, data from multiple images from different time points had to be combined. Due to imperfect steering of the microscope stage, XY positions could not be perfectly regenerated in the 3 imaging rounds (before addition of TBHP, after addition of TBHP, and after IF staining). This resulted in slight XY-shifted images compared to each other. To allow registration, the DCF-signal was also acquired after IF staining. The resulting image could not be used for quantification, but the signal was high enough to allow registration based on this channel. We used The 'Linear Stack Alignment with SIFT' plugin, which is a

lightweight SIFT-implementation for Java after the paper of David Lowe³⁰⁷, to calculate and perform a translation-based registration. A before and after example is shown in **Figure 5.8**.

Linear Stack Alignment with SIFT

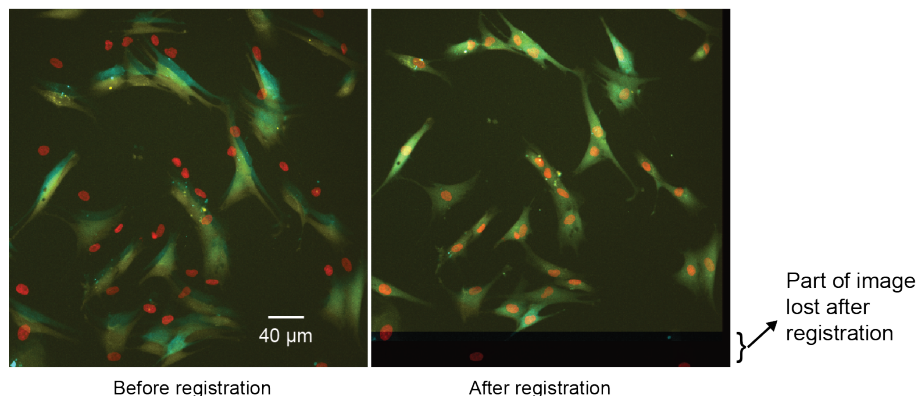


Figure 5.8: Representative example of unregistered versus registered images of the different parameters.

After registration, the DAPI channel was used to determine the locations of all individual nuclei and to create a region of interest (ROI) for each one. These ROIs were subsequently used to measure lamin A, PLA and ROS levels in their respective channels.

As measure for autophagy, we calculated the number of autophagosomal puncta per cell. These fluorescent foci were quantified by means of a custom-designed image processing pipeline, which is essentially based on a high-content analysis workflow described before and is available upon request.²⁷ In brief, the analysis consists of a few image pre-processing steps, followed by hierarchical segmentation of nuclei, cells, and spots to allow region-specific analysis of objects. Nuclear regions of interest (ROIs) are segmented in the DAPI channel after filtering with a Gaussian kernel of small radius ($\sigma=3$), automatic thresholding according to Otsu's algorithm and watershed-based separation. Cellular boundaries are then delineated by conditional region growing from the nuclear seeds restricted by a Voronoi tessellation. Finally, spots are specifically enhanced in the Cyto-ID channel by means of a Laplacian operator and binarized using an experimentally determined fixed threshold. The resulting image is then used to calculate the number of objects larger than a predefined size (>3 pixels).

4.8 Statistical analyses

Data analysis and visualization was performed in R statistical freeware (<http://www.r-project.org>). Standard statistical methods were employed, including the Shapiro-Wilk Normality Test to assess normality of the data, Levene's test to assess homoscedasticity, student's t-test, ANOVA and the Kruskal-Wallis rank sum test to assess differences between the group means and Tukey (after ANOVA) and Dunnett type (After Kruskal-Wallis) post-hoc tests to assess significance for each

group. When criteria for normality or homoscedasticity were not met, non-parametric multivariate tests from the nparcomp package were used.²³⁹ If only 2 treatments are compared two sample tests for the nonparametric Behrens-Fisher problem are performed. For more than 2 treatments, a non-parametric contrast-based multiple comparison test is used. Significance levels were indicated as follows: $p < 0.05$ (*), $p < 0.01$ (**), and $p < 0.001$ (***). For graphics and annotation, the R program was expanded with the ggplot2 package.²⁴⁰

VI

GENERAL DISCUSSION

Laminopathies display a broad range of phenotypes, from tissue specific disorders affecting striated muscle or fat tissue, to systemic diseases, such as restrictive dermopathy (RD) or the Hutchinson-Gilford Progeria Syndrome (HGPS).^{3,12} This diversity is underlined by the fact that mutations in the *LMNA* gene are linked to more diseases than any other human gene.⁴¹ Despite this diversity, many laminopathies share several features at the cellular level, including nuclear shape aberrations, heterochromatin disorganization and increased oxidative stress.^{1,7} This doctoral project aimed at exposing cellular mechanisms linking the nuclear lamina to oxidative stress and more specifically whether there are distinct pathways differentiating between loss-of-function and gain-of-function laminopathy variants.

1 Sustained siRNA-mediated knockdowns of *LMNA* and *ZMPSTE24* recapitulate the hallmarks of their patient-cell counterparts

First we had to decide which experimental models to use. Mouse models (*Mus musculus*) have been widely used to study laminopathies^{41,308}, but they are not easy to generate and require fairly high maintenance. Also, these models aren't well suited for observation of embryos or other developmental stages, nor are they compatible with many cellular assays. Models in *Caenorhabditis elegans* (nematode)³⁰⁹, or *Danio rerio* (zebrafish)³¹⁰ can counter some of these problems. Both are cheaper to create than mouse models. They also have shorter lifespans, require lower maintenance, permit easy monitoring of developmental stages and allow microscopic interrogation, thus subcellular observation. These advantages permit their use in larger-scale genetic and therapeutic screening.^{311,312} However, the usefulness of animal models in general is up for debate following contradicting reports of irreproducible results and poor recapitulation of human conditions.^{313,314} Furthermore, fundamental research into underlying intracellular disease mechanisms requires many samples to obtain statistically sound results, greatly increasing the cost of experiments. To circumvent the complexity and cost of animal models, and to enhance biological readouts, but retain physiological relevance, primary patient fibroblasts are widely used as cellular model for different laminopathies.^{60,139,203,215,216} Still, there remain some drawbacks associated with their use. First, all laminopathies are considered to be orphan diseases, with very low incidences. This makes patient material scarce. Second, and more importantly, there is an inherent genetic heterogeneity between cells from different patients that may complicate biological interpretation. A simple solution to this problem is the use of *in vitro* created model cells. Healthy (primary) cells are modified so as to resemble patient cells as faithfully as possible. This approach guarantees unlimited access to pseudo-pathological cells and at the same time rules out a huge part of the inter-patient variability because both control cells and treated cells originate from the same progenitor cells. A major advantage of this approach is the added statistical power to measure small differences between treatment and control. A

drawback is that, because of the isogenic context, random differences between biological samples can become statistically significant, while still being irrelevant in the pathological context. To counter this, multiple biological replicates should always be used when creating *in vitro* model cells. Also, to obtain a reliable *in vitro* model, a causal understanding of the disease is necessary to select a treatment that yields physiologically relevant cells. In this PhD, we focused on 2 major genetic causes of laminopathies, namely mutations that lead to a knockout of the *LMNA* gene, or loss-of-function mutations, which are mostly associated with striated muscle laminopathies³, and mutations that interfere with the maturation process of lamin A, resulting in accumulation of prelamin A (PLA) variants, or toxic gain-of-function mutations, like progerin in HGPS, or farnesylated PLA in RD.^{58,134}

In **Chapter 2** we compared various chemical, as well as genetic interventions that result in the complete depletion of A-type lamins, or the accumulation of PLA variants. The chemical treatments (AFCMe, SQV and FTI) were applied in (primary) normal human dermal fibroblasts (NHDF) and were used to block the maturation of PLA at a specific point, inducing accumulation of both farnesylated and non-farnesylated PLA. However, the efficiency was variable and we also observed several side effects, such as the formation of donut-shaped nuclei (after treatment with farnesyl transferase 276), or nuclear shrinkage and rounding (saquinavir). In addition, the model cells resulting from these treatments mostly lacked the nuclear dysmorphism that is expected upon PLA accumulation. Thus, chemical intervention did not result in the creation of faithful model cells, due to confounding side-effects.

The genetic interventions offered more specificity. On the one hand we optimized a regimen of multiple successive transfections with siRNA targeting the *LMNA* gene or the *ZMPSTE24* gene, to induce sustained lamin A/C depletion and accumulation of farnesylated PLA, respectively, in NHDF. On the other hand we applied CRISPR/Cas9 genome editing to knock out *LMNA* or *ZMPSTE24* completely in HT1080 fibrosarcoma cells. The sustained knockdown approach can be applied in primary cell cultures to transiently interfere with lamin A/C metabolism, while CRISPR/Cas9-mediated knockout allows for more permanent interventions. With regard to A-type lamin depletion, both approaches gave rise to model cells displaying a nuclear morphology bearing all the hallmarks of *LMNA* deficient cells.^{139,222} With regard to accumulation, both approaches also resulted in model cells representative of PLA accumulating patient cells, showing increased nuclear dysmorphism and increased intranuclear lamin structures, but the observed phenotype was much more pronounced in the knockdown cells. A possible explanation for this difference might be that the knockout cells went through selection and clonal expansion before analysis, which takes a long time and possibly allows the cells to adapt to the accumulation of PLA. The difference might also be cell type related, as the knockdowns were introduced in NHDF, and the knockouts in HT1080. Application of the sustained knockdown procedure in the HT1080 cells would allow answering this last question.

Since both knockdown models recapitulated the intended hallmarks of the laminopathies under investigation, and because they were generated in primary

fibroblast, which correspond to often-used patient cells, we chose to use these models in the experiments described in this PhD. Nevertheless, still other cell models can be used. The development of induced pluripotent stem cell (iPSC) technology³¹⁵ together with recent advances in genome editing technology, especially CRISPR/Cas9³¹⁶, are propelling development of many new approaches to create reliable model cells. Somatic fibroblasts from a patient can be reprogrammed to pluripotent stem cells through the transient expression of 4 transcription factors (Oct4, Sox2, Klf4 and c-Myc).³¹⁵ These patient-iPSCs are diploid, karyotypically normal and can be differentiated into many different cell types, which makes them highly relevant for disease modelling and high-content drug screening. This is especially the case for laminopathies where some mutations affect specific tissues while others induce system-wide symptoms, the possible reason for which might be situated at the stem cell level.⁵⁶ Several such iPSC-models have already been created and applied in the laminopathy field.^{317,318} Besides knocking out a gene, as we did for *LMNA* and *ZMPSTE24* in HT1080 cells CRISPR/Cas9 genome editing also enables the introduction of specific disease causing single nucleotide polymorphisms (SNPs). When combined with the patient derived iPSCs, genome editing can be used to correct the disease causing mutation, creating isogenic control cells.^{319,320} *Vice versa*, iPSCs from a healthy person can also be modified so as to introduce the specific disease causing mutations at the exact same genomic sites as they occur in real patient cells. This allows faithful expression of mutant proteins, such as progerin, at precise stoichiometric levels, without access to real patient cells. In other words, cells would be created that are, on a genetic level, perfect copies of real patient cells. Isogenic iPSCs pairs possibility to differentiate these cells into various tissues. These isogenic cell lines allow thorough assessment of causal mutations and molecular and cellular disease causing mechanisms, but can also be used in high throughput pharmacological screens to discover novel therapeutic agents and develop novel therapeutic strategies.³²¹

As a sidenote, besides the knockdown-models that were used in Chapters 4 & 5, the knockout-models we developed in HT1080 cells are currently also being used by other groups, illustrating the significance of this work.

2 High-throughput microscopy offers insight in cellular redox biology with deep coverage

Since mitochondria represent an important intracellular source of reactive oxygen species, especially under pathological conditions⁸⁰, we wanted to study both redox status and mitochondrial function in our model cells. We selected mitochondrial membrane potential ($\Delta\psi_m$) and morphology as a functional readout of mitochondrial health, and wanted to be able to measure those together with the intracellular ROS level. We therefore developed a novel high-content fluorescence microscopy method that allows simultaneous quantification of the aforementioned parameters in

living cells (**Chapter 3**). We chose CM-H₂DCFDA as fluorescent dye for ROS and TMRM to measure both $\Delta\psi_m$ and mitochondrial morphology. A major advantage is that an unambiguous determination of both factors together in space and time allows pinpointing causal relationships. For instance by including compounds that promote or reduce mitochondrial function (influence on electron transport chain) or dynamics (fusion/fission), one could now directly assess the impact on intracellular ROS levels and vice versa. Another advantage of the method lies in its generic character in a sense that virtually any combination of spectrally compatible fluorescent probes for ROS and mitochondria can be used. This was demonstrated by using the Calcein/MitoSOX combination to specifically measure mitochondrial ROS. It is becoming increasingly clear that, besides the general cell-wide effects of ROS, fast, transient, and highly localized production of low doses of specific intracellular ROS species plays an important role in cellular signal transduction and mitochondrial morphofunction. To be able to measure these, targetable ROS probes with fast equilibration kinetics are necessary. It is in this field that great progress is conceivable. As yet, not many such sensors exist. HyPer¹⁹⁶ and (Orp1)roGFP2¹⁹¹ would be good candidates, but their kinetics would still have to be improved to be able to really measure quick transient changes. *In extensu*, the workflow is easily amenable to the analysis of other organelles (e.g., the ER) or processes (e.g., calcium homeostasis), by selecting other fluorescent markers. In **Chapter 5**, we extended the assay with a *post hoc* immunostaining. Since the exact imaging locations are saved, redox analyses could be directly correlated with location proteomics in the same cells, greatly increasing the molecular readout of the experiment.

The method was originally conceived specifically for the analysis of NHDF, which are large and have a very flat morphology^{174,255}, but it should be readily applicable to many other adherent cell types. Three other groups are already successfully using the assay on HeLa, HT1080, HT29, CCD841, several endodermal cell lines, human dental pulp stem cells and rat thyrocytes. Application of the assay to suspension cells is less obvious due to difficulties with mounting and observing such cells in a physiological manner. They can be cytopun on a coverslip or cultured in serum-free media to induce adhesion, but both of these processes interfere with physiological conditions.^{322,323} However, these limitations could be overcome using micro-patterned cell culture supports that keep individual cells (adherent or non-adherent) trapped in small micro wells while maintaining their viability³²⁴, or by the use of a thermo-reversible hydrogel to trap cells during imaging.³²⁵ These methods have already been used for high-content screening of plasma membrane potential, or cellular oxygen in individual suspension cells^{326,327} or the imaging of intracellular markers in the living, highly motile kinetoplastid parasites.³²⁵ In a similar approach, by the use of miniaturized biocompatible transparent cell-containing hydrogel droplets printed on glass slides or plastic chips (e.g. by microarray spotters), the method can also be expanded to the screening of 3D cell cultures.^{328,329} For both extensions (suspension cells and 3D cell cultures), adaptations would also have to be made to the imaging modality, since morphological analysis of the mitochondrial

network in these cells would require rapid 3D-acquisition capabilities such as spinning disk confocal or Bessel beam light sheet microscopy^{330,331}, as well as to the analysis pipeline, to include the Z-dimension while calculating morphological parameters.³³² Transcending the level of cell-based assays, the method has already been adapted to cater for measurements of redox metabolism and mitochondrial morphology or density in *C. elegans*.³³³⁻³³⁵

We optimized a medium- to high-throughput workflow for 96-well plates. This results in large image datasets that require a big time-investment for their analysis. To alleviate this burden, we have conceived a dedicated ImageJ script (RedoxMetrics.ijm) for the automated extraction of intracellular and mitochondrial signals and morphological characteristics based on the acquired images. We also created a complementary and interactive automated data analysis pipeline (RedoxMetrics.app) using the Shiny web application framework for R (<https://shiny.rstudio.com>). While being measured simultaneously, processing and analysis of the redox and mitochondrial parameters are usually done separately to gain unbiased insight into the fundamental underlying processes. However, integration of all the information using data mining techniques allows the calculation of more sensitive fingerprints. In line with this, we have shown that both chemically (SQV) treated cells and laminopathy patient cells could become effectively discriminated using a combination of 5 different metrics. Such a redox fingerprint may become a valuable tool for classification of cells from different pathological conditions or could lead to novel cell-based screening methods for diagnostic purposes. It has been shown that the combination of multiple morphological parameters of the mitochondrial network permits robust classification of different phenotypes using unsupervised and supervised data mining strategies.^{254,334} Indeed, hierarchical clustering has allowed for stratifying antiretroviral drug treatments based on mitochondrial morphology fingerprints.³³⁴ Likewise, learning methods (logistic regression and support vector machines learning) have been successfully used to discriminate between primary fibroblasts of a healthy individual and a Leigh syndrome patient and to identify potential therapeutic compounds based on their mitochondrial morphofunctional phenotype.²⁵⁴ These examples demonstrate the potential of integrated image-based redox profiling.

3 Lamins as mediators of oxidative stress

Using the optimized high-content method on sustained knockdown models (LMNAkd & ZMPSTE24kd in NHDF), we set out to explore the role of lamins in cellular redox biology (**Chapter 4 & 5**). We investigated the effect of lamin A/C depletion and accumulation of farnesylated PLA on the intracellular redox status and mitochondrial function. We found that both perturbations resulted in oxidative stress. And we could correlate this with increased mitochondrial dysfunction, as evidenced by a higher $\Delta\psi_m$, lower oxygen consumption rate and more fragmented phenotype compared to control cells. Interestingly, intracellular ROS levels rose much higher upon depletion of A-type lamins than upon accumulation of

farnesylated PLA. Furthermore, lamin A/C depletion also induced a hypersensitivity towards induced ROS as compared to control cells or ZMPSTE24kd cells. Together this clearly indicates that A-type lamins exert a ROS-buffering function. Indeed, lamins have been reported to be able to act as reducing agents through their oxidizable cysteine residues¹³², much alike actin in the cytosol.¹⁵¹ At a cellular level, moderate depletion of lamin A/C, similar to haploinsufficiency, still leaves enough buffer capacity to cope with normal cellular redox homeostasis, but when the capacity declines below a certain threshold, the cell can no longer maintain a stable basal ROS level and becomes very sensitive to induced ROS, which in turn can lead to an abrupt and acute escalation of oxidative stress. From our experiments, this threshold corresponds to an almost complete absence of lamin A/C. ZMPSTE24kd and subsequent accumulation of PLA is not expected to alter the ROS buffering function, but ZMPSTE24kd cells still display mitochondrial dysfunction and experience oxidative stress. Subsequently we investigated whether PLA accumulation might cause a decreased activity of the protein degradation pathways. Decreased protein degradation (both proteasomal as autophagic) had already been detected in HGPS patient cells.^{133,215} Misfolded or immature proteins are usually degraded by the proteasome. But when the amount of aberrant proteins becomes too high, saturation may occur, thereby inhibiting normal function.²⁹⁴ The resulting accumulation of non-degraded proteins can interfere with many cellular processes such as mitochondrial electron transport and can subsequently cause increased ROS production.²⁶⁹ From our experiments, we indeed found a reduced proteasomal activity in ZMPSTE24kd cells. We also found reduced proteasomal degradation and autophagy in LMNAkd cells. There have been reports of mislocalization and subsequent proteasomal degradation of nuclear envelope proteins (SUN2, Emerin and Nesprin-1), and of upregulation of various ubiquitin ligases in *LMNA* deficient cells^{271,272,292}, both of which might result in proteasomal overload. To assess whether reduced protein degradation is indeed a causal mechanism to oxidative stress, we subjected both ZMPSTE24kd and LMNAkd cells to a treatment with the plant-derived isothiocyanate sulforaphane (SFN), known to stimulate both proteasomal degradation and autophagy.²⁹⁷ This indeed resulted in a marked reduction of basal intracellular ROS levels, adding to the hypothesis that decreased protein degradation might lead to oxidative stress, but it did not completely normalize mitochondrial function. While mitochondrial fragmentation was partially reversed, $\Delta\psi_m$ remained high, and increased even further in LMNAkd cells, hinting at the involvement of other, non-exclusive, mechanisms. The nuclear lamina interacts with a multitude of redox-responsive proteins and transcription factors, including Ankr2, Oct1 and NRF2.^{141,155,156} A recent study indicates that the stress responsive protein Ankr2 translocates into the nucleus upon oxidative stress, where it interacts with lamin A and regulates expression of stress responsive genes. However, an EDMD2-lamin A mutant was found to bind and mislocalize Ankr2 in the nucleus even under basal conditions, disturbing proper function and increasing sensitivity towards oxidative stress.¹⁵⁵ A similar mechanism was reported for NRF2, a transcription factor that activates multiple antioxidant and cytoprotective genes

through binding to antioxidant-responsive elements (ARE) motifs in their promoters.¹⁰⁸ In HGPS, NRF2 is mislocalized to the nuclear lamina, reducing expression of its targets and leading to oxidative stress.¹⁵⁶ Among these targets is also NAD(P)H dehydrogenase, quinone 1 (NQO1), a protein important for maintaining mitochondrial integrity.³³⁶ We also measured expression of NQO1 in ZMPSTE24kd cells and found a slight but non-significant reduction (data not shown), presenting a possible proteasome independent link to mitochondrial dysfunction and subsequent oxidative stress in PLA accumulating cells. Large scale transcriptomics and proteomics screening experiments, focussed on mitochondrial genes and proteins would possibly shed more light on these mitochondrial connections.

Combining all results, we hypothesize the following tentative mechanism (**Fig 1.1**). Both lamin A depletion and PLA accumulation interfere with proteasomal function. The resulting buildup of non-degraded proteins results in mitochondrial perturbation and causes increased ROS production. LA depleted cells have a lower tolerance towards this additional ROS because of their diminished lamin A/C ROS-buffer, which eventually gives rise to acute oxidative stress and subsequent apoptosis. PLA accumulation on the other hand still has a nuclear ROS-buffer, yet mislocalization of redox-responsive transcription factors decrease other anti-oxidant systems and also affect mitochondria which eventually still results in oxidative stress, however the basal ROS levels remain lower than upon complete lamin A/C depletion, allowing cellular survival and/or induction of senescence.

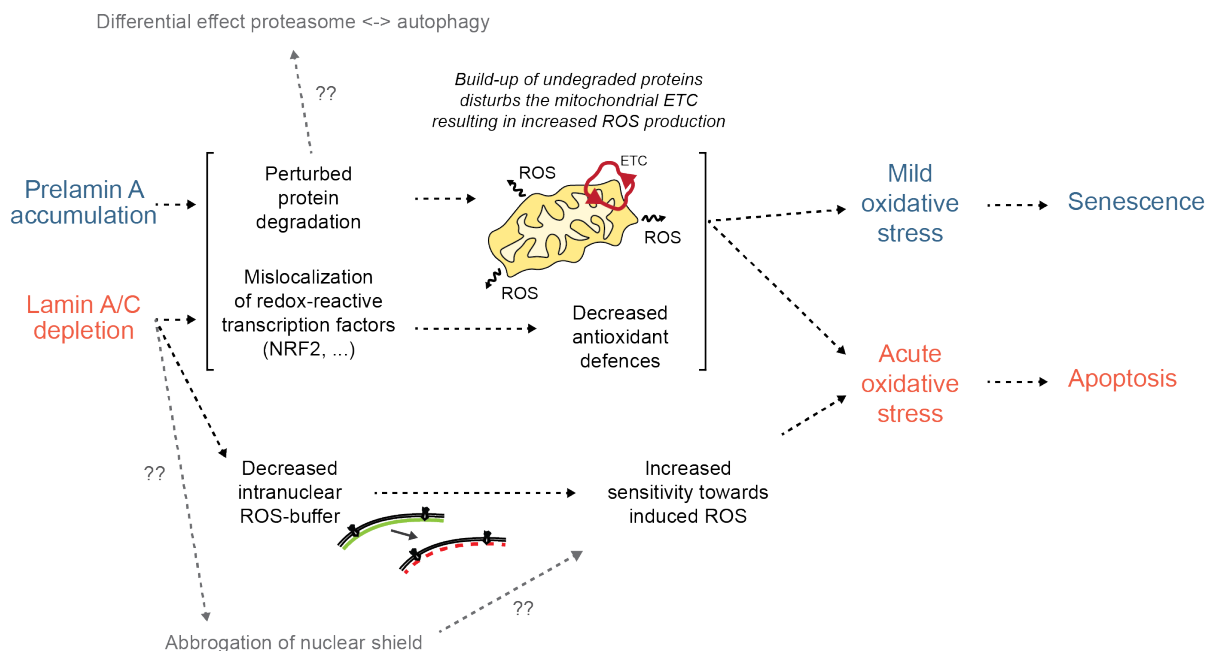


Figure 6.1: Tentative scheme displaying how lamin perturbations lead to oxidative stress and ultimately determine cell fate. Pending questions are represented by grey lines.

Several other mechanisms are likely to interfere with this pathway as well. While we did measure decreased proteasomal function in LMNAkd as well as ZMPSTE24kd

cells, lamin A/C depletion also significantly reduced autophagy while PLA accumulation had no effect. When both protein degradation pathways are impaired, the build-up of non-degraded proteins is likely quicker, adding to the severity of the oxidative stress observed in LMNAkd cells. Furthermore, besides direct ROS-buffering, the nuclear lamina also stabilizes the LINC complex that is thought to induce the formation of a perinuclear shield of protective enzymes, among which ROS defusing enzymes like CAT, GPX and GST.¹⁵⁸ Depletion of lamin A/C might also abrogate this shield, potentially leading to an even bigger overload of the protein degradation machinery. Thirdly, looking at the *modus operandi* of many redox-responsive transcription factors, which are activated upon oxidation in the cytoplasm, subsequently transfer to the nucleus where specific cysteine residues within the DNA-binding domain of each transcription factor have to be reduced before they can interact with their respective target promoter sequences¹⁰⁹, oxidants in the cytoplasm activate redox signalling, whereas oxidative stress in the nuclear compartment blocks this. Since lamin A/C depletion specifically reduced ROS-buffering capacity inside the nucleus, this might also contribute greatly to the observed acute oxidative stress in these cells. These still remain open questions that have to be addressed before a definitive model can be presented.

4 Main results and perspectives

1. Sustained knockdown of *LMNA* or *ZMPSTE24* recapitulates the cellular hallmarks of laminopathies.
2. Genome-editing holds promise for boosting physiological relevance of cell-based studies.
3. High-content microscopy allows establishing distinctive cellular redox signatures.
4. Multiplexing of markers and integration of advanced data mining will boost HCM performance beyond its original scope. This is evidenced by the adoption of the method by a group that works on the colon cancer and a group that works on space radiation.
5. Lamin A/C depletion and PLA accumulation differentially affect intracellular redox homeostasis.
6. Lamin A/C functions as an intranuclear ROS-buffer.
7. Perturbed lamin metabolism adversely affects proteasomal degradation pathways.
8. Sulforaphane rescues lamin-specific oxidative stress phenotypes and holds promise as potential therapeutic strategy

VII

BIBLIOGRAPHY

1. Sieprath, T., Darwiche, R. & De Vos, W. H. Lamins as mediators of oxidative stress. *Biochem. Biophys. Res. Commun.* **421**, 635–639 (2012).
2. Sieprath, T., Corne, T. D. J., Willems, P. H. G. M., Koopman, W. J. H. & De Vos, W. H. Integrated High-Content Quantification of Intracellular ROS Levels and Mitochondrial Morphofunction. *Adv Anat Embryol Cell Biol* **219**, 149–177 (2016).
3. Broers, J. L. V., Ramaekers, F. C. S., Bonne, G., Yaou, R. B. & Hutchison, C. J. Nuclear lamins: laminopathies and their role in premature ageing. *Physiol Rev* **86**, 967–1008 (2006).
4. Stewart, C. L., Roux, K. J. & Burke, B. Blurring the boundary: the nuclear envelope extends its reach. *Science* **318**, 1408–1412 (2007).
5. Gerace, L., Blum, A. & Blobel, G. Immunocytochemical localization of the major polypeptides of the nuclear pore complex-lamina fraction. Interphase and mitotic distribution. *J. Cell Biol.* **79**, 546–566 (1978).
6. Turgay, Y. *et al.* The molecular architecture of lamins in somatic cells. *Nature* **543**, 261–264 (2017).
7. Dechat, T. *et al.* Nuclear lamins: major factors in the structural organization and function of the nucleus and chromatin. *Genes Dev.* **22**, 832–853 (2008).
8. Gruenbaum, Y., Margalit, A., Goldman, R. D., Shumaker, D. K. & Wilson, K. L. The nuclear lamina comes of age. *Nat. Rev. Mol. Cell Biol.* **6**, 21–31 (2005).
9. Stuurman, N., Heins, S. & Aebi, U. Nuclear Lamins: Their Structure, Assembly, and Interactions. *Journal of Structural Biology* **122**, 42–66 (1998).
10. Meier, J. & Georgatos, S. D. Type B lamins remain associated with the integral nuclear envelope protein p58 during mitosis: implications for nuclear reassembly. *EMBO J.* **13**, 1888–1898 (1994).
11. Machiels, B. M. *et al.* An Alternative Splicing Product of the Lamin A/C Gene Lacks Exon 10. *J. Biol. Chem.* **271**, 9249–9253 (1996).
12. Burke, B. & Stewart, C. L. The nuclear lamins: flexibility in function. *Nat. Rev. Mol. Cell Biol.* **14**, 13–24 (2013).
13. Krimm, I. *et al.* The Ig-like Structure of the C-Terminal Domain of Lamin A/C, Mutated in Muscular Dystrophies, Cardiomyopathy, and Partial Lipodystrophy. *Structure* **10**, 811–823 (2002).
14. Herrmann, H., Baer, H., Kreplak, L., Strelkov, S. V. & Aebi, U. Intermediate filaments: from cell architecture to nanomechanics. *Nat. Rev. Mol. Cell Biol.* **8**, 562–573 (2007).
15. Kitten, G. T. & Nigg, E. A. The CaaX motif is required for isoprenylation, carboxyl methylation, and nuclear membrane association of lamin B2. *J. Cell Biol.* **113**, 13–23 (1991).
16. Sinensky, M. *et al.* The processing pathway of prelamin A. *J. Cell. Sci.* **107** (Pt 1), 61–67 (1994).
17. Barrowman, J., Hamblet, C., George, C. M. & Michaelis, S. Analysis of Prelamin A Biogenesis Reveals the Nucleus to be a CaaX Processing Compartment. *Mol Biol Cell* **19**, 5398–5408 (2008).
18. Rusinol, A. E. & Sinensky, M. S. Farnesylated lamins, progeroid syndromes and farnesyl transferase inhibitors. *J. Cell. Sci.* **119**, 3265–3272 (2006).
19. Reddy, S. & Comai, L. Lamin A, farnesylation and aging. *Exp. Cell Res.* **318**, 1–7 (2012).

20. Maske, C. P. *et al.* A carboxyl-terminal interaction of lamin B1 is dependent on the CAAX endoprotease Rce1 and carboxymethylation. *J. Cell Biol.* **162**, 1223–1232 (2003).
21. Fong, L. G. *et al.* Prelamin A and lamin A appear to be dispensable in the nuclear lamina. *J. Clin. Invest.* **116**, 743–752 (2006).
22. Casasola, A. *et al.* Prelamin A processing, accumulation and distribution in normal cells and laminopathy disorders. *Nucleus* **7**, 84–102 (2016).
23. Gruenbaum, Y. & Foisner, R. Lamins: Nuclear Intermediate Filament Proteins with Fundamental Functions in Nuclear Mechanics and Genome Regulation. *Annual Review of Biochemistry* **84**, 132–164 (2015).
24. Shimi, T. *et al.* Structural organization of nuclear lamins A, C, B1, and B2 revealed by superresolution microscopy. *Mol Biol Cell* **26**, 4075–4086 (2015).
25. Hozak, P., Sasseville, A. M., Raymond, Y. & Cook, P. R. Lamin proteins form an internal nucleoskeleton as well as a peripheral lamina in human cells. *J. Cell. Sci.* **108**, 635–644 (1995).
26. Lammerding, J. *et al.* Lamin A/C deficiency causes defective nuclear mechanics and mechanotransduction. *J. Clin. Invest.* **113**, 370–378 (2004).
27. De Vos, W. H., Van Neste, L., Dieriks, B., Joss, G. H. & Van Oostveldt, P. High content image cytometry in the context of subnuclear organization. *Cytometry A* **77**, 64–75 (2010).
28. Crisp, M. *et al.* Coupling of the nucleus and cytoplasm: role of the LINC complex. *J. Cell Biol.* **172**, 41–53 (2006).
29. Méjat, A. & Misteli, T. LINC complexes in health and disease. *Nucleus* **1**, 40–52 (2010).
30. Amendola, M. & van Steensel, B. Mechanisms and dynamics of nuclear lamina-genome interactions. *Curr. Opin. Cell Biol.* **28**, 61–68 (2014).
31. Reddy, K. L., Zullo, J. M., Bertolino, E. & Singh, H. Transcriptional repression mediated by repositioning of genes to the nuclear lamina. *Nature* **452**, 243–247 (2008).
32. Malik, P., Zuleger, N. & Schirmer, E. C. Nuclear envelope influences on genome organization. *Biochem. Soc. Trans.* **38**, 268–272 (2010).
33. Heessen, S. & Fornerod, M. The inner nuclear envelope as a transcription factor resting place. *EMBO Rep* **8**, 914–919 (2007).
34. Ivorra, C. *et al.* A mechanism of AP-1 suppression through interaction of c-Fos with lamin A/C. *Genes Dev.* **20**, 307–320 (2006).
35. Andrés, V. & González, J. M. Role of A-type lamins in signaling, transcription, and chromatin organization. *J. Cell Biol.* **187**, 945–957 (2009).
36. Markiewicz, E. *et al.* The inner nuclear membrane protein Emerin regulates beta-catenin activity by restricting its accumulation in the nucleus. *EMBO J.* **25**, 3275–3285 (2006).
37. Hellemans, J. *et al.* Loss-of-function mutations in LEMD3 result in osteopoikilosis, Buschke-Ollendorff syndrome and melorheostosis. *Nature Genetics* **36**, 1213–1218 (2004).
38. Hutchison, C. J. The role of DNA damage in laminopathy progeroid syndromes. *Biochem. Soc. Trans.* **39**, 1715–1718 (2011).
39. Gonzalez-Suarez, I. *et al.* Novel roles for A-type lamins in telomere biology and the DNA damage response pathway. **28**, 2414–2427 (2009).
40. Dechat, T. *et al.* Alterations in mitosis and cell cycle progression caused by a

- mutant lamin A known to accelerate human aging. *Proc. Natl. Acad. Sci. U.S.A.* **104**, 4955–4960 (2007).
41. Schreiber, K. H. & Kennedy, B. K. When Lamins Go Bad: Nuclear Structure and Disease. *Cell* **152**, 1365–1375 (2013).
 42. Bonne, G. *et al.* Mutations in the gene encoding lamin A/C cause autosomal dominant Emery-Dreifuss muscular dystrophy. *Nature Genetics* **21**, 285–288 (1999).
 43. Muchir, A. *et al.* Identification of mutations in the gene encoding lamins A/C in autosomal dominant limb girdle muscular dystrophy with atrioventricular conduction disturbances (LGMD1B). *Hum Mol Genet* **9**, 1453–1459 (2000).
 44. Fatkin, D. *et al.* Missense Mutations in the Rod Domain of the Lamin A/C Gene as Causes of Dilated Cardiomyopathy and Conduction-System Disease. *N. Engl. J. Med.* **341**, 1715–1724 (1999).
 45. Shackleton, S. *et al.* LMNA, encoding lamin A/C, is mutated in partial lipodystrophy. *Nature Genetics* **24**, 153–156 (2000).
 46. De Sandre-Giovannoli, A. *et al.* Homozygous Defects in LMNA, Encoding Lamin A/C Nuclear-Envelope Proteins, Cause Autosomal Recessive Axonal Neuropathy in Human (Charcot-Marie-Tooth Disorder Type 2) and Mouse. *The American Journal of Human Genetics* **70**, 726–736 (2002).
 47. Hutchinson, J. Congenital Absence of Hair and Mammary Glands with Atrophic Condition of the Skin and its Appendages, in a Boy whose Mother had been almost wholly Bald from Alopecia Areata from the age of Six. *Medico-Chirurgical Transactions* **69**, 473 (1886).
 48. Gilford, H. Ateleiosis and progeria: continuous youth and premature old age. *Br. Med. J.* 914–918 (1904).
 49. Navarro, C. L. *et al.* Lamin A and ZMPSTE24 (FACE-1) defects cause nuclear disorganization and identify restrictive dermopathy as a lethal neonatal laminopathy. *Hum Mol Genet* **13**, 2493–2503 (2004).
 50. Navarro, C. L. *et al.* Loss of ZMPSTE24 (FACE-1) causes autosomal recessive restrictive dermopathy and accumulation of Lamin A precursors. *Hum Mol Genet* **14**, 1503–1513 (2005).
 51. De Sandre-Giovannoli, A. *et al.* Lamin A truncation in Hutchinson-Gilford progeria. *Science* **300**, 2055–2055 (2003).
 52. Eriksson, M. *et al.* Recurrent de novo point mutations in lamin A cause Hutchinson-Gilford progeria syndrome. *Nature* **423**, 293–298 (2003).
 53. Zwerger, M., Ho, C. Y. & Lammerding, J. Nuclear Mechanics in Disease. *Annual Review of Biomedical Engineering, Vol 13* **13**, 397–428 (2011).
 54. Ho, C. Y. & Lammerding, J. Lamins at a glance. *J. Cell. Sci.* **125**, 2087–2093 (2012).
 55. Simon, D. N. & Wilson, K. L. The nucleoskeleton as a genome-associated dynamic ‘network of networks’. *Nat. Rev. Mol. Cell Biol.* **12**, 695–708 (2011).
 56. Gotzmann, J. & Foisner, R. A-type lamin complexes and regenerative potential: a step towards understanding laminopathic diseases? *Histochem. Cell Biol.* **125**, 33–41 (2006).
 57. Halaschek-Wiener, J. & Brooks-Wilson, A. Progeria of stem cells: Stem cell exhaustion in Hutchinson-Gilford progeria syndrome. *J Gerontol a-Biol* **62**, 3–8 (2007).

58. Goldman, R. D. *et al.* Accumulation of mutant lamin A causes progressive changes in nuclear architecture in Hutchinson-Gilford progeria syndrome. *P Natl Acad Sci Usa* **101**, 8963–8968 (2004).
59. Candelario, J., Borrego, S., Reddy, S. & Comai, L. Accumulation of distinct prelamin A variants in human diploid fibroblasts differentially affects cell homeostasis. *Exp. Cell Res.* **317**, 319–329 (2011).
60. Caron, M. *et al.* Human lipodystrophies linked to mutations in A-type lamins and to HIV protease inhibitor therapy are both associated with prelamin A accumulation, oxidative stress and premature cellular senescence. *Cell Death Differ.* **14**, 1759–1767 (2007).
61. Halliwell, B. & Gutteridge, J. in *Free Radicals in Biology and Medicine* 30–78 (Oxford University Press, 2007).
62. Bartz, R. R. & Piantadosi, C. A. Clinical review: oxygen as a signaling molecule. *Crit Care* **14**, 234 (2010).
63. Lambeth, J. D. NOX enzymes and the biology of reactive oxygen. *Nat Rev Immunol* **4**, 181–189 (2004).
64. Babior, B. NADPH oxidase: An update. *Blood* **93**, 1464–1476 (1999).
65. Turrens, J. F. Mitochondrial formation of reactive oxygen species. *The Journal of Physiology* **552**, 335–344 (2003).
66. Murphy, M. P. How mitochondria produce reactive oxygen species. *Biochem J* **417**, 1–13 (2009).
67. Dupre-Crochet, S., Erard, M. & Nüsse, O. ROS production in phagocytes: why, when, and where? *Journal of Leukocyte Biology* **94**, 657–670 (2013).
68. Bedard, K. & Krause, K.-H. The NOX family of ROS-generating NADPH oxidases: Physiology and pathophysiology. *Physiol Rev* **87**, 245–313 (2007).
69. Loschen, G., Azzi, A., Richter, C. & Flohé, L. Superoxide radicals as precursors of mitochondrial hydrogen peroxide. *FEBS Lett.* **42**, 68–72 (1974).
70. Weisiger, R. A. & Fridovich, I. Superoxide Dismutase. *J. Biol. Chem.* (1973).
71. Boveris, A. & Chance, B. The mitochondrial generation of hydrogen peroxide. General properties and effect of hyperbaric oxygen. *Biochem J* **134**, 707–716 (1973).
72. Auchère, F. & Rusnak, F. What is the ultimate fate of superoxide anion in vivo? *J. Biol. Inorg. Chem.* **7**, 664–667 (2002).
73. Gupta, S. C. *et al.* Upsides and downsides of reactive oxygen species for cancer: the roles of reactive oxygen species in tumorigenesis, prevention, and therapy. *Antioxidants & Redox Signaling* **16**, 1295–1322 (2012).
74. Go, Y.-M. & Jones, D. P. Redox control systems in the nucleus: mechanisms and functions. *Antioxidants & Redox Signaling* **13**, 489–509 (2010).
75. Lopert, P. & Patel, M. Nicotinamide Nucleotide Transhydrogenase (Nnt) Links the Substrate Requirement in Brain Mitochondria for Hydrogen Peroxide Removal to the Thioredoxin/Peroxiredoxin (Trx/Prx) System. *J. Biol. Chem.* **289**, 15611–15620 (2014).
76. Radi, R., Cassina, A., Hodara, R., Quijano, C. & Castro, L. Peroxynitrite reactions and formation in mitochondria. *Free Radical Biology and Medicine* **33**, 1451–1464 (2002).
77. Szabó, C., Ischiropoulos, H. & Radi, R. Peroxynitrite: biochemistry,

- pathophysiology and development of therapeutics. *Nat Rev Drug Discov* **6**, 662–680 (2007).
78. Thomas, C., Mackey, M. M., Diaz, A. A. & Cox, D. P. Hydroxyl radical is produced via the Fenton reaction in submitochondrial particles under oxidative stress: implications for diseases associated with iron accumulation. *Redox Report* **14**, 102–108 (2009).
 79. Franco, R., Schoneveld, O., Georgakilas, A. G. & Panayiotidis, M. I. Oxidative stress, DNA methylation and carcinogenesis. *Cancer Lett.* **266**, 6–11 (2008).
 80. Marchi, S. *et al.* Mitochondria-ros crosstalk in the control of cell death and aging. *J Signal Transduct* **2012**, 329635 (2012).
 81. Riahi, Y., Cohen, G., Shamni, O. & Sasson, S. Signaling and cytotoxic functions of 4-hydroxyalkenals. *Am. J. Physiol. Endocrinol. Metab.* **299**, E879–E886 (2010).
 82. Chen, Z.-H. *et al.* 4-Hydroxynonenal induces adaptive response and enhances PC12 cell tolerance primarily through induction of thioredoxin reductase 1 via activation of Nrf2. *J. Biol. Chem.* **280**, 41921–41927 (2005).
 83. Chiu, C.-C. *et al.* Neuroprotective effects of aldehyde dehydrogenase 2 activation in rotenone-induced cellular and animal models of parkinsonism. *Exp. Neurol.* **263**, 244–253 (2015).
 84. Sachdev, S. & Davies, K. J. A. Production, detection, and adaptive responses to free radicals in exercise. *Free Radical Biology and Medicine* **44**, 215–223 (2008).
 85. Benhar, M., Forrester, M. T. & Stamler, J. S. Protein denitrosylation: enzymatic mechanisms and cellular functions. *Nat. Rev. Mol. Cell Biol.* **10**, 721–732 (2009).
 86. Rasmussen, H. H., Hamilton, E. J., Liu, C.-C. & Figtree, G. A. Reversible oxidative modification: implications for cardiovascular physiology and pathophysiology. *Trends Cardiovasc. Med.* **20**, 85–90 (2010).
 87. Finkel, T. Signal transduction by reactive oxygen species. *J. Cell Biol.* **194**, 7–15 (2011).
 88. Traber, M. G. & Stevens, J. F. Vitamins C and E: beneficial effects from a mechanistic perspective. *Free Radical Biology and Medicine* **51**, 1000–1013 (2011).
 89. Pastore, A. & Piemonte, F. S-Glutathionylation signaling in cell biology: progress and prospects. *Eur J Pharm Sci* **46**, 279–292 (2012).
 90. Marí, M. *et al.* Mitochondrial glutathione: features, regulation and role in disease. **1830**, 3317–3328 (2013).
 91. Nathan, C. & Cunningham-Bussel, A. Beyond oxidative stress: an immunologist's guide to reactive oxygen species. *Nat Rev Immunol* **13**, 349–361 (2013).
 92. Saaranen, M. J. & Ruddock, L. W. Disulfide bond formation in the cytoplasm. *Antioxidants & Redox Signaling* **19**, 46–53 (2013).
 93. Conte, Lo, M. & Carroll, K. S. The redox biochemistry of protein sulfenylation and sulfinylation. *J. Biol. Chem.* **288**, 26480–26488 (2013).
 94. Cremers, C. M. & Jakob, U. Oxidant sensing by reversible disulfide bond formation. *J. Biol. Chem.* **288**, 26489–26496 (2013).
 95. Stangherlin, A. & Reddy, A. B. Regulation of circadian clocks by redox homeostasis. *J. Biol. Chem.* **288**, 26505–26511 (2013).

96. Mailloux, R. J., McBride, S. L. & Harper, M.-E. Unearthing the secrets of mitochondrial ROS and glutathione in bioenergetics. *Trends in Biochemical Sciences* **38**, 592–602 (2013).
97. Groitl, B. & Jakob, U. Thiol-based redox switches. *Biochimica et Biophysica Acta (BBA) - Proteins and Proteomics* **1844**, 1335–1343 (2014).
98. Dickinson, B. C. & Chang, C. J. Chemistry and biology of reactive oxygen species in signaling or stress responses. *Nat. Chem. Biol.* **7**, 504–511 (2011).
99. Grek, C. L., Zhang, J., Manevich, Y., Townsend, D. M. & Tew, K. D. Causes and Consequences of Cysteine S-Glutathionylation. *J. Biol. Chem.* **288**, 26497–26504 (2013).
100. Nakamura, T. & Lipton, S. A. Redox modulation by S-nitrosylation contributes to protein misfolding, mitochondrial dynamics, and neuronal synaptic damage in neurodegenerative diseases. *Cell Death Differ.* **18**, 1478–1486 (2011).
101. Murphy, M. P. Mitochondrial Thiols in Antioxidant Protection and Redox Signaling: Distinct Roles for Glutathionylation and Other Thiol Modifications. *Antioxidants & Redox Signaling* **16**, 476–495 (2012).
102. Harman, D. Aging: a theory based on free radical and radiation chemistry. *J Gerontol* **11**, 298–300 (1956).
103. Salmon, A. B., Richardson, A. & Perez, V. I. Update on the oxidative stress theory of aging: Does oxidative stress play a role in aging or healthy aging? *Free Radical Biology and Medicine* **48**, 642–655 (2010).
104. Moylan, J. S. & Reid, M. B. Oxidative stress, chronic disease, and muscle wasting. *Muscle & Nerve* **35**, 411–429 (2007).
105. Naderi, W., Lopez, C. & Pandey, S. Chronically increased oxidative stress in fibroblasts from Alzheimer's disease patients causes early senescence and renders resistance to apoptosis by oxidative stress. *Mech Ageing Dev* **127**, 25–35 (2006).
106. Richards, S. A., Muter, J., Ritchie, P., Lattanzi, G. & Hutchison, C. J. The accumulation of un-repairable DNA damage in laminopathy progeria fibroblasts is caused by ROS generation and is prevented by treatment with N-acetyl cysteine. *Hum Mol Genet* **20**, 3997–4004 (2011).
107. Allen, R. G. & Tresini, M. Oxidative stress and gene regulation. *Free Radical Biology and Medicine* **28**, 463–499 (2000).
108. Baird, L. & Dinkova-Kostova, A. T. The cytoprotective role of the Keap1-Nrf2 pathway. *Arch. Toxicol.* **85**, 241–272 (2011).
109. Hansen, J., Go, Y. & Jones, D. Nuclear and mitochondrial compartmentation of oxidative stress and redox signaling. *Annu. Rev. Pharmacol. Toxicol.* **46**, 215–234 (2006).
110. Winterbourn, C. C. Reconciling the chemistry and biology of reactive oxygen species. *Nat. Chem. Biol.* **4**, 278–286 (2008).
111. Koopman, W. J. H. *et al.* Mammalian Mitochondrial Complex I: Biogenesis, Regulation, and Reactive Oxygen Species Generation. *Antioxidants & Redox Signaling* **12**, 1431–1470 (2010).
112. Han, D., Antunes, F., Canali, R., Rettori, D. & Cadenas, E. Voltage-dependent anion channels control the release of the superoxide anion from mitochondria to cytosol. *J. Biol. Chem.* **278**, 5557–5563 (2003).
113. Hamanaka, R. B. & Chandel, N. S. Mitochondrial reactive oxygen species regulate cellular signaling and dictate biological outcomes. *Trends in*

- Biochemical Sciences* **35**, 505–513 (2010).
114. Giorgio, M., Trinei, M., Migliaccio, E. & Pelicci, P. G. Hydrogen peroxide: a metabolic by-product or a common mediator of ageing signals? *Nat. Rev. Mol. Cell Biol.* **8**, 722A–728 (2007).
 115. Boveris, A., Valdez, L. B., Zaobornyj, T. & Bustamante, J. Mitochondrial metabolic states regulate nitric oxide and hydrogen peroxide diffusion to the cytosol. *Biochim. Biophys. Acta* **1757**, 535–542 (2006).
 116. Rhee, S. G., Woo, H. A., Kil, I. S. & Bae, S. H. Peroxiredoxin Functions as a Peroxidase and a Regulator and Sensor of Local Peroxides. *J. Biol. Chem.* **287**, 4403–4410 (2012).
 117. Mishina, N. M. *et al.* Can We See PIP3 and Hydrogen Peroxide with a Single Probe? *Antioxidants & Redox Signaling* **17**, 505–512 (2012).
 118. Korshunov, S. S., Skulachev, V. P. & Starkov, A. A. High protonic potential actuates a mechanism of production of reactive oxygen species in mitochondria. *FEBS Lett.* **416**, 15–18 (1997).
 119. Lebedzinska, M. *et al.* Oxidative stress-dependent p66Shc phosphorylation in skin fibroblasts of children with mitochondrial disorders. **1797**, 952–960 (2010).
 120. Miwa, S. & Brand, M. D. Mitochondrial matrix reactive oxygen species production is very sensitive to mild uncoupling. *Biochem. Soc. Trans.* **31**, 1300–1301 (2003).
 121. Verkaart, S. *et al.* Superoxide production is inversely related to complex I activity in inherited complex I deficiency. **1772**, 373–381 (2007).
 122. Chouchani, E. T. *et al.* Cardioprotection by S-nitrosation of a cysteine switch on mitochondrial complex I. *Nat. Med.* **19**, 753–759 (2013).
 123. Giustarini, D., Dalle-Donne, I., Tsikas, D. & Rossi, R. Oxidative stress and human diseases: Origin, link, measurement, mechanisms, and biomarkers. *Crit Rev Clin Lab Sci* **46**, 241–281 (2009).
 124. Brown, G. C. & Borutaite, V. There is no evidence that mitochondria are the main source of reactive oxygen species in mammalian cells. *Mitochondrion* **12**, 1–4 (2012).
 125. Woolley, J. F., Stanicka, J. & Cotter, T. G. Recent advances in reactive oxygen species measurement in biological systems. *Trends in Biochemical Sciences* **38**, 556–565 (2013).
 126. Willems, P. H. G. M., Rossignol, R., Dieteren, C. E. J., Murphy, M. P. & Koopman, W. J. H. Redox Homeostasis and Mitochondrial Dynamics. *Cell Metabolism* **22**, 207–218 (2015).
 127. Koopman, W. J. H. *et al.* Human NADH:ubiquinone oxidoreductase deficiency: radical changes in mitochondrial morphology? *AJP: Cell Physiology* **293**, C22–C29 (2007).
 128. Archer, S. L. Mitochondrial dynamics--mitochondrial fission and fusion in human diseases. *N. Engl. J. Med.* **369**, 2236–2251 (2013).
 129. Rambold, A. S., Kostecky, B., Elia, N. & Lippincott-Schwartz, J. Tubular network formation protects mitochondria from autophagosomal degradation during nutrient starvation. *P Natl Acad Sci Usa* **108**, 10190–10195 (2011).
 130. Verstraeten, V. L. R. M. *et al.* The R439C mutation in LMNA causes lamin oligomerization and susceptibility to oxidative stress. *J Cell Mol Med* **13**, 959–971 (2009).
 131. Charniot, J. C. *et al.* Oxidative stress implication in a new phenotype of

- amyotrophic quadricipital syndrome with cardiac involvement due to lamin A/C mutation. *Free Radical Res* **41**, 424–431 (2007).
132. Pekovic, V. *et al.* Conserved cysteine residues in the mammalian lamin A tail are essential for cellular responses to ROS generation. *Aging Cell* **10**, 1067–1079 (2011).
 133. Viteri, G., Chung, Y. W. & Stadtman, E. R. Effect of progerin on the accumulation of oxidized proteins in fibroblasts from Hutchinson Gilford progeria patients. *Mech Ageing Dev* **131**, 2–8 (2010).
 134. Moulson, C. L. *et al.* Homozygous and compound heterozygous mutations in ZMPSTE24 cause the laminopathy restrictive dermopathy. *J. Invest. Dermatol.* **125**, 913–919 (2005).
 135. Davies, B. S. J. *et al.* An accumulation of non-farnesylated prelamin A causes cardiomyopathy but not progeria. *Hum Mol Genet* **19**, 2682–2694 (2010).
 136. Capanni, C. *et al.* Altered pre-lamin A processing is a common mechanism leading to lipodystrophy. *Hum Mol Genet* **14**, 1489–1502 (2005).
 137. Le Dour, C. *et al.* A homozygous mutation of prelamin-A preventing its farnesylation and maturation leads to a severe lipodystrophic phenotype: new insights into the pathogenicity of nonfarnesylated prelamin-A. *J. Clin. Endocrinol. Metab.* **96**, E856–62 (2011).
 138. Yan, T., Li, S. & Jiang, X. Altered Levels of Primary Antioxidant Enzymes in Progeria Skin Fibroblasts. *Biochemical and Biophysical Research Communications* (1999).
 139. De Vos, W. H. *et al.* Repetitive disruptions of the nuclear envelope invoke temporary loss of cellular compartmentalization in laminopathies. *Hum Mol Genet* **20**, 4175–4186 (2011).
 140. Barascu, A. *et al.* Oxidative stress induces an ATM-independent senescence pathway through p38 MAPK-mediated lamin B1 accumulation. *EMBO J.* 1–15 (2012). doi:10.1038/emboj.2011.492
 141. Malhas, A. N., Lee, C. F. & Vaux, D. J. Lamin B1 controls oxidative stress responses via Oct-1. *J. Cell Biol.* **184**, 45–55 (2009).
 142. Shimi, T. *et al.* The role of nuclear lamin B1 in cell proliferation and senescence. *Genes Dev.* **25**, 2579–2593 (2011).
 143. Boubriak, I. I., Malhas, A. N., Drozd, M. M., Pytowski, L. & Vaux, D. J. Stress-induced release of Oct-1 from the nuclear envelope is mediated by JNK phosphorylation of lamin B1. *PLoS ONE* **12**, e0177990 (2017).
 144. Richter, T. & Zglinicki, T. V. A continuous correlation between oxidative stress and telomere shortening in fibroblasts. *Exp Gerontol* **42**, 1039–1042 (2007).
 145. Huang, S., Risques, R. A., Martin, G. M., Rabinovitch, P. S. & Oshima, J. Accelerated telomere shortening and replicative senescence in human fibroblasts overexpressing mutant and wild-type lamin A. *Exp. Cell Res.* **314**, 82–91 (2008).
 146. Sahin, E. *et al.* Telomere dysfunction induces metabolic and mitochondrial compromise. *Nature* **470**, 359–365 (2012).
 147. Haendeler, J., Hoffmann, J., Brandes, R., Zeiher, A. & Dimmeler, S. Hydrogen peroxide triggers nuclear export of telomerase reverse transcriptase via Src kinase family-dependent phosphorylation of tyrosine 707. *Mol Cell Biol* **23**, 4598–4610 (2003).
 148. Massard, C. *et al.* hTERT: a novel endogenous inhibitor of the mitochondrial

- cell death pathway. *Oncogene* **25**, 4505–4514 (2006).
149. Mattiussi, M., Tilman, G., Lenglez, S. & Decottignies, A. Human telomerase represses ROS-dependent cellular responses to Tumor Necrosis Factor- α without affecting NF- κ B activation. *Cell. Signal.* 1–10 (2011). doi:10.1016/j.cellsig.2011.11.004
 150. Davies, B. S. J., Fong, L. G., Yang, S. H., Coffinier, C. & Young, S. G. The posttranslational processing of prelamin A and disease. *Annu Rev Genom Hum G* **10**, 153–174 (2009).
 151. Dalle-Donne, I., Rossi, R., Giustarini, D., Colombo, R. & Milzani, A. Actin S-glutathionylation: evidence against a thiol-disulphide exchange mechanism. *Free Radical Biology and Medicine* **35**, 1185–1193 (2003).
 152. Mewborn, S. K. *et al.* Altered chromosomal positioning, compaction, and gene expression with a lamin A/C gene mutation. *PLoS ONE* **5**, e14342–(2010).
 153. Nikolova, V. *et al.* Defects in nuclear structure and function promote dilated cardiomyopathy in lamin A/C-deficient mice. *J. Clin. Invest.* **113**, 357–369 (2004).
 154. Manju, K., Muralikrishna, B. & Parnaik, V. K. Expression of disease-causing lamin A mutants impairs the formation of DNA repair foci. *J. Cell. Sci.* **119**, 2704–2714 (2006).
 155. Angori, S. *et al.* Emery-Dreifuss Muscular Dystrophy-Associated Mutant Forms of Lamin A Recruit the Stress Responsive Protein Ankrd2 into the Nucleus, Affecting the Cellular Response to Oxidative Stress. *Cell. Physiol. Biochem.* **42**, 169–184 (2017).
 156. Kubben, N. *et al.* Repression of the Antioxidant NRF2 Pathway in Premature Aging. *Cell* **165**, 1361–1374 (2016).
 157. Malhas, A. N. & Vaux, D. J. The nuclear envelope and its involvement in cellular stress responses. *Biochem. Soc. Trans.* **39**, 1795–1798 (2011).
 158. Fabrini, R. *et al.* Nuclear shield: a multi-enzyme task-force for nucleus protection. *PLoS ONE* **5**, e14125 (2010).
 159. Libotte, T. *et al.* Lamin A/C-dependent localization of Nesprin-2, a giant scaffold at the nuclear envelope. *Mol Biol Cell* **16**, 3411–3424 (2005).
 160. Robijns, J. *et al.* In silico synchronization reveals regulators of nuclear ruptures in lamin A/C deficient model cells. *Sci Rep* **6**, 30325 (2016).
 161. Sylvius, N. *et al.* In vivo and in vitro examination of the functional significances of novel lamin gene mutations in heart failure patients. *J. Med. Genet.* **42**, 639–647 (2005).
 162. Sastre, J., Pallardo, F. & Vina, J. The role of mitochondrial oxidative stress in aging. *Free Radical Biology and Medicine* **35**, 1–8 (2003).
 163. Weyemi, U. *et al.* ROS-generating NADPH oxidase NOX4 is a critical mediator in oncogenic H-Ras-induced DNA damage and subsequent senescence. *Oncogene* – (2011). doi:10.1038/onc.2011.327
 164. de Mochel, N. S. R. *et al.* Hepatocyte NAD(P)H oxidases as an endogenous source of reactive oxygen species during hepatitis C virus infection. *Hepatology* **52**, 47–59 (2010).
 165. Matoba, S. *et al.* p53 regulates mitochondrial respiration. *Science* **312**, 1650–1653 (2006).
 166. Peinado, J. R. *et al.* Proteomic profiling of adipose tissue from *Zmpste24*^{-/-} mice, a model of lipodystrophy and premature aging, reveals major changes in mitochondrial function and vimentin processing. *Mol. Cell*

- Proteomics* **10**, M111.008094 (2011).
167. Gomes, L. C., Di Benedetto, G. & Scorrano, L. Essential amino acids and glutamine regulate induction of mitochondrial elongation during autophagy. *Cell Cycle* **10**, 2635–2639 (2011).
 168. Yu, T. Z., Robotham, J. L. & Yoon, Y. Increased production of reactive oxygen species in hyperglycemic conditions requires dynamic change of mitochondrial morphology. *P Natl Acad Sci Usa* **103**, 2653–2658 (2006).
 169. Trudeau, K., Molina, A. J. A. & Roy, S. High Glucose Induces Mitochondrial Morphology and Metabolic Changes in Retinal Pericytes. *Investigative Ophthalmology & Visual Science* **52**, 8657–8664 (2011).
 170. Frigault, M. M., Lacoste, J., Swift, J. L. & Brown, C. M. Live-cell microscopy - tips and tools. *J. Cell. Sci.* **122**, 753–767 (2009).
 171. Dikalov, S. I. & Harrison, D. G. Methods for detection of mitochondrial and cellular reactive oxygen species. *Antioxidants & Redox Signaling* **20**, 372–382 (2014).
 172. Wang, X. *et al.* Imaging ROS signaling in cells and animals. *J Mol Med* **91**, 917–927 (2013).
 173. Gomes, A., Fernandes, E. & Lima, J. L. F. C. Fluorescence probes used for detection of reactive oxygen species. *Journal of Biochemical and Biophysical Methods* **65**, 45–80 (2005).
 174. Koopman, W. J. H. *et al.* Simultaneous quantification of oxidative stress and cell spreading using 5-(and-6)-chloromethyl-2',7'-dichlorofluorescein. *Cytom Part A* **69A**, 1184–1192 (2006).
 175. Tarpey, M. M., Wink, D. A. & Grisham, M. B. Methods for detection of reactive metabolites of oxygen and nitrogen: in vitro and in vivo considerations. *Am J Physiol-Reg I* **286**, R431–44 (2004).
 176. Zhao, H. *et al.* Superoxide reacts with hydroethidine but forms a fluorescent product that is distinctly different from ethidium: potential implications in intracellular fluorescence detection of superoxide. *Free Radical Biology and Medicine* **34**, 1359–1368 (2003).
 177. Zielonka, J. & Kalyanaraman, B. Hydroethidine- and MitoSOX-derived red fluorescence is not a reliable indicator of intracellular superoxide formation: Another inconvenient truth. *Free Radical Biology and Medicine* **48**, 983–1001 (2010).
 178. Robinson, K. M. *et al.* Selective fluorescent imaging of superoxide in vivo using ethidium-based probes. *P Natl Acad Sci Usa* **103**, 15038–15043 (2006).
 179. Robinson, K. M., Janes, M. S. & Beckman, J. S. The selective detection of mitochondrial superoxide by live cell imaging. *Nat Protoc* **3**, 941–947 (2008).
 180. Hu, J. J. *et al.* Fluorescent Probe HKSOX-1 for Imaging and Detection of Endogenous Superoxide in Live Cells and In Vivo. *J. Am. Chem. Soc.* (2015). doi:10.1021/jacs.5b01881
 181. Dickinson, B. C., Huynh, C. & Chang, C. J. A Palette of Fluorescent Probes with Varying Emission Colors for Imaging Hydrogen Peroxide Signaling in Living Cells. ... of the American Chemical ... (2010).
 182. Dickinson, B. C., Srikun, D. & Chang, C. J. Mitochondrial-targeted fluorescent probes for reactive oxygen species. *Current Opinion in Chemical Biology* **14**, 50–56 (2010).
 183. Chang, M. C. Y., Pralle, A., Isacoff, E. Y. & Chang, C. J. A selective, cell-

- permeable optical probe for hydrogen peroxide in living cells. *J. Am. Chem. Soc.* **126**, 15392–15393 (2004).
184. Miller, E. W., Tulyathan, O., Tulyanthan, O., Isacoff, E. Y. & Chang, C. J. Molecular imaging of hydrogen peroxide produced for cell signaling. *Nat. Chem. Biol.* **3**, 263–267 (2007).
 185. Fujikawa, M., Kobayashi, K. & Kozawa, T. Direct oxidation of the [2Fe-2S] cluster in SoxR protein by superoxide: distinct differential sensitivity to superoxide-mediated signal transduction. *J. Biol. Chem.* **287**, 35702–35708 (2012).
 186. Zheng, M., Aslund, F. & Storz, G. Activation of the OxyR transcription factor by reversible disulfide bond formation. *Science* **279**, 1718–1721 (1998).
 187. Topell, S., Hennecke, J. & Glockshuber, R. Circularly permuted variants of the green fluorescent protein. *FEBS Lett.* **457**, 283–289 (1999).
 188. Baird, G. S., Zacharias, D. A. & Tsien, R. Y. Circular permutation and receptor insertion within green fluorescent proteins. *P Natl Acad Sci Usa* **96**, 11241–11246 (1999).
 189. Belousov, V. V. *et al.* Genetically encoded fluorescent indicator for intracellular hydrogen peroxide. *Nat. Methods* **3**, 281–286 (2006).
 190. Markvicheva, K. N. *et al.* A genetically encoded sensor for H₂O₂ with expanded dynamic range. *Bioorg. Med. Chem.* **19**, 1079–1084 (2011).
 191. Bilan, D. S. *et al.* HyPer-3: a genetically encoded H₂O₂ probe with improved performance for ratiometric and fluorescence lifetime imaging. *ACS Chem. Biol.* **8**, 535–542 (2013).
 192. Poburko, D., Santo-Domingo, J. & Demaurex, N. Dynamic regulation of the mitochondrial proton gradient during cytosolic calcium elevations. *J. Biol. Chem.* **286**, 11672–11684 (2011).
 193. Lukyanov, K. A. & Belousov, V. V. Genetically encoded fluorescent redox sensors. **1840**, 745–756 (2014).
 194. Gutscher, M. *et al.* Real-time imaging of the intracellular glutathione redox potential. *Nat. Methods* **5**, 553–559 (2008).
 195. Meyer, A. J. & Dick, T. P. Fluorescent Protein-Based Redox Probes. <http://dx.doi.org/10.1089/ars.2009.2948> (2010).
 196. Gutscher, M. *et al.* Proximity-based protein thiol oxidation by H₂O₂-scavenging peroxidases. *J. Biol. Chem.* **284**, 31532–31540 (2009).
 197. Drummen, G. P. C., van Liebergen, L. C. M., Op den Kamp, J. A. F. & Post, J. A. C11-BODIPY581/591, an oxidation-sensitive fluorescent lipid peroxidation probe: (micro)spectroscopic characterization and validation of methodology. *Free Radical Biology and Medicine* **33**, 473–490 (2002).
 198. Prime, T. A. *et al.* A ratiometric fluorescent probe for assessing mitochondrial phospholipid peroxidation within living cells. *Free Radical Biology and Medicine* **53**, 544–553 (2012).
 199. Iannetti, E. F. *et al.* Toward high-content screening of mitochondrial morphology and membrane potential in living cells. *Int. J. Biochem. Cell Biol.* (2015). doi:10.1016/j.biocel.2015.01.020
 200. Nicholls, D. G. Fluorescence measurement of mitochondrial membrane potential changes in cultured cells. *Methods Mol. Biol.* **810**, 119–133 (2012).
 201. Dong, H. *et al.* ‘Stainomics’: identification of mitotracker labeled proteins in mammalian cells. *Electrophoresis* **34**, 1957–1964 (2013).
 202. Forkink, M., Willems, P. H. G. M., Koopman, W. J. H. & Grefte, S. Live-cell

- assessment of mitochondrial reactive oxygen species using dihydroethidine. *Methods Mol. Biol.* **1264**, 161–169 (2015).
203. Sieprath, T. *et al.* Sustained accumulation of prelamin A and depletion of lamin A/C both cause oxidative stress and mitochondrial dysfunction but induce different cell fates. *Nucleus* **6**, 236–246 (2015).
 204. Koopman, W. J. H., Distelmaier, F., Esseling, J. J., Smeitink, J. A. M. & Willems, P. H. G. M. Computer-assisted live cell analysis of mitochondrial membrane potential, morphology and calcium handling. *Methods* **46**, 304–311 (2008).
 205. Chazotte, B. Labeling mitochondria with MitoTracker dyes. *Cold Spring Harb Protoc* **2011**, 990–992 (2011).
 206. Dickinson, B. C., Lin, V. S. & Chang, C. J. Preparation and use of MitoPY1 for imaging hydrogen peroxide in mitochondria of live cells. *Nat Protoc* **8**, 1249–1259 (2013).
 207. Hanson, G. T. *et al.* Investigating Mitochondrial Redox Potential with Redox-sensitive Green Fluorescent Protein Indicators. *J. Biol. Chem.* **279**, 13044–13053 (2004).
 208. Dooley, C. T. *et al.* Imaging Dynamic Redox Changes in Mammalian Cells with Green Fluorescent Protein Indicators. *J. Biol. Chem.* **279**, 22284–22293 (2004).
 209. Staljanssens, D., De Vos, W. H., Willems, P., Van Camp, J. & Smagghe, G. Time-resolved quantitative analysis of CCK1 receptor-induced intracellular calcium increase. *Peptides* **34**, 219–225 (2012).
 210. Casey, J. R. Why bicarbonate? *Biochem. Cell Biol.* **84**, 930–939 (2006).
 211. Zhao, B., Bilski, P. J., He, Y.-Y., Feng, L. & Chignell, C. F. Photo-induced reactive oxygen species generation by different water-soluble fullerenes (C) and their cytotoxicity in human keratinocytes. *Photochem. Photobiol.* **84**, 1215–1223 (2008).
 212. Dixit, R. & Cyr, R. Cell damage and reactive oxygen species production induced by fluorescence microscopy: effect on mitosis and guidelines for non-invasive fluorescence microscopy. *Plant J.* **36**, 280–290 (2003).
 213. Pattison, D. I. & Davies, M. J. Actions of ultraviolet light on cellular structures. *EXS* 131–157 (2006).
 214. Rabut, G. & Ellenberg, J. Automatic real-time three-dimensional cell tracking by fluorescence microscopy. *J Microsc* **216**, 131–137 (2004).
 215. Gabriel, D., Roedl, D., Gordon, L. B. & Djabali, K. Sulforaphane enhances progerin clearance in Hutchinson-Gilford progeria fibroblasts. *Aging Cell* **14**, 78–91 (2015).
 216. Scaffidi, P. & Misteli, T. Reversal of the cellular phenotype in the premature aging disease Hutchinson-Gilford progeria syndrome. *Nat. Med.* **11**, 440–445 (2005).
 217. Broers, J. L. *et al.* Dynamics of the nuclear lamina as monitored by GFP-tagged A-type lamins. *J. Cell. Sci.* **112 (Pt 20)**, 3463–3475 (1999).
 218. Jackson, A. L. & Linsley, P. S. Recognizing and avoiding siRNA off-target effects for target identification and therapeutic application. *Nat Rev Drug Discov* **9**, 57–67 (2010).
 219. Olejniczak, M. *et al.* Sequence-non-specific effects generated by various types of RNA interference triggers. *Biochim. Biophys. Acta* **1859**, 306–314 (2016).
 220. Sledz, C. A., Holko, M., de Veer, M. J., Silverman, R. H. & Williams, B.

- Activation of the interferon system by short-interfering RNAs. *Nat. Cell Biol.* **5**, 834–839 (2003).
221. Olejniczak, M., Galka, P. & Krzyzosiak, W. J. Sequence-non-specific effects of RNA interference triggers and microRNA regulators. *Nucleic Acids Res.* **38**, 1–16 (2010).
 222. De Vos, W. H. *et al.* Increased plasticity of the nuclear envelope and hypermobility of telomeres due to the loss of A-type lamins. *BBA - General Subjects* **1800**, 448–458 (2010).
 223. Malhas, A., Goulbourne, C. & Vaux, D. J. The nucleoplasmic reticulum: form and function. *Trends Cell Biol.* **21**, 362–373 (2011).
 224. Broers, J. L. V. *et al.* Decreased mechanical stiffness in LMNA^{-/-} cells is caused by defective nucleo-cytoskeletal integrity: implications for the development of laminopathies. *Hum Mol Genet* **13**, 2567–2580 (2004).
 225. Sullivan, T. *et al.* Loss of A-type lamin expression compromises nuclear envelope integrity leading to muscular dystrophy. *J. Cell Biol.* **147**, 913–919 (1999).
 226. Sui, H., Zhou, M., Chen, Q., Lane, H. C. & Imamichi, T. siRNA enhances DNA-mediated interferon lambda-1 response through crosstalk between RIG-I and IFI16 signalling pathway. *Nucleic Acids Res* **42**, 583–598 (2014).
 227. Nguyen, A., Yoshida, M., Goodarzi, H. & Tavazoie, S. F. Highly variable cancer subpopulations that exhibit enhanced transcriptome variability and metastatic fitness. *Nat Commun* **7**, 11246 (2016).
 228. Goulbourne, C. N., Malhas, A. N. & Vaux, D. J. The induction of a nucleoplasmic reticulum by prelamin A accumulation requires CTP:phosphocholine cytidyltransferase- α . *J. Cell. Sci.* **124**, 4253–4266 (2011).
 229. Baker, K. E. & Parker, R. Nonsense-mediated mRNA decay: terminating erroneous gene expression. *Curr. Opin. Cell Biol.* **16**, 293–299 (2004).
 230. Verstraeten, V. L. R. M. *et al.* Protein farnesylation inhibitors cause donut-shaped cell nuclei attributable to a centrosome separation defect. *Proceedings of the National Academy of Sciences* **108**, 4997–5002 (2011).
 231. Guo, Y. & Zheng, Y. Lamins position the nuclear pores and centrosomes by modulating dynein. *Mol Biol Cell* **26**, 3379–3389 (2015).
 232. Adam, S. A., Butin-Israeli, V., Cleland, M. M., Shimi, T. & Goldman, R. D. Disruption of lamin B1 and lamin B2 processing and localization by farnesyltransferase inhibitors. *Nucleus* **4**, 142–150 (2013).
 233. Verstraeten, V. L. R. M. *et al.* Compound heterozygosity for mutations in LMNA causes a progeria syndrome without prelamin A accumulation. *Hum Mol Genet* **15**, 2509–2522 (2006).
 234. Coffinier, C. *et al.* HIV protease inhibitors block the zinc metalloproteinase ZMPSTE24 and lead to an accumulation of prelamin A in cells. *P Natl Acad Sci Usa* **104**, 13432–13437 (2007).
 235. Kilic, F. *et al.* In vitro assay and characterization of the farnesylation-dependent prelamin A endoprotease. *J. Biol. Chem.* **272**, 5298–5304 (1997).
 236. Ran, F. A. *et al.* Genome engineering using the CRISPR-Cas9 system. *Nat Protoc* **8**, 2281–2308 (2013).
 237. Livak, K. J. & Schmittgen, T. D. Analysis of relative gene expression data

- using real-time quantitative PCR and the 2(-Delta Delta C(T)) Method. *Methods* **25**, 402–408 (2001).
238. Verschuuren, M. *et al.* Accurate Detection of Dysmorphic Nuclei Using Dynamic Programming and Supervised Classification. *PLoS ONE* **12**, e0170688 (2017).
 239. Konietzschke, F., Placzek, M., Schaarschmidt, F. & Hothorn, L. A. nparcomp: An R Software Package for Nonparametric Multiple Comparisons and Simultaneous Confidence Intervals. *Journal of Statistical Software* **61**, 1–17 (2014).
 240. Wickham, H. *ggplot2: Elegant Graphics for Data Analysis*. (Springer Science & Business Media, 2009).
 241. Sieprath, T., Corne, T., Robijns, J., Koopman, W. J. H. & De Vos, W. H. Cellular Redox Profiling Using High-content Microscopy. *J Vis Exp* e55449–e55449 (2017). doi:10.3791/55449
 242. Forkink, M. *et al.* Mitochondrial hyperpolarization during chronic complex I inhibition is sustained by low activity of complex II, III, IV and V. *Biochim. Biophys. Acta* **1837**, 1247–1256 (2014).
 243. Johnson, L. V., Walsh, M. L., Bockus, B. J. & Chen, L. B. Monitoring of relative mitochondrial membrane potential in living cells by fluorescence microscopy. *J. Cell Biol.* **88**, 526–535 (1981).
 244. Furlong, I. J., Mediavilla, C. L., Ascaso, R., Rivas, A. L. & Collins, M. Induction of apoptosis by valinomycin: mitochondrial permeability transition causes intracellular acidification. *Cell Death Differ.* **5**, 214–221 (1998).
 245. Muchir, A. *et al.* Nuclear envelope alterations in fibroblasts from LGMD1B patients carrying nonsense Y259X heterozygous or homozygous mutation in lamin A/C gene. *Exp. Cell Res.* **291**, 352–362 (2003).
 246. Black, C. B., Duensing, T. D., Trinkle, L. S. & Dunlay, R. T. Cell-Based Screening Using High-Throughput Flow Cytometry. *Assay Drug Dev Technol* **9**, 13–20 (2011).
 247. Chandra, S., Mondal, D. & Agrawal, K. C. HIV-1 protease inhibitor induced oxidative stress suppresses glucose stimulated insulin release: protection with thymoquinone. *Exp. Biol. Med. (Maywood)* **234**, 442–453 (2009).
 248. Touzet, O. & Philips, A. Resveratrol protects against protease inhibitor-induced reactive oxygen species production, reticulum stress and lipid raft perturbation. *Aids* **24**, 1437–1447 (2010).
 249. Xiang, T., Du, L., Pham, P., Zhu, B. & Jiang, S. Nelfinavir, an HIV protease inhibitor, induces apoptosis and cell cycle arrest in human cervical cancer cells via the ROS-dependent mitochondrial pathway. *Cancer Lett.* **364**, 79–88 (2015).
 250. Roumier, T. *et al.* HIV-1 protease inhibitors and cytomegalovirus vMIA induce mitochondrial fragmentation without triggering apoptosis. *Cell Death Differ.* **13**, 348–351 (2006).
 251. Matarrese, P. *et al.* Mitochondrial membrane hyperpolarization hijacks activated T lymphocytes toward the apoptotic-prone phenotype: homeostatic mechanisms of HIV protease inhibitors. *J. Immunol.* **170**, 6006–6015 (2003).
 252. Estaquier, J. *et al.* Effects of antiretroviral drugs on human immunodeficiency virus type 1-induced CD4(+) T-cell death. *J. Virol.* **76**, 5966–5973 (2002).
 253. Bociąga-Jasik, M. *et al.* Metabolic effects of the HIV protease inhibitor--

- saquinavir in differentiating human preadipocytes. *Pharmacol Rep* **65**, 937–950 (2013).
254. Blanchet, L. *et al.* Quantifying small molecule phenotypic effects using mitochondrial morpho-functional fingerprinting and machine learning. *Sci Rep* **5**, 8035 (2015).
 255. Iannetti, E. F., Smeitink, J. A. M., Beyrath, J., Willems, P. H. G. M. & Koopman, W. J. H. Multiplexed high-content analysis of mitochondrial morphofunction using live-cell microscopy. *Nat Protoc* **11**, 1693–1710 (2016).
 256. Invitrogen. *Reactive Oxygen Species (ROS) Detection Reagents*. 1–5 (Invitrogen, 2006).
 257. Zuiderveld, K. *Contrast limited adaptive histogram equalization*. *Graphics gems IV* 474–485 (Academic Press Professional, Inc., 1994).
 258. Sahoo, P. K., Soltani, S., Wong, A. & Chen, Y. C. A Survey of Thresholding Techniques. *Computer vision, graphics, and image processing* **41**, 233–260 (1988).
 259. Glasbey, C. A. An Analysis of Histogram-Based Thresholding Algorithms. *CVGIP: Graphical models and image processing* (1993).
 260. Huang, L. K. & Wang, M. Image thresholding by minimizing the measures of fuzziness. *Pattern recognition* (1995).
 261. Web Application Framework for R [R package shiny version 1.0.2].
 262. Konietzke, F., Placzek, M., Schaarschmidt, F. & Hothorn, L. A. nparcomp: An R Software Package for Nonparametric Multiple Comparisons and Simultaneous Confidence Intervals. *Journal of Statistical Software* **64**, (2015).
 263. Barascu, A. *et al.* Oxydative stress alters nuclear shape through lamins dysregulation: A route to senescence. *Nucleus* **3**, (2012).
 264. Lattanzi, G., Marmiroli, S., Facchini, A. & Maraldi, N. M. Nuclear damages and oxidative stress: new perspectives for laminopathies. *Eur J Histochem* **56**, e45 (2012).
 265. Rivera-Torres, J. *et al.* Identification of mitochondrial dysfunction in Hutchinson-Gilford progeria syndrome through use of stable isotope labeling with amino acids in cell culture. *J Proteomics* **91**, 466–477 (2013).
 266. Lawless, C. *et al.* Quantitative assessment of markers for cell senescence. *Exp Gerontol* **45**, 772–778 (2010).
 267. Zhang, D. *et al.* Regulation of SOD2 and β -arrestin1 by interleukin-6 contributes to the increase of IGF-1R expression in docetaxel resistant prostate cancer cells. *Eur J Cell Biol* **93**, 289–298 (2014).
 268. Lattanzi, G. *et al.* Lamins are rapamycin targets that impact human longevity: a study in centenarians. *J. Cell. Sci.* **127**, 147–157 (2014).
 269. Maharjan, S., Oku, M., Tsuda, M., Hoseki, J. & Sakai, Y. Mitochondrial impairment triggers cytosolic oxidative stress and cell death following proteasome inhibition. *Sci Rep* **4**, 5896 (2014).
 270. Parnaik, V. K., Chaturvedi, P. & Muralikrishna, B. Lamins, laminopathies and disease mechanisms: possible role for proteasomal degradation of key regulatory proteins. *J. Biosci.* **36**, 471–479 (2011).
 271. Muchir, A. *et al.* Proteasome-mediated degradation of integral inner nuclear membrane protein emerlin in fibroblasts lacking A-type lamins. *Biochemical and Biophysical Research Communications* **351**, 1011–

- 1017 (2006).
272. Chen, C.-Y. *et al.* Accumulation of the inner nuclear envelope protein Sun1 is pathogenic in progeric and dystrophic laminopathies. *Cell* **149**, 565–577 (2012).
 273. Osorio, F. G. *et al.* Nuclear lamina defects cause ATM-dependent NF- κ B activation and link accelerated aging to a systemic inflammatory response. *Genes Dev.* **26**, 2311–2324 (2012).
 274. Chien, Y. *et al.* Control of the senescence-associated secretory phenotype by NF- κ B promotes senescence and enhances chemosensitivity. *Genes Dev.* **25**, 2125–2136 (2011).
 275. Kojima, H., Kunimoto, H., Inoue, T. & Nakajima, K. The STAT3-IGFBP5 axis is critical for IL-6/gp130-induced premature senescence in human fibroblasts. *Cell Cycle* **11**, 730–739 (2012).
 276. Houben, F. *et al.* Cytoplasmic localization of PML particles in laminopathies. *Histochemistry* **139**, 119–134 (2013).
 277. Sahin, U. *et al.* Oxidative stress-induced assembly of PML nuclear bodies controls sumoylation of partner proteins. *J. Cell Biol.* **204**, 931–945 (2014).
 278. Guo, S., Cheng, X., Lim, J.-H., Liu, Y. & Kao, H.-Y. Control of antioxidative response by the tumor suppressor protein PML through regulating Nrf2 activity. *Mol Biol Cell* **25**, 2485–2498 (2014).
 279. Giovannini, C. *et al.* Mitochondria hyperpolarization is an early event in oxidized low-density lipoprotein-induced apoptosis in Caco-2 intestinal cells. *FEBS Lett.* **523**, 200–206 (2002).
 280. Nagy, G., Koncz, A. & Perl, A. T cell activation-induced mitochondrial hyperpolarization is mediated by Ca²⁺- and redox-dependent production of nitric oxide. *J. Immunol.* **171**, 5188–5197 (2003).
 281. Liu, J. *et al.* HP1 α mediates defective heterochromatin repair and accelerates senescence in Zmpste24-deficient cells. *Cell Cycle* **13**, 1237–1247 (2014).
 282. Liu, Y., Drozdov, I., Shroff, R., Beltran, L. E. & Shanahan, C. M. Prelamin A Accelerates Vascular Calcification Via Activation of the DNA Damage Response and Senescence-Associated Secretory Phenotype in Vascular Smooth Muscle Cells. *Circ Res* **112**, e99–e109 (2013).
 283. Plasilova, M. *et al.* Discordant gene expression signatures and related phenotypic differences in lamin A- and A/C-related Hutchinson-Gilford progeria syndrome (HGPS). *PLoS ONE* **6**, e21433 (2011).
 284. Lu, D. *et al.* LMNA E82K mutation activates FAS and mitochondrial pathways of apoptosis in heart tissue specific transgenic mice. *PLoS ONE* **5**, e15167 (2010).
 285. Wolf, C. M. *et al.* Lamin A/C haploinsufficiency causes dilated cardiomyopathy and apoptosis-triggered cardiac conduction system disease. *J. Mol. Cell. Cardiol.* **44**, 293–303 (2008).
 286. Childs, B. G., Baker, D. J., Kirkland, J. L., Campisi, J. & van Deursen, J. M. Senescence and apoptosis: dueling or complementary cell fates? *EMBO Rep* **15**, 1139–1153 (2014).
 287. Chen, Q. M., Liu, J. & Merrett, J. B. Apoptosis or senescence-like growth arrest: influence of cell-cycle position, p53, p21 and bax in H₂O₂ response of normal human fibroblasts. *Biochem J* **347**, 543–551 (2000).
 288. Bladier, C., Wolvetang, E. J., Hutchinson, P., de Haan, J. B. & Kola, I.

- Response of a primary human fibroblast cell line to H₂O₂: senescence-like growth arrest or apoptosis? *Cell Growth Differ* **8**, 589–598 (1997).
289. Macip, S. *et al.* Influence of induced reactive oxygen species in p53-mediated cell fate decisions. *Mol Cell Biol* **23**, 8576–8585 (2003).
 290. Mukhopadhyay, P. *et al.* Simultaneous detection of apoptosis and mitochondrial superoxide production in live cells by flow cytometry and confocal microscopy. *Nat Protoc* **2**, 2295–2301 (2007).
 291. Konietzschke, F., Hothorn, L. A. & Brunner, E. Rank-based multiple test procedures and simultaneous confidence intervals. *Electronic Journal of Statistics* **6**, 738–759 (2012).
 292. Muralikrishna, B., Chaturvedi, P., Sinha, K. & Parnaik, V. K. Lamin misexpression upregulates three distinct ubiquitin ligase systems that degrade ATR kinase in HeLa cells. *Mol. Cell. Biochem.* **365**, 323–332 (2012).
 293. Cao, K. *et al.* Rapamycin reverses cellular phenotypes and enhances mutant protein clearance in Hutchinson-Gilford progeria syndrome cells. *Science Translational Medicine* **3**, 89ra58–89ra58 (2011).
 294. Lobanova, E. S., Finkelstein, S., Skiba, N. P. & Arshavsky, V. Y. Proteasome overload is a common stress factor in multiple forms of inherited retinal degeneration. *Proceedings of the National Academy of Sciences* **110**, 9986–9991 (2013).
 295. Lilienbaum, A. Relationship between the proteasomal system and autophagy. *Int J Biochem Mol Biol* **4**, 1–26 (2013).
 296. Zhu, K., Dunner, K. & McConkey, D. J. Proteasome inhibitors activate autophagy as a cytoprotective response in human prostate cancer cells. *Oncogene* **29**, 451–462 (2010).
 297. Kwak, M.-K., Cho, J.-M., Huang, B., Shin, S. & Kensler, T. W. Role of increased expression of the proteasome in the protective effects of sulforaphane against hydrogen peroxide-mediated cytotoxicity in murine neuroblastoma cells. *Free Radical Biology and Medicine* **43**, 809–817 (2007).
 298. Jo, C. *et al.* Sulforaphane induces autophagy through ERK activation in neuronal cells. *FEBS Lett.* **588**, 3081–3088 (2014).
 299. Kirstein, J. *et al.* Proteotoxic stress and ageing triggers the loss of redox homeostasis across cellular compartments. *EMBO J.* **34**, 2334–2349 (2015).
 300. Doss, J. F. *et al.* Phase 1 Study of a Sulforaphane-Containing Broccoli Sprout Homogenate for Sickle Cell Disease. *PLoS ONE* **11**, e0152895 (2016).
 301. Alumkal, J. J. *et al.* A phase II study of sulforaphane-rich broccoli sprout extracts in men with recurrent prostate cancer. *Invest New Drugs* **33**, 480–489 (2015).
 302. Sudini, K. *et al.* A Randomized Controlled Trial of the Effect of Broccoli Sprouts on Antioxidant Gene Expression and Airway Inflammation in Asthmatics. *J Allergy Clin Immunol Pract* **4**, 932–940 (2016).
 303. Bahadoran, Z. *et al.* Effect of broccoli sprouts on insulin resistance in type 2 diabetic patients: a randomized double-blind clinical trial. *Int J Food Sci Nutr* **63**, 767–771 (2012).
 304. Gabriel, D., Gordon, L. B. & Djabali, K. Temsirolimus Partially Rescues the Hutchinson-Gilford Progeria Cellular Phenotype. *PLoS ONE* **11**, e0168988 (2016).

305. Cenni, V. *et al.* Autophagic degradation of farnesylated prelamin A as a therapeutic approach to lamin-linked progeria. *Eur J Histochem* **55**, e36 (2011).
306. Akinci, B. *et al.* Progeroid syndrome patients with ZMPSTE24 deficiency could benefit when treated with rapamycin and dimethylsulfoxide. *Cold Spring Harb Mol Case Stud* **3**, a001339 (2017).
307. Lowe, D. G. Distinctive image features from scale-invariant keypoints. *International Journal of Computer Vision* **60**, 91–110 (2004).
308. Zhang, H., Kieckhafer, J. E. & Cao, K. Mouse models of laminopathies. *Aging Cell* **12**, 2–10 (2013).
309. Bank, E. M. & Gruenbaum, Y. *Caenorhabditis elegans* as a model system for studying the nuclear lamina and laminopathic diseases. *Nucleus* (2011). doi:10.4161/nucl.2.5.17838
310. Koshimizu, E. *et al.* Embryonic senescence and laminopathies in a progeroid zebrafish model. *PLoS ONE* **6**, e17688 (2011).
311. Lieschke, G. J. & Currie, P. D. Animal models of human disease: zebrafish swim into view. *Nat. Rev. Genet.* **8**, 353–367 (2007).
312. Kaletta, T. & Hengartner, M. O. Finding function in novel targets: *C. elegans* as a model organism. *Nat Rev Drug Discov* **5**, 387–399 (2006).
313. Seok, J. *et al.* Genomic responses in mouse models poorly mimic human inflammatory diseases. *Proc. Natl. Acad. Sci. U.S.A.* **110**, 3507–3512 (2013).
314. Takao, K. & Miyakawa, T. Genomic responses in mouse models greatly mimic human inflammatory diseases. *Proc. Natl. Acad. Sci. U.S.A.* **112**, 1167–1172 (2015).
315. Takahashi, K. *et al.* Induction of Pluripotent Stem Cells from Adult Human Fibroblasts by Defined Factors. *Cell* **131**, 861–872 (2007).
316. Cho, S. W., Kim, S., Kim, J. M. & Kim, J.-S. Targeted genome engineering in human cells with the Cas9 RNA-guided endonuclease. *Nat Biotechnol* **31**, 230–232 (2013).
317. Jenny CY Ho *et al.* Generation of induced pluripotent stem cell lines from 3 distinct laminopathies bearing heterogeneous mutations in lamin A/C. *Aging (Albany NY)* **3**, 380 (2011).
318. Xiong, Z.-M., LaDana, C., Wu, D. & Cao, K. An inhibitory role of progerin in the gene induction network of adipocyte differentiation from iPS cells. *Aging (Albany NY)* **5**, 288–303 (2013).
319. Liu, G., Suzuki, K., Qu, J., Sancho-Martinez, I. & Yi, F. Targeted gene correction of laminopathy-associated LMNA mutations in patient-Specific iPSCs. *Cell Stem Cell* (2011).
320. Soldner, F. *et al.* Generation of isogenic pluripotent stem cells differing exclusively at two early onset Parkinson point mutations. *Cell* **146**, 318–331 (2011).
321. Bassett, A. R. Editing the genome of hiPSC with CRISPR/Cas9: disease models. *Mamm. Genome* 1–17 (2017). doi:10.1007/s00335-017-9684-9
322. Koh, C. M. Preparation of cells for microscopy using cytopsin. *Meth. Enzymol.* **533**, 235–240 (2013).
323. Mihara, K., Nakayama, T. & Saitoh, H. A Convenient Technique to Fix Suspension Cells on a Coverslip for Microscopy. *Curr Protoc Cell Biol* **68**, 4.30.1–10 (2015).
324. Deutsch, M. *et al.* A novel miniature cell retainer for correlative high-content

- analysis of individual untethered non-adherent cells. *Lab Chip* **6**, 995–6 (2006).
325. Price, H. P., MacLean, L., Marrison, J., O'Toole, P. J. & Smith, D. F. Validation of a new method for immobilising kinetoplastid parasites for live cell imaging. *Mol. Biochem. Parasitol.* **169**, 66–69 (2010).
 326. Sabati, T., Galmidi, B.-S., Korngreen, A., Zurgil, N. & Deutsch, M. Real-time monitoring of changes in plasma membrane potential via imaging of fluorescence resonance energy transfer at individual cell resolution in suspension. *J Biomed Opt* **18**, 126010 (2013).
 327. Fercher, A., O'Riordan, T. C., Zhdanov, A. V., Dmitriev, R. I. & Papkovsky, D. B. Imaging of cellular oxygen and analysis of metabolic responses of mammalian cells. *Methods Mol. Biol.* **591**, 257–273 (2010).
 328. Joshi, P. & Lee, M.-Y. High Content Imaging (HCI) on Miniaturized Three-Dimensional (3D) Cell Cultures. *Biosensors (Basel)* **5**, 768–790 (2015).
 329. Datar, A., Joshi, P. & Lee, M.-Y. Biocompatible Hydrogels for Microarray Cell Printing and Encapsulation. *Biosensors (Basel)* **5**, 647–663 (2015).
 330. Graf, R., Rietdorf, J. & Zimmermann, T. Live cell spinning disk microscopy. *Adv. Biochem. Eng. Biotechnol.* **95**, 57–75 (2005).
 331. Gao, L., Shao, L., Chen, B.-C. & Betzig, E. 3D live fluorescence imaging of cellular dynamics using Bessel beam plane illumination microscopy. *Nat Protoc* **9**, 1083–1101 (2014).
 332. Kriston-Vizi, J. & Flotow, H. Getting the whole picture: High content screening using three-dimensional cellular model systems and whole animal assays. *Cytom Part A* **91A**, 152–159 (2017).
 333. Castelein, N. *et al.* Experimental Gerontology. *EXG* **56**, 26–36 (2014).
 334. de Boer, R. *et al.* *Caenorhabditis elegans* as a Model System for Studying Drug Induced Mitochondrial Toxicity. *PLoS ONE* **10**, e0126220 (2015).
 335. Smith, R. L., De Vos, W. H., de Boer, R., Manders, E. M. M. & van der Spek, H. In vivo visualization and quantification of mitochondrial morphology in *C. elegans*. *Methods Mol. Biol.* **1265**, 367–377 (2015).
 336. Kwon, J. *et al.* Assurance of mitochondrial integrity and mammalian longevity by the p62-Keap1-Nrf2-Nqo1 cascade. *EMBO Rep* **13**, 150–156 (2012).

CURRICULUM VITAE
TOM SIEPRATH

Personalia

Tom Sieprath
Crijstraat 21
3590 Diepenbeek
België
January 30th 1987, Genk (Belgium)

Education

2011 – current:

PhD in Applied Biological Sciences: Cell and Gene Biotechnology. (Joint PhD at Ghent University and the University of Antwerp)

2009 – 2011:

Master of Science in Bioscience Engineering: Cell and Gene Biotechnology; Ghent University (Magna Cum laude)

2005 – 2008:

Bachelor in Biology; Hasselt University (Magna Cum Laude)

Scientific activities

Conferences & Workshops:

Flemish Training Network Life Sciences (FTNLS): Workshop Entrepreneurship in Life Sciences

07/05/2012 - 11/05/2012; Brussels (BE)

Attendee

12th European Light Microscopy Initiative (ELMI) Meeting

05/06/2012 - 08/06/2012; Leuven (BE)

Attendee + Poster

EMBO Practical Course: Analysis of High-Throughput Sequencing Data

29/10/12 - 03/11/12; Cambridge (UK)

Attendee + Poster

Inserm workshop #221: Genome engineering and targeting with artificial TALEs, Phase 1

24/04/2013 - 26/04/2013; Bordeaux (FR)

Attendee

Molecular Biology en Cytometry Course (MB&C)

16/05/2013 - 17/05/2013; Mol (BE)

Attendee + Presentation

VIBes in biosciences: International PhD Symposium
17/09/2014 - 19/09/2014; Antwerp (BE)
Attendee

Bio-image informatics
08/10/2014 - 10/10/2014; Leuven (BE)
Attendee + Poster

EMBO Workshop: A systems-level view of cytoskeletal function
27/10/2014 - 31/10/2014; Stockholm (SE)
Attendee + Poster

Molecular Biology en Cytometry Course (MB&C)
05/02/2015 - 06/02/2015; Antwerp (BE)
Attendee + Presentation

Interuniversity Stem Cell Meeting
20/04/2015; Leuven (BE)
Attendee

BSM vzw Annual Meeting 2015: When Materials Meet Biology
11/09/2015; Mons (BE)
Attendee + Presentation

EMBO Conference: Nuclear structure and dynamics
07/10/2015 – 11/10/2015; L'Isle sur la Sorgue (FR)
Attendee + Poster

Specialist courses Doctoral School of Life Sciences and Medecine: Light and
Fluorescence Microscopy
05/09/2016 – 07/09/2016; Ghent (BE)
Presentation

Molecular Biology en Cytometry Course
23/03/2017 - 24/03/2017; Antwerp (BE)
Presentation

The Pleiotropic Nuclear Envelope
22/08/2017 – 25/08/2017; Edinburgh (UK)
Attendee + Poster

Student supervision and training

2012 – 2013	Ludger Goeminne: Cellulaire stressrespons onder invloed van interferentie met lamine A-maturatie
2013 – 2014	Joke Robijns: Ontwikkeling van genome editing constructen voor de creatie van laminopathie modelcellijnen Sara Devos: Ontwikkeling van genome editing constructen voor de creatie van laminopathie modelcellijnen Sam Donche, Ophelia Gevaert, Marie-Gabrielle Goossens, Laura Vercauteren: De rol van lamines in cellulaire veroudering
2014 – 2015	Michaël Mostaert: Ontwikkeling van stabiele modelcellijnen voor de studie van laminopathiën
2015 – 2016	Jon Hughe: De generatie en karakterisatie van genome-edited modelcellijnen voor laminopathieën

Scientific output

1. Sieprath, T., Darwiche, R. & De Vos, W. H. Lamins as mediators of oxidative stress. *Biochem. Biophys. Res. Commun.* 421, 635–639 (2012).
2. Sieprath, T. et al. Sustained accumulation of prelamin A and depletion of lamin A/C both cause oxidative stress and mitochondrial dysfunction but induce different cell fates. *Nucleus* 6, 236–246 (2015).
3. Sieprath, T. *et al.* Integrated High-Content Quantification of Intracellular ROS Levels and Mitochondrial Morphofunction. *Adv Anat Embryol Cell Biol* 219, 149–177 (2016).
4. Robijns, J. et al. In silico synchronization reveals regulators of nuclear ruptures in lamin A/C deficient model cells. *Sci Rep* 6, 30325 (2016).
5. Corne, T. D. J. et al. Deregulation of focal adhesion formation and cytoskeletal tension due to loss of A-type lamins. *Cell Adh Migr* 91, 1–17 (2016).
6. Sieprath, T. *et al.* Cellular Redox Profiling Using High-content Microscopy. *J Vis Exp* e55449 (2017).
7. Vanlancker, E. *et al.* Oral microbiota reduce wound healing capacity of epithelial monolayers, irrespective of the presence of 5-fluorouracil. ~ *Submitted*
8. Sieprath, T. *et al.* Persistent perturbation of A-type lamin metabolism induces oxidative stress by proteasome inhibition pathways. ~ *In preparation*